

**UCLA**

**UCLA Electronic Theses and Dissertations**

**Title**

Investigation of Non-Linear Energy Transfer Dynamics of Erbium in Yttrium Aluminum Garnet

**Permalink**

<https://escholarship.org/uc/item/7q43x3pk>

**Author**

Vega, Christian

**Publication Date**

2018

Peer reviewed|Thesis/dissertation

UNIVERSITY OF CALIFORNIA

Los Angeles

Investigation of Non-Linear Energy Transfer Dynamics  
of Erbium in Yttrium Aluminum Garnet

A dissertation submitted in partial satisfaction of the  
requirements for the degree Doctor of Philosophy  
in Electrical Engineering

by

Christian Vega

2018

© Copyright by

Christian Vega

2018

## ABSTRACT OF THE DISSERTATION

Investigation of Non-Linear Energy Transfer Dynamics  
of Erbium in Yttrium Aluminum Garnet

by

Christian Vega

Doctor of Philosophy in Electrical Engineering

University of California, Los Angeles, 2018

Professor Oscar M. Stafsudd, Chair

Yttrium Aluminum Garnet (YAG,  $Y_3Al_5O_{12}$ ) crystals doped with Erbium have posed an interesting position in the field of rare earth solid state lasers as they possess the property of self-saturation, in which the upper energy level in a laser has a much shorter lifetime than that of the lower level. This is the case of the  $2.94\mu\text{m}$  transition in Er:YAG. That property at first seems to make this material unfit for use as a laser gain medium, however further research into these classes of rare earth materials revealed interesting non-linear energy transfer mechanisms that allow it to be a useful mid wave infra-red (MWIR) coherent source in the continuous wave (CW) and pulsed regimes. This came to fruition due to decades of modeling and spectroscopic research investigating the non-linear energy transfer mechanisms of excited state absorption (ESA), energy transfer up-conversion (ETU), and cross relaxation (XR). These effects show up in the

rise and fall times of the levels observed through fluorescence. Resulting in the non-exponential rise and fall characteristics and having a squared or even cubed relation to the population. The population evolution for each of the lasing levels is now affected by ions recycling energy and in turn cause the lifetimes of the levels to “effectively” change to a point where simple linear models do not adequately describe the system and its performance.

The non-linear energy transfer dynamics of Er:YAG are modeled under high resonant pump conditions. By pumping with selective resonant pumps, the interaction dynamics of the  $^4I_{11/2}$  and the  $^4I_{13/2}$  levels in the Erbium ion reveal the contributions from generally ignored non-linear energy transfer mechanisms. Specifically, the multi-photon effect known as excited state absorption (ESA) is modeled by measuring and characterizing the cross section in single crystal Er:YAG samples utilizing a pump and probe technique coupled with transient fluorescence measurements. The measured ESA cross section is then included in the rate equation modeling.

The dissertation of Christian Vega is approved.

Yuanxun Ethan Wang

Tatsuo Itoh

Gregory P. Carman

Oscar M. Stafsudd, Committee Chair

University of California, Los Angeles

2018

# Dedication

To my family that has supported me since I began this long journey into engineering. Without your love and support I would not be the person I am today nor, would I have achieved my goals. Thank you all for being there.

To my aunt and second mother Argentina Obando, who regrettably could not see me achieve my goals at the end of this journey. I will never forget all the support and encouragement you provided during my time as a student. May you rest in peace.

# Table of Contents

<b>1. Background</b>	<b>1</b>
1.1. Review of Energy Transfer Mechanisms.....	4
<b>2. Mathematical Evaluation of the Er:YAG System</b>	<b>13</b>
2.1. Background on Spectroscopically Characterizing Er:YAG.....	13
2.2. Rate Equation Modeling of the Er:YAG System.....	22
2.3. Figures of Merit.....	28
2.4. Rate Equation Simulations.....	33
2.5. Excited State Absorption Modeling.....	43
2.6. Error & Sensitivity Analysis.....	50
2.7. Concluding Remarks.....	51
<b>3. Experimental Setup &amp; Results</b>	<b>52</b>
3.1. Experimental Setup for Measuring Fluorescent Instability.....	53
3.2. Experimental Setup for Measuring Excited State Absorption.....	72
<b>4. Analysis of the Fluorescence Instability &amp; Impact on Modeling</b>	<b>80</b>
4.1. Rate Equation Simulations with Ion-Ion and Measured ESA Interactions.....	80
4.2. Third Order Ion-Ion Effects.....	87

<b>5. Pathway Forward on Characterizing Er:YAG</b>	<b>89</b>
<b>Appendix A: Additional Simulation &amp; Experimental Scans</b>	<b>95</b>
A.1 Additional Rate Equation Simulations.....	95
A.2 Analogy of Fluorescence Instability to an Astable Oscillator Circuit.....	112
<b>Appendix B: Equipment List &amp; Parameters</b>	<b>114</b>
<b>Appendix C: Additional Experimental Transient Scans</b>	<b>117</b>
C.1 808nm Pulsed Pumped 1% Er:YAG Pillbox with No 3 $\mu$ m Laser.....	118
C.2 808nm CW Pumped 1% Er:YAG Pillbox with No 3 $\mu$ m Laser.....	144
C.3 808nm Pulsed Pumped 50% Er:YAG Pillbox with No 3 $\mu$ m Laser.....	165
C.4 808nm CW Pumped 50% Er:YAG Pillbox with No 3 $\mu$ m Laser.....	191
C.5 808nm Pulsed Pumped 50% Er:YAG Wave Guide with No 3 $\mu$ m Laser.....	212
C.6 808nm CW Pumped 50% Er:YAG Wave Guide with No 3 $\mu$ m Laser.....	238
C.7 Pump Beam Profiles.....	259
<b>Appendix D: Simulation Code</b>	<b>264</b>
D.1 Rate Equation Code .....	264
D.2 ESA Measurement Code .....	277
D.3 Transient Scan Code .....	278
<b>Bibliography</b>	<b>290</b>

# List of Figures

1.0 Er:YAG Energy Level Diagram .....	4
1.1 Forster Energy Transfer Diagram .....	6
1.2 Dexter Energy Transfer Diagram .....	6
1.3 Cooperative Absorption Diagram .....	7
1.4 Cooperative Luminescence Diagram .....	7
1.5 Cross Relaxation Diagram (Favorable & Unfavorable) .....	7
1.6 Energy Transfer Up-Conversion Diagram (Favorable & Unfavorable) .....	8
1.7 Two-Level Energy Diagram Depicting ETU & XR .....	9
1.8 Two-Level Energy Diagram Depicting ESA .....	12
2.1a Er:YAG Energy Diagram Depicting Possible Third Order Transitions .....	19
2.1b Er:YAG Energy Diagram Depicting Possible ESA Transitions by Wavelength .....	20
2.2 Normalized Fluorescence vs. Varying Pump Intensity .....	21
2.3 Approximate Population Inversion vs. Pump Rate .....	29
2.4 Ratio of Intrinsic Oscillation Threshold to Oscillation Threshold .....	32
2.5 Simulated Input Pump Intensity with Added Gaussian Noise .....	37
2.6 Transient $N_2$ Response .....	38
2.7 Expanded View of transient $N_2$ Response to Show Instability .....	39
2.8 FFT of transient $N_2$ Response .....	40
2.9 Expanded View of transient $N_5$ Response to Show Instability .....	41
2.10 FFT of transient $N_5$ Response .....	42
2.11 Simulated Input Pump Intensity with White Gaussian Noise .....	45
2.12 Transient $N_2$ Response (Including ESA) .....	46

2.13 Expanded View of transient N <sub>2</sub> Response to Show Instability (Including ESA)	47
2.14 FFT of transient N <sub>2</sub> Response (Including ESA)	48
2.15 Expanded View of transient N <sub>5</sub> Response to Show Instability (Including ESA)	49
2.16 FFT of transient N <sub>5</sub> Response (Including ESA)	50
3.1 Transient Scan of 50% Er:YAG Pillbox Pumped by the 962nm laser	54
3.2 Pumping Scheme for A Thick Sample vs. a Thin Sample	60
3.3 Pillbox and Waveguide Sample Geometry	61
3.4 Original and Modified Measurement Setup for Fluorescence Instability	64
3.5 Thermally Stabilized 962nm Pump Spectra	65
3.6 Thermally Stabilized 808nm Pump Spectra	65
3.7 Transient Scan of 808nm Pump Beam	66
3.8 FFT of Transient Scan of 808nm Pump Beam	67
3.9 Transient Scan of <sup>4</sup> I <sub>11/2</sub> Fluorescence from 50% Er:YAG Pillbox	68
3.10 FFT of <sup>4</sup> I <sub>11/2</sub> Fluorescence from 50% Er:YAG Pillbox	69
3.11 Transient Scan of <sup>4</sup> S <sub>3/2</sub> Fluorescence from 50% Er:YAG Pillbox	70
3.12 FFT of <sup>4</sup> S <sub>3/2</sub> Fluorescence from 50% Er:YAG Pillbox	71
3.13 Er:YAG Energy Level Diagram with Common ESA Pathways	77
3.14 Pump and Probe Measurement Setup	78
3.15 Transient Scan of Pump and Probe Measurement	79
4.1 Er:YAG Energy Level Diagram with Common ESA Pathways	80
4.2 Simulation of <sup>4</sup> I <sub>11/2</sub> Level Under 808nm Pump and No ESA	83
4.3 FFT of <sup>4</sup> I <sub>11/2</sub> Level Simulation	84
4.4 Simulation of <sup>4</sup> I <sub>11/2</sub> Level Under 808nm Pump with ESA	85
4.5 FFT of <sup>4</sup> I <sub>11/2</sub> Level Simulation with ESA	86
4.6 Example Fluorescence Yield Plot with Non-Exponential Rise & Decay	88

5.1 Laser Amplifier Setup.....	93
5.2 Laser Resonator Setup.....	94
5.3 Laser Chaos Measurement Setup.....	94

# List of Tables

2.1 Parameter Values for Simulations.....	36
3.1 Er:YAG Sample List.....	55

## Acknowledgements

I would personally like to thank Professor Oscar Stafsudd, my advisor, who has provided exceptional, guidance, wisdom, and support during my time as a graduate student. Without your unwavering patience, off the cuff humor, and methodical wisdom I would not have been able to overcome the anxiety and stress that comes with being a graduate student. The times I spent learning under your tutelage fundamentally shaped how I view the field of engineering. The amount of knowledge I gained will stay with me forever and solidifies my belief that attending UCLA and having you as an advisor was the best decision that I have made in my professional career. I am a much better engineer and educator because of you. I would formally would like to extend my gratitude to Jacquie Stafsudd, Oscar's wife, who has also been very supporting. Your unique wisdom on life during graduate school and in industry has motivated me to tackle whatever challenges I will encounter in my professional career. Both of you have helped me through my stressful years as a student and ultimately gave me the strength to reach the coveted finish line of my dissertation defense. I will cherish all the guidance and memories that I have gained in this chapter in my life and with Professor Stafsudd's retirement, I sincerely wish them the best in their new chapter in life. It was an honor learning from both of you and gaining your friendship.

I would like to express my gratitude in the guidance and support from Dr. Ramesh Shori. Your advice on my thesis experiments were fundamental to my successful dissertation defense. I would literally have not been able to conduct my experiments without the Erbium samples, particularly the 50% waveguide sample, or the power supplies, oscilloscopes, optical choppers, pump lasers, filters, and all other misc. equipment I had to borrow. I am very appreciative of

your patience you exercised as I managed my time between my teaching apprenticeship, my internship, and conducting my research. The input you and Professor Stafsuud provided on my experiments proved to be very fruitful in terms of the results. I hope the data provided in this work will aide in any future endeavors you may have. I am also very appreciative for you sitting on my dissertation committee as an invited guest. Much like the guidance Professor Stafsuud provided, the guidance provided by Dr. Shori is invaluable to my growth in my professional career and is a constant reminder to maintain focus as I move forward.

Other individuals who helped in my thesis work were Dr. Brad Liu and Dr. Asael Papour. I would like to thank you for mentoring me during my time as a master's student and helping me acclimatize myself to life at UCLA as a graduate student. Dr. Liu provided unique guidance as his work serves as foundation for the work presented in this thesis. I am very appreciative of him allowing me to use some of his plots from his thesis (reference 1). My deepest gratitude to the both of you and my best wishes for your future endeavors.

I cannot have an acknowledgement section without personally thanking the administrative staff that has helped me during my time at UCLA. Ms. Deeona Columbia, Mr. Ryo Arreola, Julio Vega, Mandy McWeeney, Jose Cano, Joshua Ramos, Maria Guerrero, and whoever else I might have missed, thank you for all the help. It could have been something that might have seemed small and insignificant though it went a long way. Your professionalism and kindness made my experience at UCLA very memorable. Deeona and Ryo I am personally indebted to you for all the guidance and assistance provided in my times of need. You made my pathway to graduation much simpler ensuring I would get all my forms in on time.

The rest of the committee members that were able to find time in their busy schedules to be a part of this effort, thank you. I would especially like to thank Dr. Ethan Wang for being able to sit on my committee last minute and substitute Dr. Warren Grundfest, who I am appreciative of sitting on my qualification exam. It was unfortunate that you were not able to sit on my committee for my final defense. I wish the best for all of you.

I would like to go back to my years as a high school student at Ranch High School in Las Vegas, Nevada and my time as an undergraduate student at the University of Nevada, Las Vegas, thank you to my high school calculus teacher Mrs. Susan Corbett for being a strong influence in my appreciation and understanding of the mathematical sciences. I would like to thank my engineering professors Dr. Robert Schill, Dr. Jacob Baker, Dr. Sahjendra Singh, Dr. Muthukumar Venkatesan, Dr. Pushkin Kachroo, Dr. Yahia Baghzouz, and Dr. Biswajit Das along with lab director and manager Mr. Brandon Blackstone. It was a pleasure being in your classes as it built the foundations that I stand on today as a professional.

To my friends at UCLA Mathew Biedka, Harrison Cheng, Eric Stocker, Emma Hurst, Arpi Beshlikyan, Jean Paul Santos, Bach Vu, Tim Wilson, Keita Nagashima, Wisley Yang, Aria Sarraf, Samuel Barclay, Mustafa Daloglu, Donovan and Doug from XDR, and Sina Basir-Kazeruni thank you for making graduate school enjoyable as I maneuvered the obstacles it posed.

Finally, to my family, again I am very thankful to have such caring people in my life. All the patience and care has seemed to pay off. I will continue to cherish the wonderful memories as I create new ones with you and move forward in my career. You out all the people in my life deserve the greatest credit for being there every single step of the way.

## VITA

2009-2013

B.S. Electrical Engineering  
University of Nevada, Las Vegas

2013-2015

M.S. Electrical Engineering  
University of California, Los Angeles

2014-2018

Teaching Assistant  
University of California, Los Angeles  
Department of Electrical Engineering

2015-2018

Systems Engineering Intern  
Northrop Grumman Aerospace Systems

2018-

Optical Systems Engineer  
Northrop Grumman Aerospace Systems

# Chapter 1

## Background

The goal of this thesis is to incorporate dynamic instabilities, that appear as oscillations in the fluorescence under resonant optical pumping due to energy transfer mechanisms in Er:YAG, to provide a more accurate mathematical modeling capability. Examples of this fluorescence oscillation (instability) are provided in appendix C with the experimental setup explained in chapter 3 section 1. Ultimately the continued analysis of this rare-earth single crystal system, which began many decades ago, will lead to a rate equation model that accurately accounts for all relevant physical phenomena that influences the lasing behavior. Iteration of established models with transient spectroscopic data presented in this thesis are but a piece of the growing knowledge base into the study of rare-earths with hopes of an eventual definitive closed form solution. With that it is important to first review the history into the study of rare-earths for use in infra-red (IR) light sources.

In the world of coherent infra-red sources there is a need for sources that emit mid-wave infra-red (MWIR) radiation, typically defined as 2-5 $\mu\text{m}$ . The usefulness of such wavelengths comes from applications in materials processing, defense, and the biomedical sciences [1-3,7-11, 13, 17]. Diode lasers have provided a cost-effective means in generating infra-red light though, due to physical limitations, are stalled around the short wave infra-red (SWIR). Beyond that band has been the territory of solid state and fiber lasers such as Holmium and Thulium in glass and in YAG [4-9]. Anything beyond in the mid to long wave infra-red (MWIR – LWIR) is the domain

of quantum cascade lasers (QCLs) and gas lasers. Unfortunately, QCLs generally require bulky and expensive cryogenic cooling systems to operate and output up micro joule level. While gas lasers require large high voltage power supplies and large lengthy cavities to acquire enough gain for its operating modes. Given the limitations of the available technology a compact system that operates at more manageable temperature and power ranges has been desired. Current work that has focused on these issues has been centered on rare earth doped solid state lasers. Erbium in YAG is one such example as its' unique energy structure allowed for generation of MWIR light in the CW and pulsed regimes [10-18, 34-37, 41, 42] at the 2.94 $\mu$ m wavelength.

Er:YAG was first heavily researched for its' laser line at 2.94 $\mu$ m which is a useful wavelength corresponding to the  $^4I_{11/2} \rightarrow ^4I_{13/2}$  transition. A strong water absorption line which leads to non-invasive dentistry and skin treatments [2, 3]. At the start of the extensive research into Er:YAG, in the 70's and 80's, most of the work in that era was conducted in the eastern bloc nations under the Soviet Union as there was a dual use for commercial communications and defense applications in tracking and countermeasures for munition guidance systems. Valuable spectroscopic measurements and modeling data have been achieved during this era on the other side of the iron curtain [22, 35-42]. Given this need, typical laser metrics for Er:YAG host materials are available, stemming from the plethora of past work that derived: emission cross-section, fluorescence lifetimes, cross-relaxation rates, up conversion rates, and the rate equations [15-34]. During the telecommunications boom Er:YAG was investigated for its  $^4I_{13/2} \rightarrow ^4I_{15/2}$  transition corresponding to the 1.6 $\mu$ m transition [13], which was used in commercial fiber optic communications. The electronics and photonics industries invested heavily into diode development for cheap sources in the near infra-red regime (NIR).

Focus was shifted back to the 2.94 $\mu\text{m}$  wavelength. As the research continued, certain drawbacks have prevented full scale use of the material, mainly the undesirable lifetimes of the  $^4\text{I}_{11/2}$  and  $^4\text{I}_{13/2}$  laser levels. The cause is the condition known as self-saturation, in which their lifetimes are inverse of what is needed for laser action to occur. In this case the terminal  $^4\text{I}_{13/2}$  level possess a much larger lifetime (order of magnitude difference) than that of the initial  $^4\text{I}_{11/2}$  level. Conventional wisdom would lead one to believe that this self-saturated material is not useful for lasing, as one requires the terminal laser level ions to quickly decay to ground and allowed to be pumped back into the initial laser level. Hence optical gain can be extracted from the material under resonant pump. Fortunately, Erbium possesses a unique energy band structure that allows non-linear energy transfer processes to take hold and effectively change the lifetimes of the laser levels allowing the material to be used for lasing action. Figure 1.0 provides an energy band diagram utilized in reference [1]. This figure along with select others from reference [1] have been included with permission by Dr. Brad Liu, the author of [1]. Detail about its structure will be explained throughout this thesis beginning with the following section.

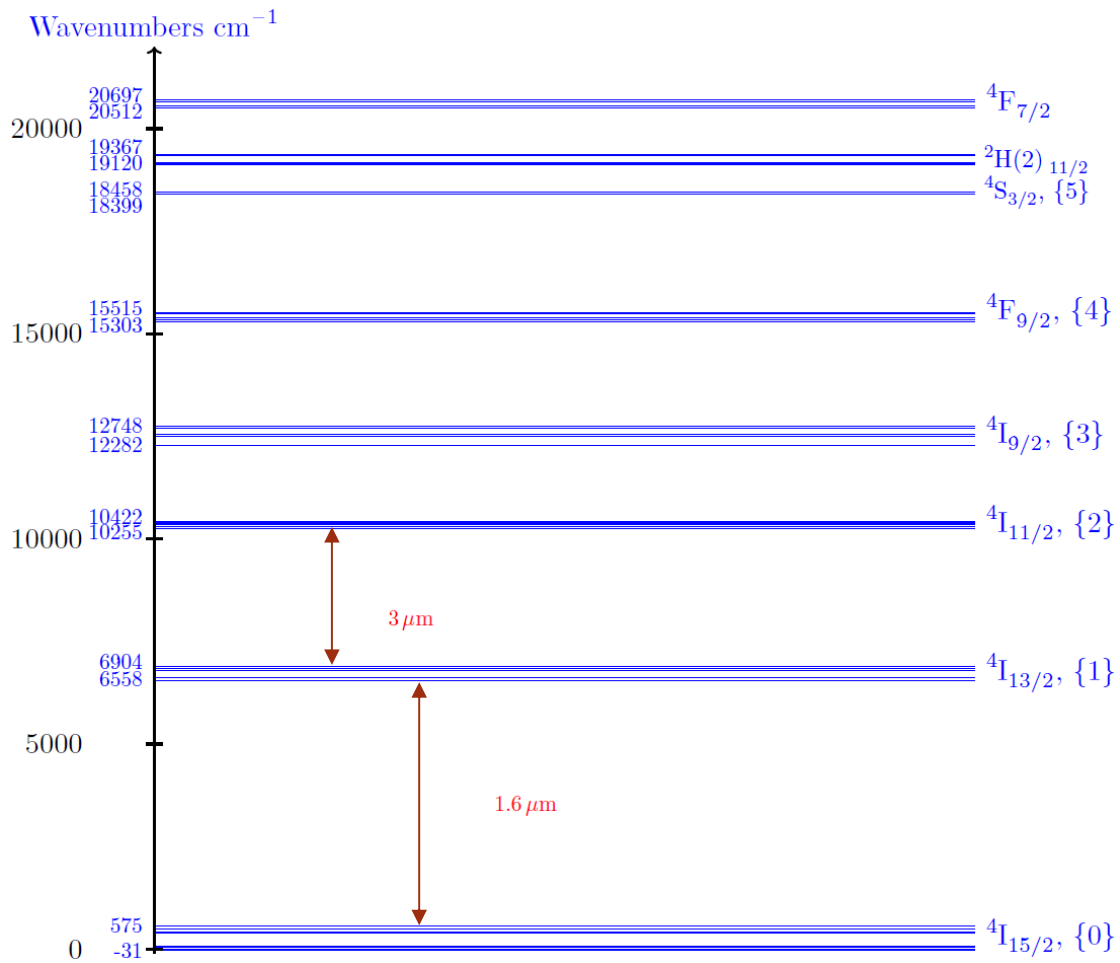


Figure 1.0 The energy diagram of Er:YAG showing the two major laser transitions used.

Included with permission from Dr. Liu [1].

## 1.1 Review of Energy Transfer Mechanisms

Before exploring the spectroscopic characteristics of Er:YAG a review of energy transfer dynamics is necessary to layout a foundation of the modeling presented in chapter 2. The main foundation of energy transfer between ions can be traced back to the study of intermolecular

energy transfer between Tripaflavin and Rhodamine B done in 1948 by Forster [45]. The energy transfer is a resonant one which the molecules can be modeled as dipole-dipole interactions. The strength of the interaction was found to be inversely proportional to the intermolecular distance to the sixth power,  $r^{-6}$ . However energy transfer in solid-state materials, particularly Erbium and its rare earth counterparts, can occur through forbidden states. Ions can exchange energy amongst their neighbors through various non-radiative processes. This was theorized by Dexter in 1953 [43], and subsequently modified a little over a decade later to include higher order multipolar exchanges [46]. This work demonstrated the non-exponential decay in fluorescence that results from the ion-ion interaction. The experiments carried out led to the observation of cooperative absorption, where a single photon can excite multiple ions. The energy at which these ions are excited sum to the energy of the pump photon. This resonant optical absorption effect was theoretically modeled by Dexter [44]. This model revealed that effect was dependent on the dipole-dipole interaction and was indifferent of the ion type. Thus, dissimilar ions can transfer energy to each other. In the case of Erbium these co-dopants, usually impurities in the form of other rare earths, can effectively change the lifetime of the  $^4I_{13/2}$  dramatically [1,16-22]. A reverse process is possible called cooperative luminescence, which is utilized to demonstrate a laser that was co-doped with four different rare earths and made to lase at two separate wavelengths, 2.1 $\mu\text{m}$  and 2.9 $\mu\text{m}$  [14]. Figures 1.1 and 1.2 show diagrams illustrating the Forster and Dexter energy transfer processes respectively. Figures 1.3 and 1.4 demonstrate cooperative absorption and its reverse process cooperative luminescence respectively.

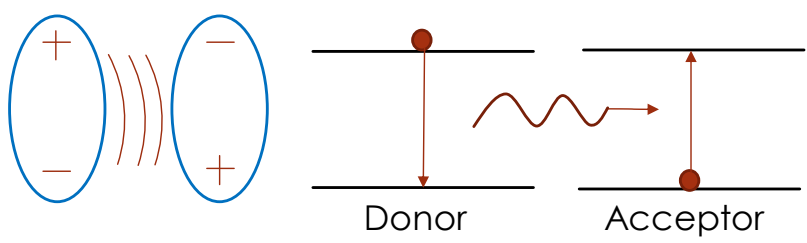


Figure 1.1 Diagram depicting Förster Energy Transfer

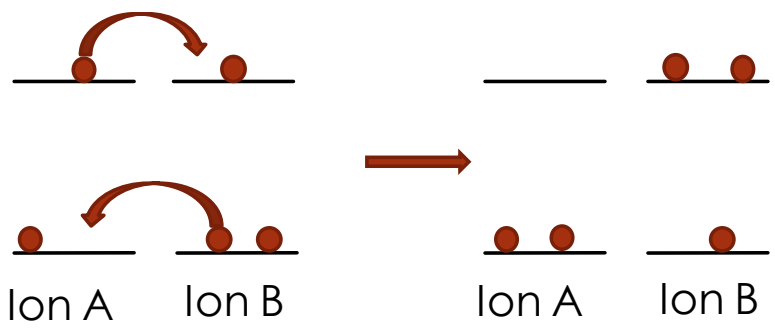


Figure 1.2 Diagram depicting Dexter Energy Transfer

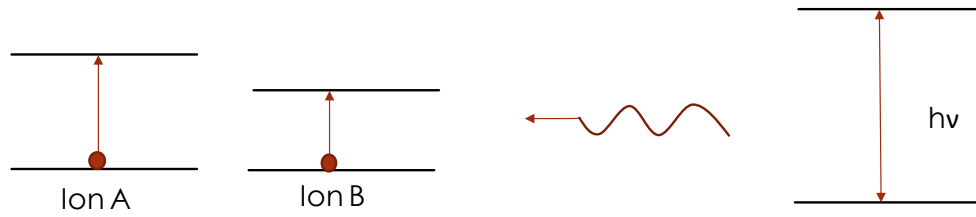


Figure 1.3 Cooperative absorption showing a single photon of energy  $h\nu$  being absorbed by two ions whose energy bands taking part in the action sum to the photon energy.

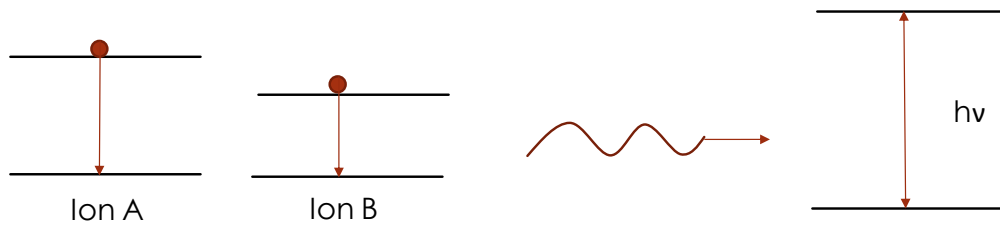


Figure 1.4 Cooperative luminescence, reverse of figure 1.3, showing two excited ions emitting a single photon of energy  $h\nu$  that is the sum of the energy drops of the two ions.

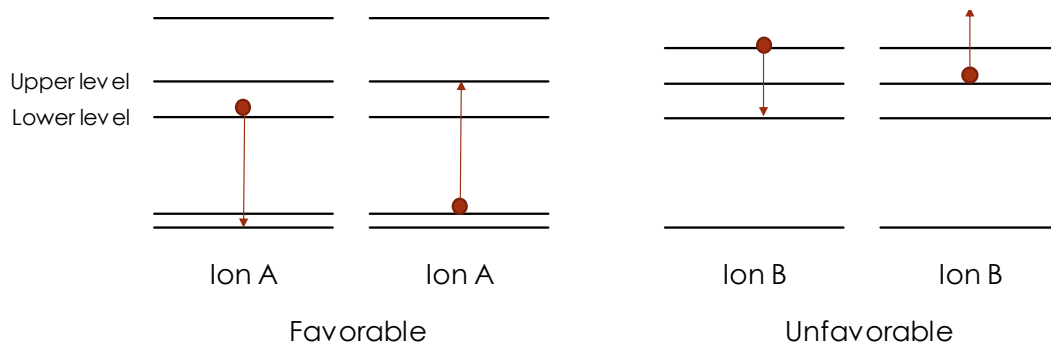


Figure 1.5 Diagram depicting Cross Relaxation (XR) of the (a) favorable and (b) unfavorable kind.

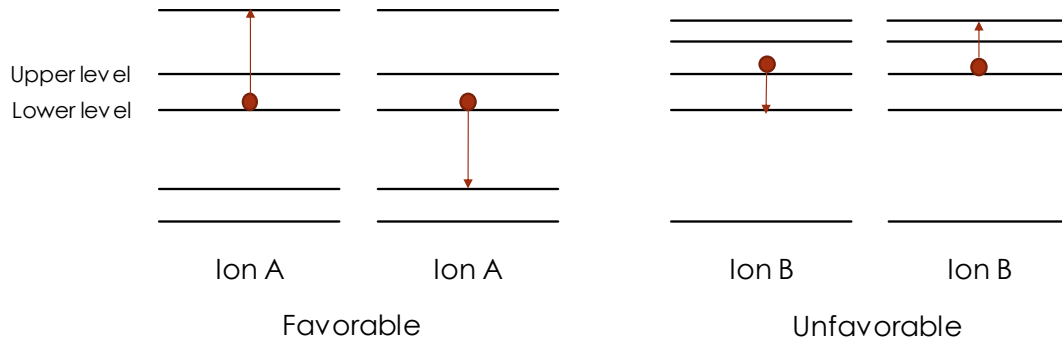


Figure 1.6 Diagram depicting Energy Transfer Up-conversion (ETU) of the (a) favorable and (b) unfavorable kind.

These ion-ion mechanisms form the foundation of the parameters used in the laser rate equations, namely cross-relaxation (XR) and energy transfer up-conversion (ETU). Where by a non-radiative decay of an ion is resonant with a separate transition level of a neighboring ion. The ions themselves do not have to be exclusively of the same type [22,47]. These processes are shown in figures 1.5 and 1.6. More explicitly, figure 1.7 shows the visualization of the mathematical expression that is used in rate equation modeling, as seen in equations 1.1 and 1.2, ETU and XR have a  $N^2$  dependence. Which demonstrates that these processes involve two ions. It is noted that the  $E_1$  population level has a factor of two for the ETU and XR terms due to two ions either being excited or deexcited to or from that level respectively, as shown in figure 1.5. It is important to also note that excited state absorption (ESA), which will be mentioned shortly, will also give effectively the same dependence in a single ion scenario. Higher order effects in the form of three or four ion interactions can occur, though these effects can generally be neglected [1,24]. What can also be deduced is that ETU and XR are complimentary processes of each other. Whether ETU or its reverse process takes hold in a certain situation is tied to the pump scheme [16-32]. In addition, there are favorable and unfavorable energy transfer processes

dependent on the pump scheme. This is also the case for the next energy transfer process which will be discussed which is excited state absorption (ESA).

$$\frac{dN_{2,ETU}}{dt} = W_{11}N_1^2 \quad (1.1a)$$

$$\frac{dN_{1,ETU}}{dt} = -2W_{11}N_1^2 \quad (1.1b)$$

$$\frac{dN_{0,ETU}}{dt} = W_{11}N_1^2 \quad (1.1c)$$

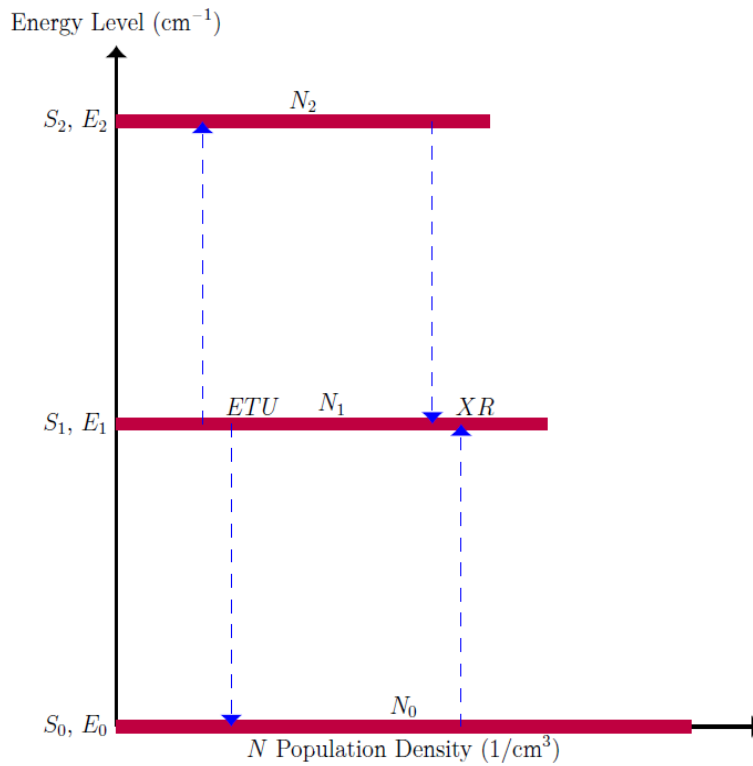


Figure 1.7 Accompanying energy diagram to equations 1.1 and 1.2 showing the relation of the ion-ion transfer mechanisms to the different energy levels of this system. Note in this example the  $S_1$  level loses two ions to ETU but gains two from XR (Included with permission from author of reference [1]).

$$\frac{dN_{2,XR}}{dt} = -W_{20}N_1N_0 \quad (1.2a)$$

$$\frac{dN_{1,XR}}{dt} = 2W_{20}N_1N_0 \quad (1.2b)$$

$$\frac{dN_{0,XR}}{dt} = -W_{20}N_1N_0 \quad (1.2c)$$

In contrast to ETU and XR, ESA is an interaction of an already excited ion to reach a higher energy level than that of the corresponding pump photon. This is due to an energy gap that is formed between an excited level and a higher energy level that is resonant to the pump photon energy. Therefore, the energy gap from the ground to the excited level is the same as the gap from the excited level to the specific higher level. To illustrate the example, let us consider a three-level system with levels  $S_2$ ,  $S_1$ , and  $S_0$ . Their energies are  $E_2$ ,  $E_1$ , and  $E_0$  respectively and have population densities  $N_2$ ,  $N_1$ , and  $N_0$  as shown in figure 1.8. With that we have the band gaps  $\Delta E_{10} = E_1 - E_0$  and  $\Delta E_{21} = E_2 - E_1$ . Although as stated before, to have ESA the upper band gap must equal the lower one, therefore  $\Delta E_{21} = \Delta E_{10}$ . Furthermore, it can be seen that two photons are required to reach the upper level. As a result, the population of the upper level,  $N_2$  is proportional to the pump intensity squared,  $I_0^2$ . This relationship can be generalized to a n-photon system with the population of the upper level proportional to  $I_0^n$ . This was shown to be the case as demonstrated by Liu [1].

With these mechanisms, the energy can be “recycled” to a higher level to be re-emitted as a photon, even at an energy higher than the pump photon. This is the case in Er:YAG with a NIR resonant pump that causes an observable green fluorescence [1]. It is important to stress that since these processes are non-linear with their relation to the pump or population of a level, the rise and fall behavior of the fluorescence of such a system is no longer linear. The influences

these processes have on the fluorescence has been reviewed by Liu [1]. The main foundation of traditional fluorescence rate equation modeling assumes that the ground population can be considered fixed. Though in certain situations, such as heavy pumping and high doping, certain materials have a varying ground population due to these non-linear mechanisms. Using the system depicted in figure 1.7 and 1.8 the rate equation system can be derived as stated in [1].

The resulting system of rate equations includes the non-linear terms,  $\alpha_0$  the ESA rate,  $W_{11}$  the ETU rate and,  $W_{20}$  the XR rate. These rates under resonant high pump will effectively change the apparent fluorescence lifetime rate of the lasing levels. As can be noted from the rate equations, as the population grows the non-linear terms begin to dominate. This is attributed to the  $N^2$  relation, indeed even the ESA can be expressed in terms of  $N^2$  [1]. These mechanisms play a critical role in the spectroscopic behavior of Er:YAG which will be described in detail throughout this thesis.

$$\frac{dN_2}{dt} = -\frac{N_2}{\tau_2} + \alpha_1 I N_1 + W_{11} N_1^2 - W_{20} N_2 N_0 \quad (1.3a)$$

$$\frac{dN_1}{dt} = \frac{N_2}{\tau_{21}} - \left( \alpha_1 I - \frac{1}{\tau_1} \right) N_1 + \alpha_0 I N_0 - 2W_{11} N_1^2 + 2W_{20} N_2 N_0 \quad (1.3b)$$

$$\frac{dN_0}{dt} = \frac{N_2}{\tau_{20}} + \frac{N_1}{\tau_1} + \alpha_0 I N_0 + W_{11} N_1^2 - W_{20} N_2 N_0 \quad (1.3c)$$

$$\frac{1}{\tau_2} = \frac{1}{\tau_{21}} + \frac{1}{\tau_{20}} \quad (1.3d)$$

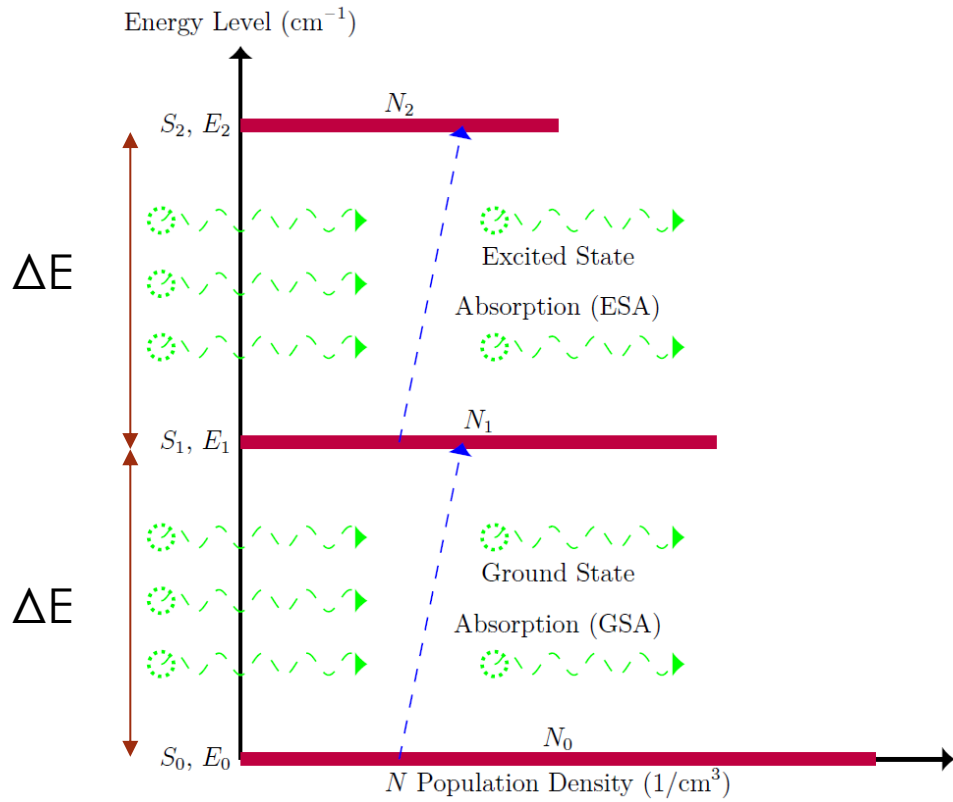


Figure 1.8: Accompanying energy diagram for equations 1.3 showing the relation of typical ground state absorption (GSA) under pumping with intensity  $I$  and ESA possible through the energy gap from level 2 to level 1 being equal to the one from level 1 to the ground state (Included with permission from author of reference [1]).

## Chapter 2

### Mathematical Evaluation of the Er:YAG System

The energy band structure of the Er:YAG system is rich in resonances that allow for ion-ion and multiphoton absorption process to develop that result in unique spectroscopic properties. Indeed, as demonstrated on various occasions lasing at  $2.94\mu\text{m}$  has been achieved under CW and pulsed operation with a variety of pump schemes [10-13, 35, 36]. Carefully selecting what pump scheme is used along with the doping profile of the crystal can significantly change what mechanisms are active and in turn affect the laser performance. This is the case for Erbium doped in a variety of inert solid-state host crystals which can be taken advantage of by selectively co-doping other rare earths to improve laser performance [7,15,19,21,32,43,47,55,63,78-84,86]. All these effects will be described to the extent of how they are included in the rate equations describing the Er:YAG system.

#### 2.1 Background on Spectroscopically Characterizing Er:YAG

In order to measure the non-linear effects outlined in chapter 1 for Er:YAG, the fluorescence output of each of the involved levels can be captured and analyzed for its transient behavior. Typically, the rise and fall time of the fluorescence response to a pulsed input is the metric used to characterize the lifetime of specific energy levels. Spectroscopic measurements carried out by Liu demonstrated the rise and fall behaviors are not a pure exponential and will differ from one another resulting from the different energy transfer mechanisms present [1]. Distinguishing the separate time constants in a fluorescence yield can be extremely difficult as a

large signal to noise ratio is required [54,75]. This is especially the case if there are multiple fluorophores present in the sample. In solid state crystal samples, the source of secondary fluorophores will come from impurities. Due to the unique structure of rare earths, when they co-mingle with each other, dependent on which pairs of elements are present, they can greatly quench or add fluorescence yield [5,7,8,15,19,29,55,60,63,84,86]. An excellent explanation of the matching parity wave functions mixing causing forbidden transitions to occur can be found in [74]. In certain cases, this phenomenon is taken advantage of to produce materials that fluoresce at previously unattainable wavelengths [16,17,64]. This of course are the ion-ion interactions we briefly discussed in chapter 1. Sample purity was of great concern due to its tendency of producing differing results in the same type of crystal with the difference being the manufacturing method and crystal grower [29]. With further advancements in material purity and preparation in the crystal growth industry, sample purity went from three or four 9's in the early nineties to five or six 9's in recent times [1]. It is important to distinguish that in this thesis sample purity is referred in the context of what is considered traditional impurities such as calcium or magnesium affecting the energy transfer processes. However, impurities in the form of rare-earths can be present based on the manufacturing method. The effect that these dopants have will vary with the Erbium doping. This is due to the unique properties of Erbium, namely that its atomic radius is of the similar order of magnitude to that of Yttrium which it replaces in the YAG structure. Therefore, the crystal field does not vary as much due to straining compared to doping with Neodymium which has an atomic radius much larger than Yttrium. For mid wave IR systems Erbium in YAG is usually doped at or above 15% atomic weight (at. wt.). Erbium doping percolates at around 15% at. wt. causing every Erbium ion to be in contact with all other Erbium ions through its neighbors. Erbium to Erbium interaction is "one jump" from each other

at these doping levels, interacting through the bulk material. This is despite the fact that interaction between ions occurs with a strength proportional to  $\frac{1}{r^6}$  with  $r$  being the atomic radius of the Erbium ion [1]. Therefore, very small impurities can affect the bulk as essentially the impurity is connected to the Erbium ions in the bulk. With the uncertainty of sample purity mitigated by more refined growth techniques and sample preparation the non-linear contributions to the fluorescence can be characterized with higher confidence.

Generally single exponential decays are expected when measuring fluorescence, though the energy structure of Erbium, and various other rare earths for that matter, allows for unique non-linear energy conversion mechanisms to take place, such as XR, ETU, and ESA. In Erbium these effects have been well documented [4,18-46,49,55-67,77-86], showing they cause changes in the lifetime in certain energy levels [1]. The diagrams in figure 2.1 shows possible mechanisms, some which have been simulated and measured [1,18-46]. As can be seen it is possible to excite ions that are in the  $^4I_{13/2}$  state and re-pump them to higher energy levels. They can then decay down to the  $^4I_{9/2}$  level which has a rapid non-radiative decay to the  $^4I_{11/2}$  level and populate this state. Then with its nominal lifetime the ions will decay downward either to the  $^4I_{13/2}$  state or the ground state. Where the repumping process occurs, the non-linear ESA, XR, and ETU will contribute based on the pump intensity and spectra coupled with sample doping. The result is an “effectively” longer lifetime for the  $^4I_{11/2}$  level which typically is around 100 $\mu$ s for 50% Er:YAG. Liu reported an “effective” lifetime of around 400 $\mu$ s for this level under heavy resonant pump (962nm). It is important to note that the actual natural lifetime does not change but that the net effect from the non-linear energy transfer mechanisms. Conversely the  $^4I_{13/2}$  level goes from a typical 1ms lifetime to around 800 $\mu$ s “effective” lifetime. Indeed, the non-linear ion-ion and multi-photon transfer mechanisms causes a greater than unity quantum efficiency that

helps overcome the self-saturation issue the  ${}^4I_{11/2} \rightarrow {}^4I_{13/2}$  laser transition has [1,24]. This is how the lifetimes change “artificially” to appear more favorable for lasing operation. A byproduct, in the case of strong 962nm pumping is a visible fluorescence in the green region. Red and blue fluorescence are also present, albeit much weaker [1]. As will be shown in this work strong pumping with 808 nm also starts a visible green fluorescence. These lifetimes of the RGB fluorescence have been previously recorded and are short compared to the lifetimes of the lower levels (labeled 1-5 in figure 2.1), leading to the justification in the rate equation modeling that upper levels relax rapidly [24].

It was shown in Liu’s measurements that the rise time for powdered (ceramic) and single crystal Er:YAG samples consisted of regular GSA coupled with ESA, XR, and ETU effects. While the fall time consisted of the natural decay coupled with XR and ETU effects [1]. These effects can be identified through observing the rise and fall times on a semi-log scale. A typical single time constant decay or rise will appear as a straight line. Non-linear effects such as ESA, XR, and ETU will influence the fluorescent behavior such that it has segmented slopes. In other words, the fluorescent behavior will appear as a piecewise function consisting of different linear segments of different slopes. What is particularly revealing is there appears to be a threshold input power along with the pump wavelength itself that triggers this behavior. It seems that 10 kW/cm<sup>2</sup> is the threshold from the experimentation done in [1]. Some of the samples from the batch used in reference [1] were used in the experiments carried out in this thesis.

To maximize the effects of ESA, XR, and ETU it is best to pump with NIR resonant sources, in our case a 962nm and 808nm pump laser diode are available. These wavelengths are of importance as it excites ions via  ${}^4I_{15/2} \rightarrow {}^4I_{11/2}$  energy level transition for the former and the  ${}^4I_{15/2} \rightarrow {}^4I_{9/2}$  transition followed by a rapid non-radiative decay to the  ${}^4I_{11/2}$  energy level for the

latter. As shown in figure 1.0 the  $^4I_{11/2}$  level forms the upper laser level for the 2.94 $\mu$ m transition. Therefore, direct pumping with a tuned source will be beneficial in contributing to the population inversion. The lucrative telecommunications industry has given way to commercial high-power laser diode sources that meet the requirement of direct pumping to the upper laser level. With these sources available it was natural to investigate the behavior of Er:YAG under different power levels. Under low pump intensities the natural fluorescence of the principle levels, as outlined in figure 2.1, were measured in [22-41]. The ion-ion interactions and multi-phonon non-radiative decays pose a smaller presence compared to GSA, and ESA when the doping concentration is low. Under light pumping there are less ions excited to upper levels therefore the probability an ion – ion interaction can occur is a much smaller effect due to the directly proportional relation to the square of the population. Reduced multi-phonon interactions are a result of lower sample temperature under light pumping assuming similar environmental conditions. Therefore, the natural radiative fluorescent rates can be gathered, verified in [1].

That begs the question; “what about the relation of these effects when it comes to doping?” Clearly higher doping profiles will increase the likeliness that the gain medium will be excited by ion-ion interactions. Dependent of the type of element being doped into a host, a higher doping profile may strain the crystal structure so much, it increases the probability of ion-ion interactions occurring, along with absorption line broadening. By extension other factors such as impurity concentration can act as a sensitizer or fluorescence quencher. Fortunately, excellent past literature exists looking at doping variation [1,29], impurity effects, including a secondary or tertiary co-dopant [18-21,29], input power variation [1,66], and even temperature variation [2,62].

Of interest is the behavior of 50 % Er:YAG under various pump intensities, Liu demonstrated for the  $^4S_{3/2}$  and the  $^4F_{9/2}$  energy levels that varying the input pump intensity and plotting the fluorescence of these levels respectively on a log scale shows the relation  $I_{\text{fluorescence}} \sim I_{\text{input}}^x$  where “x” is the number of photons involved. This relation identifies what multi-ion processes are present. Figure 2.2 shows the respective data collected by Liu [1]. Noting that  $x = 2$  is a two-ion process and remembering from chapter 1 relates to ETU, XR, and indirectly to ESA dominant processes outlined in figure 2.1. There are three ion processes also shown that are present seemingly further verified by the transient measurements of the  $^4S_{3/2}$  fluorescence presented in chapter 3. The exponent factor “x” in both cases are not whole numbers. For the  $^4S_{3/2}$  level we have a factor of  $x = 2.2691$ . This suggests that predominantly two ion processes are contributing to the fluorescence behavior with a small contribution from three ion processes. Following this line of interpretation, it may seem confusing for the  $^4F_{9/2}$  fluorescence versus pump intensity, as the factor is  $x = 1.7149$ . This means that these multi-ion processes are fighting each other with rapid non-radiative decay also contributing. This information, though very revealing of the energy transfer dynamics of the Er:YAG system, do not specifically identify what exact mechanisms are active with the specific pump scheme used in [1]. Additional spectroscopic measurements were taken as outlined in reference [1] though not being able to directly measure transients caused by three ion interactions. Further measurements are needed to account for additional mechanisms that are typically ignored. Particularly the ESA information has been minimal in the literature, therefore a pump and probe technique outlined in [42,43] was used to measure the ESA cross section. This cross-section information was used in chapter 4 to simulate a detailed rate equation model to recreate transient behavior measured and presented in

chapter 3. The simulations showed additional transient measurements are needed to fully encompass the mechanisms contributing to fluorescence.

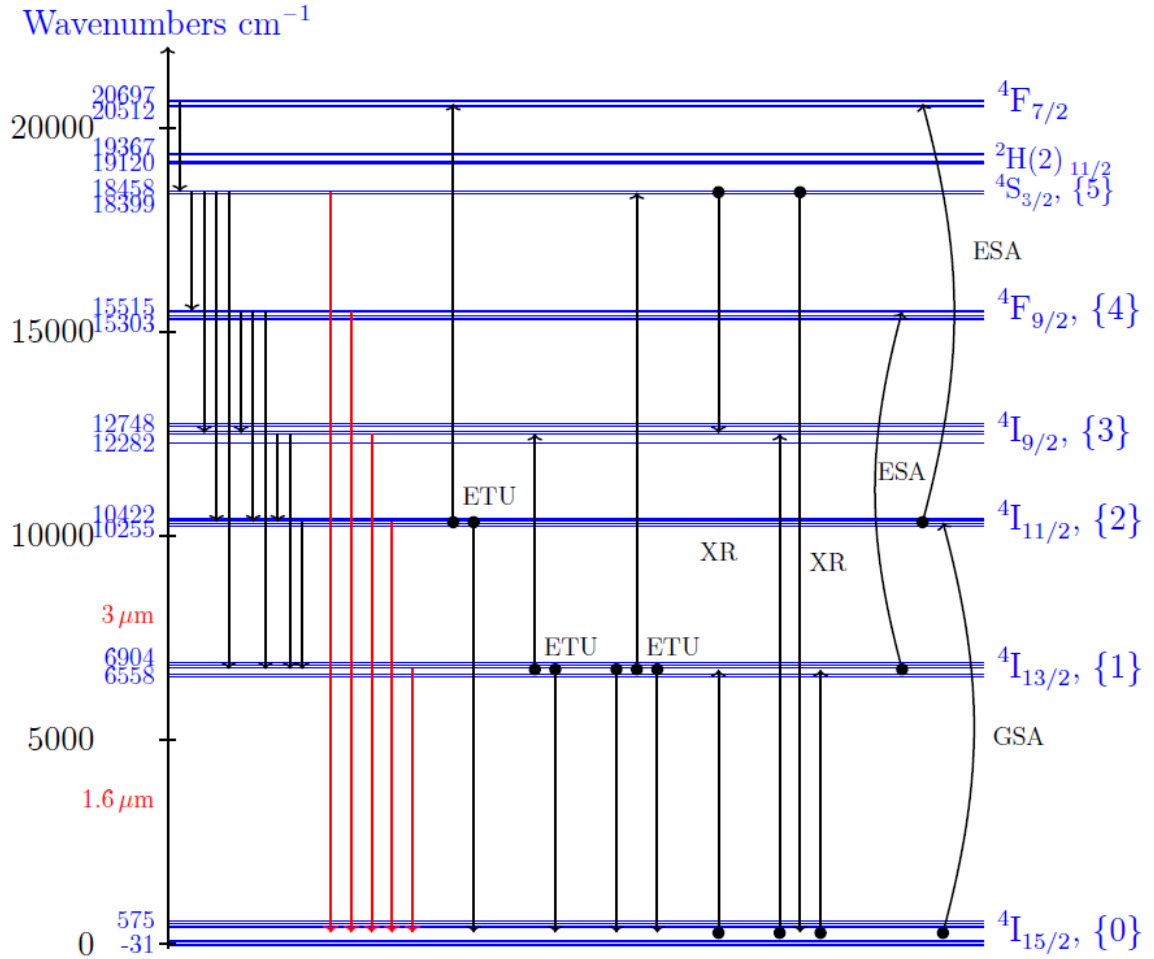


Figure 2.1a: Energy level diagram of Er:YAG and possible third order transitions. (Included with permission from author of reference [1]).

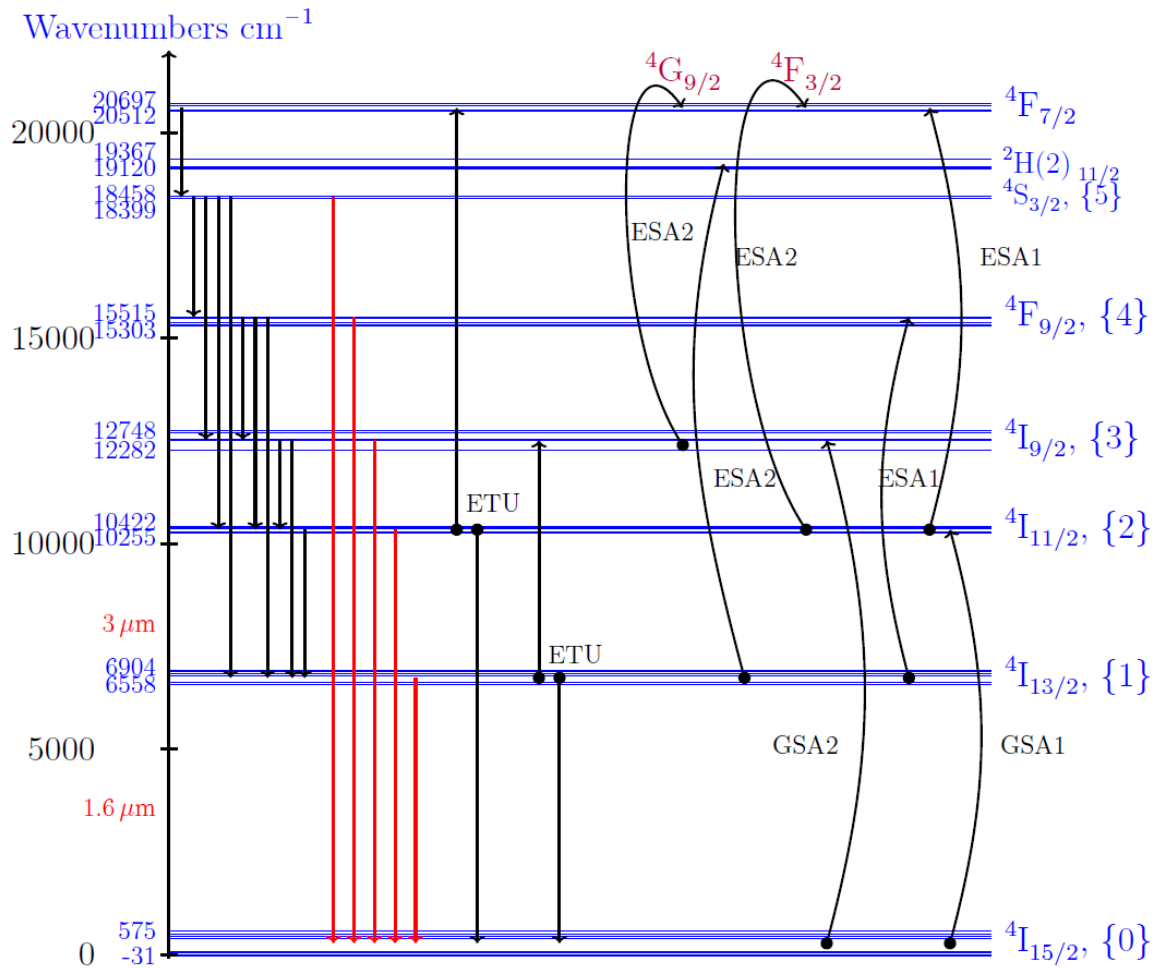


Figure 2.1b: Non-linear energy transfer mechanisms in Er:YAG with possible ESA transitions corresponding wavelength. (Included with permission from author of reference [1]).

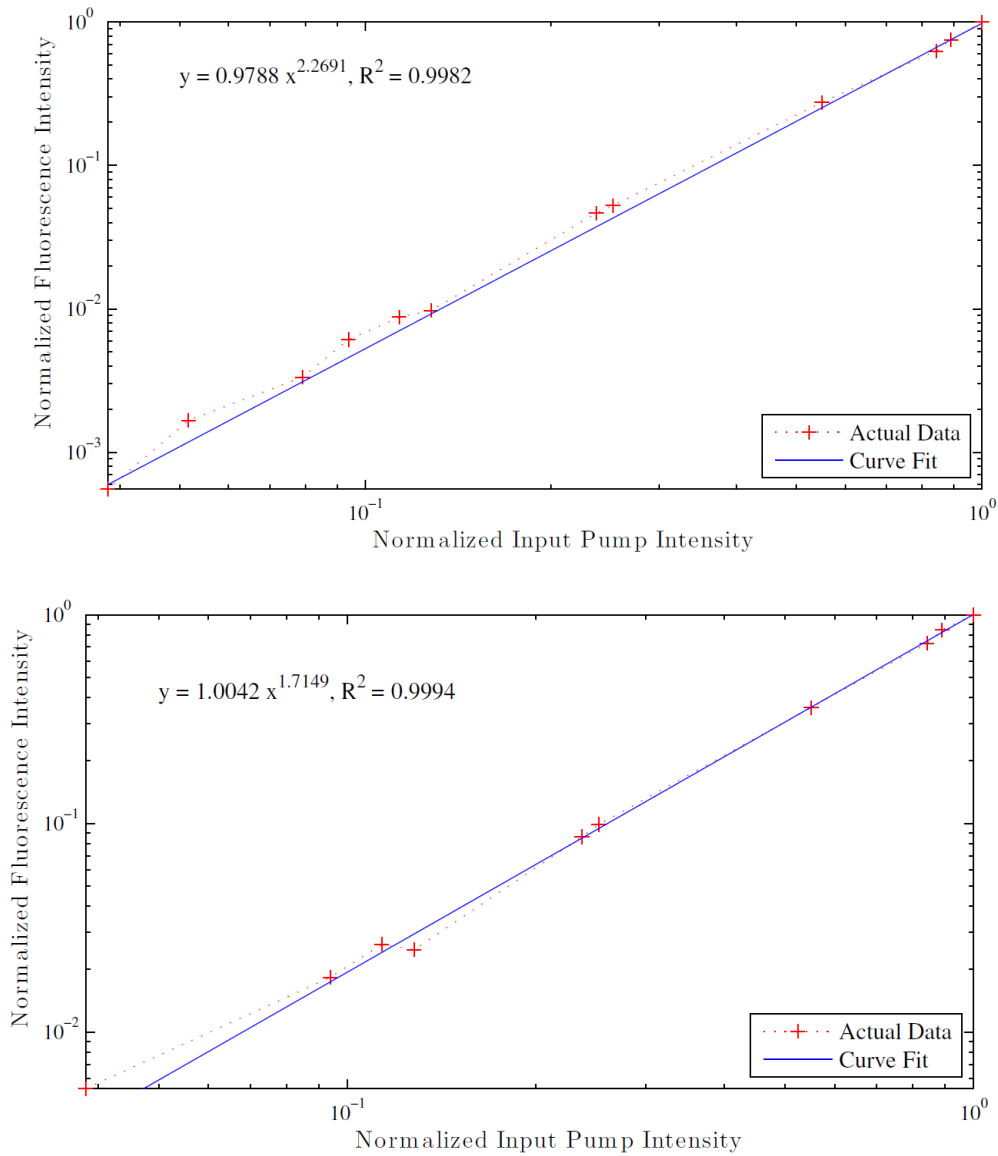


Figure 2.2 Normalized fluorescence versus varying pump intensity of (a) [Top plot] the  $4S_{3/2}$  level and (b) [bottom] the  $4F_{9/2}$  level.

(Included with permission from author of reference [1]).

## 2.2. Rate Equation Modeling of the Er:YAG System

This section opens with the typical rate equation modeling that has been extensively developed over the last 40 years for Er:YAG. The Typical rate equations are inherently non-linear due to the ion-ion and ESA interactions. A coupled five or six level system is utilized for modeling. Fortunately, very detailed analysis and simplifications have been introduced by Serban Georgescu et. al. centered around the  ${}^4I_{11/2} \rightarrow {}^4I_{13/2}$  transition corresponding to the 2.94 $\mu\text{m}$  laser. The mathematical modeling done in this thesis will be heavily based on Georgescu's modeling [22-26,30,32-34] with modifications appropriate to the experimental setup described in chapter 3.

To understand the complexity of the rate equations expressing the mechanisms within the Er:YAG system, it is important to look at the self-saturation condition and how it is defined. Let us consider a simple effective two-level laser system, such as the one depicted in figure 1.8, with no energy transfer processes other than external pumping and an understood fixed ground state population. Under hard pumping conditions this assumption does not hold as the ground state population will be varying significantly over time. Self-saturation is defined as

$$\alpha T_2 < \beta_{21} \beta T_1 \quad (2.1)$$

where  $\alpha$  and  $\beta$  are the Boltzmann population coefficients of the Stark sublevels participating in the lasing action. The term  $\beta_{21}$  represents an efficiency defined as the fraction of the excited ions at the initial laser energy level that through radiative or non-radiative means reach the terminal laser level. The rate equations are outlined in equations 2.2 (a) and (b) must be solved at steady state to derive the self-saturation condition. It is important to differentiate self-saturation form

saturation that is defined in this case by the effective gain between two different Stark levels going to zero.

$$\frac{dN_2}{dt} = -\frac{N_2}{T_2} + R_{p2}N_0 \quad (2.2a)$$

$$\frac{dN_1}{dt} = -\frac{N_1}{T_1} + \beta_{21}\frac{N_2}{T_2} + R_{p1}N_0 \quad (2.2b)$$

With  $N_i$   $i = 0,1,2$  the populations of the ground state, lower, and upper laser levels respectively and  $T_i$   $i = 1,2$  the fluorescence lifetimes of the lower and upper laser levels. The pump rates to each level are defined as  $R_{pi}$   $i = 1,2$ . Under steady state conditions we have  $\frac{dN_i}{dt} = 0$  with  $i = 1,2$  which leads to the relationship outlined in equation 2.3(a). Under Georgescu's model the pumping was to the upper laser level, therefore relationship 2.3(a) simplifies to 2.3(b).

$$\alpha T_2 R_{p2} N_0 \geq \beta \beta_{21} T_1 (R_{p1} + R_{p2}) N_0 \quad (2.3a)$$

$$\frac{T_2}{T_1} \geq \frac{\beta \beta_{21}}{\alpha} \quad (2.3b)$$

To achieve population inversion, the condition in equation 2.3(b) must be met. Therefore, the right combination of terms previously discussed will determine if population inversion is feasible. This is dependent primarily on the transition being looked at and what crystal medium is used. Unfortunately for Er:YAG what causes the self-saturation and prevents population inversion are the lifetimes of the respective lasing levels  ${}^4I_{11/2} \rightarrow {}^4I_{13/2}$ . The  ${}^4I_{11/2}$  level has a time constant of  $T_2 = 100 \mu s$  while that of the  ${}^4I_{13/2}$  varies significantly in the literature,  $T_2 = 1 ms$  to  $6.4ms$ , primarily due to sample impurity [1,29]. Results predicted by this simpler theory cannot be reconciled with the experimental data since the non-linear behavior can dominate the

system. Hence this simplified model cannot be used as the non-linear energy transfer mechanisms must be accounted for.

The main ion-ion energy exchange mechanisms at play according to references [1,22-26,30,32-34] are the up conversion from the lower laser level described by the exchange ( ${}^4\text{I}_{13/2} \rightarrow {}^4\text{I}_{15/2}$ ) + ( ${}^4\text{I}_{13/2} \rightarrow {}^4\text{I}_{9/2}$ ) followed by a rapid non-radiative decay to the upper laser level ( ${}^4\text{I}_{9/2} \rightarrow {}^4\text{I}_{11/2}$ ) and the up conversion from the upper laser level depicted by the exchange ( ${}^4\text{I}_{11/2} \rightarrow {}^4\text{I}_{15/2}$ ) + ( ${}^4\text{I}_{11/2} \rightarrow {}^4\text{F}_{7/2}$ ). The first ion-ion interaction described will have a beneficial effect on lasing as the upper laser level is being replenished. Conversely, the second exchange mechanism would be detrimental as the upper laser level is being depleted of ions that cannot be used for optical gain. In addition to these two-ion up conversion processes, cross relaxation from the  ${}^4\text{I}_{9/2}$  and the  ${}^4\text{S}_{3/2}$  levels must be accounted for [22-27]. Equation set 2.4 (a) – (f) represents the full six level system under the assumption that the ground state population is stationary with respect to time. Therefore, the laser resonator rate equation system is composed of five levels and six coupled equations [24].

$$\frac{dN_5}{dt} = -(a_{50} + a_{51} + a_{52} + a_{53} + a_{54} + w_{54})N_5 - w_{50}N_5N_0 + w_{22}N_2^2 + R_{p5}N_0 \quad 2.4(a)$$

$$\frac{dN_4}{dt} = -(a_{40} + a_{41} + a_{42} + a_{43} + w_{43})N_4 + (a_{43} + w_{54})N_5 + R_{p4}N_0 \quad 2.4(b)$$

$$\begin{aligned} \frac{dN_3}{dt} = & -(a_{30} + a_{31} + a_{32} + w_{32})N_3 + a_{53}N_5 + (a_{43} + w_{43})N_4 + w_{11}N_1^2 \\ & + w_{50}N_5N_0 - w_{30}N_3N_0 + R_{p3}N_0 \end{aligned} \quad 2.4(c)$$

$$\begin{aligned} \frac{dN_2}{dt} = & -(a_{20} + a_{21} + w_{21})N_2 + a_{52}N_5 + a_{42}N_4 + a_{32}N_3 - 2w_{22}N_2^2 - \sigma(\alpha N_2 - \beta N_1)\varphi \\ & + R_{p2}N_0 \end{aligned} \quad 2.4(d)$$

$$\begin{aligned} \frac{dN_1}{dt} = & -a_{10}N_1 + a_{51}N_5 + a_{41}N_4 + a_{31}N_3 + (a_{21} + w_{21})N_2 - 2w_{11}N_1^2 \\ & + w_{50}N_5N_0 + 2w_{30}N_3N_0 + \sigma(\alpha N_2 - \beta N_1)\phi + R_{p1}N_0 \end{aligned} \quad 2.4(e)$$

$$\frac{d\phi}{dt} = \frac{c\phi l_p}{l + (n - l)l} [\sigma(\alpha N_2 - \beta N_1) - \rho] + k \frac{N_2}{T_2} \quad 2.4(f)$$

The energy levels being modeled are the  $^4I_{15/2}$ ,  $^4I_{13/2}$ ,  $^4I_{11/2}$ ,  $^4I_{9/2}$ ,  $^4F_{9/2}$ , and  $^4S_{3/2}$  thermalized at room temperature with the  $^2H_{21/2}$  level with populations  $N_0$  to  $N_5$  respectively. The pump rates to each respective level are noted as  $R_{pi}$  with  $i = 1-5$ .  $T_i$  are the lifetimes of the respective levels. The emission cross section is represented by  $\sigma$ , with the speed of light  $c$ , the photon density inside the laser resonator  $\phi$ , and the round-trip loss  $\rho$ . The active medium refractive index is noted by  $n$ , with length  $l$ . The length of the resonator itself is  $l'$ . There is also a proportionality coefficient of the fluorescence term starting the lasing action noted as  $\kappa_{se}$ . The radiative transition rates from level  $i \rightarrow j$  are represented by the coefficients  $a_{ij}$ . Similarly, the multi-phonon transitions are denoted by the coefficients  $w_{ij}$ . The radiative transition rates are defined as the sum of the electric dipole and magnetic dipole probabilities defined in equation 2.5. The radiative lifetime is just the inverse of the summation of the radiative transition probabilities shown in equation 2.6

$$a_{ij} = A_{ij}^{ed} + A_{ij}^{md} \quad 2.5$$

$$T_i^{rad} = (\sum a_{ij})^{-1} \quad 2.6$$

The multi-phonon probability rate is related to the radiative lifetime by equation 2.7.

$$w_{ij} = \frac{1}{T_i^{fl}} - \frac{1}{T_i^{rad}} \quad 2.7$$

$T_i^{fl}$  is the low Er concentration weak resonant pump fluorescence lifetime, which was experimentally determined [22-27]. Radiative and non-radiative times were found by

spectroscopic measurements of individual levels. Judd-Ofelt modeling was utilized to derive the electric dipole probabilities  $A_{ij}^{ed}$ . A derived expression referred to in reference [24] was used to find the magnetic dipole probabilities  $A_{ij}^{md}$ . It is important to note that Judd-Ofelt analysis, at least in the literature reviewed, has given order of magnitude accuracy at best. From this notion the following simplifications were made acknowledging the accuracy of the derived electric dipole probabilities, namely that the non-radiative terms in equation set 2.4 dominated over the radiative ones. The only exception being that  $a_{10} \gg \omega_{10}$ . The resulting rate equations (2.8 a-f) show some simplifications though this system can be even further simplified by looking at the cross relaxation of the  $^4S_{3/2}$  level and its relation to the lasing action. Since usually Er:YAG systems are moderately or highly doped, the excitation from this level can be considered equally distributed over the laser levels. The resulting efficient cross relaxation and the fact that  $T_1, T_2 \gg T_3, T_4, T_5$  along with  $\beta_{21} = 1$  we now have a collapsed two-level system (eq. 2.9 a-c). A closed form can be achieved by setting  $R_1 = R_{p1} + R_{p5}$ ,  $R_2 = R_{p2} + R_{p3} + R_{p4} + R_{p5}$ , resulting in equations 2.10 (a-b) [24]. From inspection it can be deduced that the solutions to the simplified two-level system resembles that of a quadratic system of equations. The resulting mathematical form of the closed form steady state solution would require that there are two population solutions for each level. In the derivation of this system outlined in reference [24] the other solutions were not physically feasible and was hence ignored. Experimental spectroscopic measurements conducted in reference [1] revealed the possibility of fluctuating population levels occurring at the laser level. The measurements demonstrated in chapter 3 point to confirmation that the laser levels are fluctuating between two solutions.

$$\frac{dN_5}{dt} = -\frac{N_5}{T_5} - w_{50}N_5N_0 + w_{22}N_2^2 + R_{p5}N_0 \quad 2.8(a)$$

$$\frac{dN_4}{dt} = -\frac{N_4}{T_4} + \frac{N_5}{T_5} + R_{p4}N_0 \quad 2.8(b)$$

$$\begin{aligned} \frac{dN_3}{dt} = & -\frac{N_3}{T_3} + \frac{N_4}{T_4} + w_{11}N_1^2 + w_{50}N_5N_0 - w_{30}N_3N_0 \\ & + R_{p3}N_0 \end{aligned} \quad 2.8(c)$$

$$\begin{aligned} \frac{dN_2}{dt} = & -\frac{N_2}{T_2} + \frac{N_3}{T_3} - 2w_{22}N_2^2 - \sigma(\alpha N_2 - \beta N_1)\varphi \\ & + R_{p2}N_0 \end{aligned} \quad 2.8(d)$$

$$\begin{aligned} \frac{dN_1}{dt} = & -\frac{N_1}{T_1} + \frac{N_2}{T_2} - 2w_{11}N_1^2 + w_{50}N_5N_0 + 2w_{30}N_3N_0 + \sigma(\alpha N_2 - \beta N_1)\varphi \\ & + R_{p1}N_0 \end{aligned} \quad 2.8(e)$$

$$\frac{d\varphi}{dt} = \frac{c\varphi l_p}{l + (n-l)l} [\sigma(\alpha N_2 - \beta N_1) - \rho] + k \frac{N_2}{T_2} \quad 2.8(f)$$

$$-\frac{N_2}{T_2} - w_{22}N_2^2 + w_{11}N_1^2 - \rho\varphi + R_2N_0 = 0 \quad 2.9(a)$$

$$-\frac{N_1}{T_1} + \frac{N_2}{T_2} + w_{22}N_2^2 - 2w_{11}N_1^2 + \rho\varphi + R_1N_0 = 0 \quad 2.9(b)$$

$$\alpha N_2 - \beta N_1 = \frac{\rho}{\sigma} \quad 2.9(c)$$

$$R_1 = R_{p1} + R_{p5} \quad R_2 = R_{p2} + R_{p3} + R_{p4} + R_{p5} \quad 2.9(d)$$

$$N_1 = \frac{-1 + \sqrt{1 + 4w_{11}T_1^2(R_1 + R_2)N_0}}{2w_{11}T_1} \quad 2.10(a)$$

$$N_2 = \frac{-1 + \sqrt{1 + 4w_{22}T_2^2 \left[ (R_1 + 2R_2)N_0 - \frac{N_1}{T_1} \right]}}{2w_{22}T_2} \quad 2.10(b)$$

### 2.3. Figures of Merit

Georgescu's analysis led to what he defined as figures of merits [24] that aid in modeling and predicting the behavior and performance factors. One such figure was how population inversion relates to the pump wavelengths. Let us take the expressions 2.10 and assume high pump intensities, which is appropriate for this work, these expressions will simplify to equations 2.11 (a-b).

$$N_1 \approx \sqrt{\frac{(R_1 + R_2) * N_0}{\omega_{11}}} \quad 2.11(a)$$

$$N_2 \approx \sqrt{\frac{(R_1 + 2R_2)N_0}{\omega_{22}}} \quad 2.11(b)$$

Now Georgescu uses these expressions of 2.11 and substitutes them into the condition of population inversion resulting in 2.12 (a-b).

$$\alpha N_2 - \beta N_1 > 0 \quad 2.12(a)$$

$$\alpha N_2 - \beta N_1 \approx \alpha \sqrt{\frac{(R_1 + 2R_2)N_0}{\omega_{22}}} \left( 1 - \frac{\beta}{\alpha} \sqrt{\frac{\omega_{22}}{\omega_{11}}} \sqrt{\frac{R_1 + R_2}{R_1 + 2R_2}} \right) > 0 \quad 2.12(b)$$

Notice how the second square root expression within the parenthesis is only dependent on pumping conditions, which is essentially the spectral content of the pumps, this can be related to a figure of merit taken by the terms multiplied by that expressions to those of 2.13 (a-b).

$$p \equiv \frac{\beta}{\alpha} \sqrt{\frac{\omega_{22}}{\omega_{11}}} \quad 2.13(a)$$

$$p \leq \sqrt{\frac{R_1 + R_2}{R_1 + 2R_2}} \quad 2.13(b)$$

The self-saturation condition is supplanted when under heavy pump, so population inversion can be achieved. This is the basis for selecting certain wavelengths at certain power levels as the sources have become available. Visually the threshold can be described via plot as the population inversion against the pump rate. The threshold itself is the loss defined as  $\frac{\rho}{\sigma}$ . This is displayed in figure 2.3

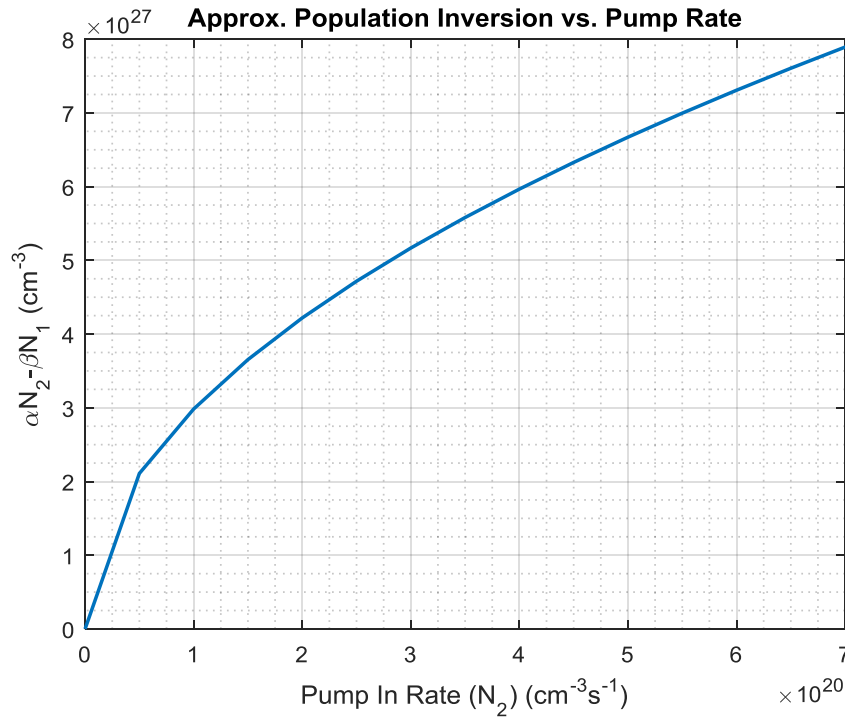


Figure 2.3 Simulated 962nm pump at 10kW/cm<sup>2</sup>. Threshold not visible as the input pump intensity is so high.

The figure of merit introduced in equations 2.13 reveals the roles of the common up conversion parameters  $\omega_{22}$  and  $\omega_{11}$  which originate from the  $^4I_{11/2}$  and  $^4I_{13/2}$  respectively.

Georgescu derives the photon flux density expression for the scenario that has been summarized in this section revealing that  $\omega_{22}$  plays a significant role in that a small  $\omega_{22}$  will be beneficial due to a reduced emission threshold and extending the range of the laser transitions, while the relationship to  $\omega_{11}$  is more complex [24]. Given the derived expression for photon flux density, Georgescu defined the quantum efficiency for this system as capable of super unitary efficiency. Looking at the quantum efficiency expression defined in equation 2.14 it is noted that, dependent on the pump scheme, the efficiency can exceed one.

$$\eta_i = \frac{[R_2 + (R_2 + R_2)(1 - p^2)]}{R_{pi}} \quad 2.14$$

Further investigation revealed the possibility in relaxing the threshold in overcoming the self-saturation, as defined by the figure of merit  $p$ , by carefully selecting the pump wavelength such that ESA to the  $^4S_{3/2}$  helps remove ions faster from the lower laser level. However, modeling for low doped samples where ion-ion interactions were negligible revealed that ESA alone cannot relieve the constraints set by the self-saturation threshold. This is a primary reason why MWIR laser sources with Erbium as the gain ion are usually doped at high levels.

Various other figures of merits were defined by Georgescu that accounted for cross relaxation, sensitizer ions, and oscillation threshold [22-27]. The oscillation threshold figure of merit entails the non-linear up conversion mechanisms that are required for population inversion, which must account for the reality that these mechanisms themselves require a certain amount of energy to achieve any significance regardless of other loss mechanism or lack thereof. Again, reviewing the definition of the figure of merit for population inversion defined in equation set 2.13, the material parameters and pump spectra are what set the population inversion threshold.

For pumping in the  ${}^4I_{11/2}$  level we have equation set 2.15 defining the intrinsic oscillation threshold (a), the dimensionless threshold (b), and the dimensionless lifetime [24].

$$s_0 = \frac{[2(\tau - 1)(1 - p^2 + \tau)]}{(2 - p^2)^2} \quad 2.15(a)$$

$$s_0 \equiv 2\omega_{11}T_1^2R_pN_0 \quad 2.15(b)$$

$$\tau \equiv \frac{\beta T_1}{\alpha T_2} \quad 2.15(c)$$

The values Georgescu used for Er:YAG are listed in table 2.1, which show that an intrinsic oscillation threshold (IOT) will always exist [24]. More broadly the oscillation threshold (OT) is defined in equation set 2.16 for pumping into the  ${}^4I_{11/2}$  level [24]. Taking the ratio of the IOT over OT and plotting it over round trip cavity loss illustrates the effect of IOT when pumping. IOT is dependent on concentration and losses. By inspection of equation set 2.16 the doping can have a significant effect that is much easily interpreted visually as seen in figure 2.4. In this thesis, 50 % Er:YAG at. wt. is the baseline that will be used for all simulation work unless stated otherwise.

$$s = s_0 + \frac{u}{1 - p^2} + \frac{2 * t^2 + (t - u)(1 - p^2 - t + \tau)}{(1 - p^2)^2} + \frac{(t + \tau)(1 - p^2 + t + \tau)\sqrt{1 + 2 * u * (1 - p^2) / (t + \tau)^2}}{(1 - p^2)^2} \quad 2.16 (a)$$

$$t \equiv \frac{2\omega_{22}\beta T_1 \rho}{\alpha^2 \sigma} \quad 2.16(a)$$

$$u \equiv 2\omega_{11}T_1^2 \left( \frac{\omega_{22} \rho^2}{\alpha^2 \sigma^2} + \frac{1}{\alpha T_2} \frac{\rho}{\sigma} \right) \quad 2.16(a)$$

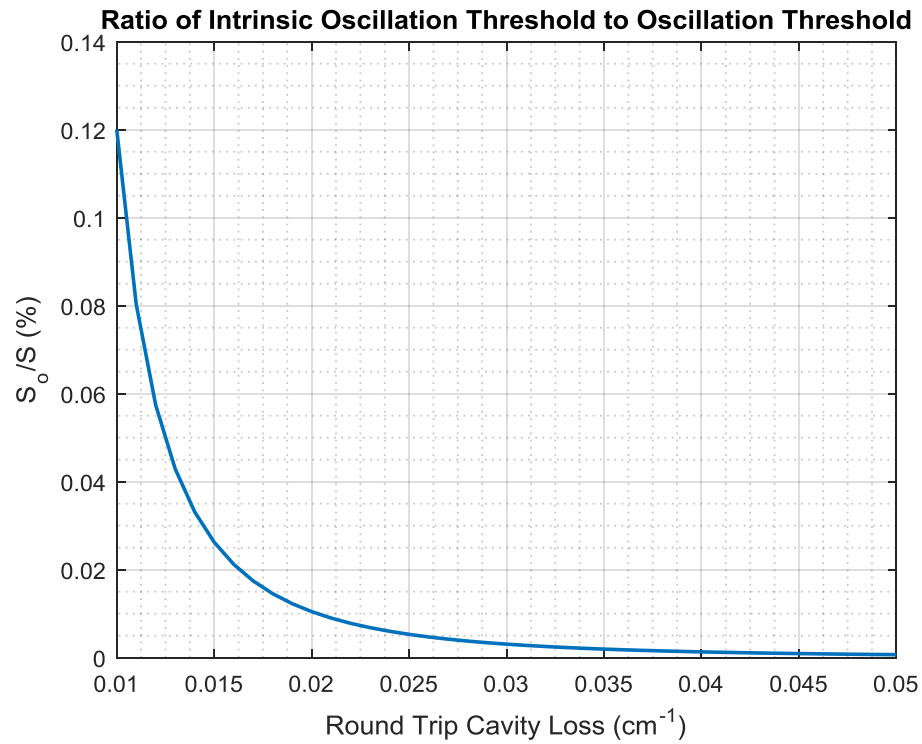


Figure 2.4: Intrinsic oscillation threshold figure of merit using a 962nm pump at 10kW/cm<sup>2</sup>

Looking at this ratio for other doping profiles reveals another tool in selecting appropriate doping for a laser system. Georgescu plotted the IOT/OT ratio vs cavity loss and doping percentage providing a much more detailed picture of why a higher percentage doping is favorable for an Er:YAG MWIR laser system [24].

## 2.4. Rate Equation Simulations

The complexity of the Er:YAG rate equation system stems from the necessity to include the non-linear energy transfer mechanisms which are crucial to achieve population inversion as outlined in section 2.2. The non-linear energy transfer mechanism also causes a peculiar behavior of “instability” of fluctuating fluorescence first discovered, at least through the literature review for this thesis, by Liu [1]. The “instability” manifested itself as an oscillatory transient present during the fluorescence of Er:YAG single crystal samples excited by an NIR laser source. The setup used by Liu was for measuring the fluorescence behavior with respect to pump intensity as summarized by figure 2.2. Though differing from Georgescu’s laser resonator setup, the observed transient behavior seemed to agree with the theoretical quadratic solutions derived by Georgescu expressed by equation set 2.10. Liu was utilizing a simple pump scheme to measure fluorescence therefore; no lasing action would occur. As a result, the rate equations can be simplified. Though the base equations form a set of six coupled equations. The reason being that Liu was using much higher pump intensities than any referenced work in this thesis. Noting from Liu’s work third order ion-ion interactions were measured and due to higher pump intensities, the probability of ESA interactions was much higher. Ground state behavior must also be accounted for as it can no longer be considered stationary. Therefore, the possibility of analytically solving the equations were slim as a closed form was improbable. Thankfully numerical analysis can be done to solve the rather large system of equations with modern software tools. The Euler method is sufficient to model to iteratively solve this system with a sufficient sampling rate. The population evolution is analyzed graphically to show the non-exponential behavior of the rise and fall, which coincides with the measured fluorescence responses Liu measured showing multi-time constant decay and rise profiles [1]. Equation set

2.17 defines a simplified Georgescu model that is not a laser resonator (only fluorescence is modeled). The intention of the model is to look at the population behavior in a simple pumping scheme that is used to capture fluorescence much like what was used by Liu. For now, only the ion-ion interactions will be looked at in this section. ESA will later be accounted for after reporting on the ESA cross section measurements made based on references [42,43] in chapters 3 and 4.

The parameters for the simulation are given in table 2.1 with references provided. The Euler method used the definition of a derivative to approximate the solution of a differential equation and allows solving complex coupled systems iteratively (equation 2.18). For Er:YAG the smallest lifetime is that of level  $N_3$ ,  $T_3 = 0.05 \mu s$  [18,24]. In order to minimize error, a time step of  $\Delta t = 1 \text{ ns}$  is used. The local truncation error can be defined as  $LTE = y(t_o + \Delta t) - y_1 = \frac{1}{2}\Delta t^2 y''(t_o) + \text{higher order terms}$ . The approximate value  $y_1$  is the previous value  $y(t_o)$  added by the time step multiplied by the function value  $f(t_o, y_o)$ ,  $y_1 = y_o + \Delta t * f(t_o, y_o)$ . This value is subtracted from the Taylor series expansion of  $y(t_o + \Delta t) = y(t_o) + \Delta t * y'(t_o) + \frac{1}{2}\Delta t^2 y''(t_o) + \text{higher order terms}$ , to give the LTE. The pump was set to a fixed value of  $10 \frac{kW}{cm^2}$  that included Gaussian noise (20% variation). The other simulation variables provided in [24] except for  $T_1 = 1.1 \text{ ms}$  [1]. Simulations were conducted for a single 1ms pulse. A delay was added to show the rise and fall behavior. Appendix A has supplemental simulation plots from the ones provided here.

$$\frac{dN_5}{dt} = -\frac{N_5}{T_5} - w_{50}N_0N_5 + w_{22}N_2^2 \quad 2.17(a)$$

$$\frac{dN_4}{dt} = -\frac{N_4}{T_4} + \frac{N_5}{T_5} \quad 2.17(b)$$

$$\frac{dN_3}{dt} = -\frac{N_3}{T_3} + \frac{N_4}{T_4} + w_{11}N_2^2 + w_{50}N_0N_5 \quad 2.17(c)$$

$$\frac{dN_2}{dt} = -\frac{N_2}{T_2} + \frac{N_3}{T_3} - 2w_{22}N_2^2 + R_{p2}N_0 \quad 2.17(d)$$

$$\frac{dN_1}{dt} = -\frac{N_1}{T_1} + \frac{N_2}{T_2} - 2w_{11}N_1^2 + w_{50}N_0N_5 \quad 2.17(e)$$

$$\frac{dN_0}{dt} = -R_{p2}N_0 + w_{11}N_2^2 + w_{22}N_2^2 - w_{50}N_0N_5 \quad 2.17(d)$$

$$\frac{dX}{dt} = \lim_{h \rightarrow \infty} \frac{X(t+h) - X(t)}{h} \approx \frac{X(t+\Delta t) - X(t)}{\Delta t} \text{ for very small } \Delta t \quad 2.18$$

Table 2.1 Parameter Values for Simulations

Parameter	Value	Notes
$T_1$	6400 $\mu\text{s}$	[24]
$T_2$	100 $\mu\text{s}$	[24]
$T_3$	0.05 $\mu\text{s}$	[24]
$T_4$	1.5 $\mu\text{s}$	[24]
$T_5$	16.7 $\mu\text{s}$	[24]
$\omega_{11}$	$1.3 \times 10^{-15} \text{cm}^{-3} \text{s}^{-1}$	[24]
$\omega_{22}$	$3.7 \times 10^{-15} \text{cm}^{-3} \text{s}^{-1}$	[24]
$\omega_{50}$	$1.06 \times 10^{-15} \text{cm}^{-3} \text{s}^{-1}$	[24]
$\alpha$	0.22	[24]
$\beta$	0.05	[24]
$\sigma_{02}$	$2.6 \times 10^{-20} \text{cm}^2$	[24]
$T_1$	1100 $\mu\text{s}$	[1]
$I_p$	$10 \text{ kW}/\text{cm}^2$	[1]
$\lambda_p$	962nm	Experiment
$\nu_p = \lambda_p/c$	$3.21 \times 10^{-20} \text{s}^{-1}$	Experiment
$R_p = \sigma_{02} I_p / (h\nu_p)$	$1.2591 \times 10^3 \text{s}^{-1}$	Experiment

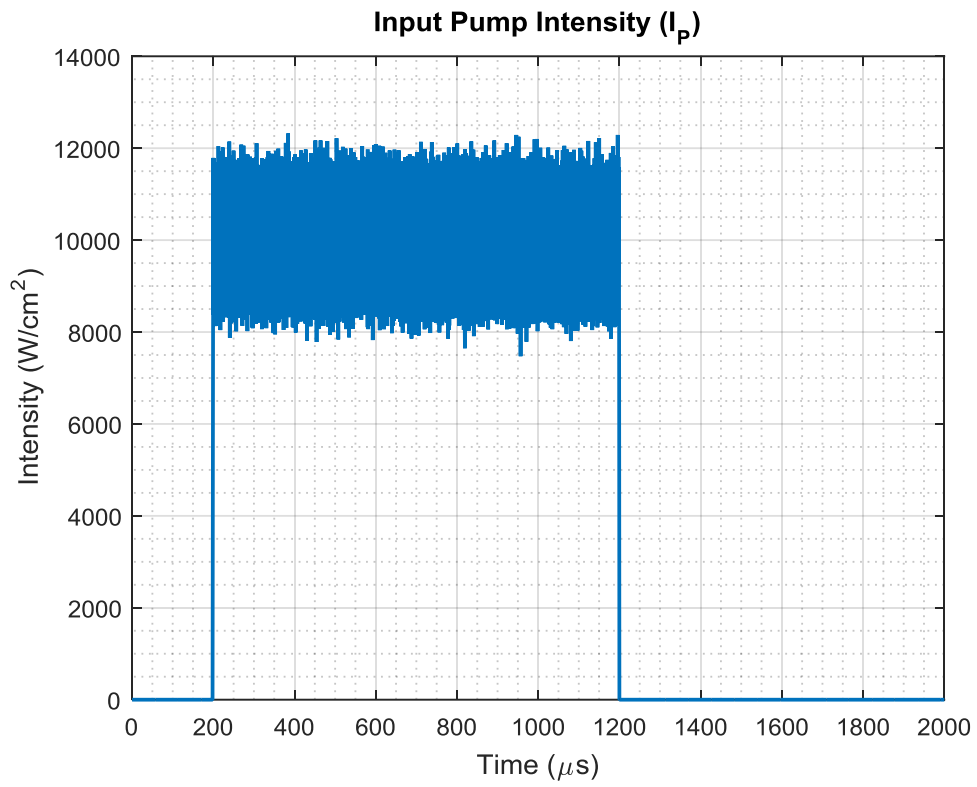


Figure 2.5: Simulated input pump with added Gaussian noise with 20% variation.

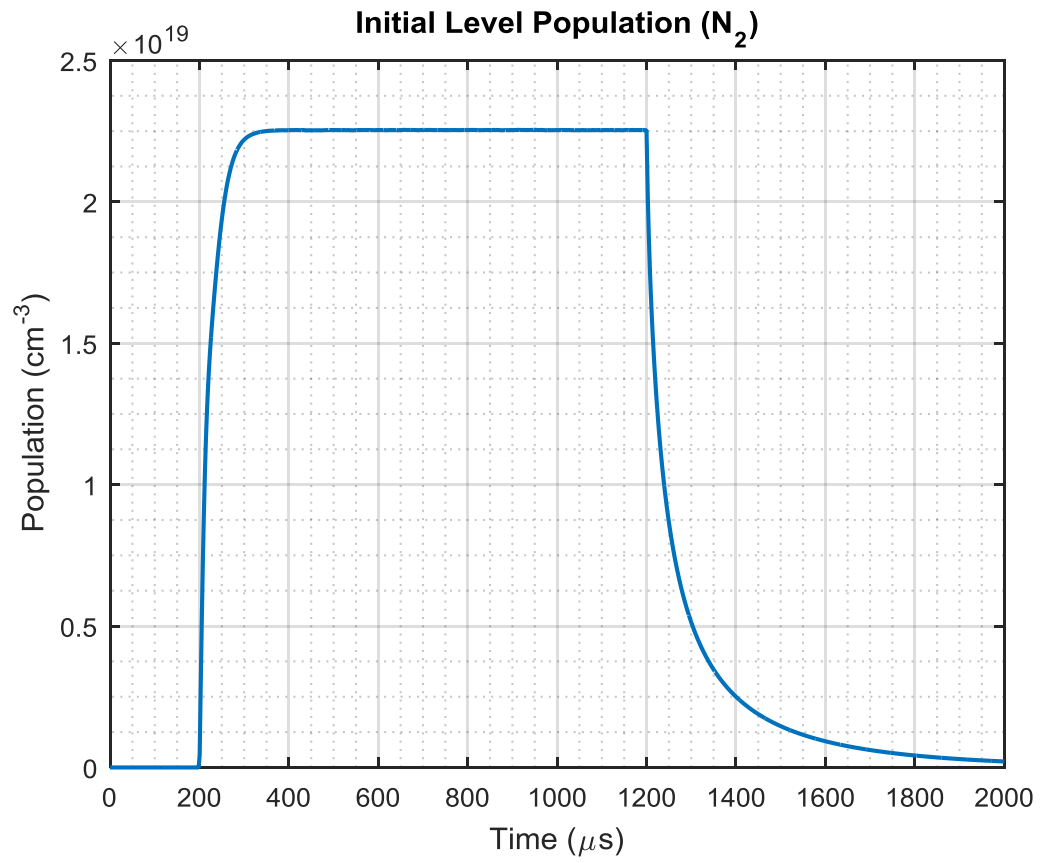


Figure 2.6: Simulation results showing the transient N<sub>2</sub> population

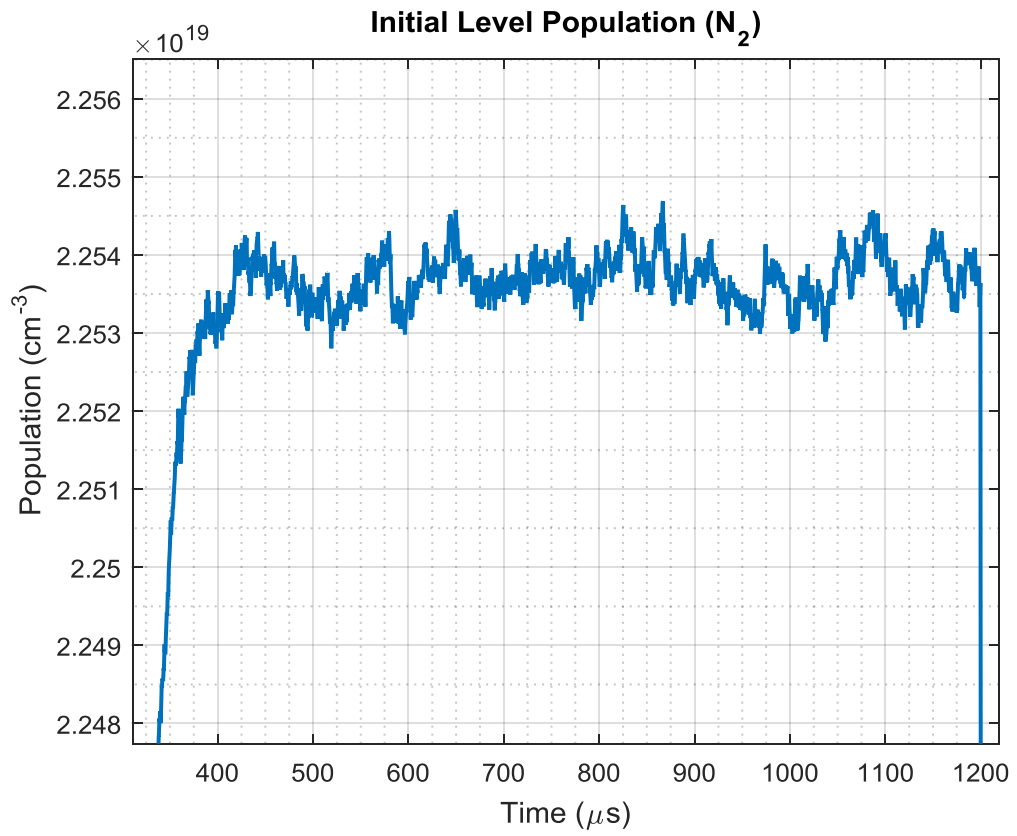


Figure 2.7: Simulation results of the  $N_2$  population expanded to show instability.

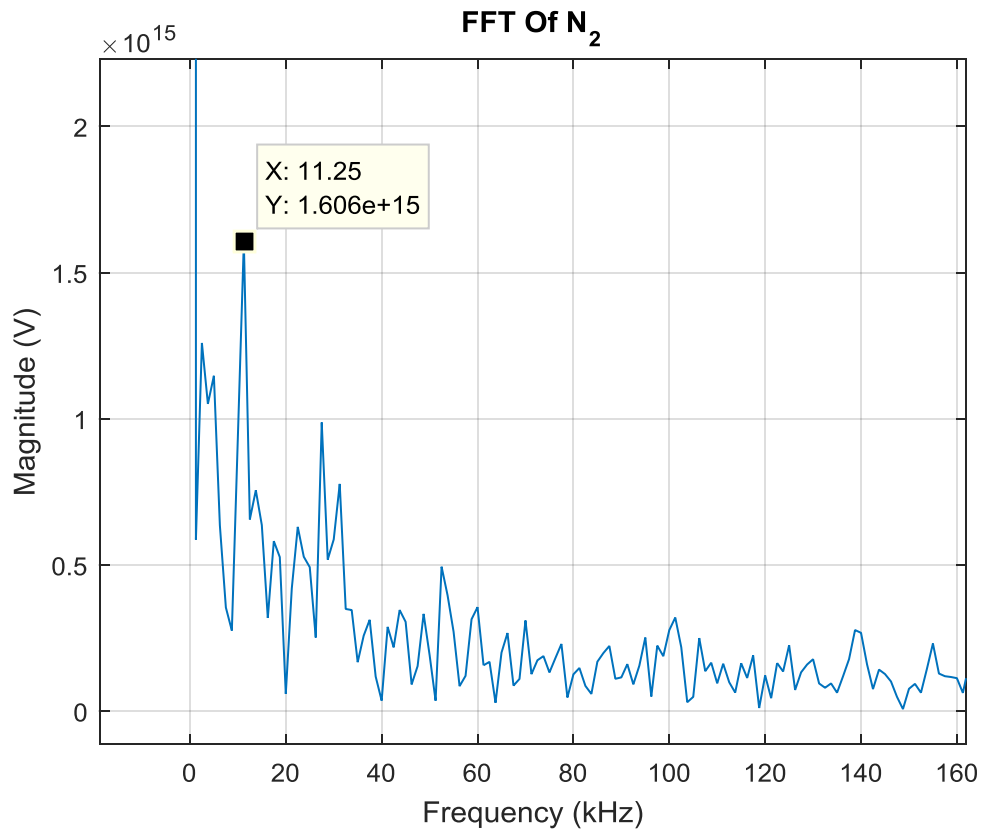


Figure 2.8: Simulation results showing FFT of N<sub>2</sub>. Spikes correspond to pump noise.

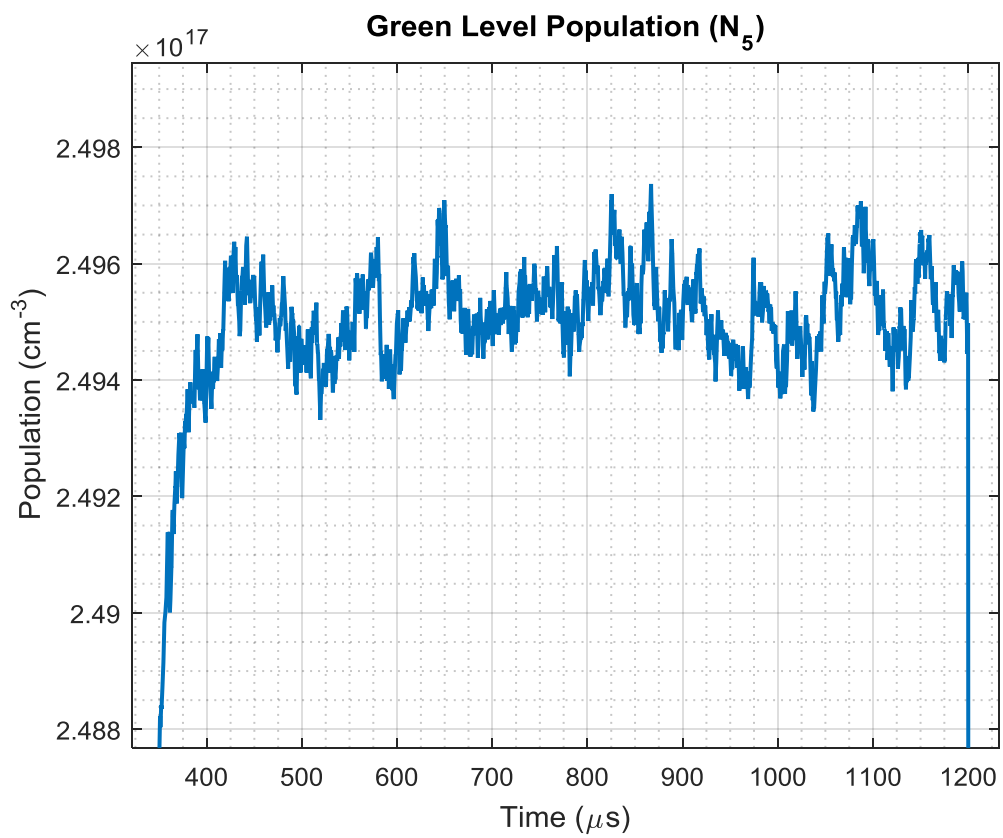


Figure 2.9: Expanded view of  $N_5$  population to show instability.

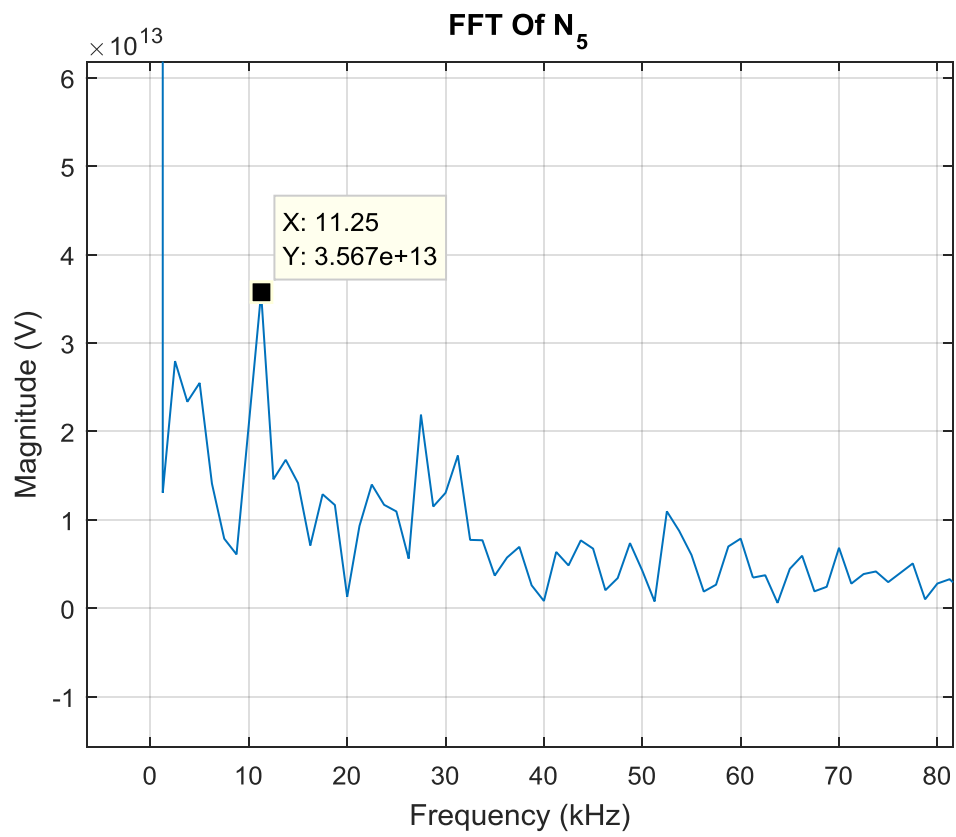


Figure 2.10: FFT of figure 2.9.

## 2.5 Excited State Absorption Modeling

The excited state absorption plays a dominant role in low doped Er:YAG as elaborated by various authors [1,4,22,26-32,58,65,80-83]. In the spectroscopic results shown in chapter 3, ESA plays a role in the manifestation of the periodic oscillation that matches closely to the lifetime of the level  $^4S_{3/2}$ . The ESA measurements presented in chapter 3 were based on the pump and probe techniques developed in references [42,43]. These techniques as reviewed in chapter 3 rely on a coherent source for the probe beam and a broadband lamp as a pump to excite multiple levels. This technique primarily was limited by the fact that in the 1990's when the original paper by Koetke and Huber was written, NIR resonant coherent sources were not as widely available. For the experiments presented in this work, having two separate NIR coherent sources proved to be particularly advantageous as a simpler variation of the pump and probe technique was implemented. This technique like the more complex versions utilize the Beer-Lambert law to derive the ESA cross section from the probe intensity output when a pump is off compared to the output when the probe is on. The modified rate equations are presented in this chapter as equation set 2.19. Though now equations 2.19(c) & 2.19(f) includes the ESA term (in red). Only the ESA term derived from the lower level ( $^4I_{13/2}$ ) is considered as the ESA cross section for a 962nm pump was experimentally determined for low doped samples under moderate to low pump in references [28,30,42]. This ESA term is  $\sigma_x = 3.7 \cdot 10^{-21} \text{ cm}^2$ . Looking at figures 2.11 to 2.16 shows the rate equation simulations with the ESA derived in the literature. Inspecting the simulation plots there is no significant periodic oscillation matching to the lifetime of the  $^4S_{3/2}$  level. The FFTs verified this observation. Demonstrating the need for the pump-probe measurement under a high intensity resonant pump on high concentration samples.

$$\frac{dN_5}{dt} = -\frac{N_5}{T_5} - w_{50}N_0N_5 + w_{22}N_2^2 + \sigma_x\varphi N_1 \quad 2.19(a)$$

$$\frac{dN_4}{dt} = -\frac{N_4}{T_4} + \frac{N_5}{T_5} \quad 2.19(b)$$

$$\frac{dN_3}{dt} = -\frac{N_3}{T_3} + \frac{N_4}{T_4} + w_{11}N_2^2 + w_{50}N_0N_5 + R_{p3}N_0 \quad 2.19(c)$$

$$\frac{dN_2}{dt} = -\frac{N_2}{T_2} + \frac{N_3}{T_3} - 2w_{22}N_2^2 \quad 2.19(d)$$

$$\frac{dN_1}{dt} = -\frac{N_1}{T_1} + \frac{N_2}{T_2} - 2w_{11}N_1^2 + w_{50}N_0N_5 - \sigma_x\varphi N_1 \quad 2.19(e)$$

$$\frac{dN_0}{dt} = -R_{p3}N_0 + w_{11}N_2^2 + w_{22}N_2^2 - w_{50}N_0N_5 \quad 2.19(f)$$

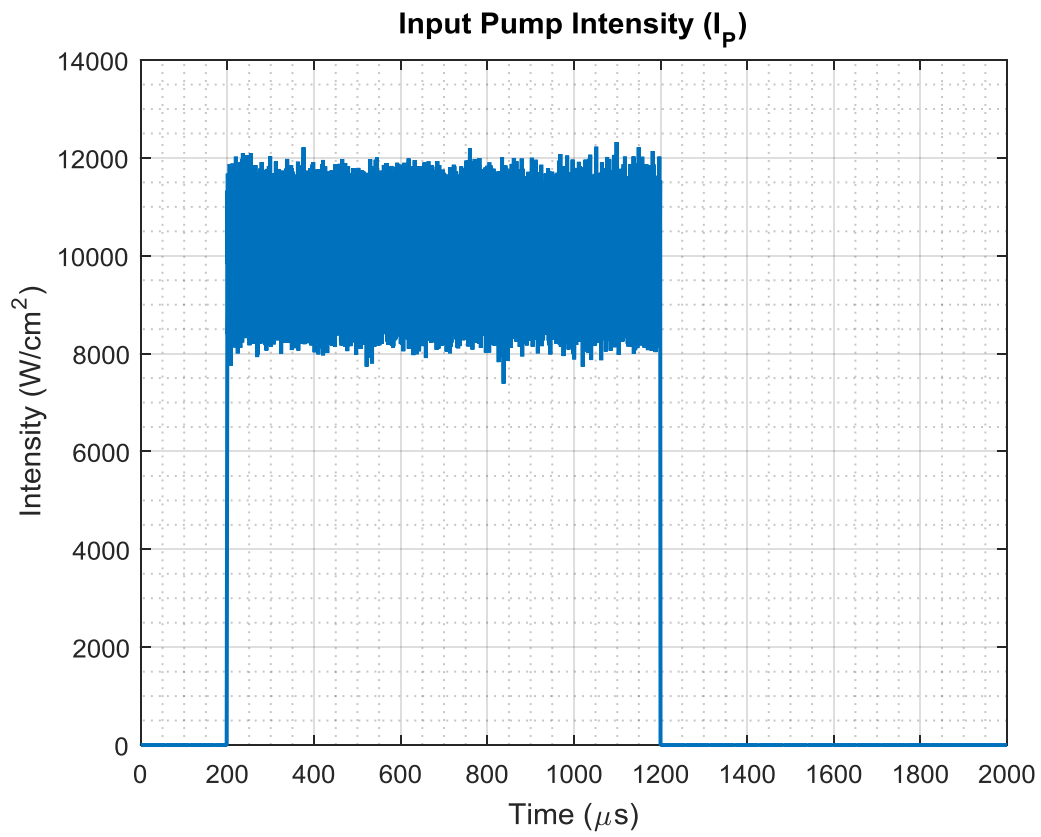


Figure 2.11: Simulated input pump with white gaussian noise.

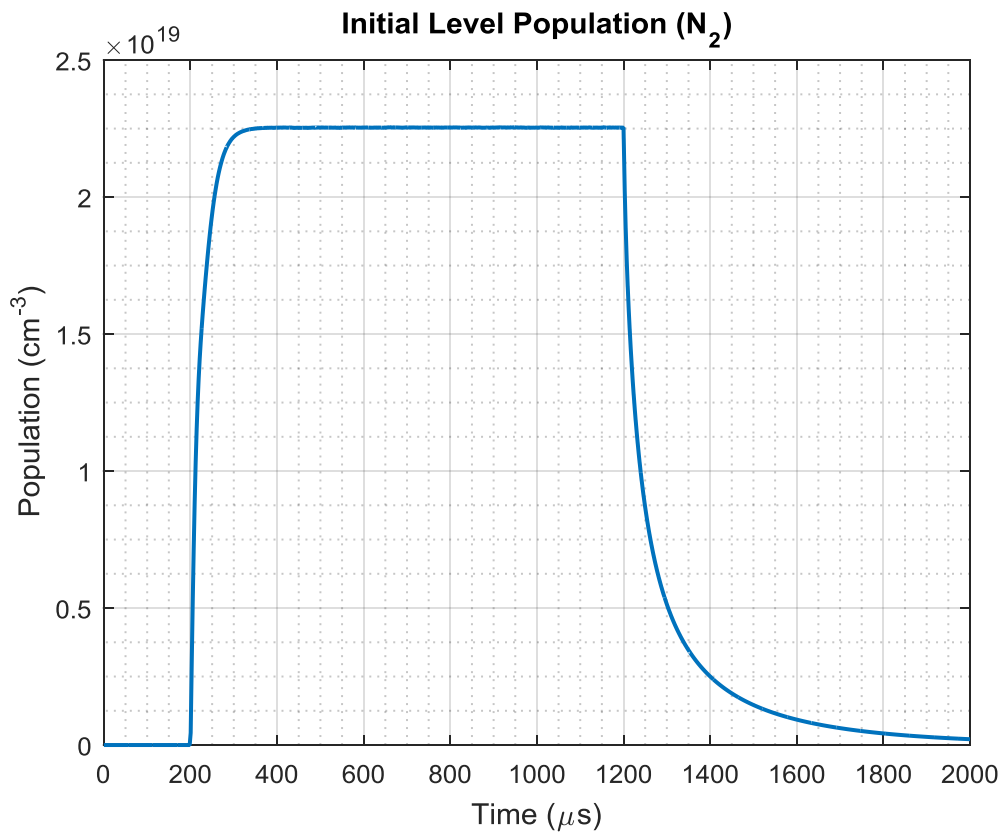


Figure 2.12: Simulation results of the N<sub>2</sub> population.

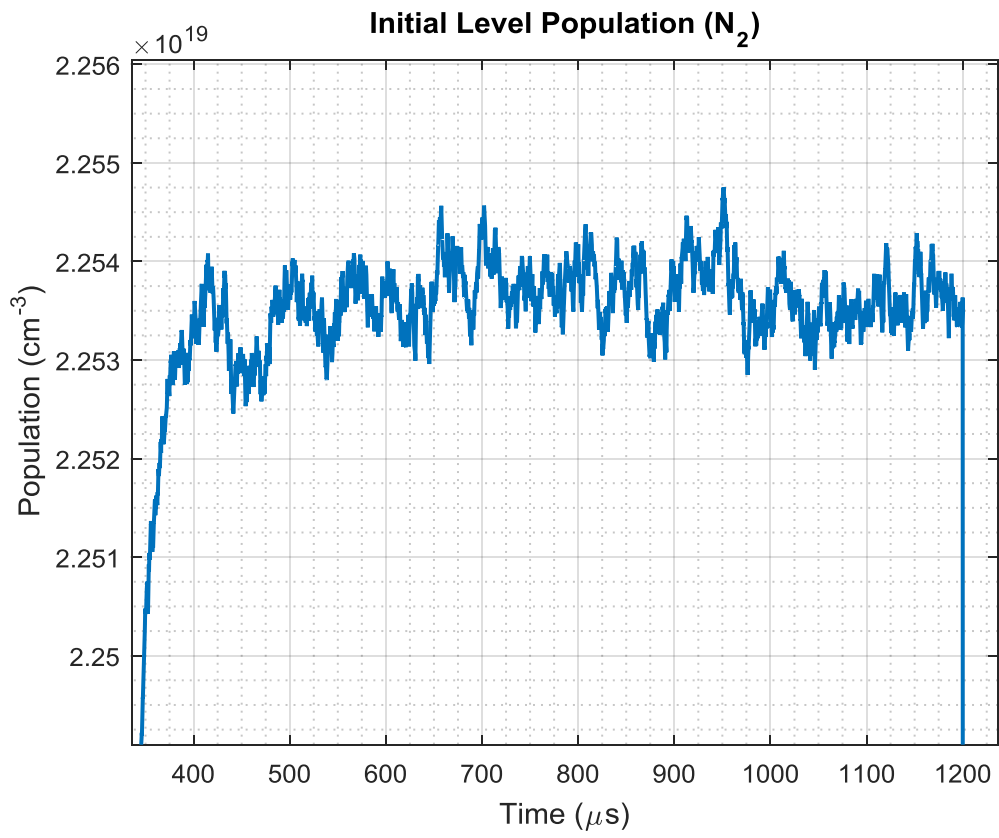


Figure 2.13: Simulation results of the  $N_2$  population expanded view in to show instability.

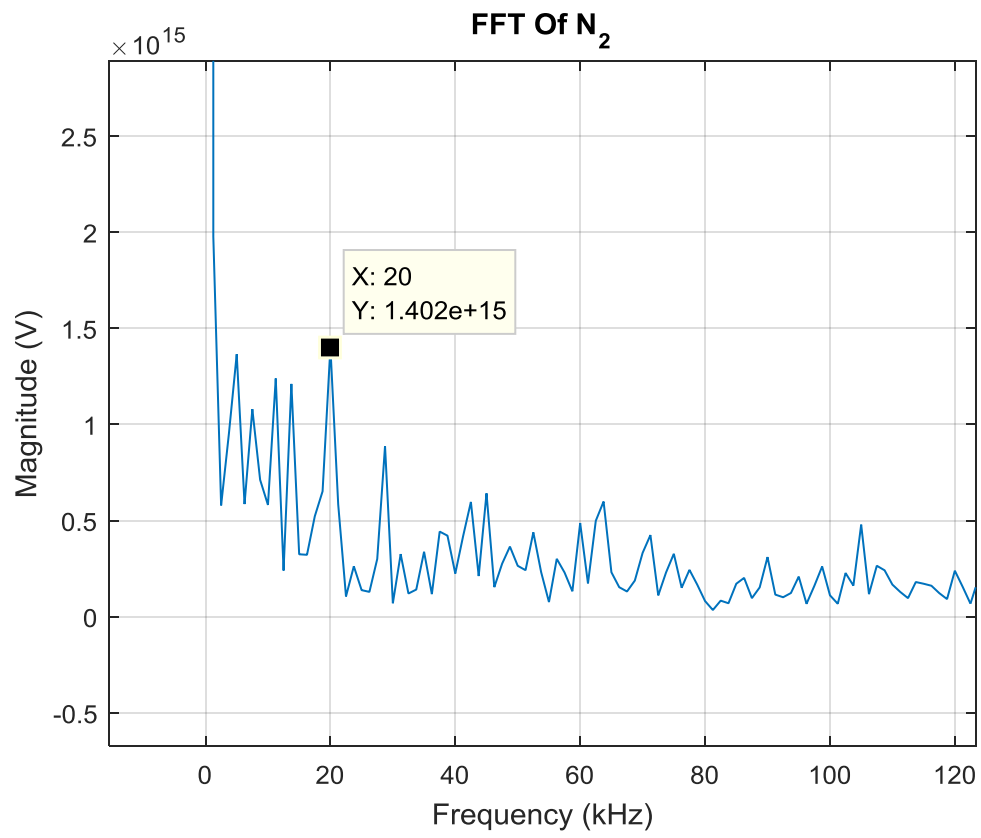


Figure 2.14: Simulation results of N2 FFT.

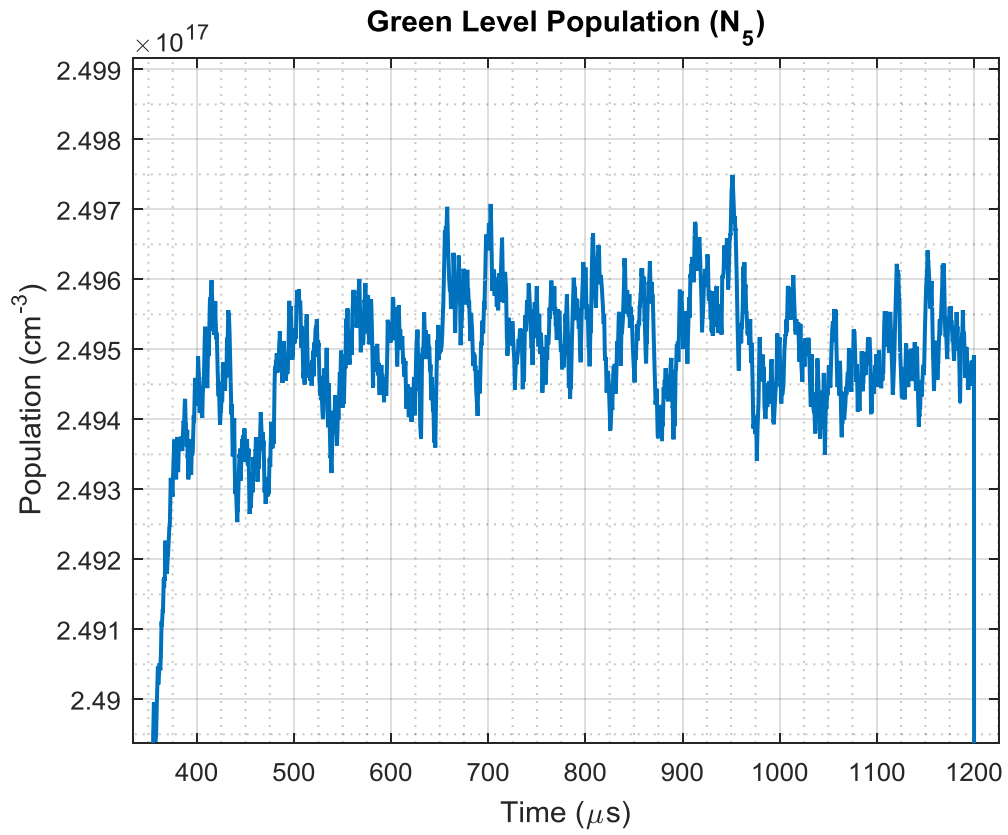


Figure 2.15: Simulation results of the  $N_5$  population expanded in view to show instability.

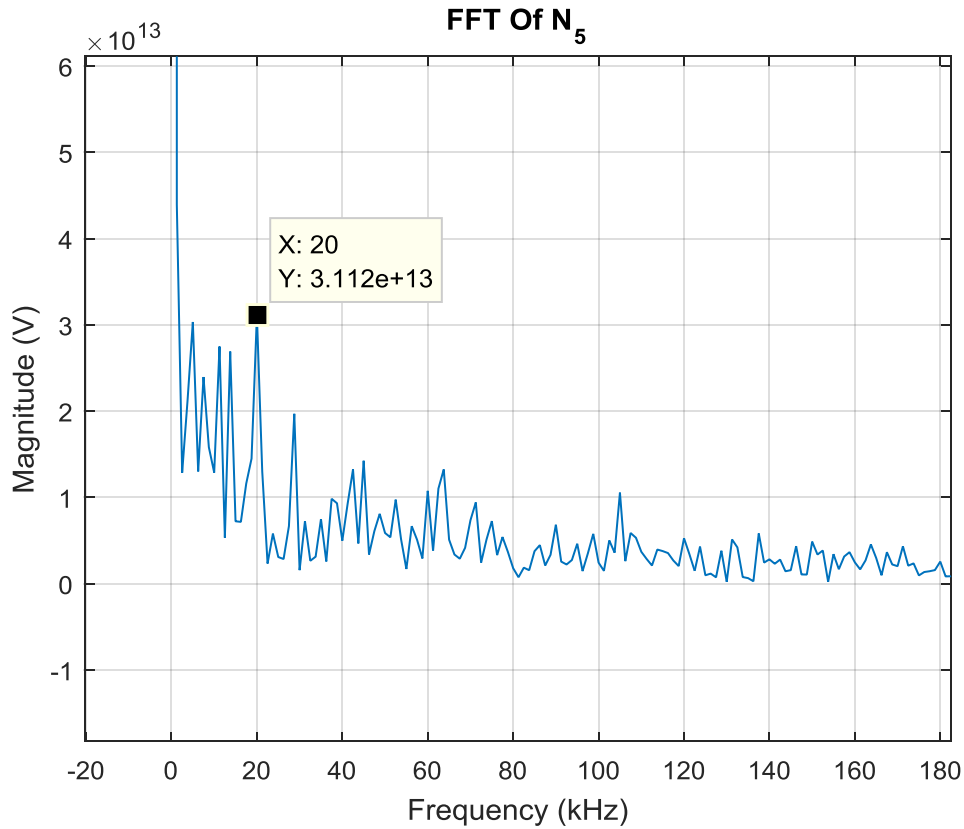


Figure 2.16 Simulation results of the FFT on the transient present in N5.

## 2.6 Error & Sensitivity Analysis

The rate equations presented have, in a simplified form, been solved by Runge-Kutta methods [30]. Showing that the eigen-value matrix has two significant bifurcation points, a steady state point and a Hopf bifurcation point that will cause the system to oscillate. Indeed, it was shown that there are three distinct operation regions of an Er:YAG 2.94 $\mu$ m laser. CW, under threshold, and self-pulsing were derived and plotted in Georgescu's analysis. It is important to note that this analysis was done assuming a low doped sample as the ion-ion interactions were ignored. The steady state bifurcation point denotes the region of stability. Operating in the region

greater than this point will put the system in the stable CW region as the real portions of the eigen values are negative. Additional simulations noted relaxation oscillations before the system settled to the CW region.

The Hopf bifurcation denotes the self-pulsing region as the real parts of the eigenvalues become positive. This region is the unstable region of operation that is an example of laser chaos. Clearly the behavior that will be shown in chapter 3 is related to this behavior outlined in [30]. As will be discussed in chapter 3 further detailed spectroscopic data is needed to be included in a more detailed rate equation model. As higher order terms are needed to trigger the instability.

There is a clear error in the type of modeling and assumptions made when composing the rate equations. The Euler method used in this work has a local truncation error that can be reduced significantly by selecting a small enough sample size. The Euler method is a first order explicit method that is part of the Runge-Kutta family denoted by its simplicity but lacks the accuracy and stability of the high order methods. The classical fourth order Runge-Kutta method largely the most common of the family should be applied if the truncation error from the Euler method cannot be reduced.

## **2.7 Concluding Remarks**

This chapter demonstrates the mathematical complexity and the challenges posed by the rate equation models and the difficulty in capturing all significant non-linear energy transfer mechanisms. As was seen the six-level system, considered the most general version, can be simplified to two level system if certain physical and experimental criterion is met. What was particularly revealing was the elusion to two separate solutions. This pattern will be described in from the laser chaos point of view and suggest the Er:YAG system naturally poses these oscillation modes.

## Chapter 3

### Experimental Setup & Results

The previous chapter reviewed the foundations of the Er:YAG system revealing the intricate non-linear energy transfer mechanisms interacting under high intensity resonant pumping. The inclusion of the non-linear energy transfer mechanisms in the rate equations quantitatively describe how these various non-linear interactions shape the population evolution and by extension the fluorescence yield. In the case of Er:YAG under high resonant pump an oscillatory behavior super imposed onto the fluorescence was achieved by Liu [1] in a laboratory setting. This chapter will present experimental transient fluorescence measurements displaying the oscillatory instability present in the output across samples with varying Erbium concentration and geometry. Evaluation of the instability of the fluorescence present in Er:YAG under high intensity resonant pump requires a straightforward setup based off a fluorescence measurement scheme presented by Liu [1]. Characterizing the instability requires elimination of other potential sources of error such as power supply noise appearing in the pump beam or etalon effects of filters. Therefore, a variation of the setup utilized by Liu proved beneficial as these considerations were already accounted for.

### 3.1 Experimental Setup for Measuring Fluorescent Instability

The measurements required high-power IR lasers resonant with the  ${}^4I_{15/2} \rightarrow {}^4I_{11/2}$  or the  ${}^4I_{15/2} \rightarrow {}^4I_{9/2}$  transition. The measurable fluorescence instability is activated with a sufficient pump intensity around  $10\text{kW/m}^2$  that was confined in a  $100\mu\text{m}$  diameter beam [1]. Liu pumped directly to the  ${}^4I_{11/2}$  utilizing a 962nm laser diode coupled through a fiber. A fiber coupled 808nm laser diode was used to pump to the  ${}^4I_{9/2}$  level. The laser sources were placed on large metallic (copper and aluminum) heatsinks with computer fans mounted underneath for cooling. The fibers were held by fiber holders. The 962nm laser diode had a bare fiber output and had to be regularly stripped and cleaved as heating losses caused the fiber tip to burn. The 808nm laser diode has a FC type connector. Both fiber holders were on a 3-axis stage and had fine 3-axis tuning on the mounts themselves. A Thorlabs 2 blade chopper spinning at 99Hz was placed in front of whichever laser output was in use (primarily 962nm). A 5cm plano-convex quartz lens with an 8cm principal focal length focused the beam down onto the crystal sample. The pump backscatter from the lens was captured by a Thor Labs silicon photo-diode with a baffle and was used to monitor the pump. A fiber coupled Ocean Optics UV-NIR spectrometer was used to monitor the input beam spectra and ensure that wavelength shifts from thermal fluctuations ceases after the diodes thermally stabilized. A Xantrex XFR 20-130 or XPD 7.5-67 power supply drove the laser diodes. These power supplies are well regulated and were verified by Liu that these supplies did not cause significant variations of the output beam intensities. The fluorescence was captured from a 0.5cm diameter by 0.5cm long cylindrical pillbox sample, whose doping concentration is provided in table 3.1 and whose geometry is shown in figure 3.3(a). These samples were mounted and properly heatsinked with an aluminum block with heatsinking fins. Each sample was bolted to the block with a copper sheet cover and with Indium

foil placed on the sample-aluminum interface to improve thermal contact. A 0.5-inch hole was cut through the aluminum block to create a through path for the pump. A silicon detector was used to capture the transmission of the pump through the sample. An InGaAs detector with a 1400nm long pass filter was adjacent to the sample to capture the 1.6 $\mu$ m fluorescence. A Hamamatsu R955 photomultiplier tube with a selection of glass filters was used to capture the Red, Green, and Blue fluorescence individually. The entire setup is provided in figure 3.4(a) and demonstrated the fluorescence instability. An example is presented in figure 3.1 depicting the 50% Er:YAG pillbox pumped by the 962nm laser diode. Sporadic fluctuations are clearly present at the peak of the fluorescence transient scan. The fluctuations are around 14% of the peak

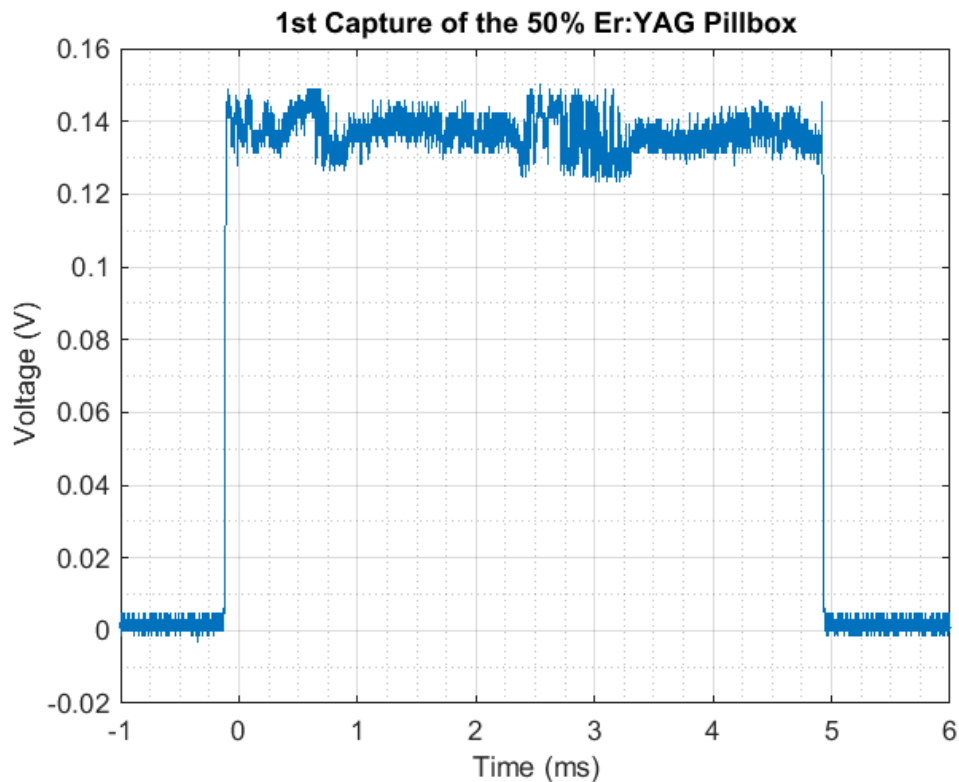


Figure 3.1. Transient scan of 50% Er:YAG pillbox pumped by the 962nm laser. Signal was hampered by noise and strong absorption by thickness of sample.

fluorescence value. The instability is however not entirely due to the non-linear mechanisms unique to the crystal medium. There are certain experimental errors that are contributing to the dramatic fluctuations, making it difficult to isolate the non-linear effects.

Er:YAG Sample Type	Er:YAG Sample Doping (% at. wt.)
Pillbox	1
Pillbox	3
Pillbox	5
Pillbox	25
Pillbox	50
Pillbox	60
Waveguide	50

Table 3.1: Sample list

Using this setup resulted in a beam diameter around 100 $\mu$ m incident on the front surface of the sample. This scheme proved very useful for exciting fluorescence from the  $^4I_{11/2}$  level as the sample would dramatically absorb the 962nm light. This is a consequence of the 40 cm $^{-1}$  (~250 $\mu$ m) absorption constant for 50 % at. wt. Er:YAG at 962nm, corresponding to ~20

absorption constants for the pillbox. However, there was a clear drawback of such a thick sample. Consider figure 3.2(a) showing a gaussian beam propagating through a pillbox sample. Ignoring reflection losses, the pump beam focused at the front face will have two loss factors causing uneven pumping: the absorption from the sample as the beam travels the length of the sample and beam spread due to diffraction. Resulting in a lower beam intensity which will fail to trigger the multiple non-linear energy transfer mechanisms in a significant fashion to be able to observe the fluorescence instability. In the example of the gaussian beam shown in figure 3.2(b) the beam is focused at the center of the sample and will already suffer losses by the absorption. When it reaches a Rayleigh length at the exit of the sample, it results in another drop in intensity equivalent to  $e^{-1}$  (~37%) of the peak at the center. Collimation of the pump can mitigate the effects though it will still be at the mercy of the material absorption. Another drawback using these samples manifests itself in background noise from the lower intensity fluorescence originating from the unevenly pumped sections. Therefore, a measurement may be thrown off by a strong background fueled by this lower intensity fluorescence, overloading the detector and affecting its sensitivity resulting in difficulty capturing the small fluctuations caused by the non-linear mechanisms. Liu mentions this effect in his work and suggests using an iris to limit the field of view of the detector and hence reducing the background fluorescence seen by the detector. Of course, the light being imaged onto a detector at the center of the field of view still must travel through the sample. Hence this approach would only cut down the strong background by a certain amount. If the samples were cooled and cooled detectors were utilized to maximize sensitivity, there may be enough signal fidelity to capture the non-linear mechanisms. Optimal operating temperature for an Er:YAG laser was demonstrated by the Army research lab to be around 77 K [62]. Cooling a sample and setting up detectors to operate at this temperature range

would require liquid helium, which is too costly for this work. Given all the complexity and lack of available equipment to carry out such a task, a thinner sample was needed. As it would ease the focusing requirements to achieve even pumping in the gain medium (see figure 3.2 (c)). That sample would be the second geometry used (figure 3.3(b)), which was a waveguide measuring 2cm high, 0.8cm long, and 0.5cm wide made from two slabs of undoped YAG sandwiching a 500 $\mu$ m thick piece of 50% at. wt. Er:YAG. The undoped YAG aides in in heatsinking and mitigating radiation trapping which causes a strong fluorescence background [68]. Undoped YAG also helps in the transition from the air to Er:YAG interface in terms of refractive index. Noting that Air = 1, Er:YAG 50% = 1.837, YAG @808nm = 1.8212, and YAG @962nm = 1.8168. The waveguide sample is optically polished on all sides reducing scattering/reflection losses. With any crystal sample for use in spectroscopic studies, various other factors will affect its fluorescence behavior. One example is sample purity which can drastically vary performance from crystals of the same doping concentrations. This is a result of the purity of the raw materials, growth method, and sample preparation. Varying fluorescent lifetimes of specific energy levels for Er:YAG were reported due to varying sample purity [1,21,29]. Modern samples, such as the ones used in this thesis, thankfully have a sufficient purity to rule out rouge actors affecting the fluorescence behavior. Specifically, these samples were made from base materials that are defined as five to six “9’s” purity, meaning typical impurities associated with whatever means of crystal growth are kept to  $1^{-3}$  or  $1^{-4}$  % of the sample. Older samples where typically three to four 9’s.

Further modifications were done to the original experimental setup to streamline the measurements for the multiple samples listed in table 3.1. First was to change the principal laser diode source to 808nm which directly pumps to the  $^4I_{9/2}$  level. With the 0.05 $\mu$ s lifetime of the

$^4I_{9/2}$  level, the ions can be considered to de-excite by rapid non-radiative decay to the  $^4I_{11/2}$  level. Essentially pumping with 808nm effectively directly feeds the  $^4I_{11/2}$  level. At 808nm for the 50% doping concentration, the absorption constant is around  $4 \text{ cm}^{-1}$ . Which for the 50% Er:YAG pillbox sample translates to 2 absorption constants. The waveguide sample is only 0.2 absorption constants, which is why this geometry is very beneficial. The incident pump beam was measured to have a beam width around  $76\mu\text{m}$  using the  $1/e^2$  definition and at an intensity of above  $50\text{kW}/\text{cm}^2$ . This well exceeded the threshold discovered by Liu to cause instability in the fluorescence and caused a visible green fluorescence to occur. Figure 3.6 shows the thermally stabilized spectra of the 808nm diode with Appendix C Figure C.7.4 containing the spatial beam profile. For reference the thermally stabilized spectra of the 962nm pump diode is provided in figure 3.5. The samples were properly heatsinked with the same aluminum block and Indium foil setup. The main pump laser was mounted onto a large aluminum computer style heatsink with a 70mm fan. The fiber was mounted on the same 3-axis translation stage with the fiber mount having the 3-axis precision controls. A 50mm sapphire convex-convex lens with a 6-inch focal length focused the pump beam onto the center of the sample. Given the discussion associated with figure 3.2, focusing onto the center allowed for a uniform beam through the Erbium gain medium. The beam however needed to be focused onto the surface of the pillbox samples and therefore would not be evenly pumped, though due to the high intensity proved to be sufficient. A 30-blade chopper allowed for the pump to be modulated at a pulse width of 1ms. This width is important as it matched the nominal lifetime of the  $^4I_{13/2}$  level and ten times that of the  $^4I_{11/2}$  level. This allows the fluorescence to be primarily affected by the dynamics of the  $^4I_{11/2}$  level. A total of three silicon photo detectors (One Thorlabs Si DET36A and two DET10A) were used to measure the pump source, the fluorescence of the  $^4I_{11/2}$  level, and the green fluorescence which

originated from the  $^4S_{3/2}$  level thermalized with the  $2H_{11/2}$  level. A tuned amplifier (Stanford Research SR530) provided isolation to the fundamental oscillation frequency that was witnessed when measuring the fluorescence, which will be shown to be close to the lifetime of the  $^4S_{3/2}$  level. The DET36A detector measuring the  $^4I_{11/2}$  fluorescence was equipped with a 950nm long pass filter (Thorlabs FEL 0950) while one of the DET10A detectors measuring the green fluorescence had a notch filter centered at 540nm (Thorlabs FB540-10) along with three hot mirrors (Thorlabs 90% Transmission 450nm-750nm). The last photodiode, tasked to measure the pump source, was taking a sample of the incident light from the backscatter off the sapphire lens with a baffle. A third pump source was also utilized to try to measure the interaction of the NIR pumps with a 2.94 $\mu$ m laser. The intent was to de-excite the upper laser level ( $^4I_{11/2}$ ) and to investigate the possibility of the MWIR laser locking onto the witnessed instability. There were some difficulties with this approach which was eventually dropped. A continued discussion is provided in chapter 5. The MWIR source is a Shuemann MirPac Window Model with a maximum output power of 1W continuous wave through a germanium window aperture and a TEM<sub>00</sub> beam shape [16,17]. The beam was chopped with a 30-blade chopper pulsing the laser at around 100 $\mu$ s pulses with a 50% duty cycle. The beam is colinear and counter propagating to the main pump beam, therefore a beam block is needed on both ends. For the 2.94 $\mu$ m beam block, a gold faced prism with a mirror finish measuring 2 x 2.5mm was placed right after the main focusing lens. The prism was carefully placed close to the sapphire lens where it would obstruct a small portion of the main pump beam while completely blocking the transmitted 2.94 $\mu$ m beam. Conveniently the gold prism was used to direct the transmitted MWIR laser to be imaged onto a InAs detector (Judson J12) with a 1-inch f1 ZnSe lens. A germanium coated sapphire window to block the bright background scatter caused by the main pump beam was placed in front of the

ZnSe lens. To block the pump beam, a large germanium window with a 50mm diameter and 10mm length was placed at an angle behind the sample holder to redirect the transmitted pump and fluorescence to a 40mm convex-convex quartz lens ( $f = 5.5\text{cm}$ ), imaging onto the silicon photodetector with the 950nm long pass filter. The germanium window allowed the MWIR beam to propagate with minimum internal losses. A Teledyne Lacroix DPO 7140 oscilloscope captured all the data saved to a convenient comma separated value format. Sampling error is minimized with the 750 MHz bandwidth of the oscilloscope. Figure 3.4(b) is a diagram of the test setup for the fluorescence measurements.

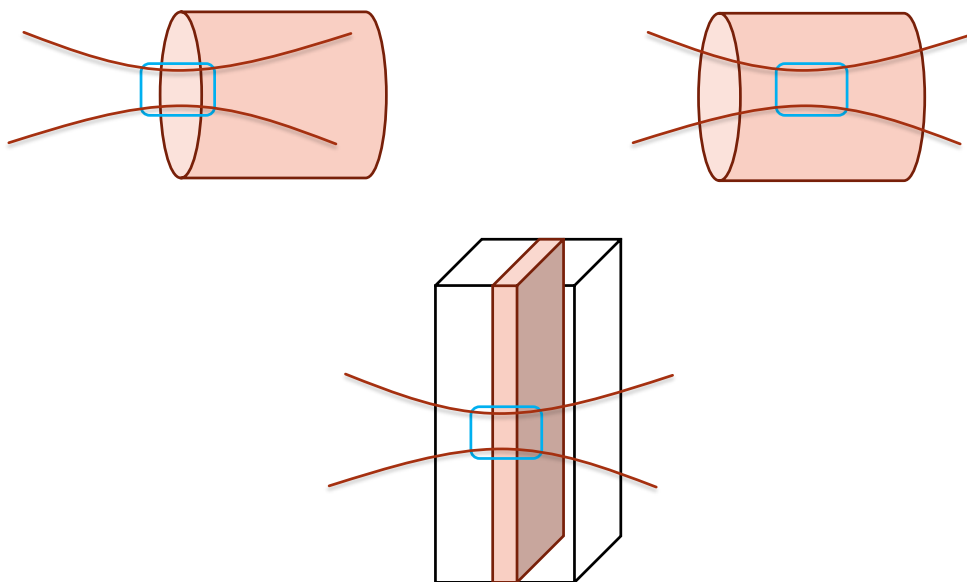


Figure 3.2: Pumping scheme for a thick sample vs. a thin sample. The blue boxes represent the beam center where the width is constant assuming a Gaussian beam.

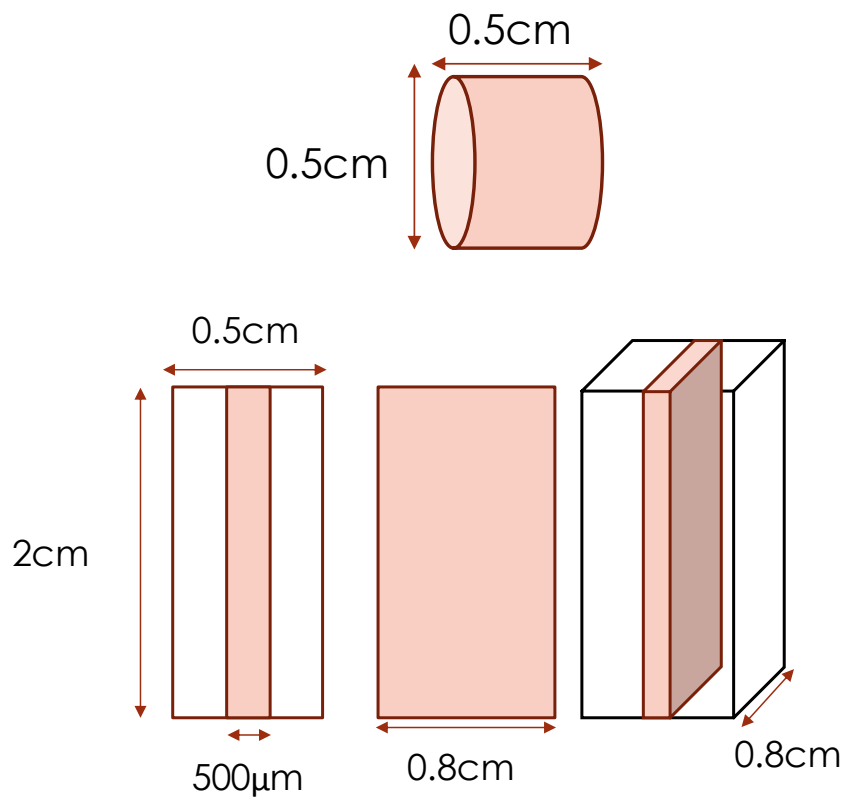


Figure 3.3: Pillbox and Waveguide sample geometry

As stated seven samples were measured, six pillbox samples and one waveguide, with the dopant concentration ranging from 1% to 60% at. wt. The variety of doping concentration allows exploring the strength of the non-linear effects particularly due to the ion-ion interactions. In chapter 2, the ion-ion interactions were demonstrated to drastically change the energy dynamics of Er:YAG allowing to beat the self-saturation condition. The complex nature was expressed mathematically by the rate equations and the coupling caused by the ion-ion terms. Lower doped samples will be dominated by the ESA effect with high intensity resonant pumping. With the percolation effect mentioned in the previous chapter, typically occurring around 15% dopant concentration, the ion-ion interactions will be a significant factor as each Erbium ion will be able to interact to any Erbium ion through its neighbors. These behaviors manifest themselves as a small observable oscillation when under high pump. The oscillatory behavior appears as a quasi-sinusoidal signal superimposed on both the  $^4I_{11/2}$  and  $^4S_{3/2}$  fluorescence. The following set of plots provided from figures 9-12 are 50% Er:YAG waveguide fluorescence transient plots of these levels accompanied with their fast Fourier transforms (FFTs) of the oscillations under pulsed pumping at 808nm. The FFTs show a dominant frequency of around 60 kHz translating to around a 16.7 $\mu$ s period which coincides directly to the  $^4S_{3/2}$  lifetime. A significant second harmonic was also present in most of the scans. Figures 7-8 show the pump beam and it's FFT revealing no significant harmonics that may cause the instability. The oscillations themselves are attributed to the ESA and ion-ion interactions upconverting ions to the  $^4S_{3/2}$  &  $2H_{11/2}$  levels from the  $^4I_{11/2}$  and  $^4I_{13/2}$  levels. The ions will then decay either through phonon interaction or fluorescence to ground. As stated by Georgescu, the phonon decays will occur between the nearest neighboring level [22-27]. In the case of Er:YAG the nearest lower level to the  $^4S_{3/2}$  &  $2H_{11/2}$  levels is the  $^4F_{9/2}$  level. This level serves as an intermediate level from the  $^4S_{3/2}$  &  $2H_{11/2}$

(green) to the  ${}^4I_{11/2}$  level.  ${}^4F_{9/2}$  level itself has a lifetime of around  $1.5\mu\text{s}$  and any ion at this energy will generally rapidly decay via phonon interaction and will reach the  ${}^4I_{9/2}$  level. With its  $0.5\mu\text{s}$  lifetime an immediate decay to the  ${}^4I_{11/2}$  is expected. Looking through the select transient scans provided in Appendix C shows variation in the fundamental frequency of oscillation between 60kHz to 65kHz. The spread can be attributed to the variation in exchange of ions occurring between the intermediate  ${}^4F_{9/2}$  and  ${}^4I_{9/2}$  levels as the ions are decaying to the  ${}^4I_{11/2}$  level and re-excited by ESA to the green levels. These interactions will become more complex as the doping increases.

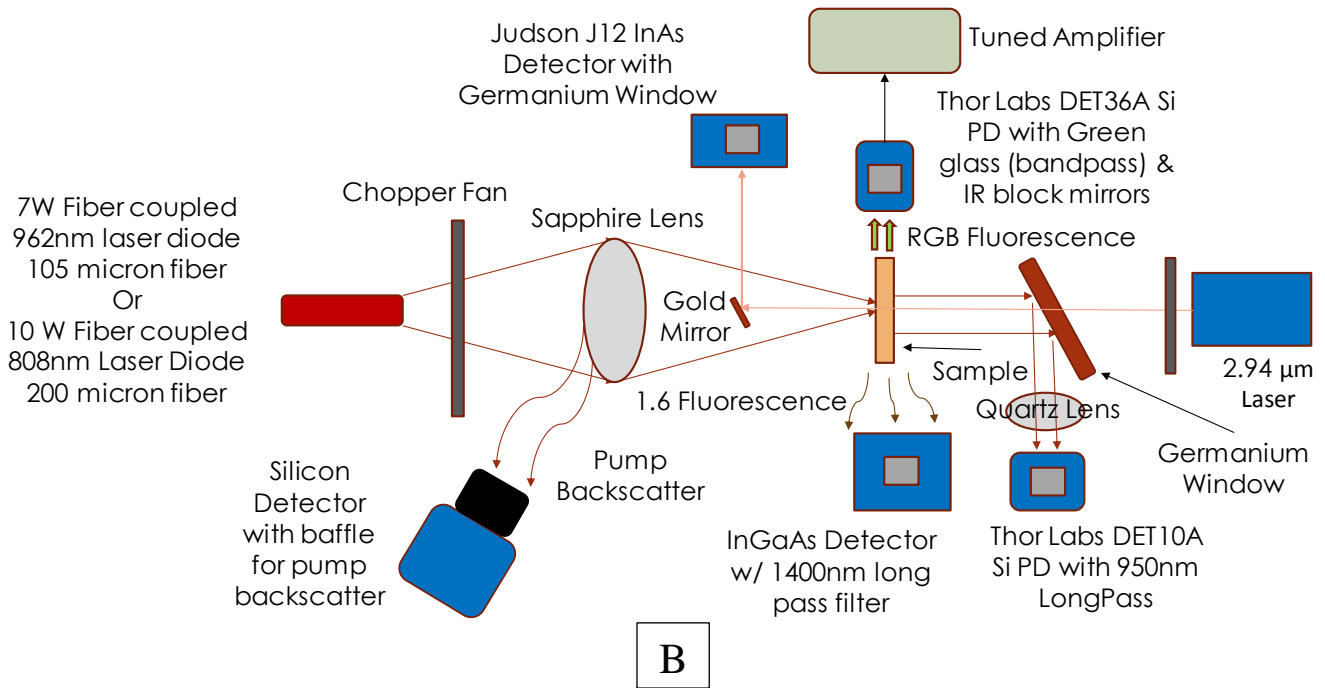
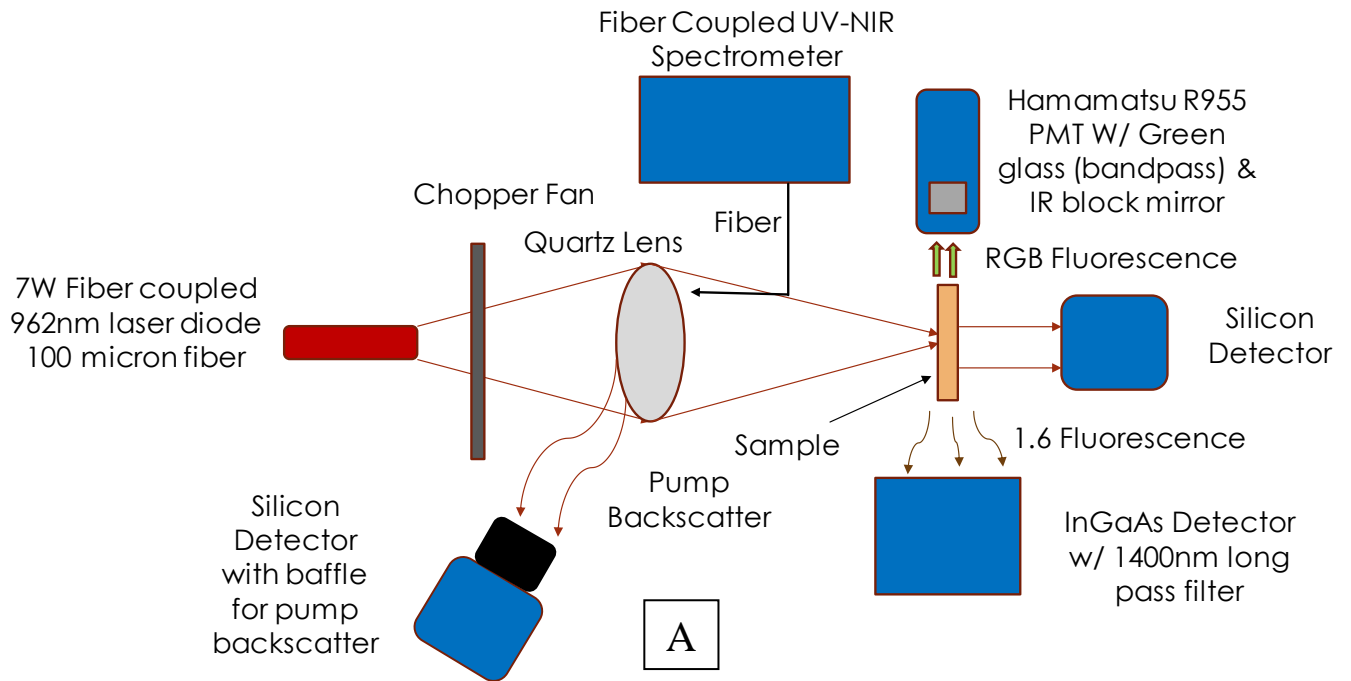


Figure 3.4: (A) Original Setup, (B) Setup for measuring fluorescence instability

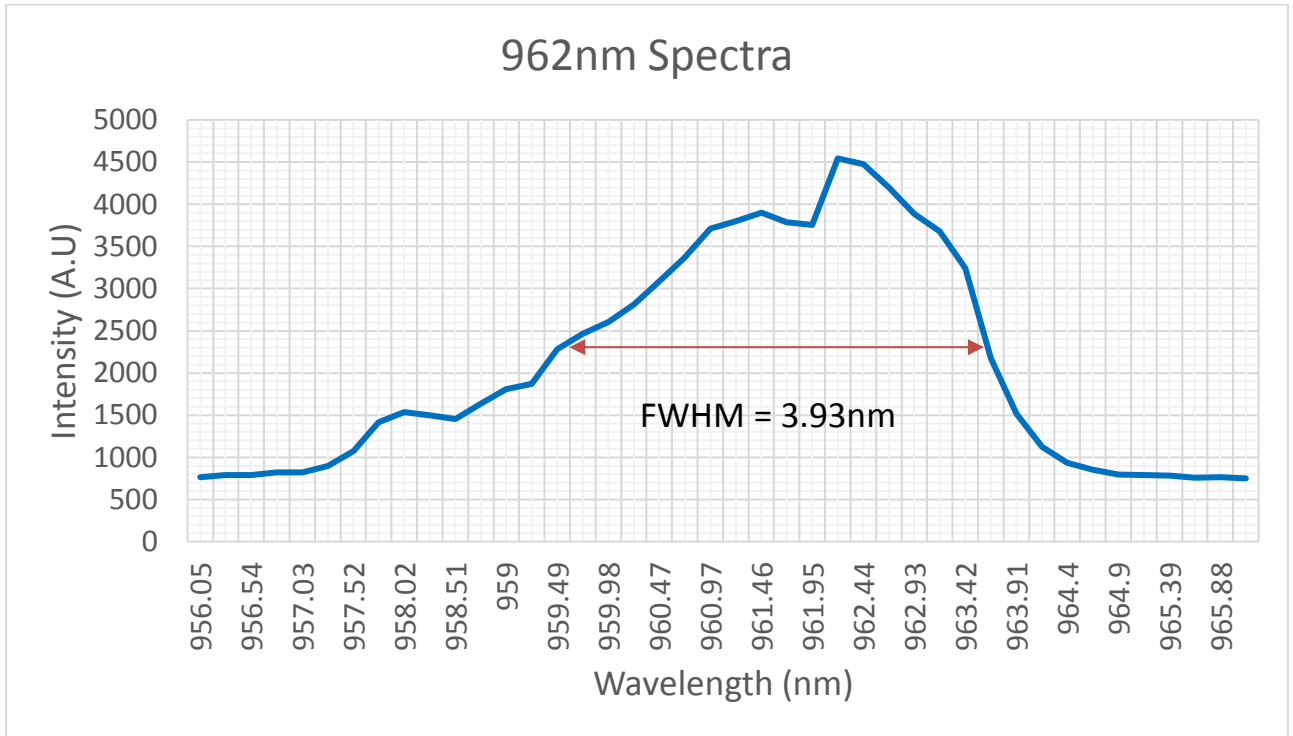


Figure 3.5: 962nm Pump profile, thermally stabilized after 15 minutes.

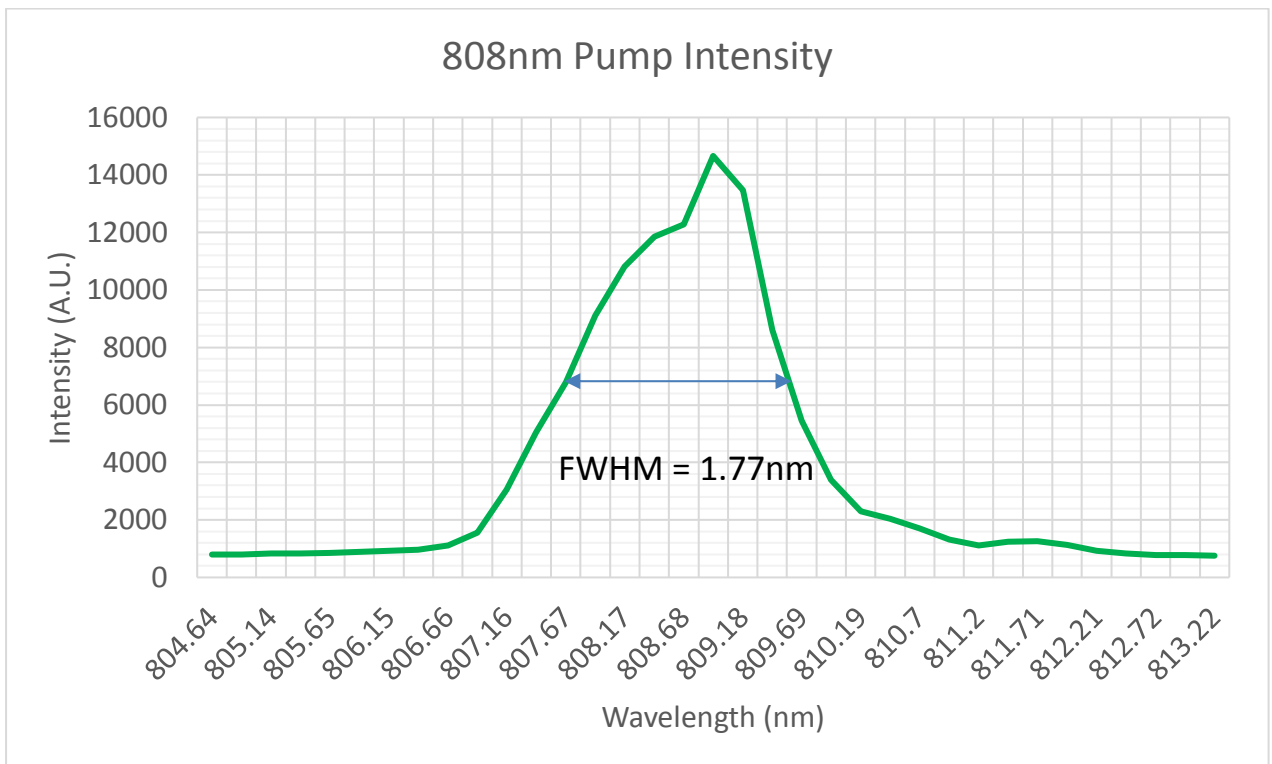


Figure 3.6: 808nm Pump profile, thermally stabilized after 15 minutes

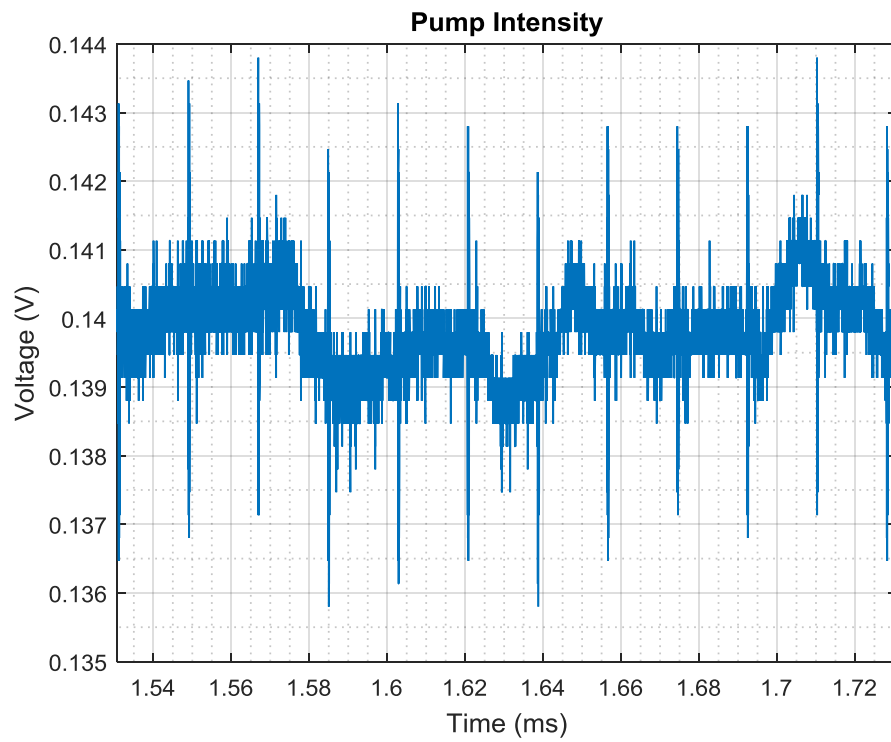


Figure 3.7: Transient scan of 808nm pump beam.

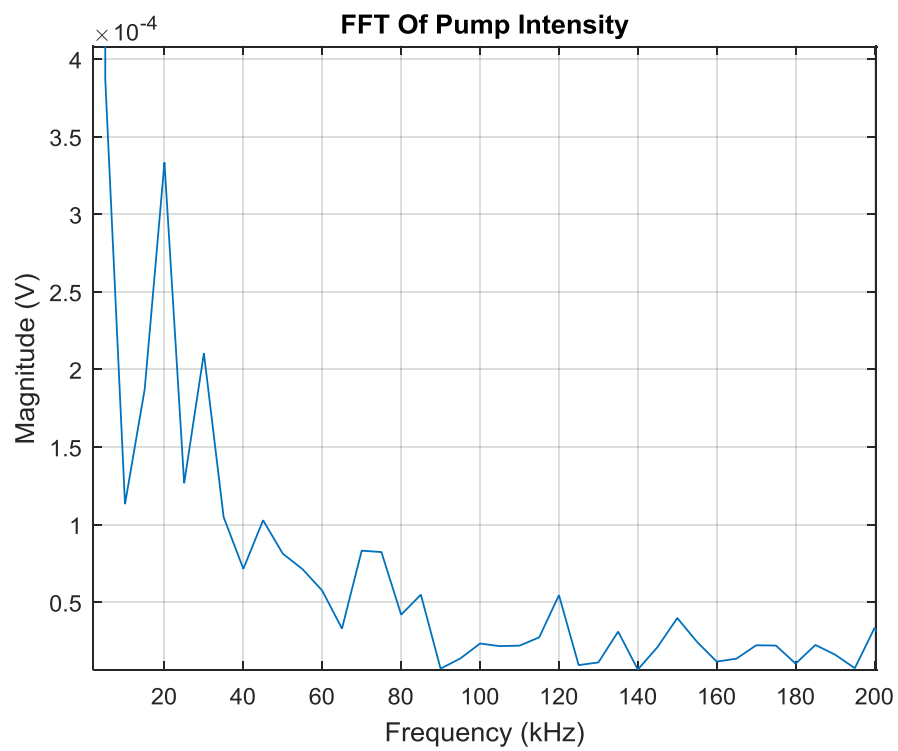


Figure 3.8: FFT of 808nm pump beam showing no significant signal at 60 kHz

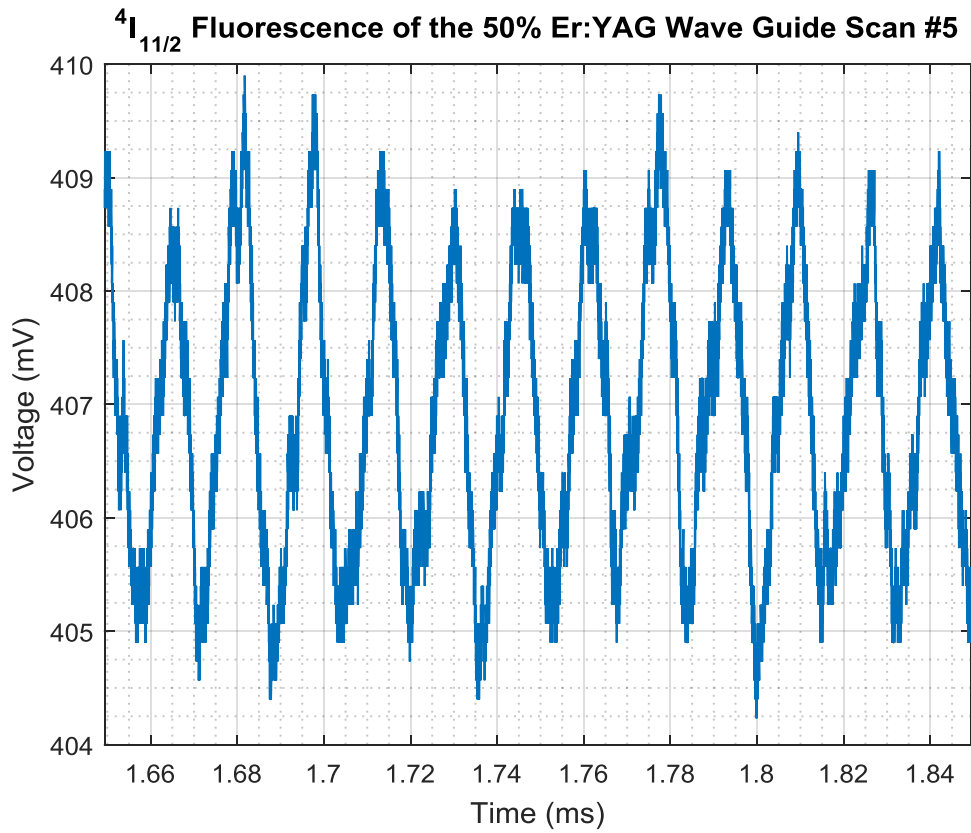


Figure 3.9: Transient scan of the  $^4I_{11/2}$  level. Appendix C has a large selection of transient scans. Each sample had 5 scans averaged to provide useful statistics summarized in appendix C.

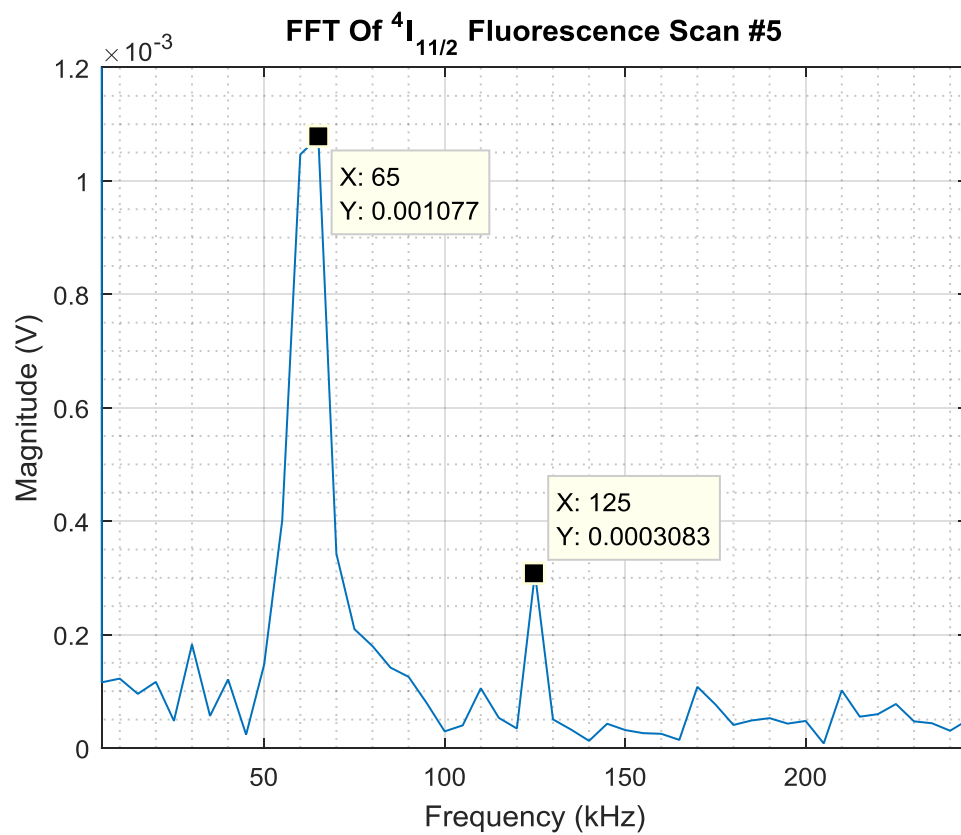


Figure 3.10: FFT of the transient scan of the  ${}^4I_{11/2}$  level.

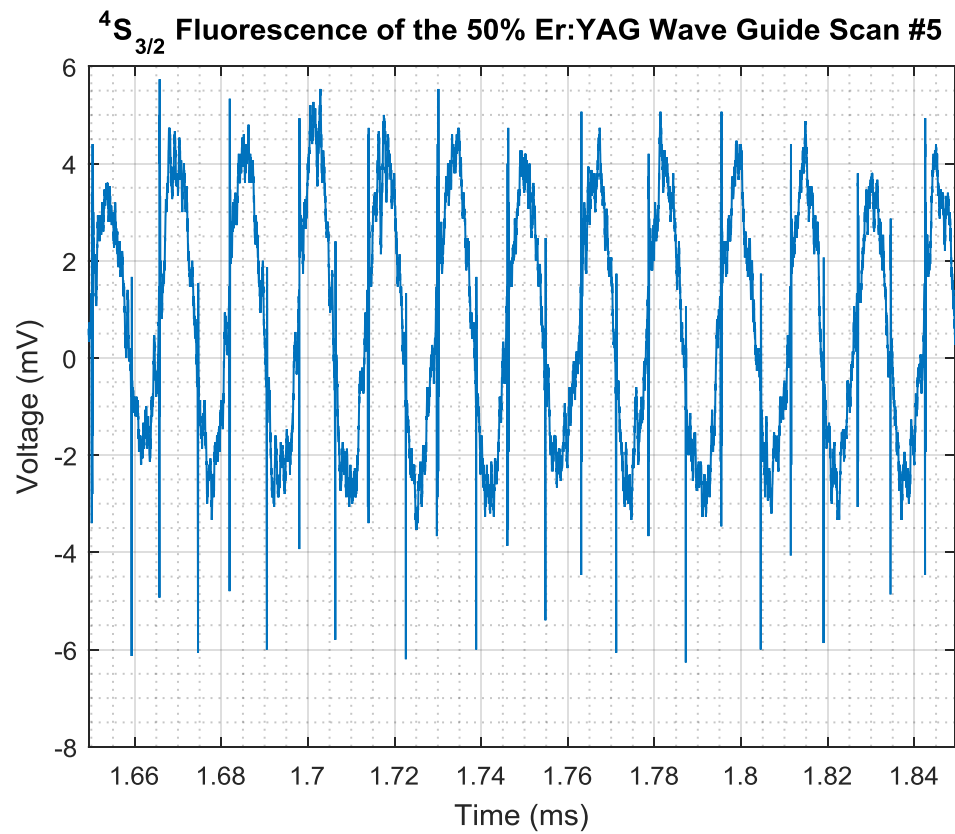


Figure 3.11: Transient scan of the  $^4S_{3/2}$  level.

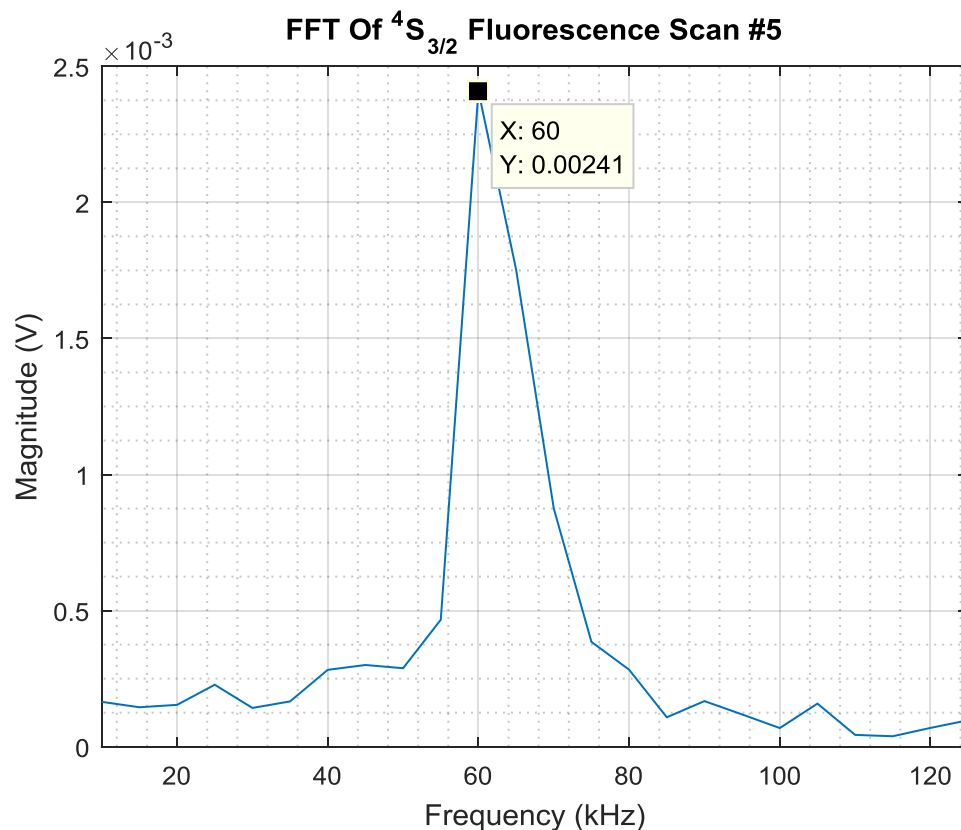


Figure 3.12: FFT of transient scan of the  $^4S_{3/2}$  level.

The previous set of transient scans show that the dominant frequency of oscillation was close to the lifetime of the  $^4S_{3/2}$  level and up on both the  $^4S_{3/2}$  and  $^4I_{11/2}$  level fluorescence signals. The fluorescence yield is of course tied to the pump intensity and wavelength, therefore looking at the magnitude of the instability compared to the total yield shows that it is a small effect ( $> \sim 1\%$ ). The change to the 808nm pump technique had significant benefit as can be seen by comparing figure 3.1 to figures 9-12. The instability is clearly measurable even in the presence of a strong background signal from the high intensity pump. The background will ultimately

affect the measurable yield as it can saturate detectors and limit sensitivity. To resolve this issue shunt resistors were placed on the photo-diodes capturing the fluorescence. 5.14k $\Omega$  for the  $^4I_{11/2}$  detector and 100k $\Omega$  for the  $^4S_{3/2}$  detector. Despite this the pillbox samples are still two absorption constants thick, therefore there will be significant attenuation and scatter of the pump beam contributing to the background and lowering fidelity. This is where the waveguide sample is advantageous as the length of the Erbium medium is smaller than the Rayleigh length of the pump beam. Coupled with the small absorption length of the sample it makes it ideal to utilize this sample to measure the ESA cross section.

### 3.2 Experimental Setup for Measuring Excited State Absorption

The ESA has generally been ignored in Er:YAG modeling as it is dependent primarily, as shown in chapters 1 and 2, on the input pump intensity. The form of the ESA expression  $\sigma_x \phi N$  demonstrates the direct relationship to the input intensity ( $\phi$ ), it is therefore natural to ignore these effects under conditions of low pump intensity. Further justification is added as typical Er:YAG modeling centers around samples with high doping concentration. Modeling has been conducted with inclusion of ESA within rate equations for Er:YAG however, it was for low doped samples and the ion-ion interactions were not included [27-31]. What resulted is four distinct paths, two from the  $^4I_{11/2}$  and two from the  $^4I_{13/2}$ , that depended on the pump wavelength (the case of 808nm or 962nm). In the work carried out for this thesis, 808 nm was the primary wavelength and activated a strong ESA pathway from  $^4I_{13/2} \rightarrow ^4S_{3/2}$  &  $2H_{11/2}$  noted in the literature. Figure 3.13 outlines the common ESA pathways.

Measuring ESA has proven to be straightforward with credit to Koetke and Huber [42] and later Boulanger et. al. [43] for development of a pump and probe technique for measuring

the ESA cross section of low doped Er:YAG over a wide wavelength band. The experiment utilized a broadband flash lamp and a Krypton ion laser for a pump and probe respectively. Due to the broadband nature of the pump and to increase signal fidelity, a set of choppers and lock-in amplifiers were added to isolate the change in the intensity of the probe beam when the pump was off and switched to on. With the use of single wavelength sources, a simplified version of the setup that Koetke and Huber utilized was implemented allowing the lock-in amplifiers to be removed. The 808nm laser is set as the pump beam while the 962nm laser probes the  $^4I_{11/2}$  level as it will incrementally excite ions upwards to the higher energy levels. The pump was set to the  $50\text{kW}/\text{cm}^2$  intensity while the probe was set to  $>1\text{kW}/\text{cm}^2$ . The spatial beam profile of the 962nm laser is provided in figure C7.2 in appendix C. Figure 3.14 illustrates the simplified pump and probe setup.

The ESA cross section is derived based on the pump having a larger repetition rate than the probe beam. The crystal's transmission changes based on whether it is pumped or unpumped. While under heavy pump the ground state is depleted leading to bleaching. Upper levels are populated allowing ESA and stimulated emission to occur. Assuming a crystal with length  $L$ , with Erbium concentration  $n$ , and with probe beam intensity  $I_0$ , the Lambert-Beer law can be applied as outlined by in [42]. The probe beam transmission intensity measured from the portion of the unpumped crystal is expressed as equation 3.1. With the probe beam transmission intensity measured corresponding to the pumped crystal as equation 3.2. Here the summation term is over all populated excited states  $i$ . The term  $n_i$  represents the population densities of the excited states. The term  $n_e$  represents the total excitation density. The GSA, ESA, and emission cross section are represented by the terms  $\sigma_{GSA}$ ,  $\sigma_{ESA}$ , and  $\sigma_{em}$  respectively. Combining expressions 3.1 and 3.2 result in equation 3.3. The objective is to capture the change in the transmission of the probe

beam noting that the signal to noise can be small with CW sources. Koetke and Huber utilized a double modulation scheme where the pump was chopped at a much slower rate than the probe beam. Then the captured signals were feed to separate lock in amplifiers. A flash lamp was used in the original work therefore a monochromator was utilized. Using single wavelength sources eliminates the need for a monochromator. Huber's setup measures the difference in the pumped and unpumped intensity (equation 3.4), which eliminates errors due to probe beam drift.  $\Delta I$  is typically small allowing for the simplification in equation 3.5 to be valid. Which allows equation 3.3 to be simplified to equation 3.6. Here  $\Delta I' = A\Delta I$ , where A is the amplification factor from the lock-in amplifiers.  $I_0$  is replaced by the modulated probe beam intensity I. The terms  $n_e$  and A do not need to be known as the relation in equation 3.7 can be used, derived from calibrating out the bleaching bands. The system can then measure what is expressed in equation 3.8. With expansive spectroscopic research and use of resonant single wavelength sources allows for a significant simplification of Huber's finalized expression shown in equation 3.9. With the 808nm pump and 962nm probe the only significant ESA transition is  ${}^4I_{11/2} \rightarrow {}^4S_{3/2}$ . The ratio  $n_i/n_e \approx 1$  with the GSA and emission cross sections obtained by measurements conducted by Georgescu [22, 24, 27, 29, 31] with  $\sigma_{GSA} = 2.6 * 10^{-20} cm^2$  &  $\sigma_{em} = 1.8 * 10^{-20} cm^2$ , and  $L = 500\mu m$ .

What is left is the term  $n_e$  which is the number of atoms per cubic cm that are pumped out of the ground state which can be derived in a straight forward fashion with published data. Using the experimentally measured  $50kW/cm^2$  intensity value we can multiply this value by the absorption constant for the pump wavelength and the term  $(1-e^{-1})$  which accounts for power absorbed in one absorption constant. The power per cubic cm is  $P_r = 50 \frac{kW}{cm^2} * 4cm^{-1} * (1 - e^{-1}) = 1.26 * 10^5 \frac{W}{cm^3}$ .

We now take  $\frac{hc}{\lambda} = \frac{6.26*10^{-34} J*s[3*10^8 \frac{m}{s}]}{808*10^{-9}m} = 2.325 * 10^{-19} J$  which can then be taken to

calculate  $\# \text{Photons}/s = \frac{2.52 \cdot 10^4 \frac{W}{cm^3}}{2.325 \cdot 10^{-19} J} = 54.376 \cdot 10^{22} s^{-1} cm^{-3}$ . Then leading to  $\frac{\# \text{ of atoms}}{cm^3} =$

$[\# \text{ photons per sec}] * \left[ \text{rise time of } {}^4I_{\frac{9}{2}} + \text{rise time of } {}^4I_{\frac{13}{2}} \right] = 54.376 \cdot 10^{22} s^{-1} cm^{-3} * (290 \cdot 10^{-6} s + 880 \cdot 10^{-6} s)$ . The 808nm laser pumps ions to the  ${}^4I_{9/2}$  level and ESA initiating from the  ${}^4I_{13/2}$  state transfers ions to the  ${}^4S_{3/2}$  state. With  $\frac{\# \text{ of atoms}}{cm^3} = 6.362 \cdot 10^{20}$  and the fact that for 50% Er:YAG there is roughly  $7 \cdot 10^{21}$  atoms per cubic cm, we have  $\frac{6.362 \cdot 10^{20}}{7 \cdot 10^{21}} = 9.1\%$  of the atoms pumped out of the ground state. Similar calculation for a 962nm laser at  $10 \text{ kW/cm}^2$  yields  $\sim 9.6\%$  of the atoms pumped out of the ground state. Therefore, the ESA cross section can be directly derived. Although limitations of the lasers available prevent the experiment to be ran utilizing the 808nm laser as a probe beam. A shorter wavelength laser is necessary (at  $>50 \text{ kW/cm}^2$ ). Georgescu's spectroscopic data shows 799.5nm to be appropriate for a probe beam, though the linewidth must be small to not overlap with the pump [30,31]. Lasers in the 650-670nm band would also suffice. Finally inspecting the plots in figure 3.15 and taking the difference of the captured signal of the probe transmission when the crystal is pumped and unpumped (voltage values can be used as only the ratio is necessary) then rearranging equation 3.9 results in equation 3.10 with the value of the ESA cross section of  $1.1854 \cdot 10^{-18} \text{ cm}^2$ . If the same exact calculations were done under the assumption the 808nm pump beam was at  $10 \text{ kW/cm}^2$  then the ESA cross section would have been  $2.9285 \cdot 10^{-17} \text{ cm}^2$ .

$$I_u = I_0 e^{-\sigma_{GSA} n L} \quad (3.1)$$

$$I_p = I_0 \exp[-\sigma_{GSA}(n - n_e)L + \sum_i \frac{n_i}{n_e} (\sigma_{em,i} - \sigma_{ESA,i}) n_e L] \quad (3.2)$$

$$\ln \left[ 1 + \frac{I_p - I_u}{I_u} \right] = n_e L \left[ \sigma_{GSA} + \sum_i \frac{n_i}{n_e} (\sigma_{em,i} - \sigma_{ESA,i}) \right] \quad (3.3)$$

$$\Delta I = I_p - I_u \quad (3.4)$$

$$\ln \left[ 1 + \frac{I_p - I_u}{I_u} \right] \approx \Delta I / I_u \quad (3.5)$$

$$\Delta I / I = n_e L A \left[ \sigma_{GSA} + \sum_i \frac{n_i}{n_e} (\sigma_{em,i} - \sigma_{ESA,i}) \right] \quad (3.6)$$

$$n_e L A = (\Delta I / I) / \sigma_{GSA} \quad (3.7)$$

$$\sum_i \frac{n_i}{n_e} (\sigma_{em,i} - \sigma_{ESA,i}) \quad (3.8)$$

$$\frac{\Delta I}{I} = n_e L \left[ \sigma_{GSA} + \frac{n_i}{n_e} (\sigma_{em,i} - \sigma_{ESA,i}) \right] \quad (3.9)$$

$$\frac{-\Delta I}{I * n_e * L} + \sigma_{GSA} + \sigma_{em} = \sigma_{ESA} = 1.1854 * 10^{-18} \text{ cm}^2 \quad (3.10)$$

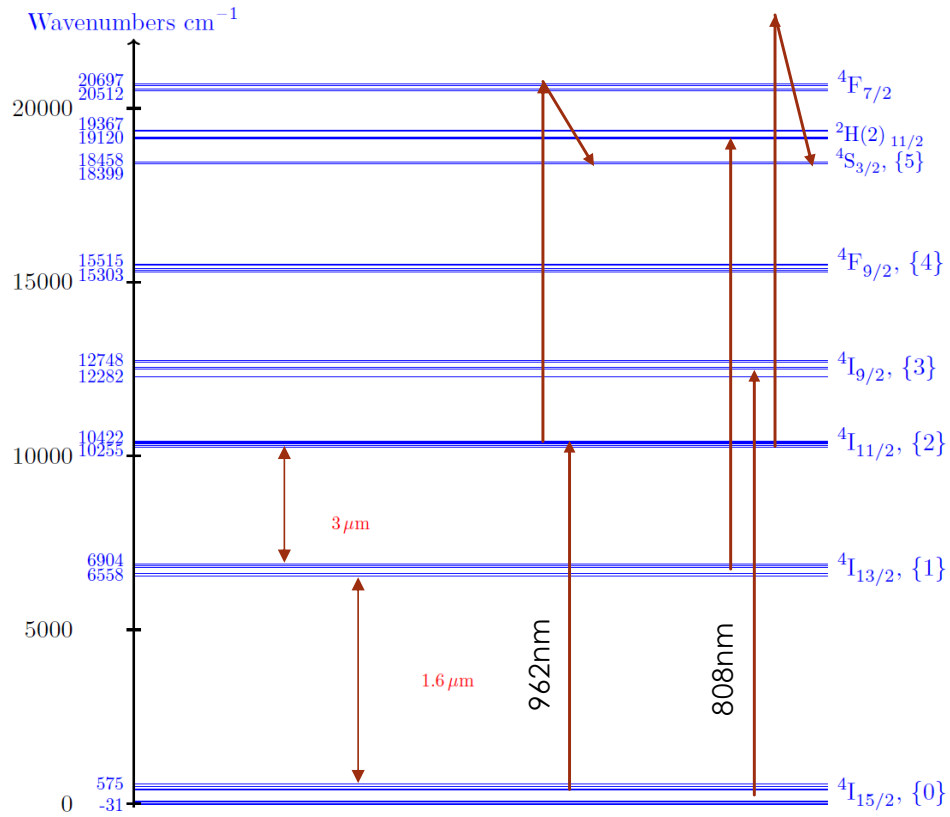


Figure 3.13: Energy level diagram displaying the cyclical pattern of ions flowing from the  $^4I_{11/2}$  level to higher energy levels and then to the  $^4S_{3/2}$  level. The levels above the  $^4S_{3/2}$  level have a sufficiently short lifetime and small energy spacing which can therefore be treated as feeding immediately to the  $^4S_{3/2}$  level.

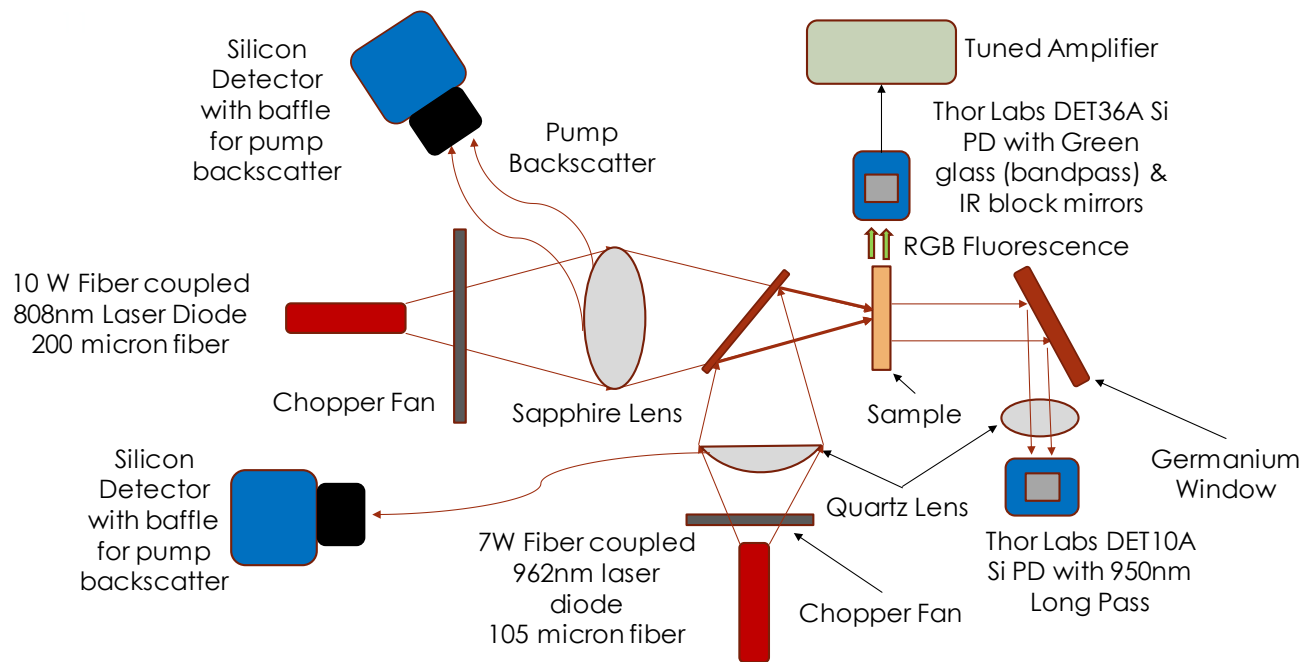


Figure 3.14: Pump and Probe setup with the 808nm pump beam set to  $50\text{kW}/\text{cm}^2$  and the 962nm probe beam set to  $1\text{kW}/\text{cm}^2$ .

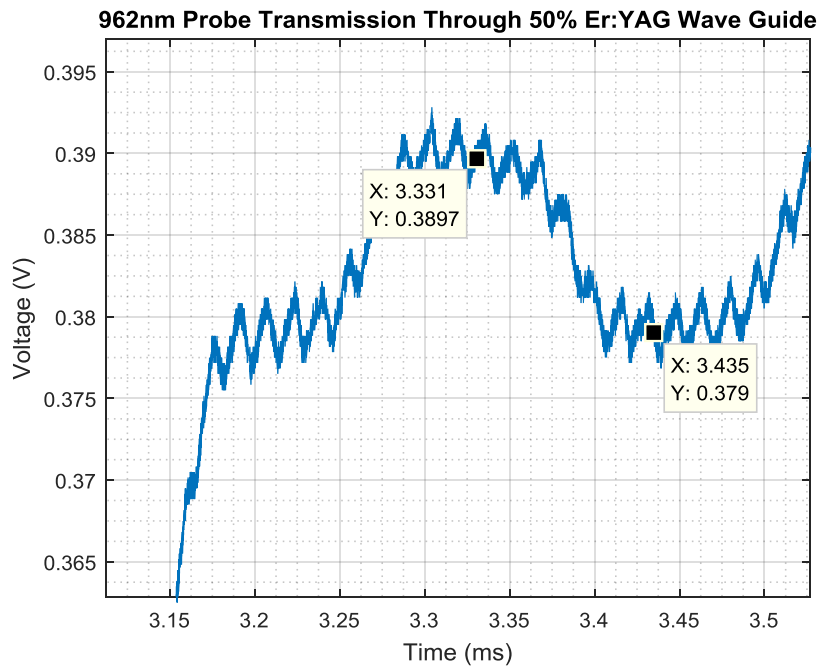
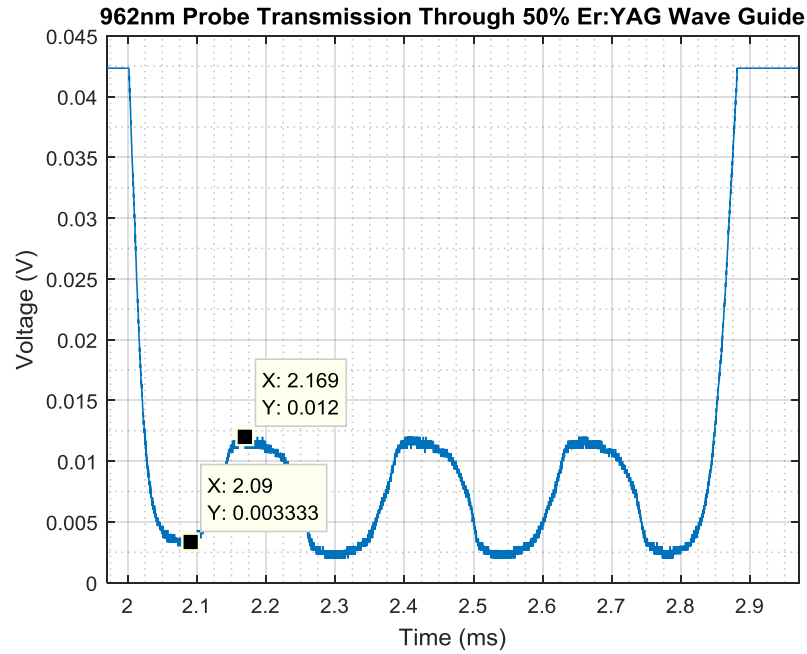


Figure 3.15: Transient scans of the ESA measurement using the pump and probe scheme in figure 3.14. (a) Top plot is the fluorescence of the  $^4I_{11/2}$  level under no pump. (b) The bottom plot is the fluorescence under pump. The 808nm pump beam is running at  $50.058\text{kW}/\text{cm}^2$  while the 962nm probe beam is at  $1.871\text{ kW}/\text{cm}^2$ .

## Chapter 4

# Analysis of the Fluorescence Instability & Impact on Modeling

This chapter serves as a bridge to better connect Georgescu's theoretical and spectroscopic work with the fluorescence instability witnessed in chapter 3 by integrating the measured ESA cross section into the rate equation model with the ion-ion interactions. The measured behavior is then compared to the simulation. The results show that additional measurements are needed to capture higher order non-linear effects influencing the fluorescence instability. The significance of these higher order terms to the fluorescence instability are expanded upon at the end of this chapter.

### 4.1 Rate Equation Simulations with Ion-Ion and Measured ESA Interactions

The transient spectroscopic scans demonstrate the effect of non-linear energy transfer mechanisms in Er:YAG manifesting as the oscillatory (periodic) instability embedded in the fluorescence. The fluctuations are shown to oscillate at a period closely matching the natural lifetime of the  ${}^4S_{3/2}$  level. As shown from the energy level diagrams in figure 2.1, the non-linear mechanisms (ESA & ion-ion) excite ions to the  ${}^4S_{3/2}$  level which then mostly non-radiatively decay to the  ${}^4F_{9/2}$  followed by additional rapid non-radiatively decay to the  ${}^4I_{11/2}$ . Afterwards, these ions can then be re-excited by these non-linear mechanisms resulting in a cyclical energy transfer pattern, shown in figure 4.1. Modifications to the original Georgescu rate

equations lacked suitability in accounting for the transient fluorescence under high intensity resonant pumps. Despite the addition of the ESA cross section from literature [22, 26-31], the transient simulations done in chapter 2 did not directly mimic the experimental results. However, the value for the cross section was measured from a low concentration sample under moderate pump. Which resulted in the use of the pump and probe technique used in [5-7] to derive the ESA cross section from a high concentration sample under high intensity resonant pump as demonstrated in chapter 3. The thin geometry and the undoped YAG sandwich present in the 50% Er:YAG sample had the additional benefit of smaller absorption and thermal losses. The contribution of the new ESA value can be expressed as two terms shown in equation set 4.1. The ESA terms, highlighted in red, contribute to the coupling of the  $^4I_{11/2}$  and  $^4S_{3/2}$  levels. Transient simulations shown in figures 4.2 through 4.5 reveal no discernible periodic oscillation. The FFT's of the transient scans do display spikes at or near 60 kHz though they are not prominent enough with respect to the noise floor to be of any significance. This directly follows

$$\frac{dN_5}{dt} = -\frac{N_5}{T_5} - w_{50}N_0N_5 + w_{22}N_2^2 + \sigma_x\phi N_2 \quad 4.1(a)$$

$$\frac{dN_4}{dt} = -\frac{N_4}{T_4} + \frac{N_5}{T_5} \quad 4.1(b)$$

$$\frac{dN_3}{dt} = -\frac{N_3}{T_3} + \frac{N_4}{T_4} + w_{11}N_2^2 + w_{50}N_0N_5 \quad 4.1(c)$$

$$\frac{dN_2}{dt} = -\frac{N_2}{T_2} + \frac{N_3}{T_3} - 2w_{22}N_2^2 + R_{p2}N_0 - \sigma_x\phi N_2 \quad 4.1(d)$$

$$\frac{dN_1}{dt} = -\frac{N_1}{T_1} + \frac{N_2}{T_2} - 2w_{11}N_1^2 + w_{50}N_0N_5 \quad 4.1(e)$$

$$\frac{dN_0}{dt} = -R_{p2}N_0 + w_{11}N_1^2 + w_{22}N_2^2 - w_{50}N_0N_5 \quad 4.1(d)$$

from the discussion in section 2.5 that the rate equation model, though technically more accurate with the inclusion of the measured ESA cross section, continues to lack the critical third order ion-ion effects discussed in Liu's conclusion of his thesis [1].

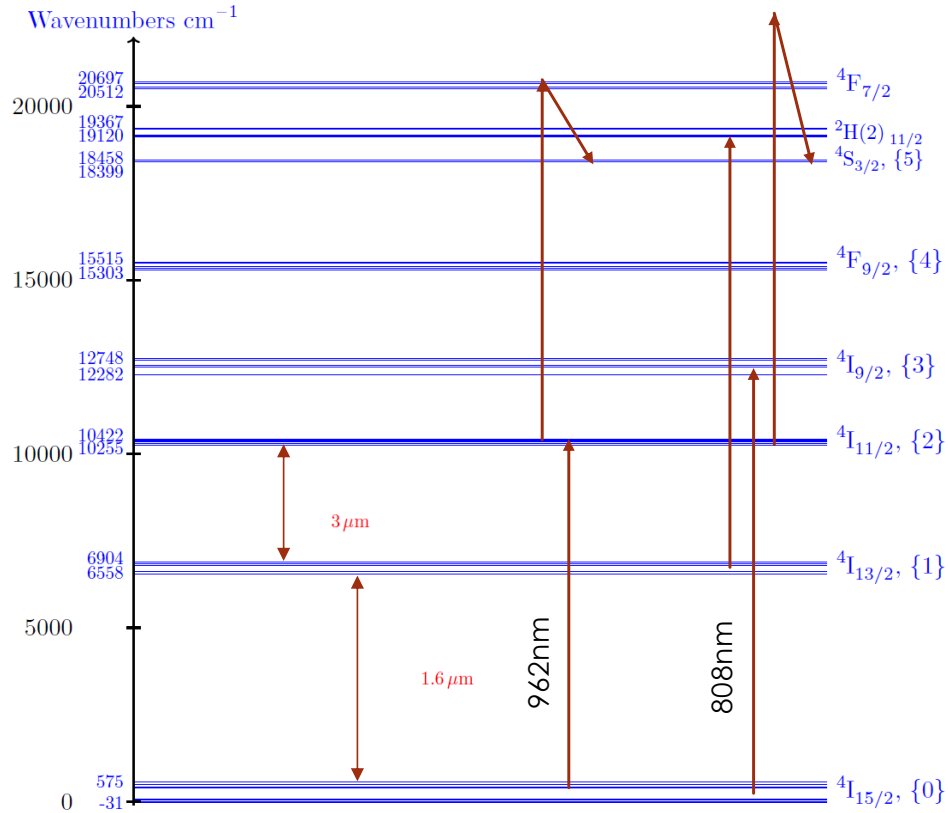


Figure 4.1: Energy level diagram displaying the cyclical pattern of ions flowing from the  $4I_{11/2}$  level to higher energy levels and then to the  $4S_{3/2}$  level. The levels above the  $4S_{3/2}$  level have a sufficiently short lifetime and small energy spacing which can therefore be treated as feeding immediately to the  $4S_{3/2}$  level.

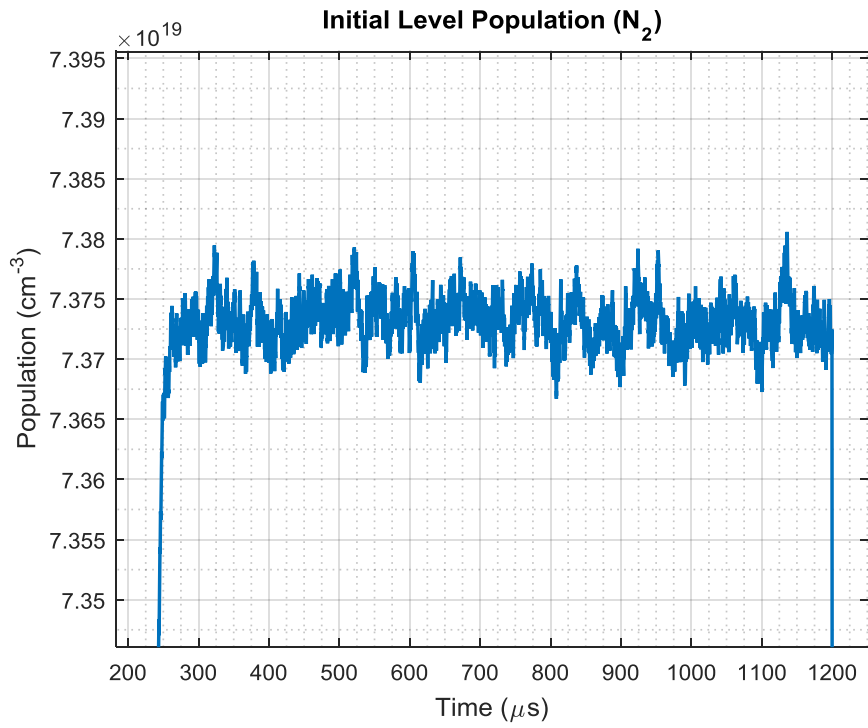


Figure 4.2: Simulation Result for the  ${}^4I_{11/2}$  with no ESA terms.

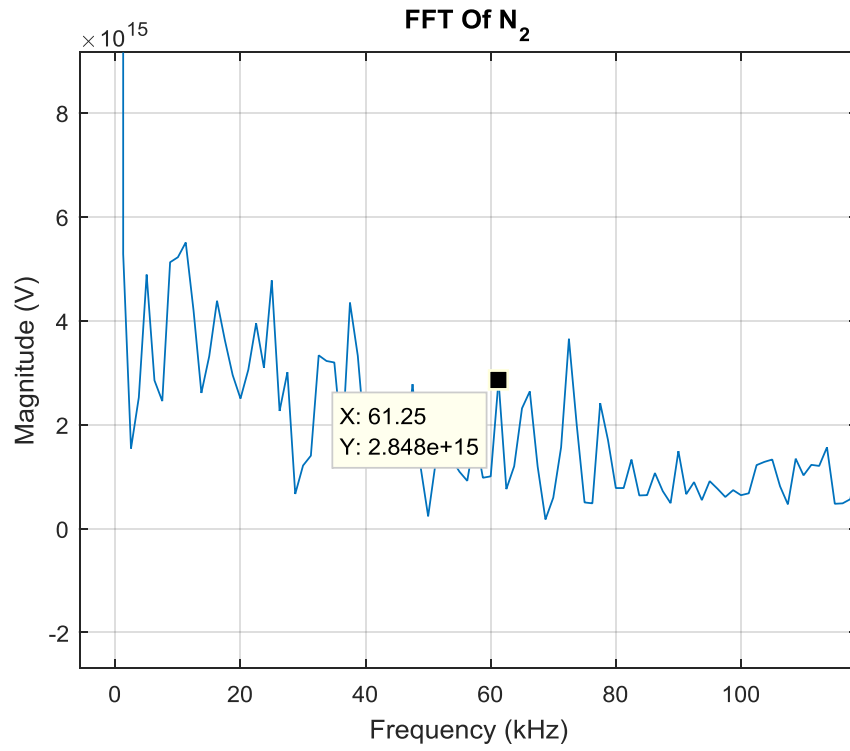


Figure 4.3: FFT of the simulation presented in figure 4.2. The spike at 60kHz is below the noise floor and cannot be considered significant.

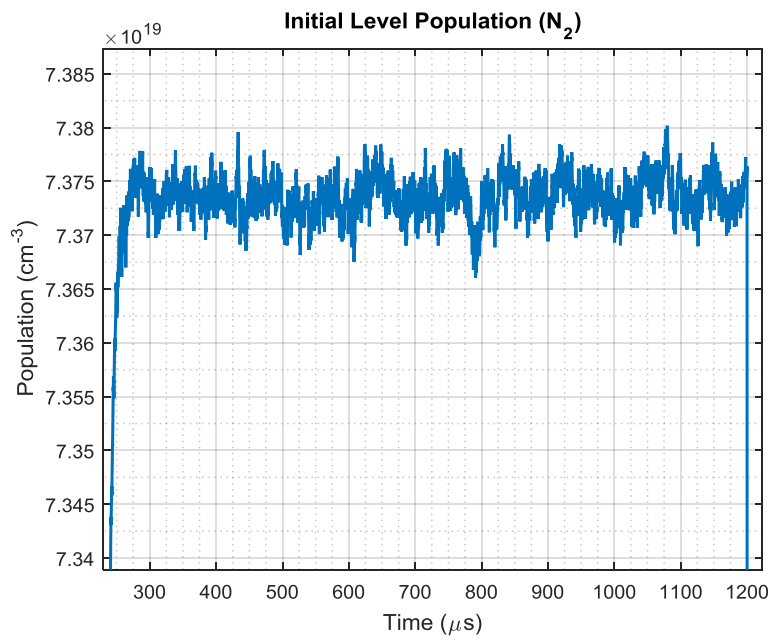


Figure 4.4: Simulation Result for the  ${}^4I_{11/2}$  level with the ESA cross section measured in chapter 3 included.

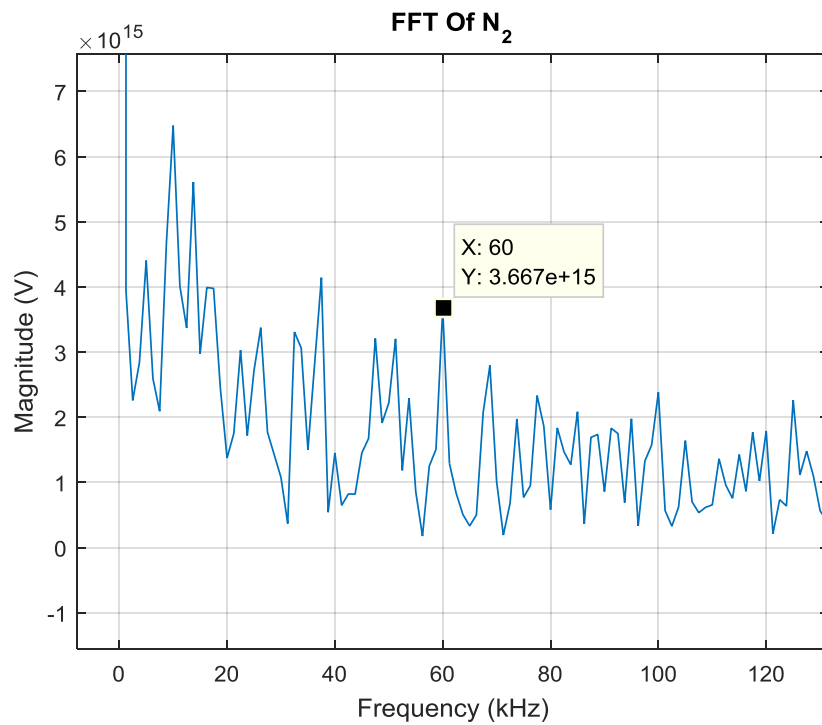


Figure 4.5: FFT of the simulation presented in figure 4.4. The spike at 60kHz is more prominent though still below the noise floor and cannot be considered significant.

## 4.2 Third Order Ion-Ion Effects

From the concluding section in Liu's work it was determined that the rate equation model required seven additional terms to account for third order ion-ion interactions. Figure 2.1 shows some of these transitions and were discussed in [1,30-32]. Indeed, there is literature that discusses three photon phenomena [78]. Of course, these third order effects were indirectly measured from fluorescence yield spectroscopy with various input intensity levels as shown in figure 2.2. A revealing example is shown in figure 5.1 (taken with permission from reference [1]) where recording the changes in the slope of the fluorescence rise/decay required the respective curves to be plotted in a semi-log scale and fitted in a piecewise fashion. The changes in slope correspond to the regions where non-linear effects of a certain order began to contribute significantly to the output fluorescence. Despite the third order effects being present, again verified in figure 2.2, there are only two changes in the slope measured. These third order ion-ion interactions will have a  $N^3$  type dependence. Therefore, the pump intensity must be at or above a certain threshold for these effects to take place in a significant manner. Just as in this work and in [1] a nominal threshold of  $10\text{kW}/\text{cm}^2$  was required to measure the lower order ion-ion interactions and ESA, this very threshold has proven to be sufficient for third order effects to be measurable by certain techniques. Under the assumption of pulsed pumping at or above threshold, as the input intensity rises there will be a point where the second order non-linear effects are sufficient enough to change the fluorescence rise rate. Eventually there will be a point where the third order effects will also affect the fluorescence rise rate. On the decay the converse occurs where the higher order effects "turn off" at certain points. This is where the changes in slopes come from and result in non-exponential behavior. Therefore, three unique slopes should be present, the section where the third order effects are sufficiently large will be near the peak of

the fluorescence output (assuming square pulses). As in the case of figure 4.6 the pump intensity was strong enough where these mechanisms were active, though the detector lacked the fidelity to measure it. Potential methods for measuring these third order effects are presented in chapter 5 as a high SNR is required.

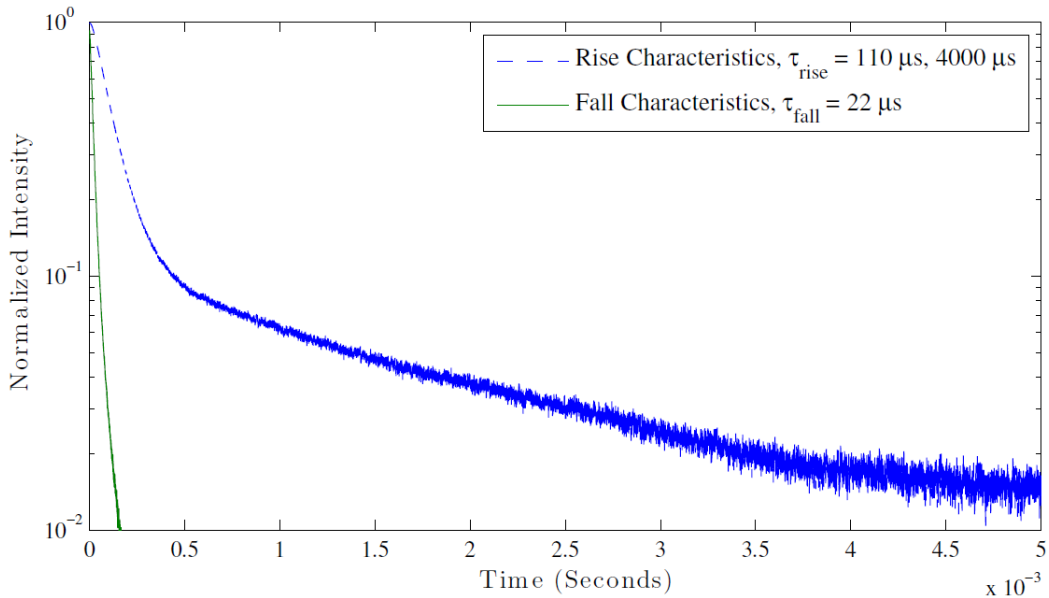


Figure 4.6: Transient fluorescence yield demonstrating non-exponential decay. Manifestation of multiple time constants are shown by distinct slopes on a semi-log scale. The sample is a 50% Er:YAG pillbox with geometry outlined in appendix B pumped with a 962nm laser diode at  $10\text{kW}/\text{cm}^2$ . Third order effects are active but do not appear as an additional change of slope. This change of slope should occur near the peak of the fluorescence yield. The equipment used to capture the fluorescence is not sensitive enough. This plot was taken from [1] with permission from the author.

## Chapter 5

### Pathway Forward on Characterizing Er:YAG

The work presented in this thesis reviewed the foundations of energy transfer mechanisms within rare-earths and how that formed the rate equations for the Er:YAG system. Previous mathematical models failed to adequately demonstrate this instability as only certain non-linear mechanisms were accounted for. ESA was generally ignored as it was directly related to the pump intensity multiplied by the level population. Which in turn was dominated by ion-ion interactions for higher concentration systems, hence was excluded from various models utilizing a moderate to lower intensity pump. As presented in this work, transient spectroscopic measurements were conducted to measure the ESA cross section of certain energy level transitions in the crystal. Interestingly the laser modeling for low doped Er:YAG lasers done by Georgescu et. al. alluded to fluorescence instability by showing that two possible solutions existed when the rate equations accounted for multiple non-linear energy transfer pathways. The rate equation modeling for high doped samples accounting for ion-ion interaction under a moderate resonant pump were simplified to a second order form which lead to two possible solutions, though one set was not physically possible and ignored. The lack of modeling including both types of non-linear energy transfer mechanisms was remedied with spectroscopic measurement methods already developed on specialized high purity samples. From there analysis was done by iteratively solving the rate equations using the Euler method.

Unfortunately, as discussed in the previous chapter, even with the inclusion of the ESA cross-section under high intensity resonant pumping, the rate equation model used did not

adequately demonstrate the oscillatory instability. Indeed, the cause for this error was discovered in the reference literature showing third order ion-ion interactions. These effects would prove to be significant in high concentration samples as fluorescence yield measurements carried out by Liu revealed third order effects can contribute up to 27% to the yield [1]. Capturing the non-exponential fluorescence rise and decay at a sufficient fidelity would be extremely challenging as a significantly high SNR is needed. For example, a simple multi-exponential decay made of two separate time constants would require an SNR of around 10,000 to 1 using time-resolved fluorescence imaging [75]. Other factors deterring the accuracy are the equipment utilized, uneven pumping, unfavorable geometry, etc. A stable pump beam along with sufficiently sensitive detectors and precise optics are particularly crucial in looking for third order effects in the fluorescence. Thin, ideally one absorption constant, high purity specialized samples can greatly reduce the errors introduced by uneven pumping, absorption, and rare-earth impurities. A set of waveguide samples, equivalent to the one used for the pump and probe measurement in chapter 3, can provide insightful data on how the doping profile changes the population dynamics. This of course would include the third order effects, that were shown in Liu's analysis. The natural progression from this discovery is to capture the third order effects as it manifests itself in the rise and fall time of the fluorescence output. Dopant concentrations of 1,3,5,15,25,50, and 60% would be recommended as any future endeavor would entail plotting the transient fluorescence behavior with hopes of capturing the variation, if any, of the instability. An added benefit is that all the transient spectroscopic measurements outlined in chapter 3 can be redone to collect more accurate data. A further avenue of exploration would be to conduct these experiments under various pump intensities to generate similar plots to ones done by Liu [1] and provided in this work with permission in figure 2.2. In addition, exploration of the contributions

of sample percolation to the fluorescence can be evaluated. The transient behavior of the fluorescence can further be modeled by changing the pump source or by using multiple resonant pump sources. An example set up can use the 2.94 $\mu\text{m}$  laser as a probe beam like the setup in chapter 3 section 1. The probe beam interactions with the gain medium under a high intensity 962nm or 808nm pump can be monitored for instability as it transmits through the sample. A laser amplifier, illustrated in figure 5.1, constructed from a waveguide sample would explore such a property. Alternative evaluation of the fluorescence dynamics can be explored in a simple laser resonator setup using a high intensity resonant pump, shown in figure 5.2. This setup can be used to “lock” the generated beam to the fluorescence instability by tuning the cavity mirrors such that the cavity mode corresponds to a harmonic of the fundamental frequency of the instability. In the case of the work presented in this thesis, the cavity mode should be set to a harmonic of  $\sim 60\text{kHz}$ . Also, as stated before, an extension of all these experiments would be to use multiple pump beams. Naturally all three sources listed in appendix B can be used together to measure the fluorescence dynamics. Additional resonances in Er:YAG occur at  $\sim 650\text{nm}$ ,  $\sim 540\text{nm}$ , and  $\sim 485\text{nm}$ , which can be excited by commercial laser sources. With the recommended thin sample sizes and appropriate optics, it would ease the focusing requirement of converging multiple beams onto the same spot to reach the intensity threshold noted by Liu [1]. Cooled detectors are highly recommended particularly for measuring the MWIR, since room temperature detectors for this waveband are generally slow and lack sensitivity. With the necessary fluorescence data generated from these additional experiments, further development of a precise laser device can be achieved.

The accuracy of the rate equations forms a fundamental part in making laser devices. The efficiency of extracting optical gain and the output beam evolution define the performance of a

laser. As mentioned in chapter 4, there are seven additional terms in the rate equation system for Er:YAG. These seven terms along with the lower order non-linear terms are a form of laser chaos. Various papers reviewing the concept of laser chaos has been authored over the years [67-73]. Comparing the simplified rate equation model for an Er:YAG laser to the Maxwell-Bloch equations depicting laser chaos reveal that the Er:YAG system can be described as having 2 phase dimensions defined by 2 separate dampening rates. To have laser chaos, 3 damping rates are needed. Technically, the Er:YAG laser systems has that third dampening rate in the form of the cavity loss rate. However, it is generally fixed and if one were to use the Maxwell-Bloch equations for the Er:YAG system, one of the equations would simplify. Indeed, this was what Georgescu essentially solved for in his laser modeling work. If one were to modulate the cavity loss, then the full set of Maxwell-Bloch equations can apply, and the laser will become chaotic. Measuring the chaos can be accomplished by taking the laser resonator setup of figure 5.2 and modify it to where a portion of the signal detected from the output beam intensity is feedback as a control signal to an electro-optic modulator placed inside the laser cavity, shown in figure 5.3. The modulator modulates the cavity loss, adding a third dampening rate to the system. Indeed, this very behavior was elaborated upon by Toma & Georgescu in [30], describing a self-pulsing region of operation for the Er:YAG laser. Originating from solving the eigen-values in a stability analysis formed from a variation of the rate equations only accounting for ESA. A Hopf bifurcation point, a consequence of the solved eigen value matrix, specifically the photon flux and cavity loss, define the self-pulsing region. In fact, varying the cavity loss showed two additional operating regions defined as CW and “under laser threshold”. With these straightforward experiments, it could potentially bring together decades of work culminating into a fieldable power scalable device advancing room temperature MWIR coherent sources.

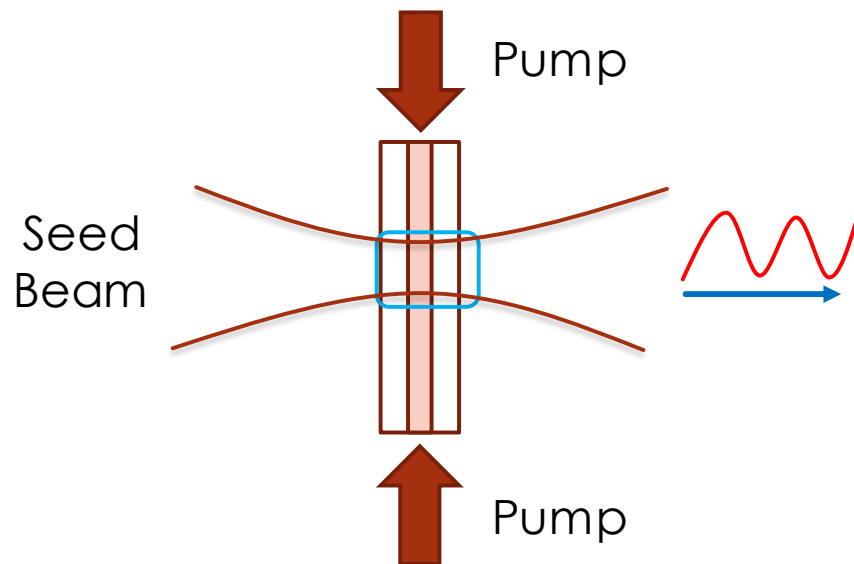


Figure 5.1 Laser amplifier setup using the waveguide sample. Direct co-linear pumping is more desirable than side pumping (shown here for illustrative purposes) as it provides better beam quality.

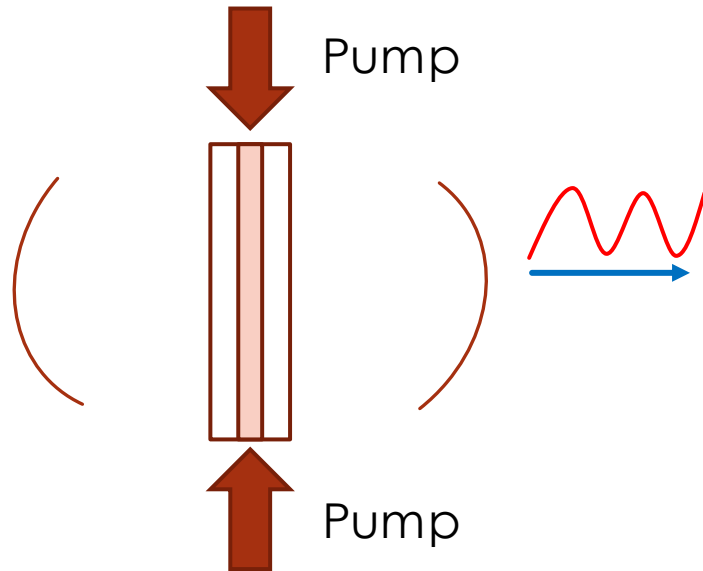


Figure 5.2 Laser resonator setup using the waveguide sample. Laser cavity mirrors can be tuned to correspond to a harmonic of the fundamental frequency of fluorescence instability.

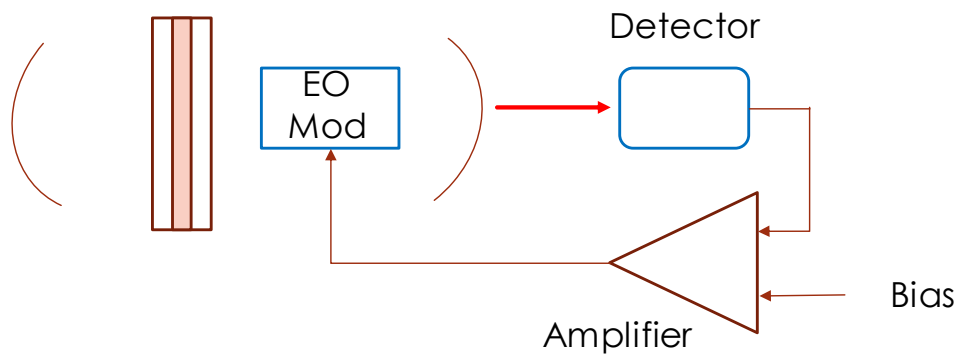


Figure 5.3 Laser Chaos measurement setup. Just as in figure 5.3 the cavity mirrors can be tuned to match a harmonic of the fluorescence instability. In addition, a co-linear pump scheme is preferable.

# Appendix A: Additional Simulation & Experimental Scans

## A.1 Additional Rate Equation Simulations

The following simulations to follow in this section are a supplement to those presented in section 2.4.

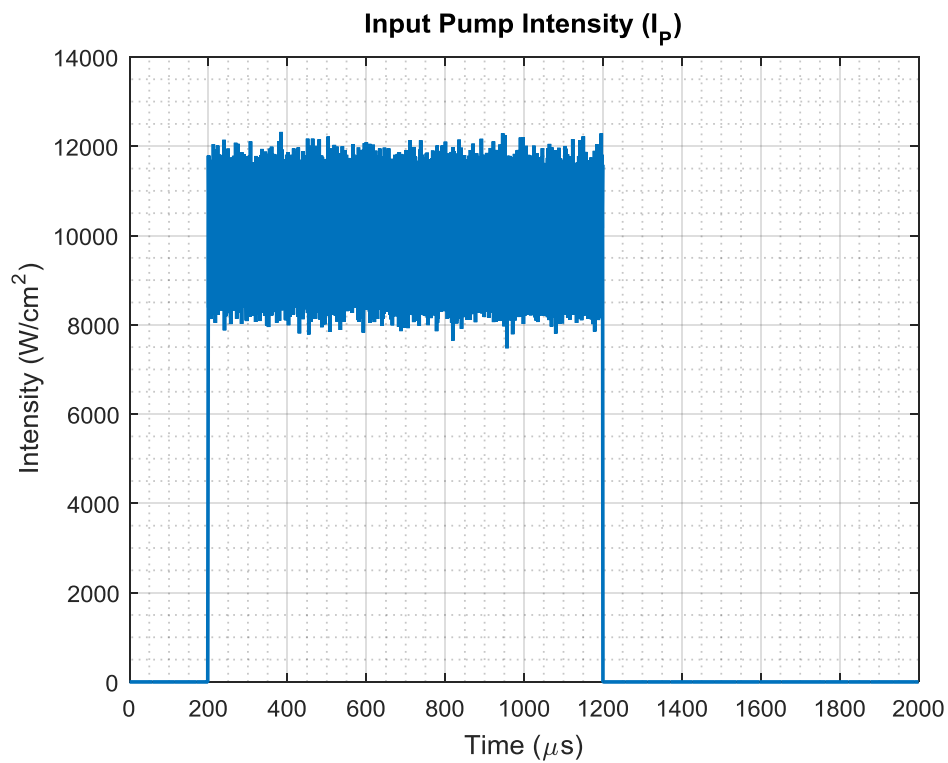


Figure A.1.1 Simulated input pump with a 20% gaussian noise added.

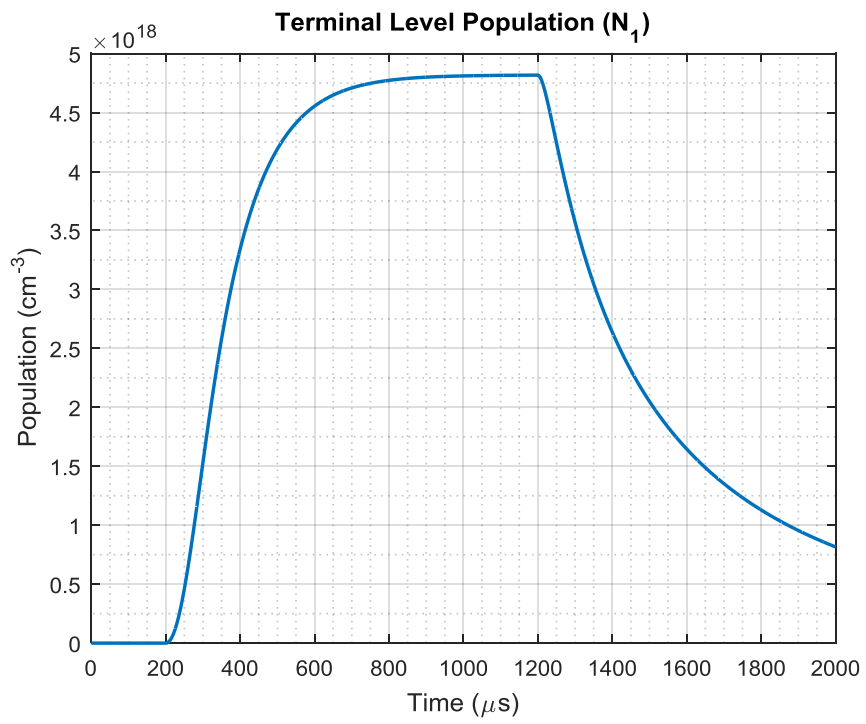


Figure A.1.2 Simulation result for the  ${}^4I_{13/2}$  with no ESA terms.

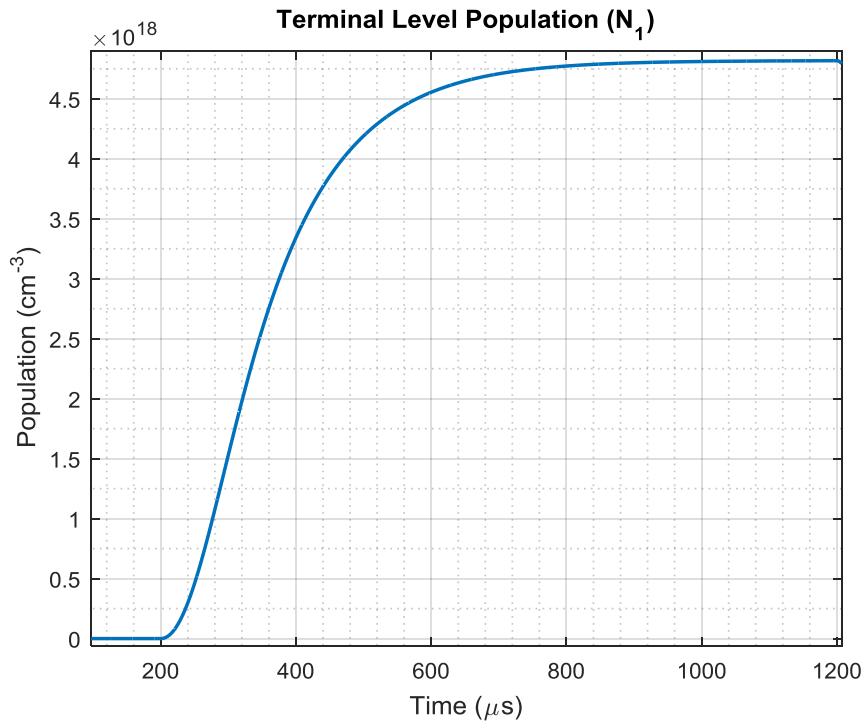


Figure A.1.3 Simulation result for the  ${}^4I_{13/2}$  rise. Rise time using the 63% definition is  $377.3\mu\text{s}$ .

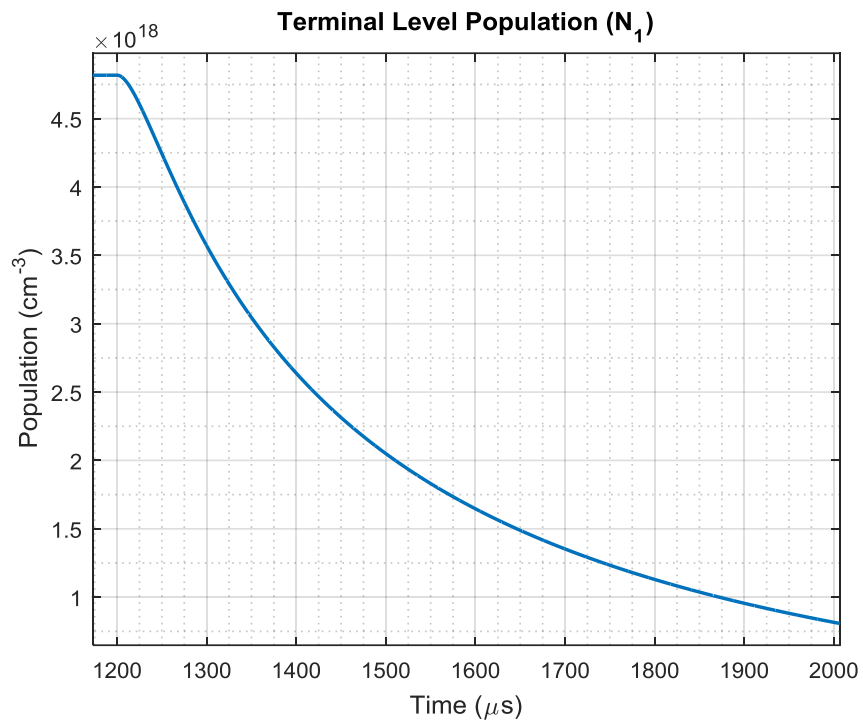


Figure A.1.4 Simulation result for the  ${}^4I_{13/2}$  fall. Fall time using the 37% rule is 362 $\mu\text{s}$ .

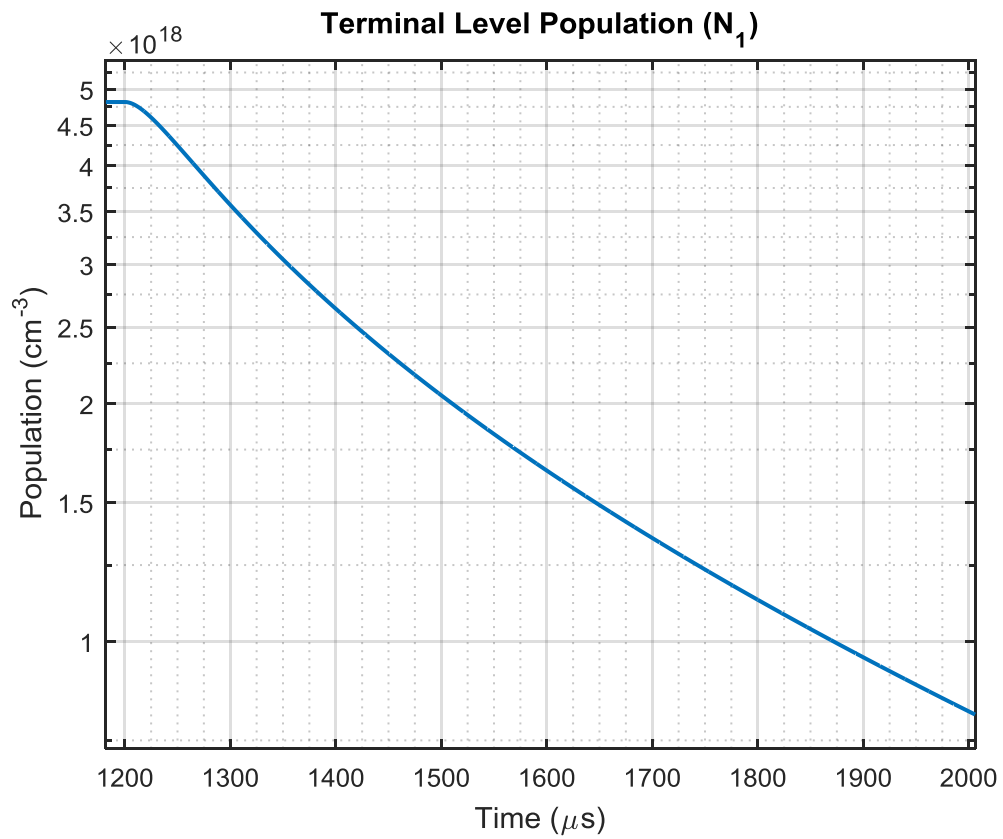


Figure A.1.5 Simulation result for the  ${}^4I_{13/2}$  fall. Falling edge on a semi-log plot shows multi-exponential behavior.

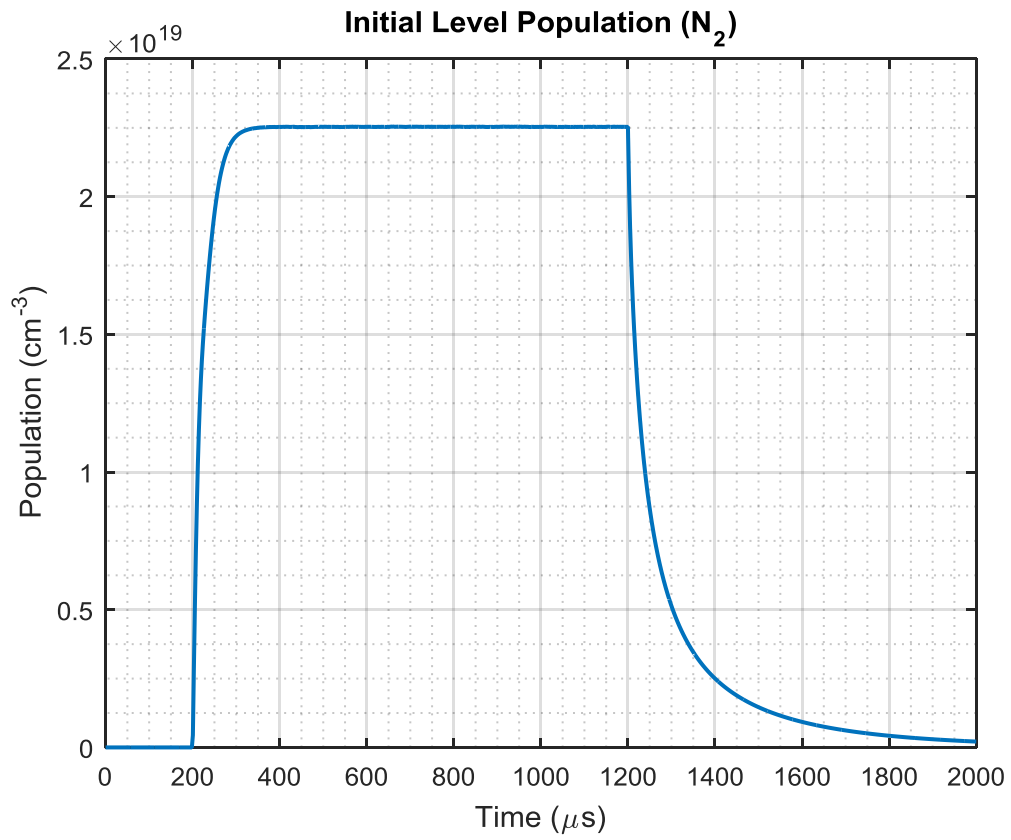


Figure A.1.6 Simulation result for the  ${}^4I_{11/2}$  with no ESA terms.

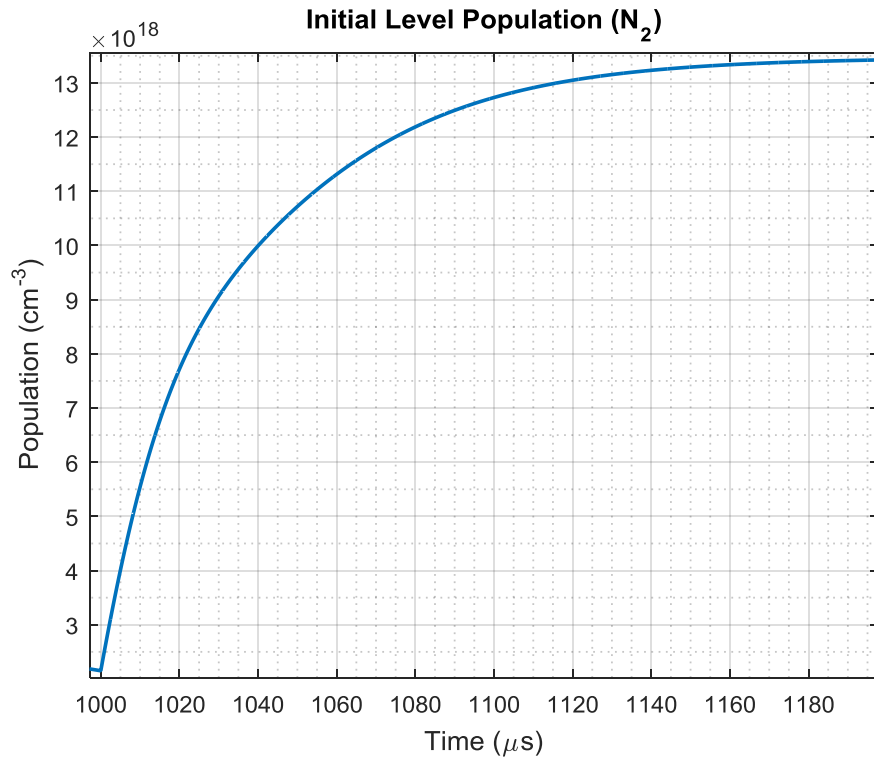


Figure A.1.7 Simulation result for the  ${}^4I_{11/2}$  rise. Rise time using the 63% definition is  $315.5\mu\text{s}$ .

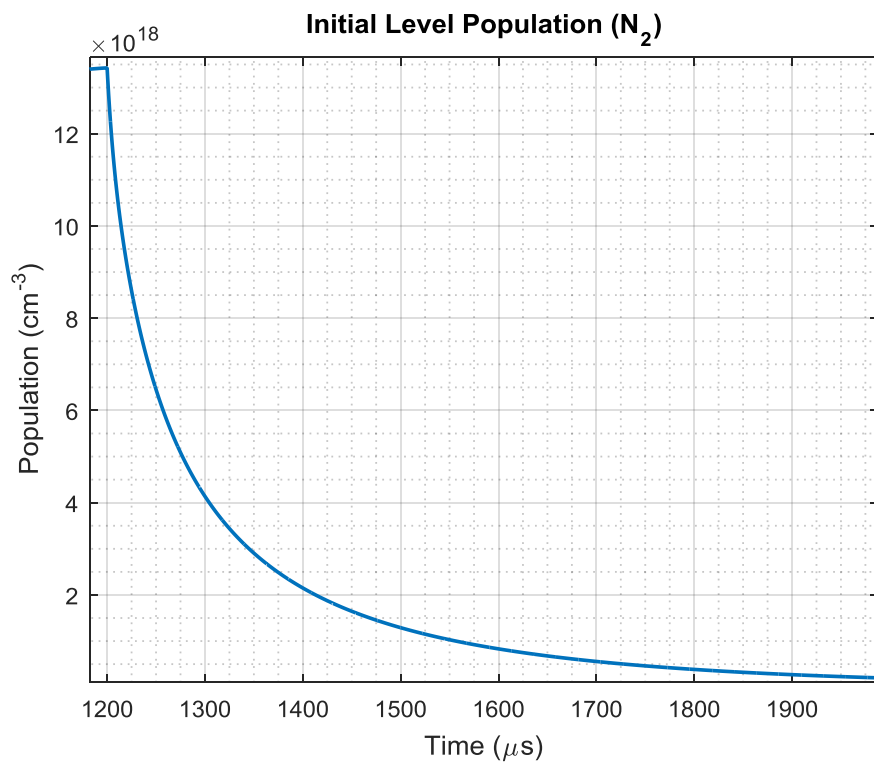


Figure A.1.8 Simulation result for the  ${}^4I_{11/2}$  fall. Fall time using the 37% rule is  $176 \mu\text{s}$ .

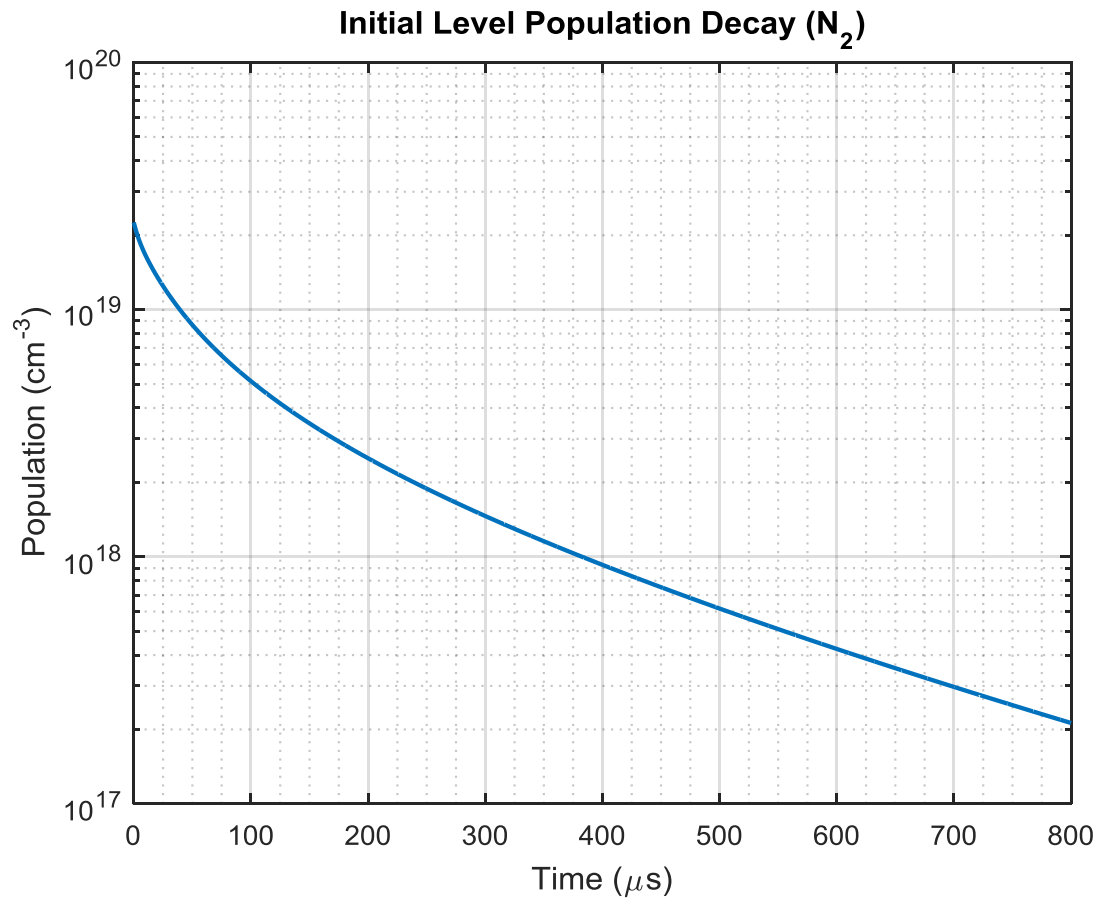


Figure A.1.9 Simulation result for the  ${}^4I_{11/2}$  fall. Falling edge on a semi-log plot shows multi-exponential behavior.

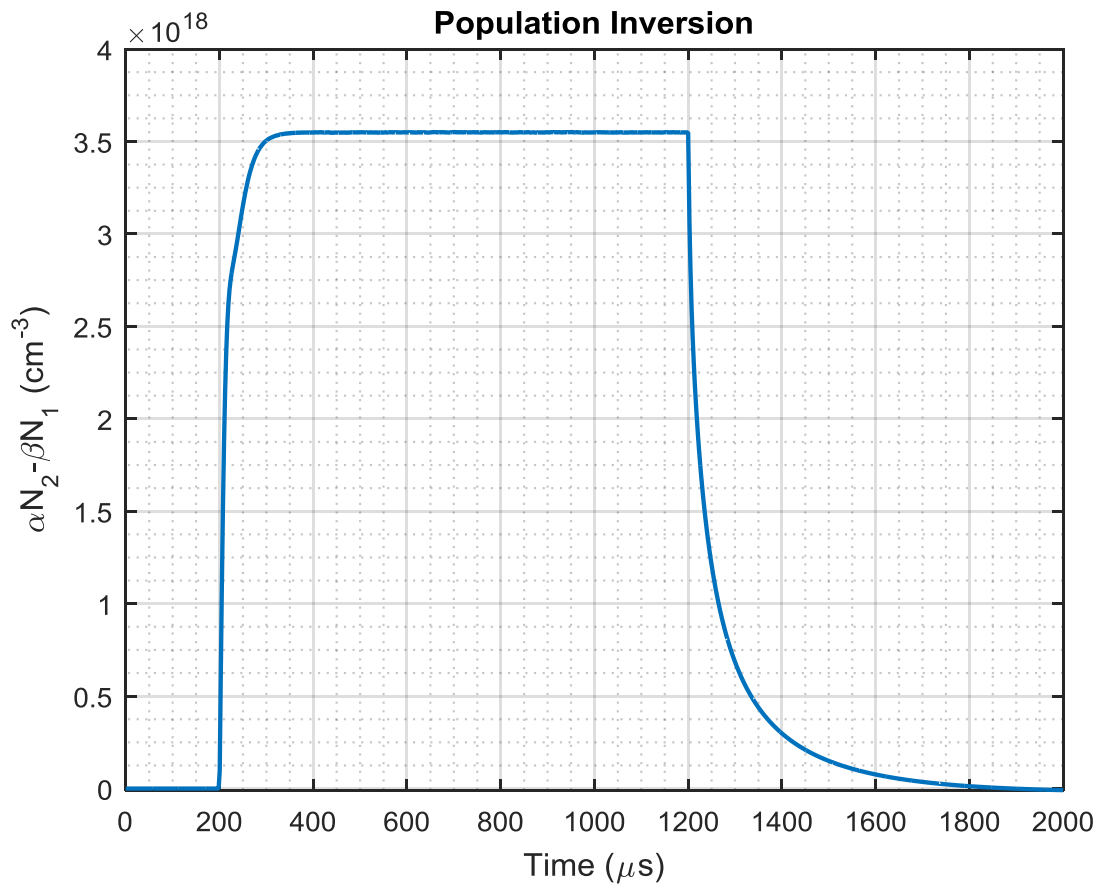


Figure A.1.10 Simulation result for the population inversion with no ESA terms.

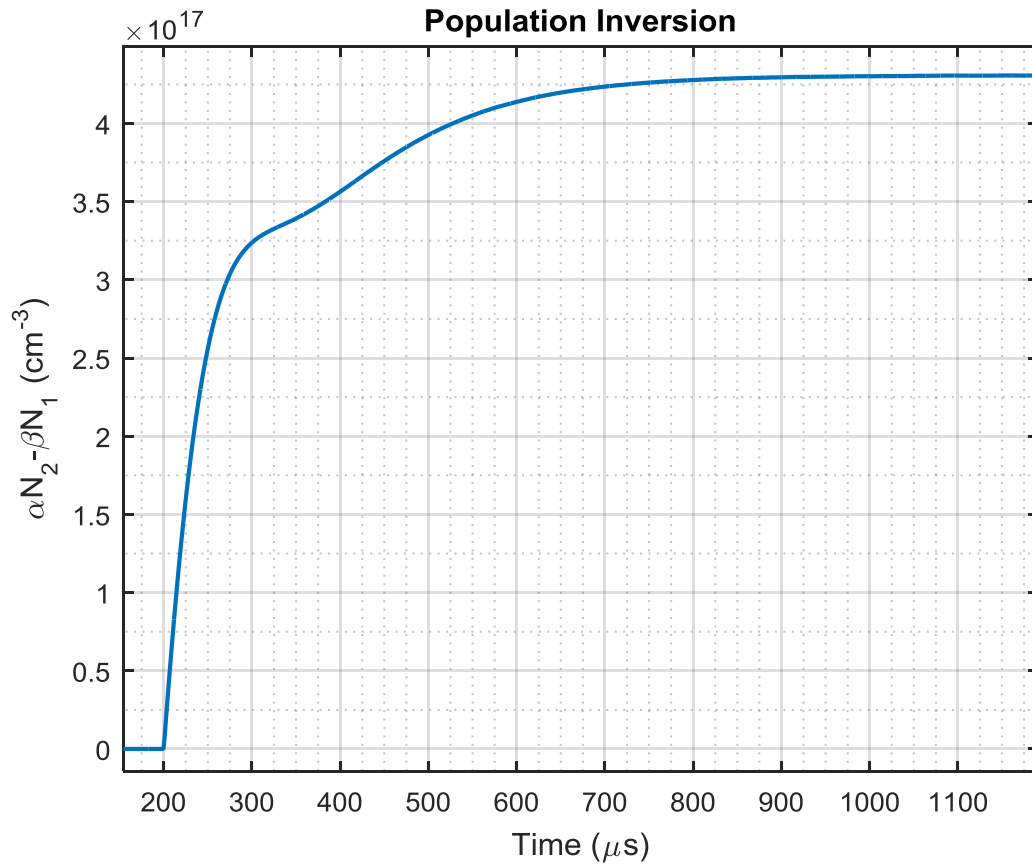


Figure A.1.11 Simulation result for the population inversion rise. Rise time using the 63% definition is 256 $\mu\text{s}$ .

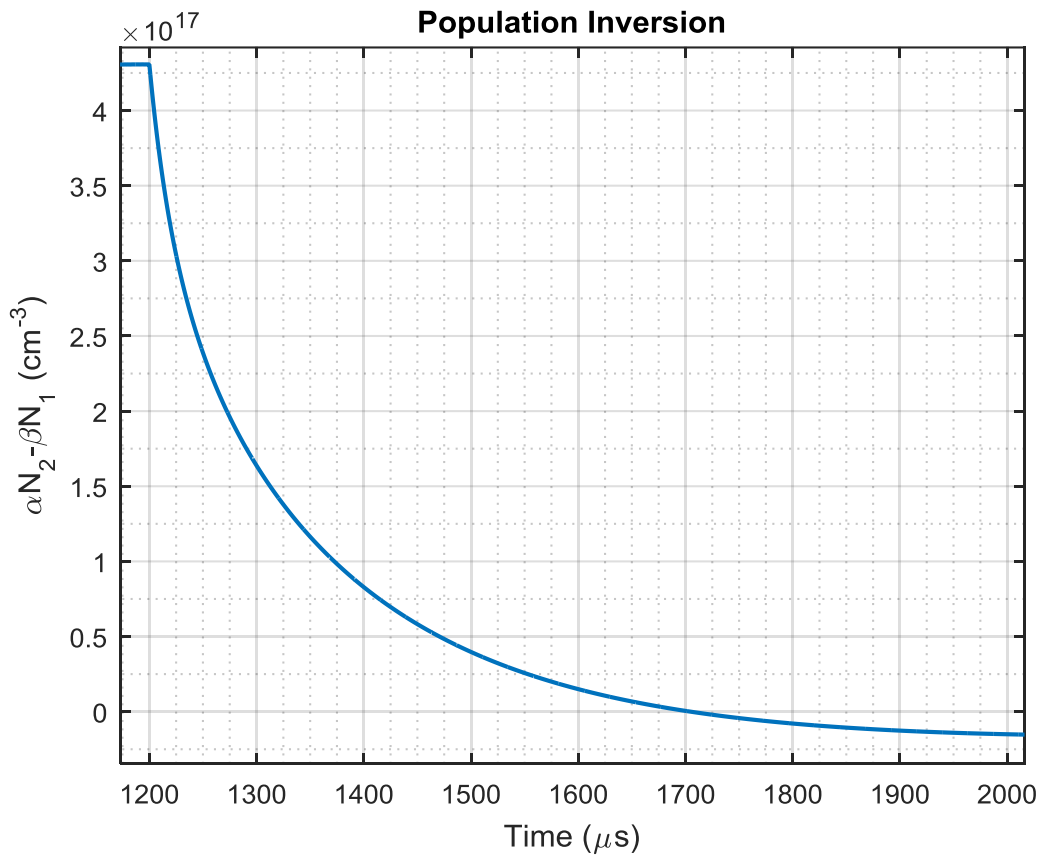


Figure A.1.12 Simulation result for the population inversion fall. Fall time using the 37% rule is  $105 \mu\text{s}$ .

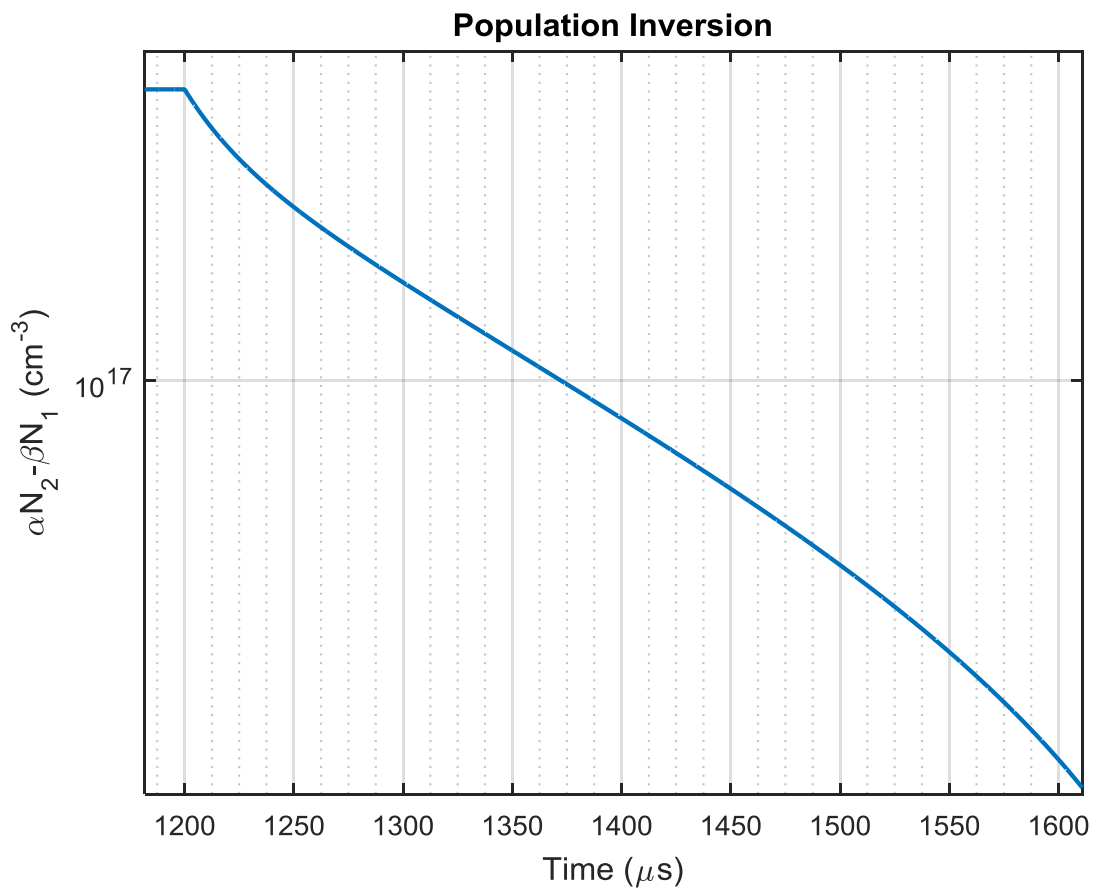


Figure A.1.13 Simulation result for the population inversion fall. Falling edge on a semi-log plot shows multi-exponential behavior

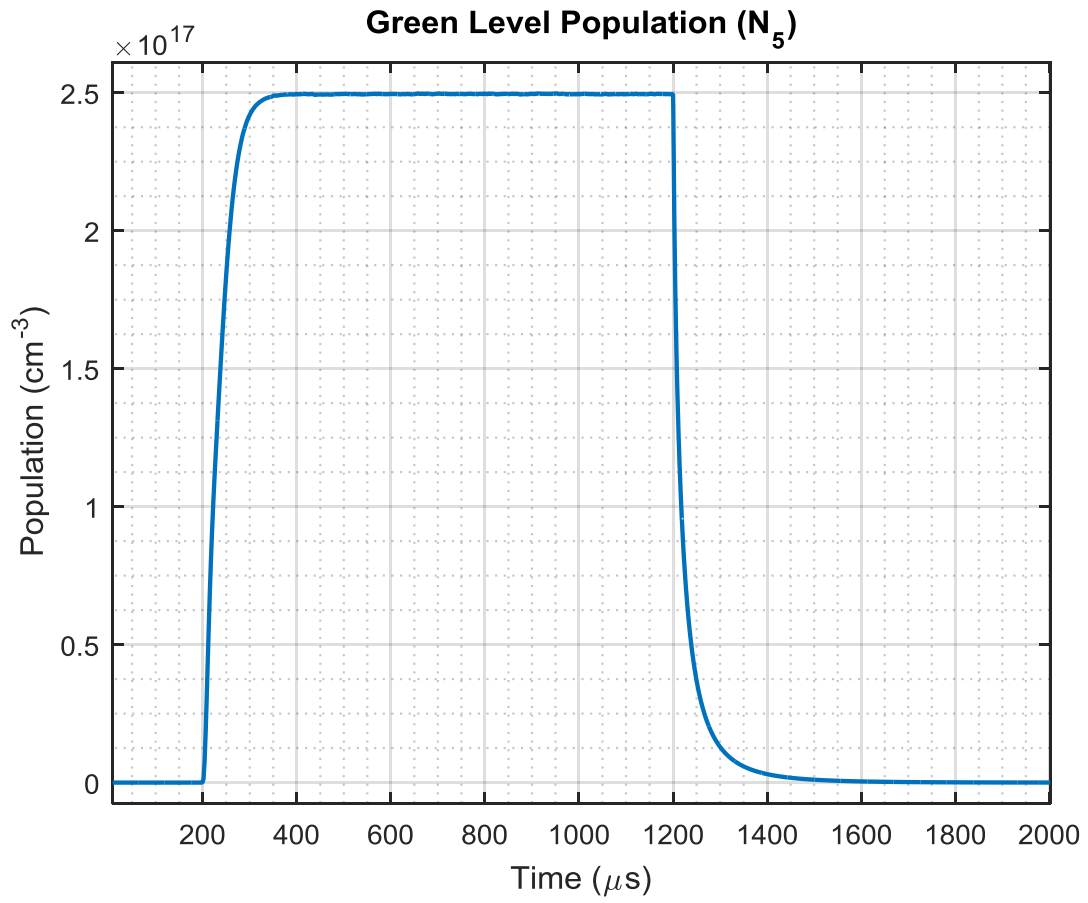


Figure A.1.14 Simulation result for the  ${}^4S_{3/2}$  with no ESA terms.

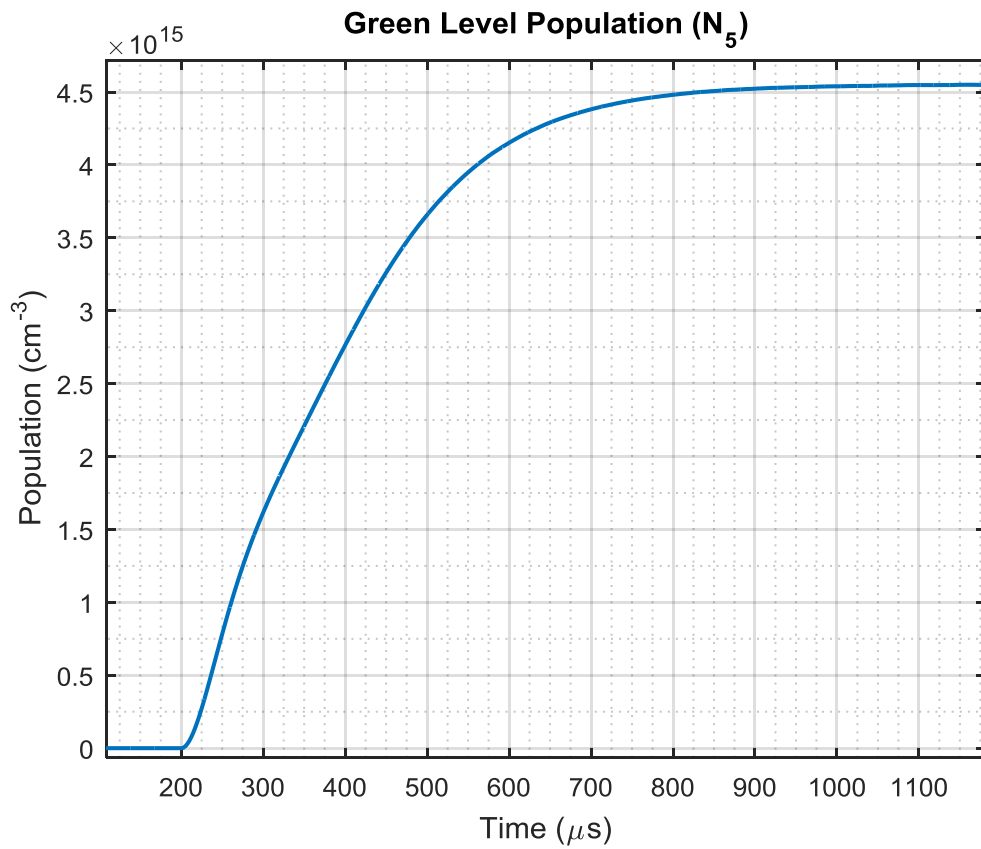


Figure A.1.15 Simulation result for the  ${}^4S_{3/2}$  rise. Rise time using the 63% definition is  $409.8\mu\text{s}$ .

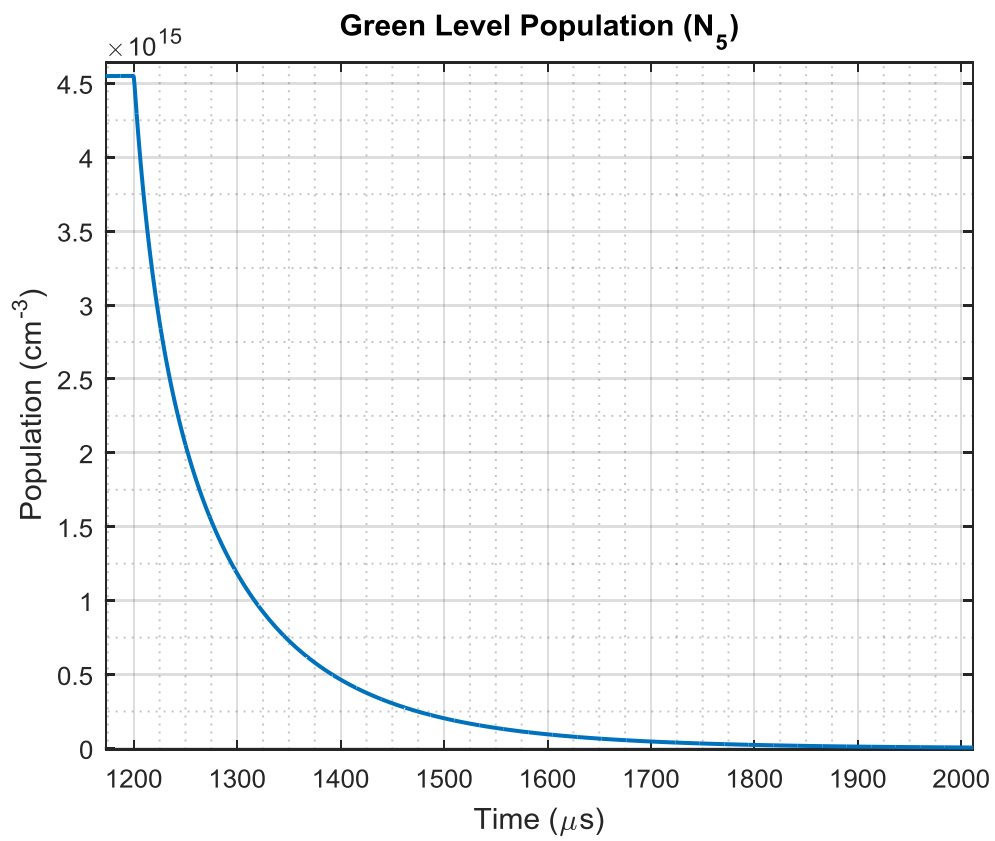


Figure A.1.16 Simulation result for the  ${}^4S_{3/2}$  fall. Fall time using the 37% rule is  $67 \mu\text{s}$ .

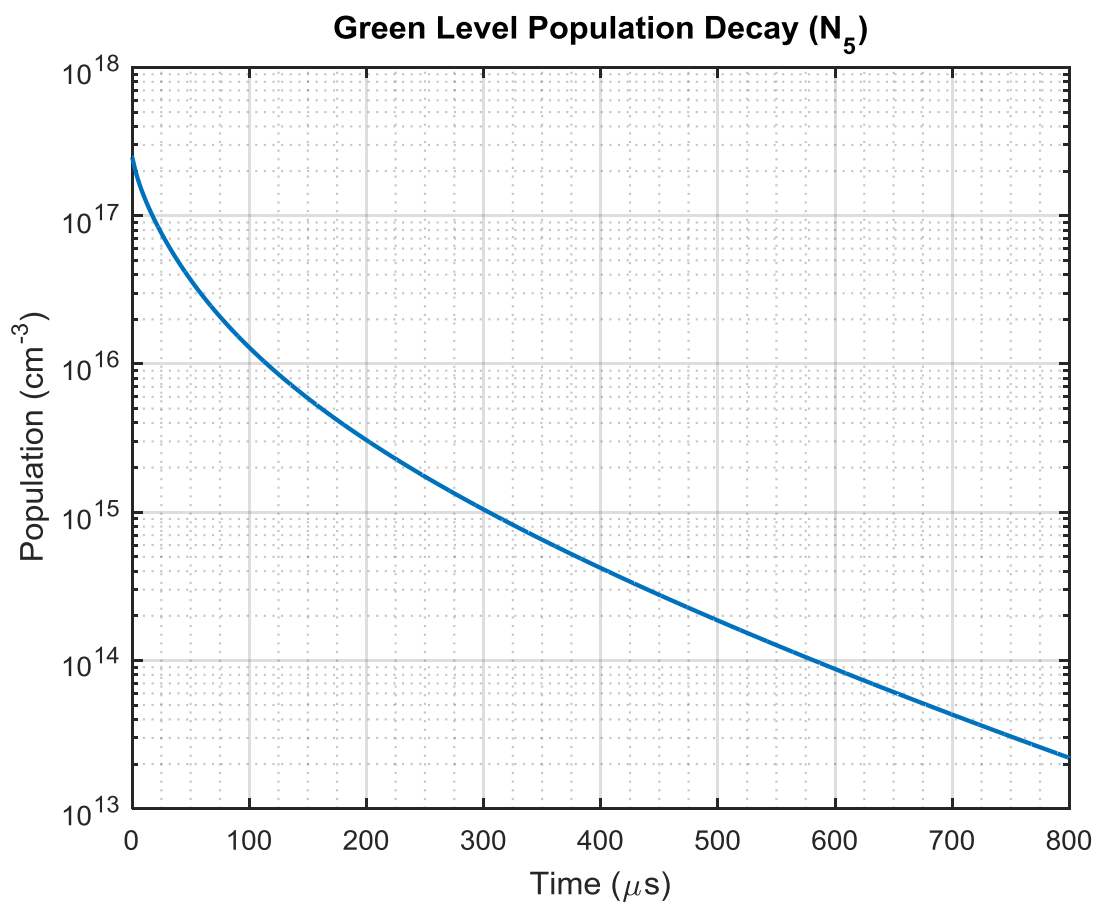


Figure A.1.17 Simulation result for the  $^4S_{3/2}$  fall. Falling edge on a semi-log plot shows multi-exponential behavior

## A.2 Analogy of Fluorescence Instability to an Astable Oscillator

### Circuit

The instability behavior that manifests itself in Er:YAG under high intensity pump might analogously be modeled by a typical oscillator circuit that is used as a clock for digital circuits. The analogy stems from the inherently unstable feedback system that describe both systems. Looking at a typical negative feedback system in figure A.2.1(a) we find that if the value of  $AH$  is  $-1$  then the transfer function of the complete system is infinite and may oscillate. Of course, the system is limited by the input power supply and will oscillate between the rails in the case of an electronic oscillator. This is caused by the feedback becoming positive at certain frequencies. This is the principle from which oscillators are based on. The Barkhausen criterion is met when  $AH = -1$ , which is when the loop gain is unity and has a 180-degree phase shift. This causes the output to be unstable and in the case of an electronic amplifier the output will travel towards the power supply rail values. Once near the limit that amplifier gain will change and as a result the feedback gain can change which will ultimately force the term  $AH$  to be limited. Upon reaching the limit the system is linear as it reverses direction towards the opposite power supply rail. Figure A.2.1(c) illustrates a Wien bridge oscillator which is a common oscillator used in audio systems. A full review of this circuit including deriving its transfer function is given in reference [90]. Figure A.2.1(d) is the result in simulating Wien bridge circuit depicted in figure A.2.1(b), the transient response is a sinusoidal waveform. The feedback mechanism that is causing this oscillation in this circuit can be compared to the ESA and the ion-ion energy transfer interactions along with the natural decay acting as feedback mechanisms described in chapter 4.

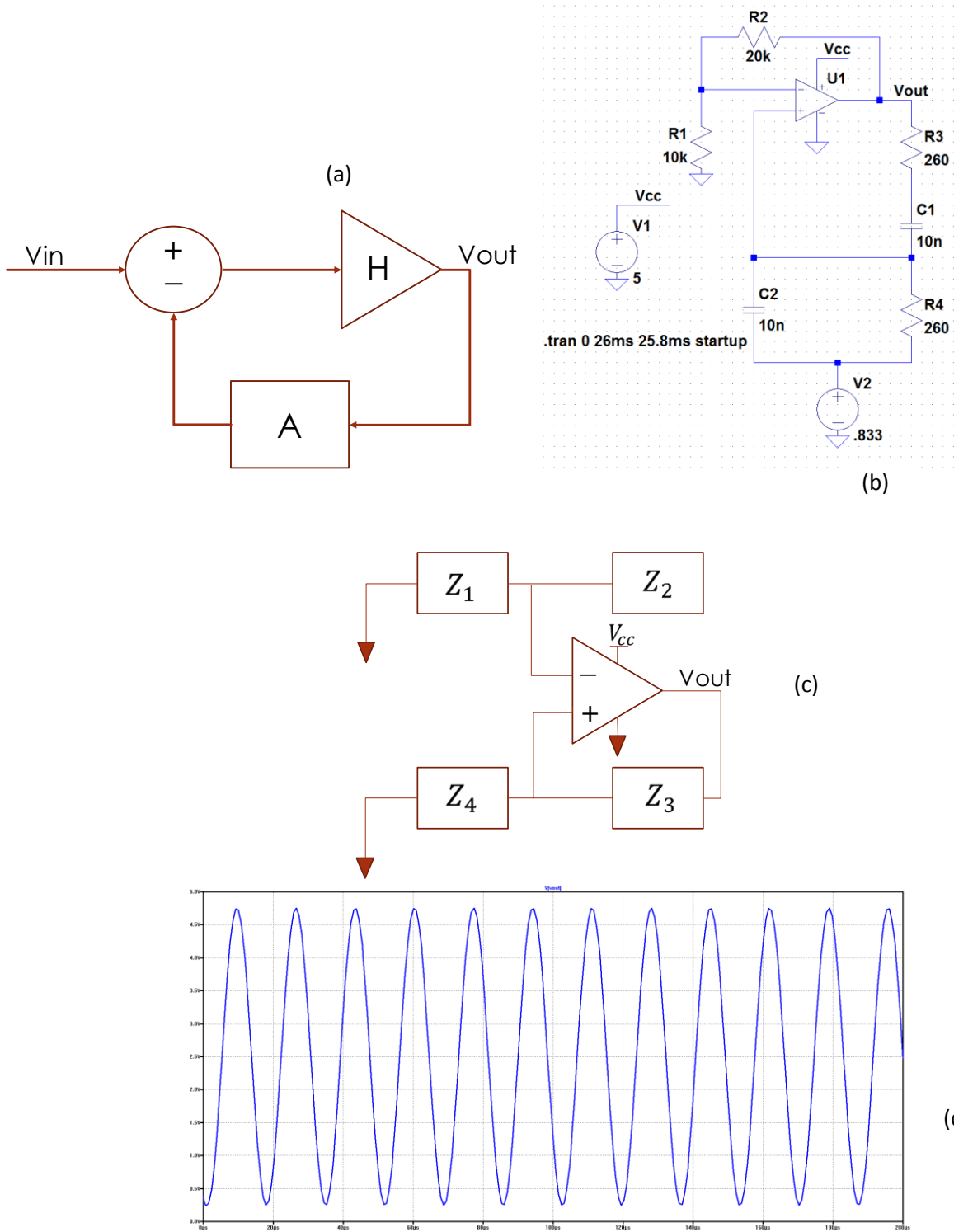


Figure A.2.1: (A) Typical feedback system. (B) Wien bridge circuit. (C) Generalized diagram of (B). (D) Transient simulation of (B).

## Appendix B : Equipment List & Parameters

### Er:YAG Samples

Table 3.1 Test Samples	
Sample Type	Sample Doping (% at. wt.)
<b>Pillbox</b>	<b>1</b>
<b>Pillbox</b>	<b>3</b>
<b>Pillbox</b>	<b>5</b>
<b>Pillbox</b>	<b>25</b>
<b>Pillbox</b>	<b>50</b>
<b>Pillbox</b>	<b>60</b>
<b>Waveguide</b>	<b>50</b>

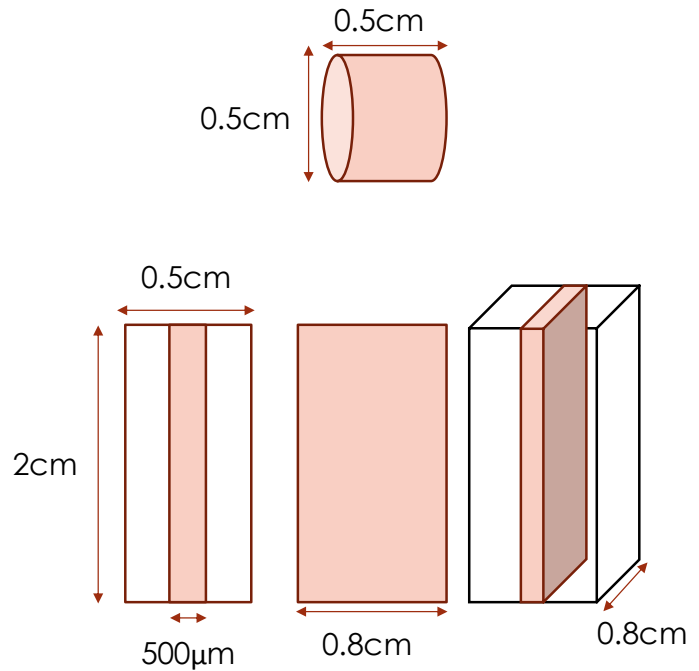


Figure B.1 Sample Geometry

### Lenses

- 1) NRC LM-2 Convex-Convex  $f = 5.5\text{cm}$   $D = 42.63\text{mm}$
- 2) Compound Achromat  $f_1 = 2.5\text{cm}$   $f_2 = 7\text{cm}$   $D = 3.5\text{cm}$
- 3) Quartz Plano-Convex lens  $f_1 = 5.5\text{cm}$   $f_2 = 8\text{cm}$   $D = 4.8\text{cm}$
- 4)  $\text{CaF}_2$  Convex-Convex  $f = 14.5\text{cm}$   $D = 4.5\text{cm}$
- 5) Sapphire lens Convex-Convex  $f = 6\text{in}$   $D = 1.77\text{in}$
- 6) ZnSe Convex-Convex  $f = 1\text{in}$   $D = 1\text{in}$

## Laser Sources

1) nLIGHT element® e06 Fiber Coupled Diode Laser

30W output with 200 $\mu$ m fiber @ 808nm

2) Sheumann SheauPac Fiber Coupled Diode Laser

7W output with 105 $\mu$ m/125 $\mu$ m fiber 0.15 NA @ 962nm

3) Sheumann MirPac Window MWIR Laser

1W output with Germanium window TEM 00 @ 2940nm

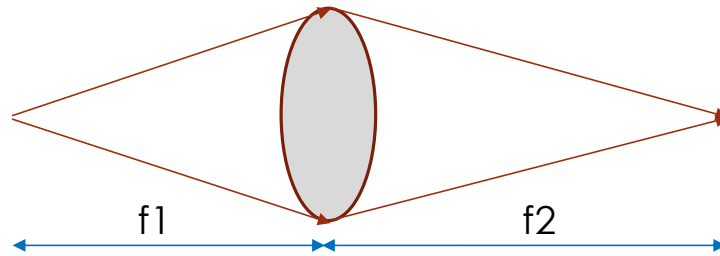


Figure B.2 Lens geometry guide for lenses 2 and 3

## Power Supplies

1) Xantrex XFR 20-130 0-200V 0-130A

2) Xantrex XPD 7.5-67 0-7.5V 0-67A

3) Extech Industries 382260 80W Switching Power Supply

## Oscilloscopes

1) Tektronix DPO 7104 Digital Phosphor Oscilloscope 1GHz

2) Teledyne LeCroy Wave Surfer 3074 750 MHz Oscilloscope 4GS/s

## Optical Choppers

1) ThorLabs MC1000A with 2 blade fan

2) Stanford Research Systems INC. SR540 with 30 blade fan

3) Stanford Research Systems INC. SR540 with 6 blade fan

## Spectrometers

1) Jarrell-Ash 1 meter spectrometer

2) Jarrell-Ash 0.5 meter spectrometer

- 3) Ocean Optics HR4000CG-UV-NIR Spectrometer

### **Lamps**

- 1) Oriel Model 6000 Halogen Lamp

### **Camera**

- 1) Astrovid 2000 CCD camera (for measuring laser diode spatial profile)
- 2) Astrovid StellaCam-EX

### **Lock-In Amplifiers**

- 1) EG&G Princeton Applied Research Model 5209
- 2) Stanford Research Model SR530

### **Detectors**

- 1) ThorLabs DET10A Silicon Detector with Thorlabs FB550-40 filter and Princeton Applied Research Model 124A Lock-In Amplifier with Model 117 Differential Pre Amplifier shunted with 100 K $\Omega$  resistor
- 2) ThorLabs DET36A Silicon Detector with Thorlabs FEL 950nm Long pass with 5.14K $\Omega$  shunt resistor
- 3) ThorLabs DET10A Silicon Detector with baffle
- 4) Judson J12 Series InAs MWIR Detector

### **Optical Filters**

- 1) Thorlabs FB540-10 Bandpass @ 540nm +/- 2nm
- 2) Thorlabs FEL 950nm Longpass
- 3) 3x Thorlabs Hot Mirrors 90% Transmission 450nm-670nm
- 4) Balzer 90% transmission glass filter

### **Misc. Optics**

- 1) Glass prism with single gold coated side measuring 1cm in height by 1.3cm in length
- 2) Germanium window with 2inch diameter and 0.5inch in height

## Appendix C: Additional Experimental Transient Scans

The following simulation scans show a portion of the available samples pumped with the 808nm pump laser diode under CW and chopped at 1ms. The scans involving the 3 $\mu$ m laser are not included but will be summarized in a future published paper. The five best transient scans are provided showing the oscillation frequency with the Fast Fourier Transform (FFT) of the transient scan. The FFTs show that the oscillation frequency across all samples roughly match to the lifetime of the  $^4S_{3/2}$  level (16.7 $\mu$ s  $\sim$  60 kHz). The rise and fall times of the  $^4S_{3/2}$  and  $^4I_{11/2}$  levels are also provided averaged over 1000 scans and calculated using the 10-90% rule (default on Matlab). It is also important to note that the values are affected by the finite rise and fall of the pump beams. After the transient scans, the intensity profiles of the pump diodes are plotted along with the power measurements are provided. The pump diodes are left running for at least 20 minutes to allow for thermal stabilization. Finally, the 808nm beam is utilized to measure the reflection loss of the 50% Er:YAG waveguide sample.

Additional scans of the other samples were done and will be provided in summary in a future published paper. The main focus of this work was to look at high doped samples under high intensity resonant pump. The 1 % sample data is presented here to compare the instability oscillation frequency to the high doped sample as XR effects should not be present in low doped samples unless ion-ion clumping is involved.

## C.1 808nm Pulsed Pumped 1% Er:YAG Pillbox with No 3μm Laser

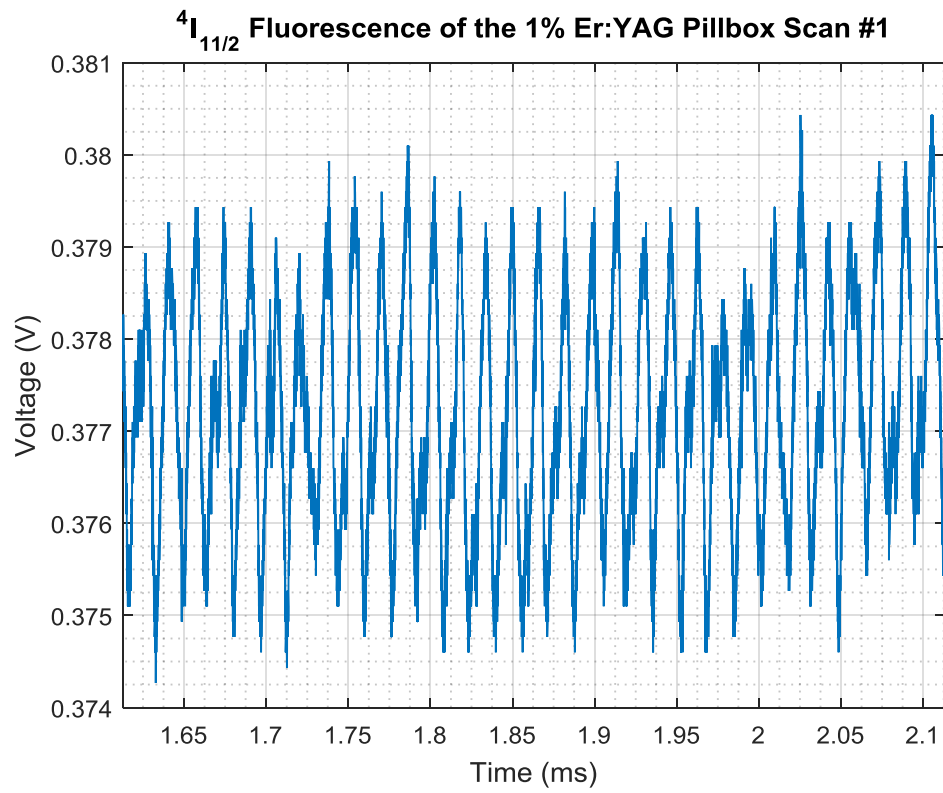


Figure C.1.1: Transient scan of the  $^4I_{11/2}$  level.

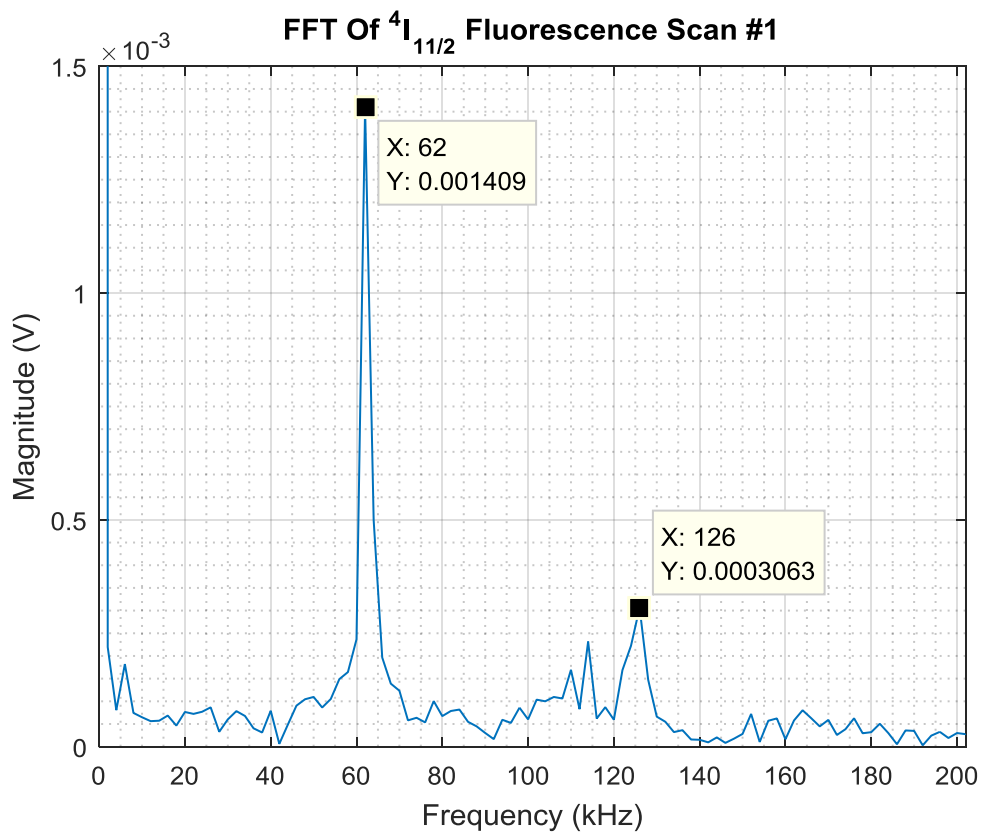


Figure C.1.2: FFT of transient scan of the  ${}^4I_{11/2}$  level.

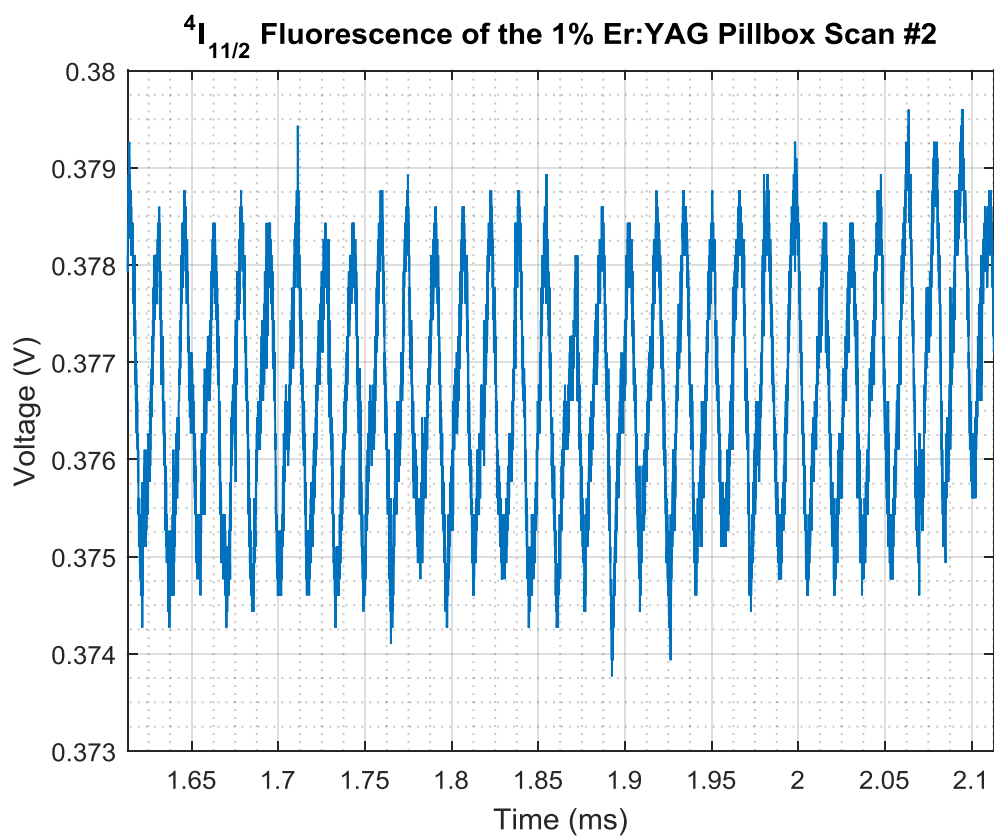


Figure C.1.3: Transient scan of the  $^4I_{11/2}$  level.

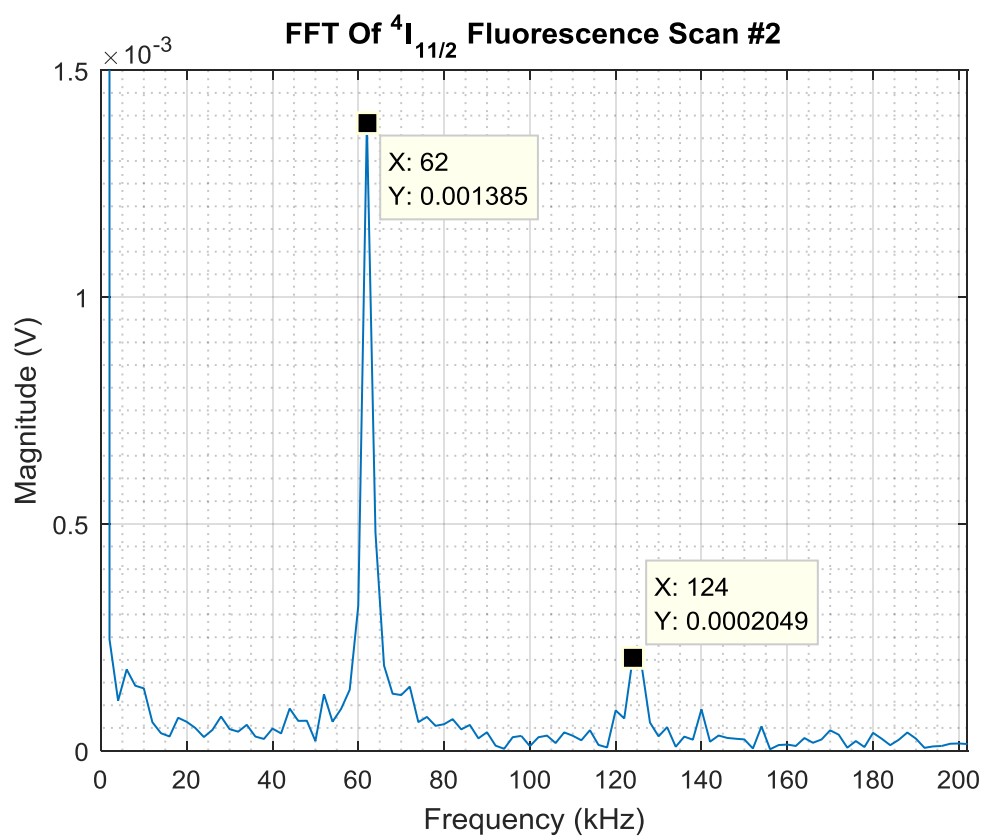


Figure C.1.4: FFT of transient scan of the  ${}^4I_{11/2}$  level.

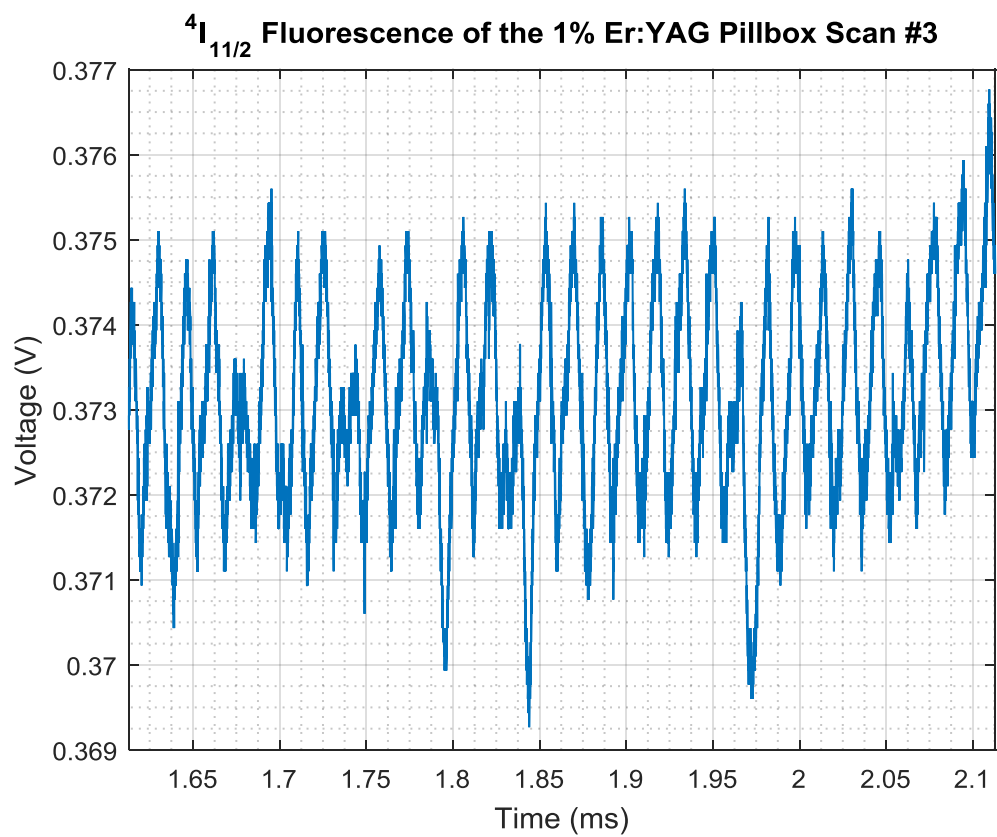


Figure C.1.5: Transient scan of the  $^4I_{11/2}$  level.

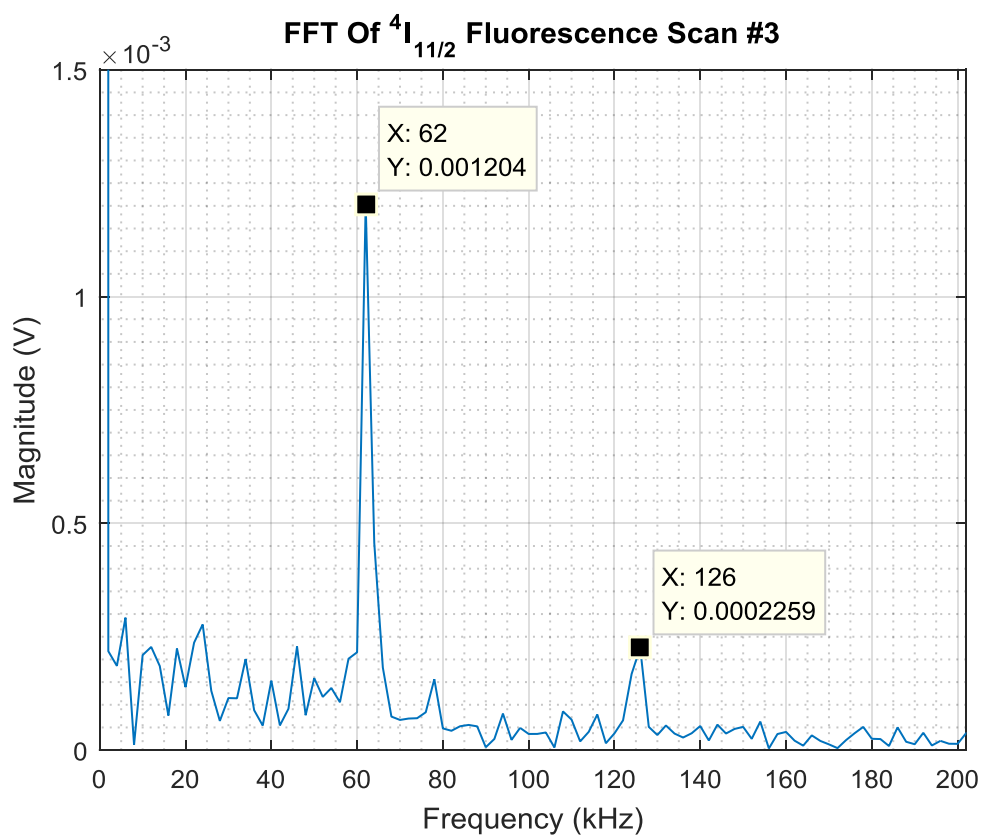


Figure C.1.6: FFT of transient scan of the  $^4I_{11/2}$  level.

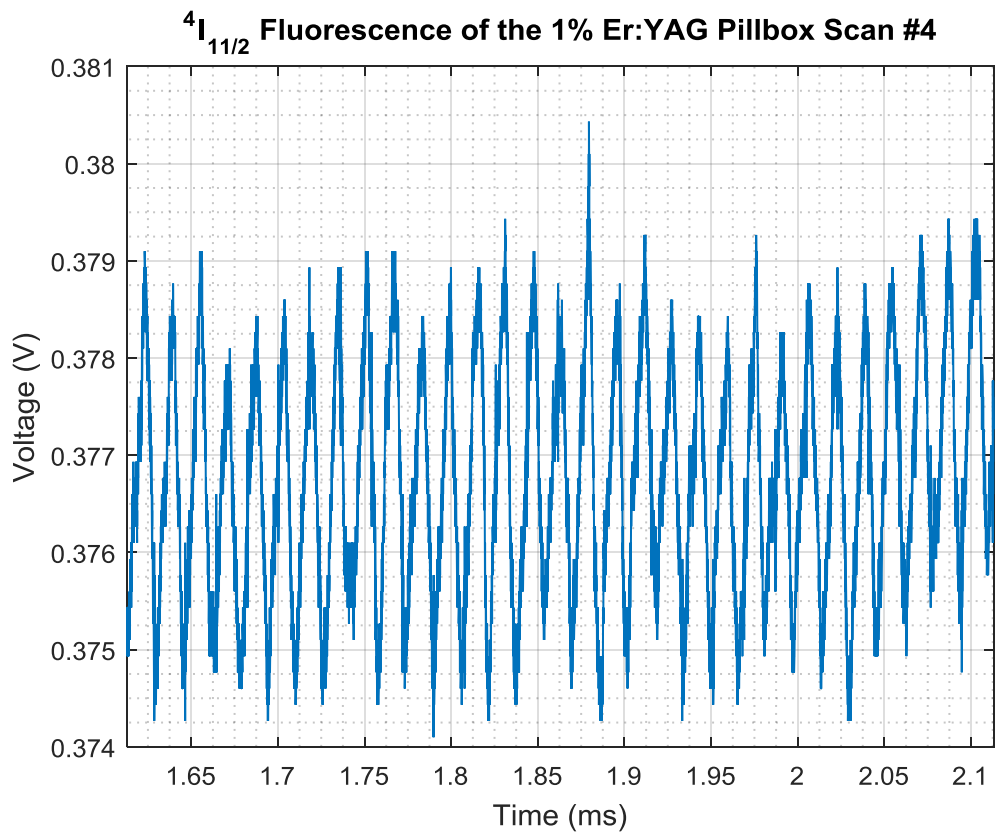


Figure C.1.7: Transient scan of the  $^4I_{11/2}$  level.

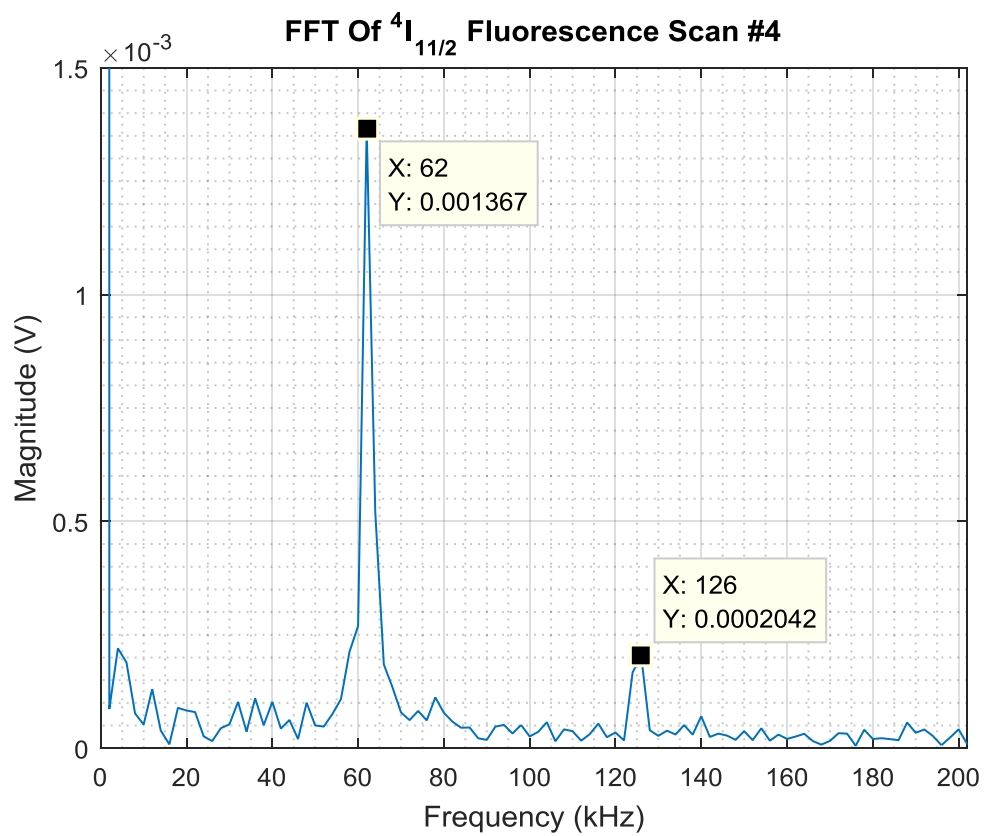


Figure C.1.8: FFT of transient scan of the  $^4I_{11/2}$  level.

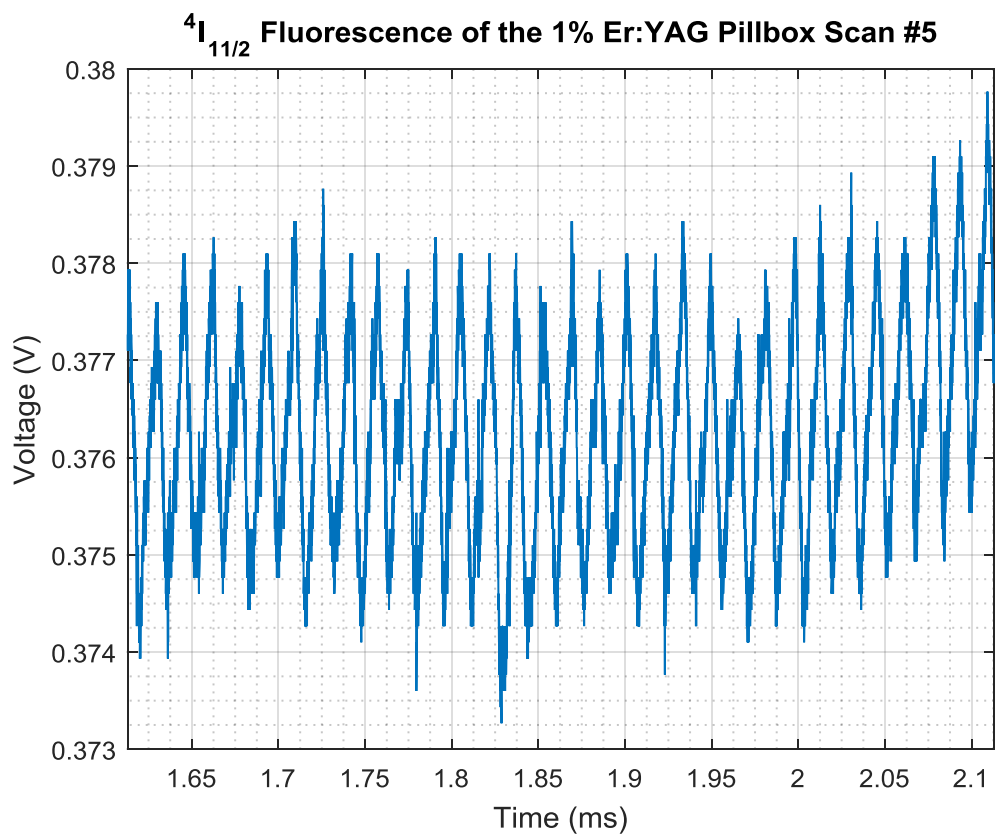


Figure C.1.9: Transient scan of the  $^4I_{11/2}$  level.

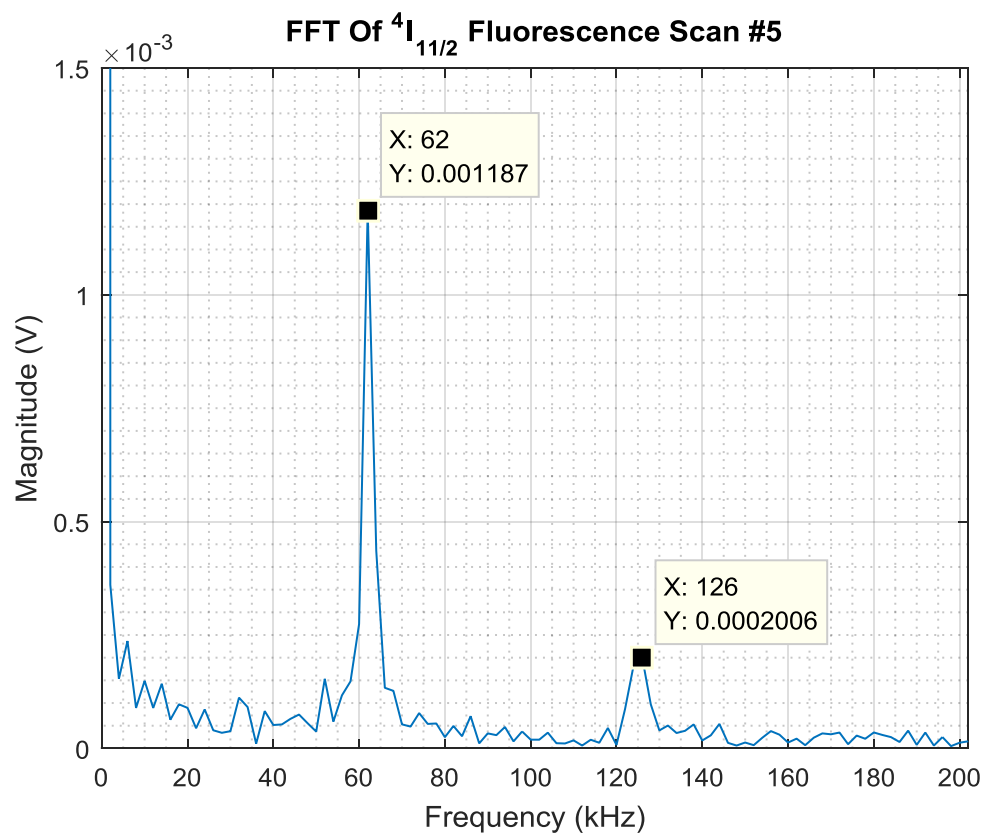


Figure C.1.10: FFT of transient scan of the  ${}^4I_{11/2}$  level.

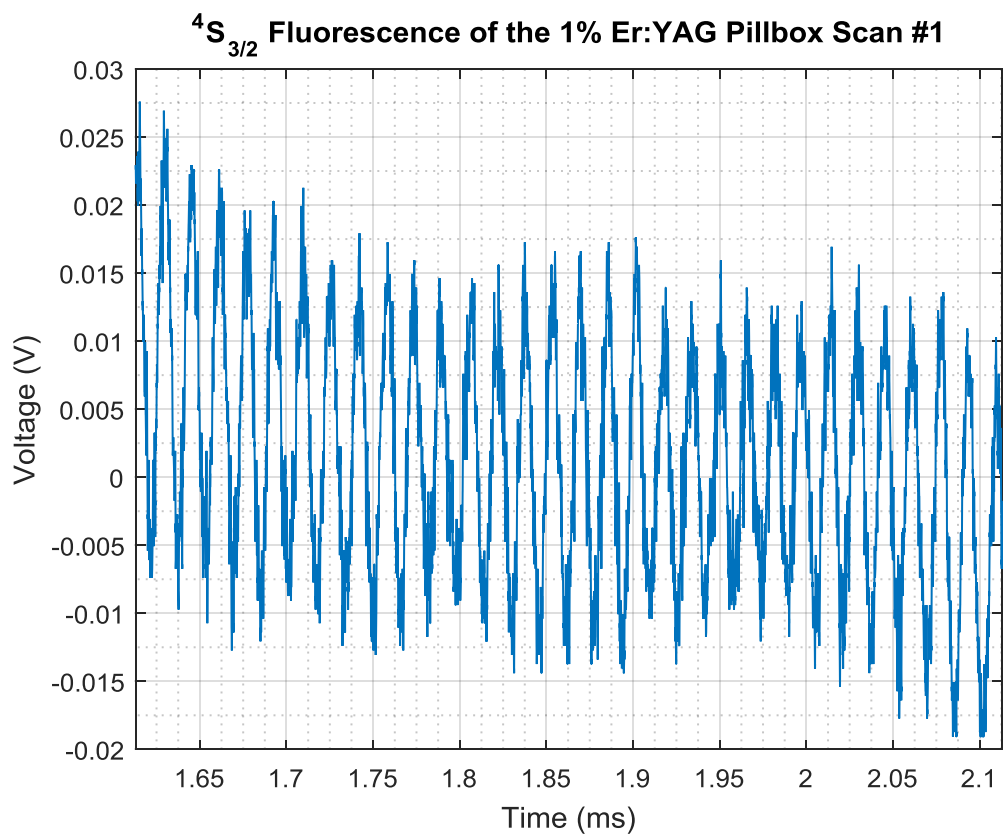


Figure C.1.11: Transient scan of the  $^4S_{3/2}$  level.

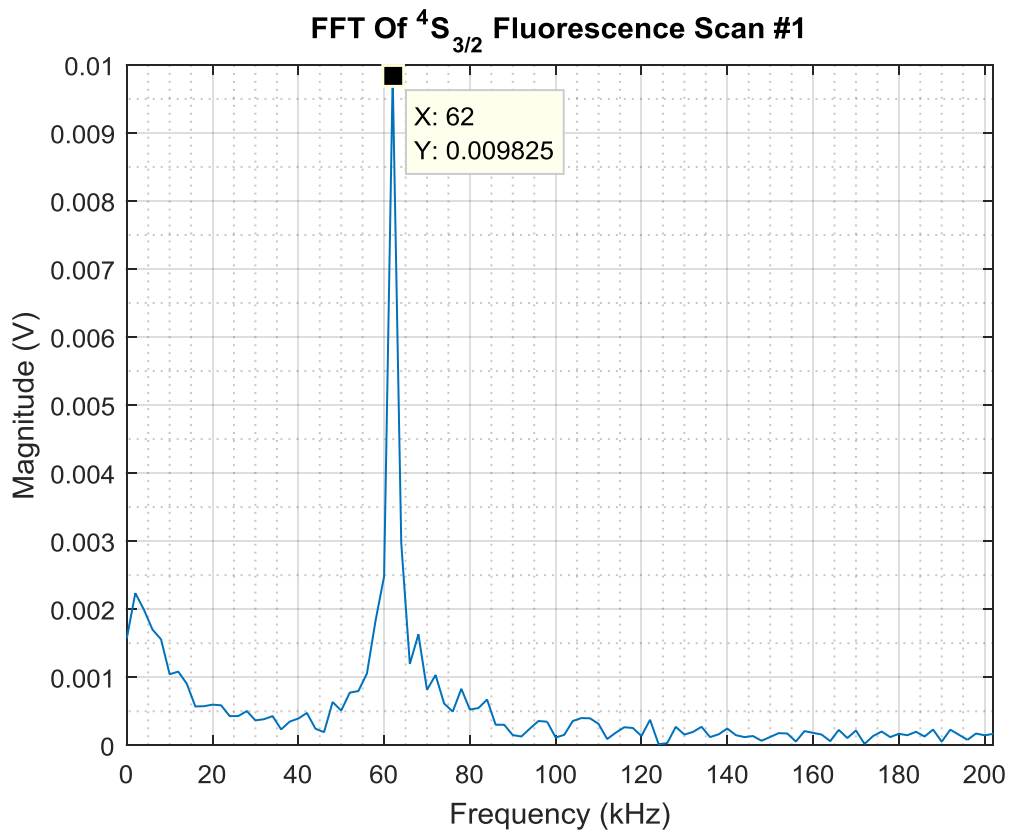


Figure C.1.12: FFT of transient scan of the  $^4S_{3/2}$  level.

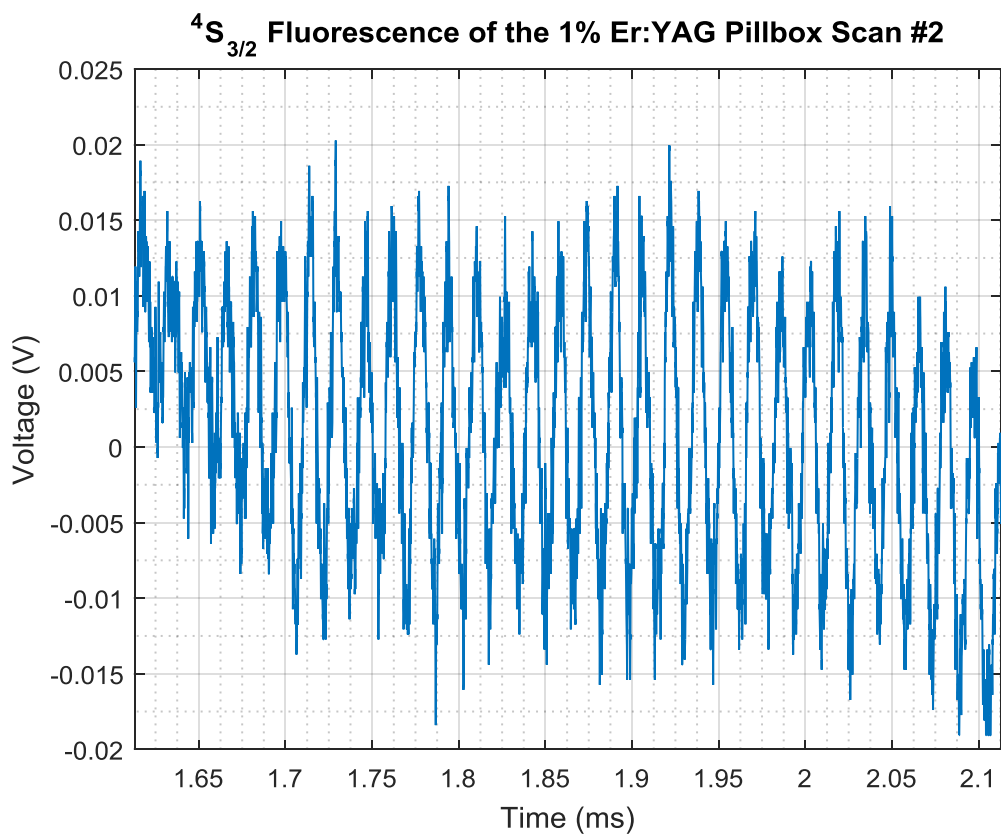


Figure C.1.13: Transient scan of the  $^4S_{3/2}$  level.

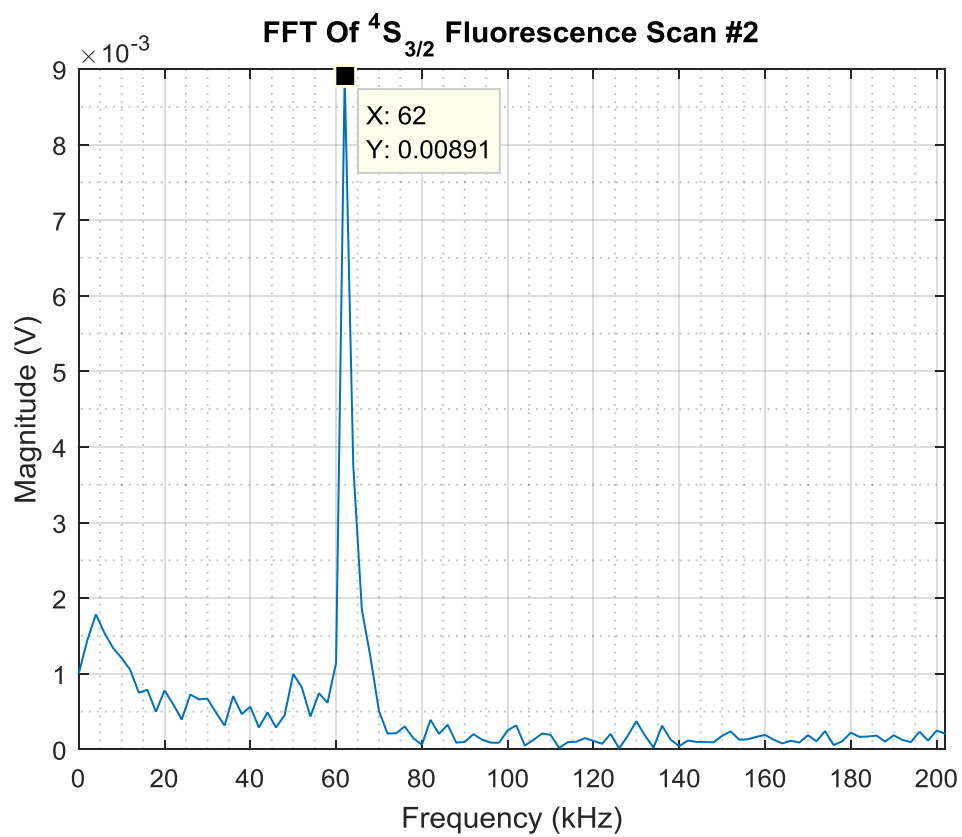


Figure C.1.14: FFT of transient scan of the  $^4S_{3/2}$  level.

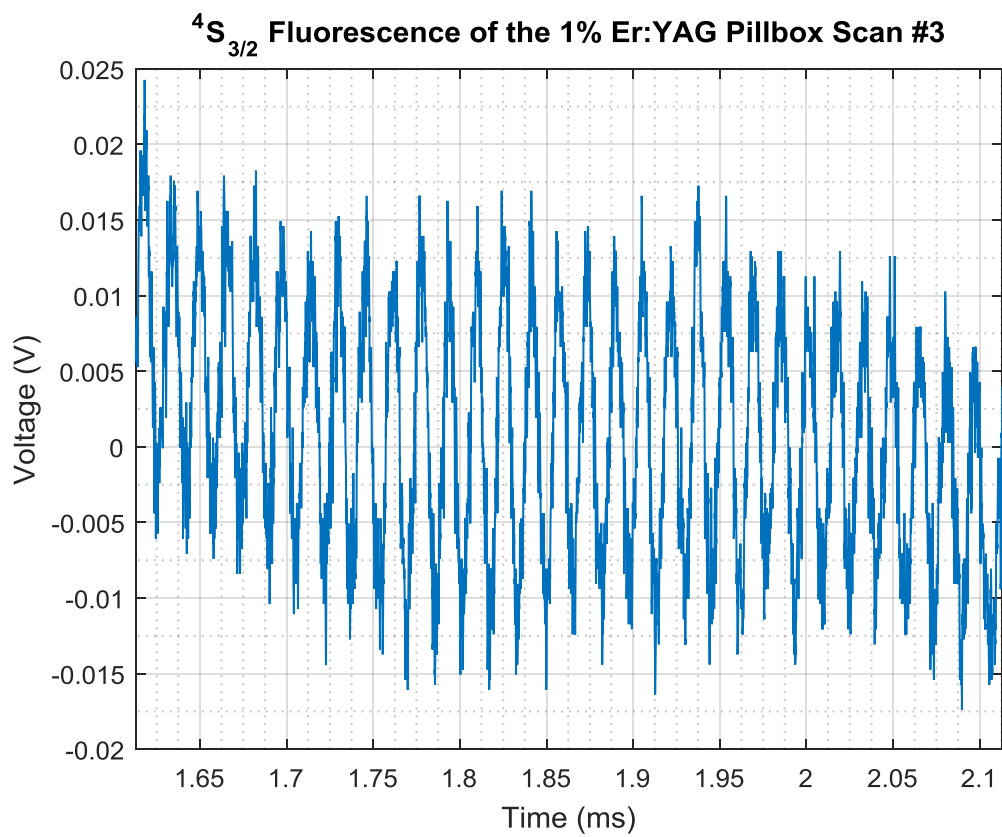


Figure C.1.15: Transient scan of the  $^4S_{3/2}$  level.

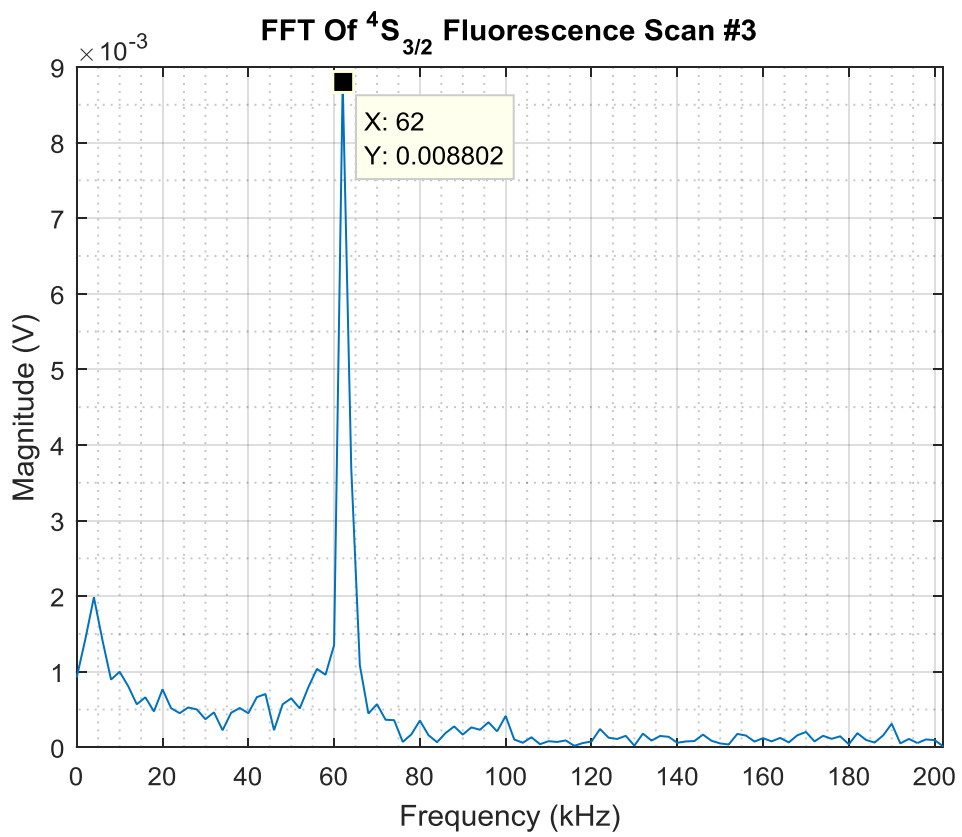


Figure C.1.16: FFT of transient scan of the  $^4S_{3/2}$  level.

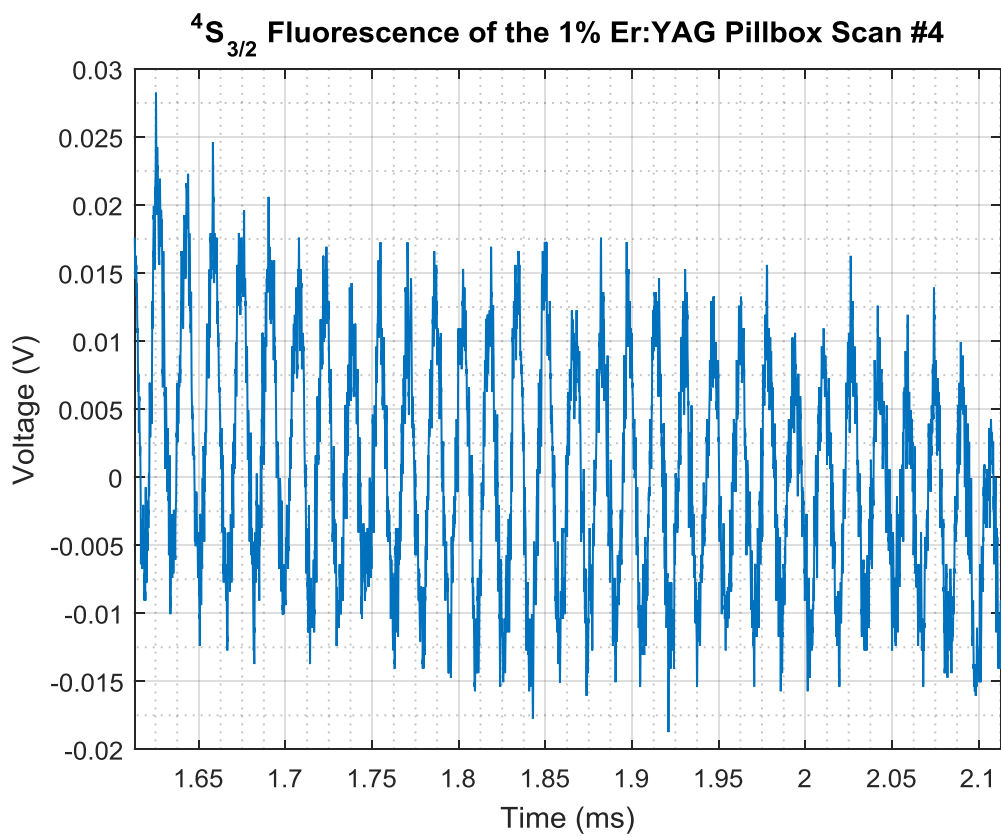


Figure C.1.17: Transient scan of the  $^4S_{3/2}$  level.

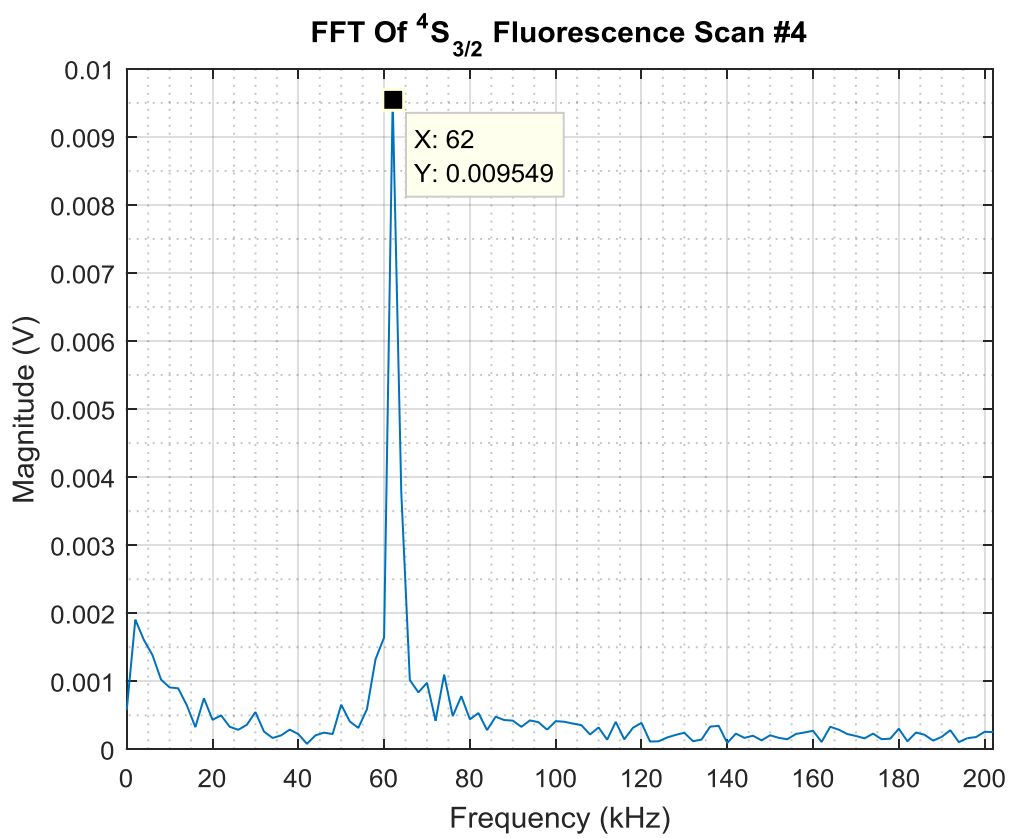


Figure C.1.18: FFT of transient scan of the  $^4S_{3/2}$  level.

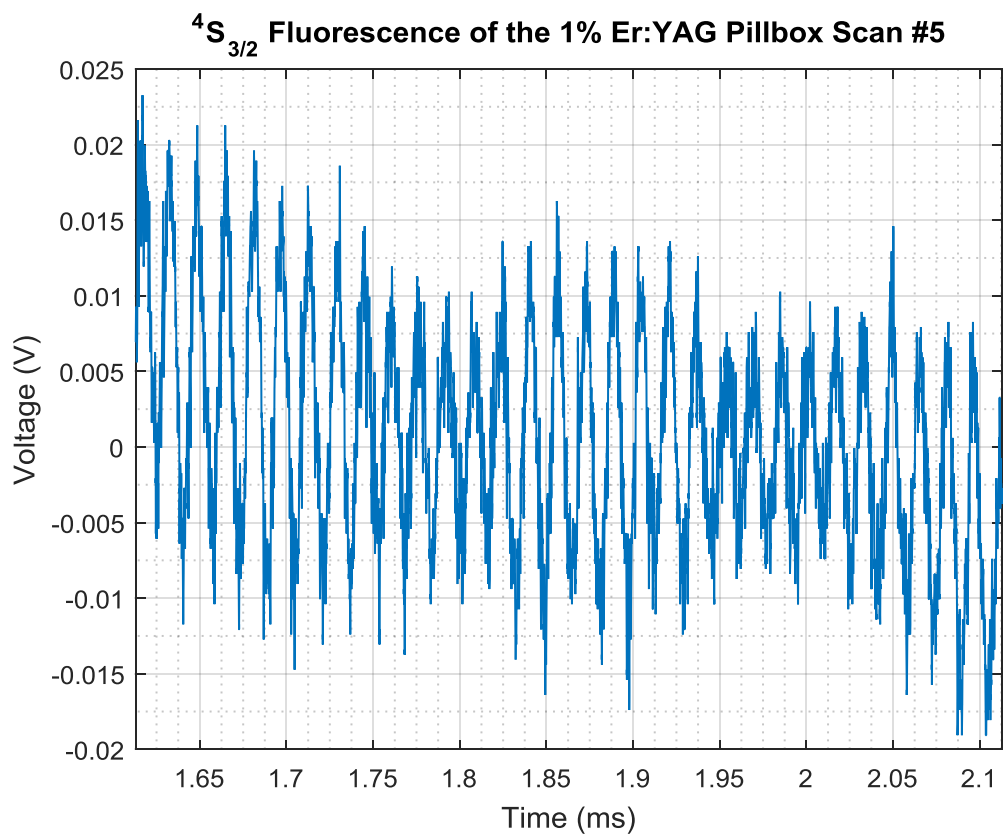


Figure C.1.19: Transient scan of the  $^4S_{3/2}$  level.

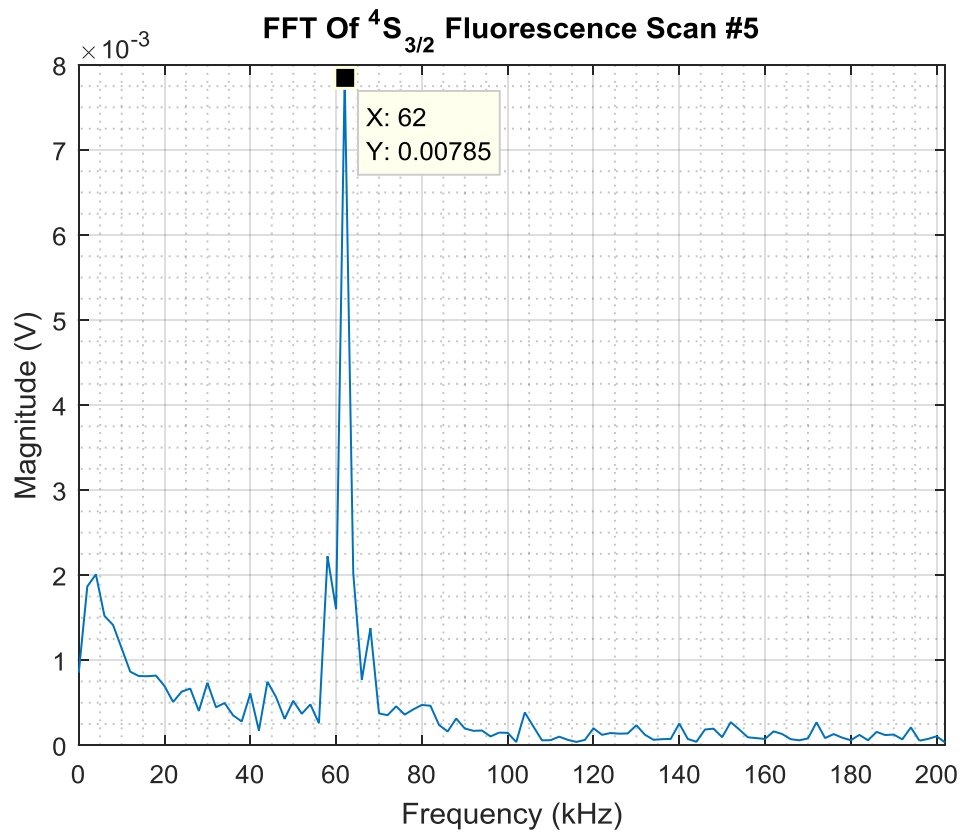


Figure C.1.20: FFT of transient scan of the  $^4S_{3/2}$  level.

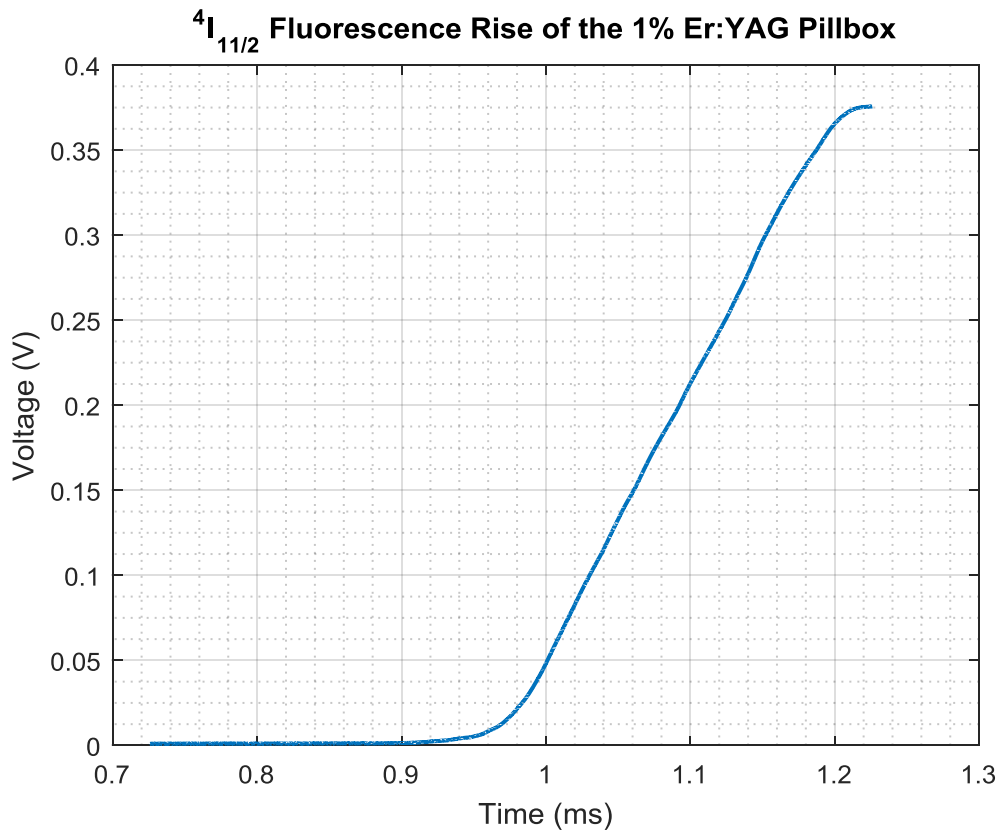


Figure C.1.21: Rise of the  $^4I_{11/2}$  level.

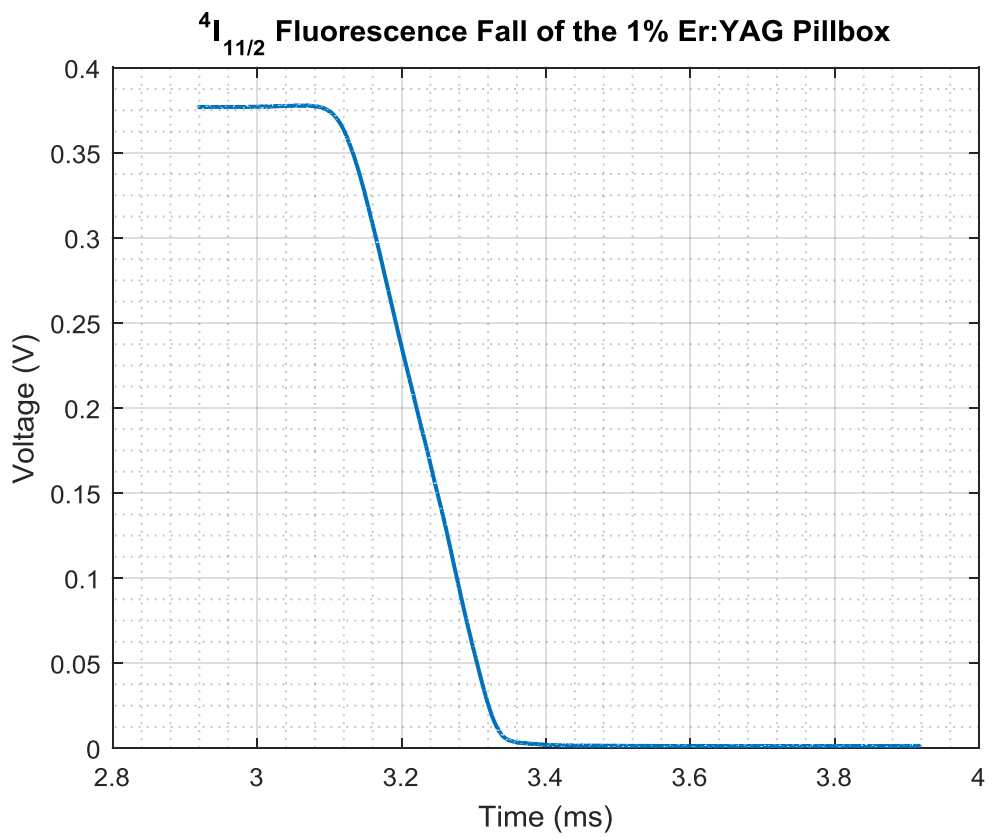


Figure C.1.22: Fall of the  $^4I_{11/2}$  level.

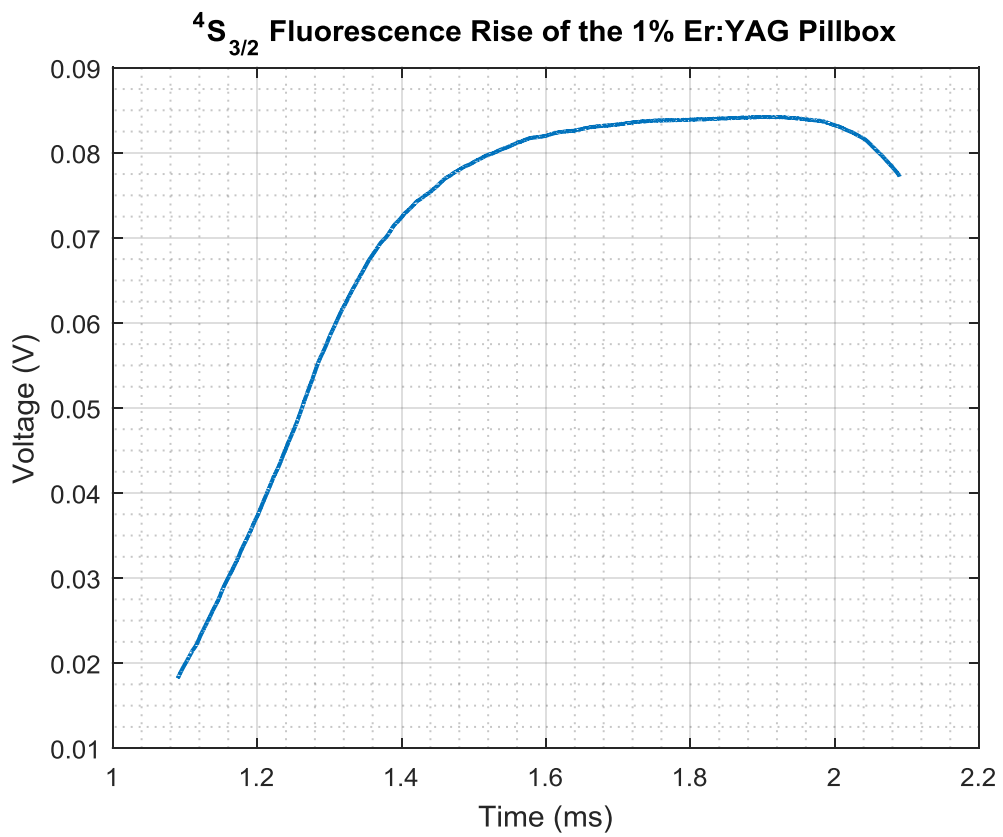


Figure C.1.23: Rise of the  $^4S_{3/2}$  level.

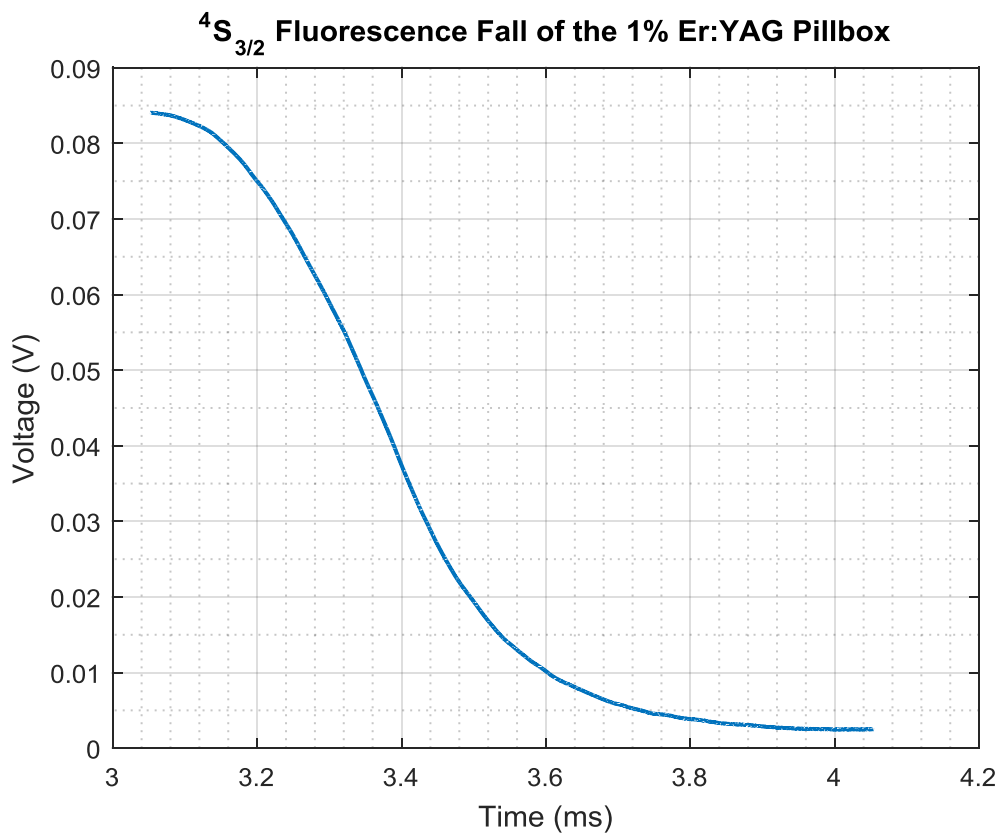


Figure C.1.22: Fall of the  $^4S_{3/2}$  level.

Transient Statistics ${}^4I_{11/2}$ Level Fluorescence Oscillation	
Number of Scans	5
Mean Value of Oscillation Frequency (KHz)	61.9988
Standard Deviation of Frequency (KHz)	8.1348 E-15
2 <sup>nd</sup> Harmonic of ${}^4I_{11/2}$ Level Fluorescence Oscillation	
Number of Scans	5
Mean Value of Oscillation Frequency (KHz)	125.9975
Standard Deviation of Frequency (KHz)	0.8944

Table C.1.1: Statistics of the transient scans of the  ${}^4I_{11/2}$  level.

Transient Statistics ${}^4S_{3/2}$ Level Fluorescence Oscillation	
Number of Scans	5
Mean Value of Oscillation Frequency (KHz)	61.9988
Standard Deviation of Frequency (KHz)	8.1348 E-15

Table C.1.2: Statistics of the transient scans of the  ${}^4S_{3/2}$  level.

${}^4I_{11/2}$ Level Fluorescence	
Number of Sweeps	1000
Rise Time ( $\mu\text{s}$ )	181.73
Fall Time ( $\mu\text{s}$ )	169.44

Table C.1.3: Rise and Fall statistics of the transient scans of the  ${}^4I_{11/2}$  level.

${}^4S_{3/2}$ Level Fluorescence	
Number of Sweeps	1000
Rise Time ( $\mu\text{s}$ )	324.01
Fall Time ( $\mu\text{s}$ )	393.53

Table C.1.4: Rise and Fall statistics of the transient scans of the  ${}^4S_{3/2}$  level.

## C.2 808nm CW Pumped 1% Er:YAG Pillbox with No 3μm Laser

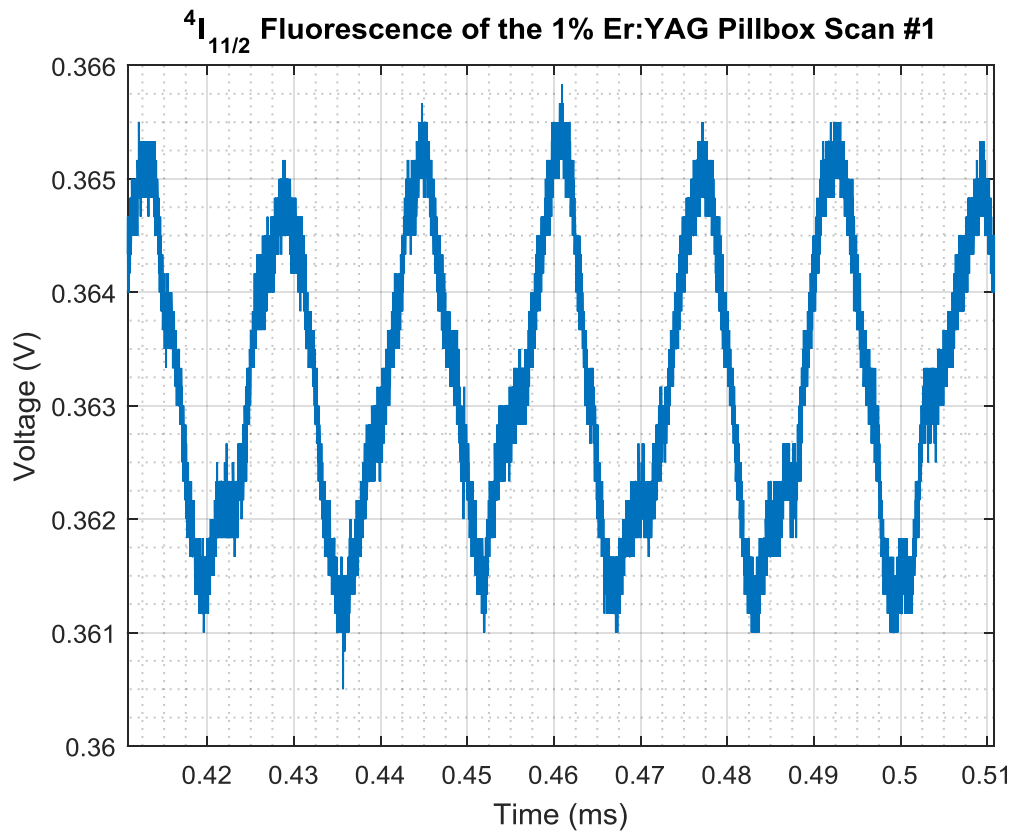


Figure C.2.1: Transient scan of the  $^4I_{11/2}$  level.

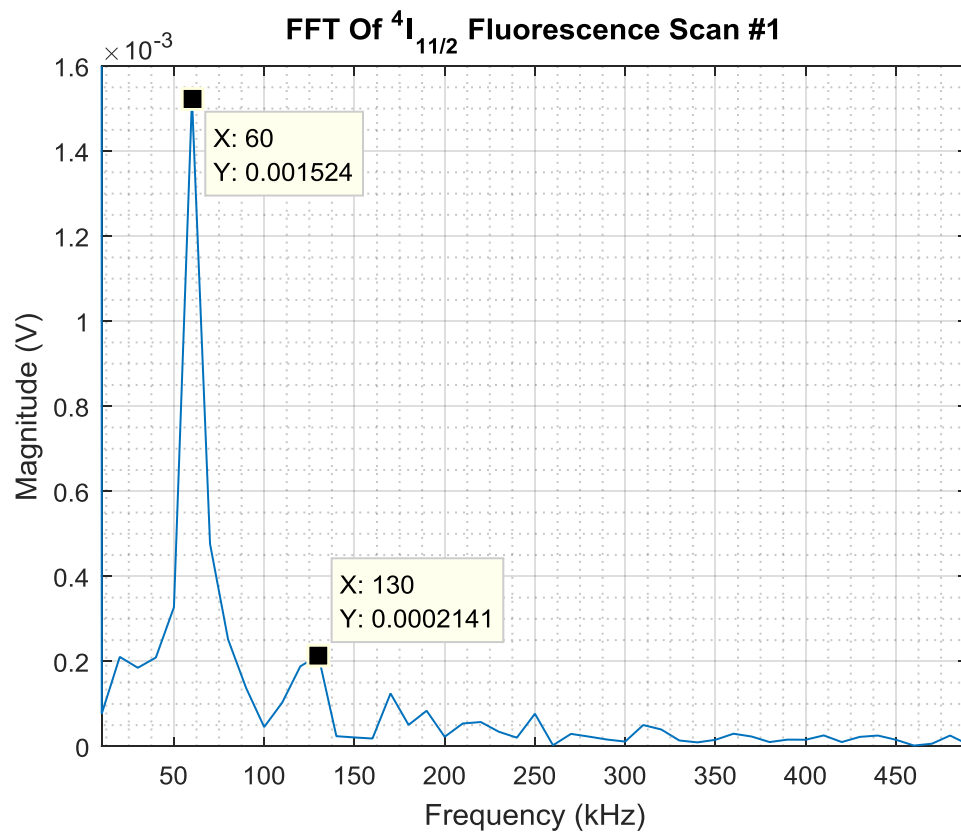


Figure C.2.2: FFT of transient scan of the  ${}^4I_{11/2}$  level.

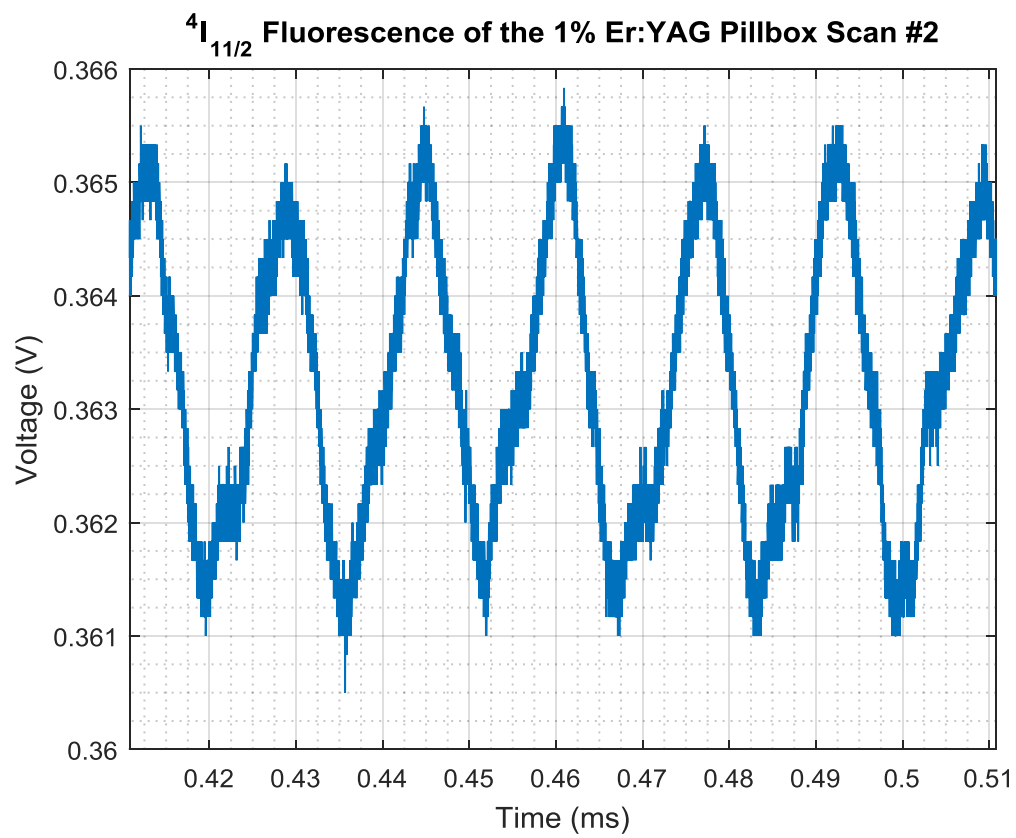


Figure C.2.3: Transient scan of the  $^4I_{11/2}$  level.

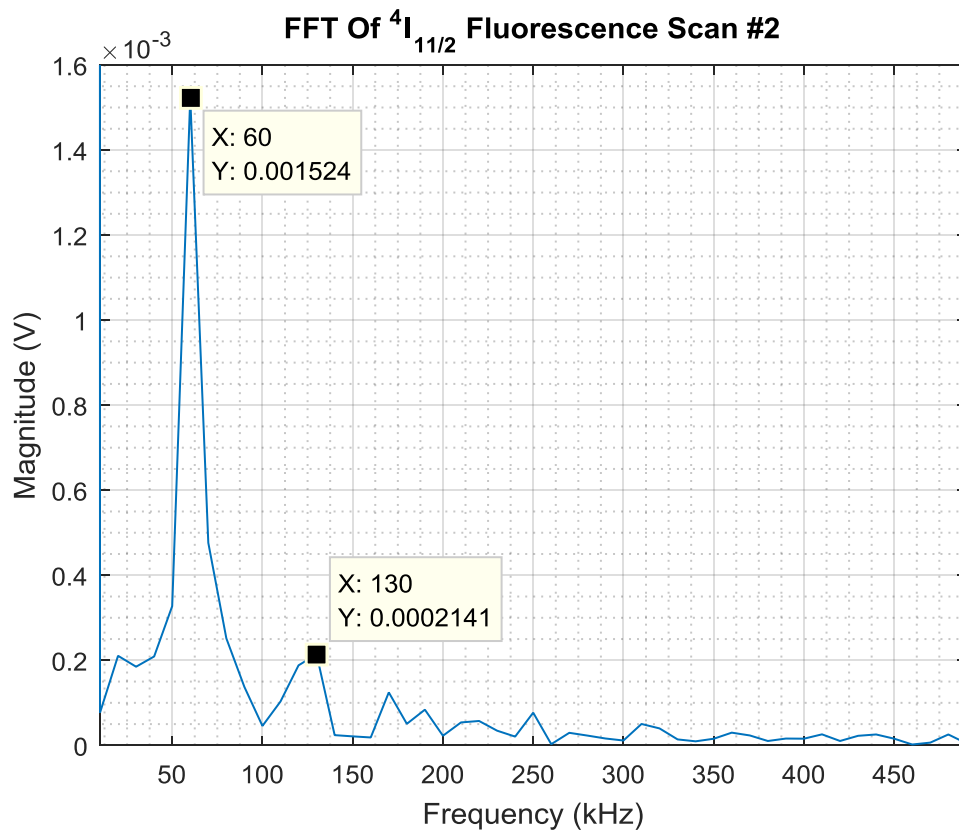


Figure C.2.4: FFT of transient scan of the  $^4I_{11/2}$  level.

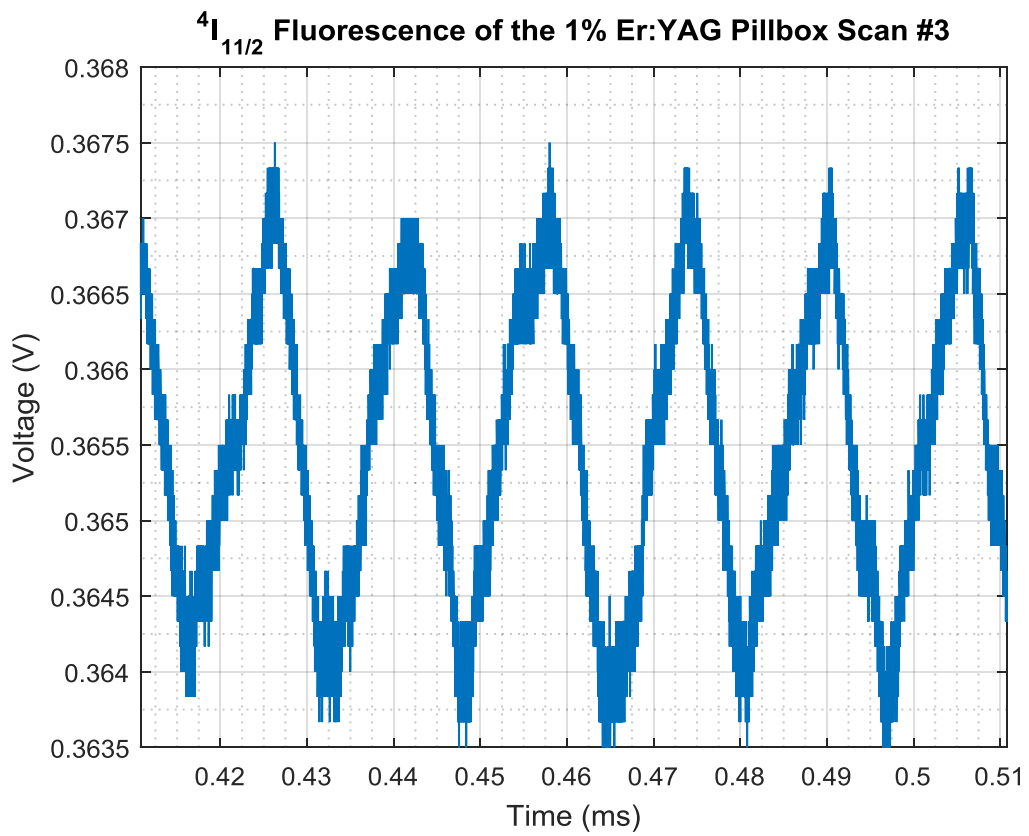


Figure C.2.5: Transient scan of the  $^4I_{11/2}$  level.

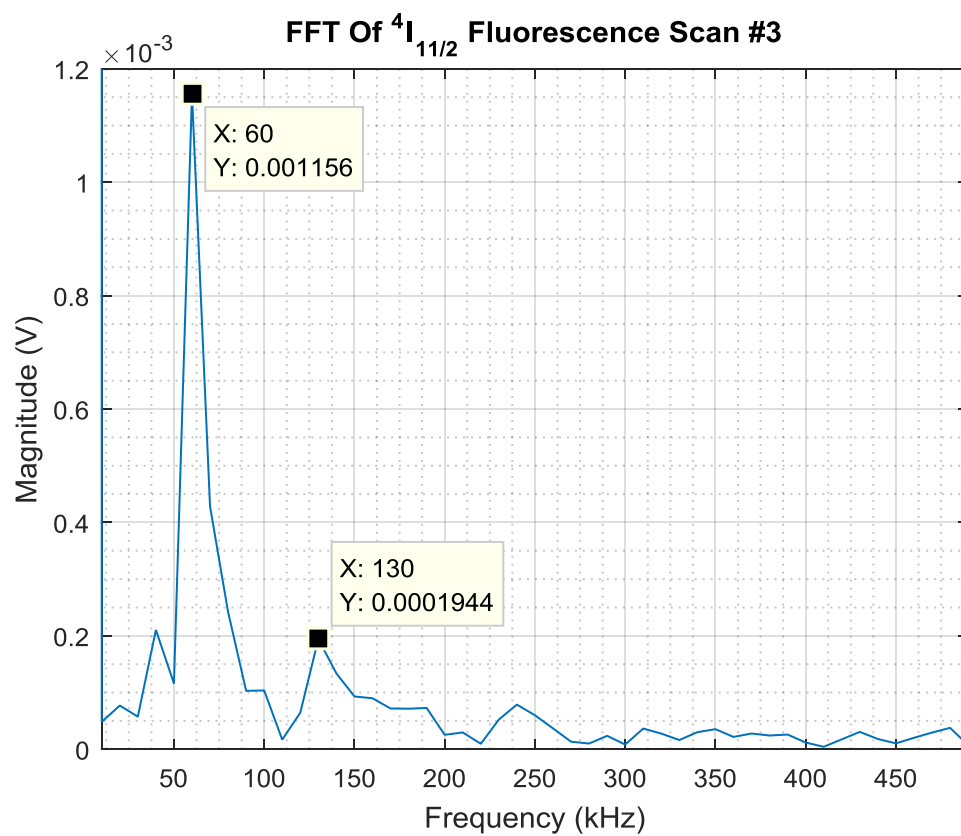


Figure C.2.6: FFT of transient scan of the  ${}^4I_{11/2}$  level.

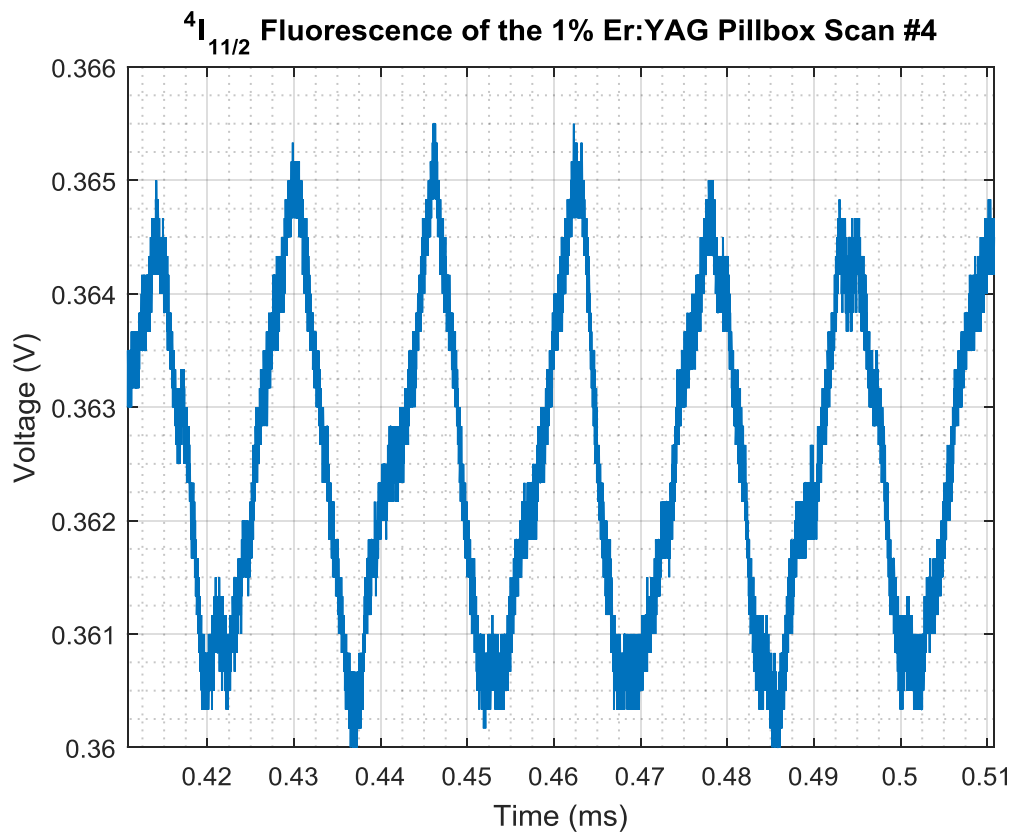


Figure C.2.7: Transient scan of the  $^4I_{11/2}$  level.

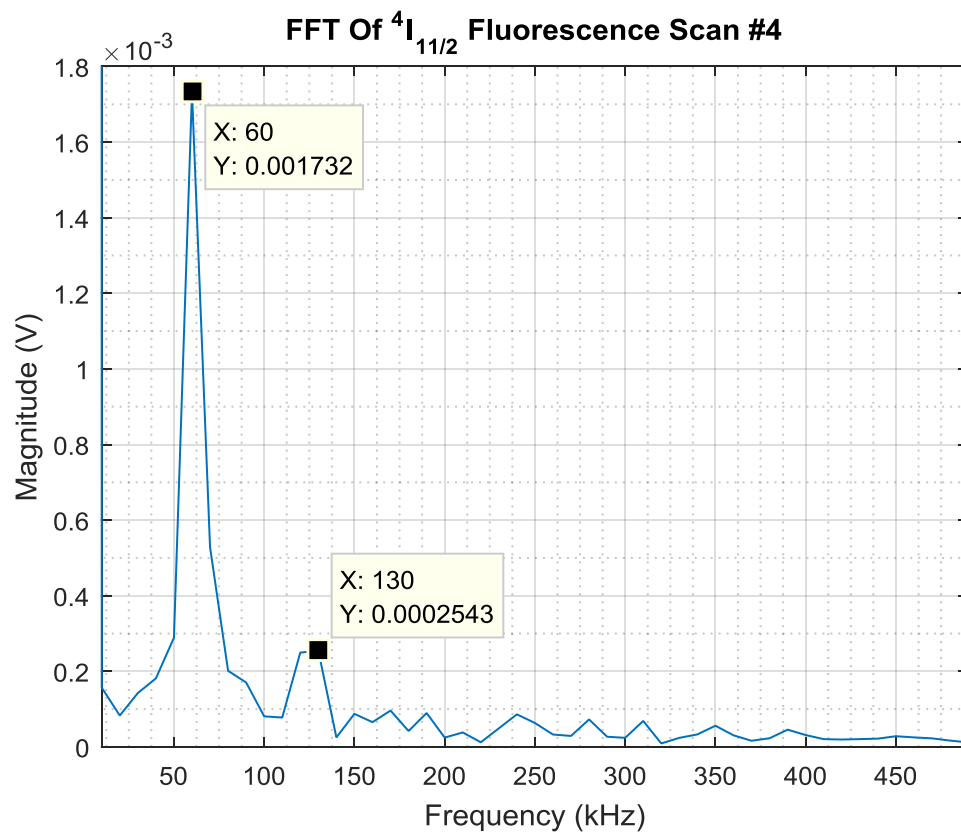


Figure C.2.8: FFT of transient scan of the  ${}^4I_{11/2}$  level.

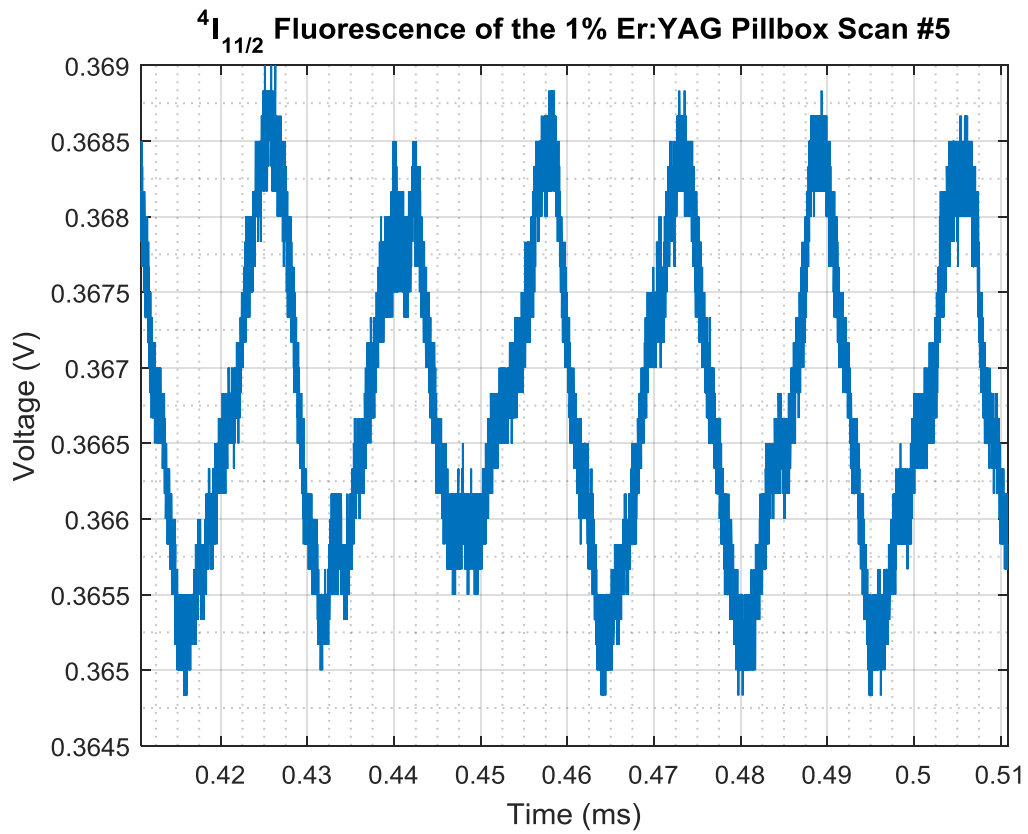


Figure C.2.9: Transient scan of the  $^4I_{11/2}$  level.

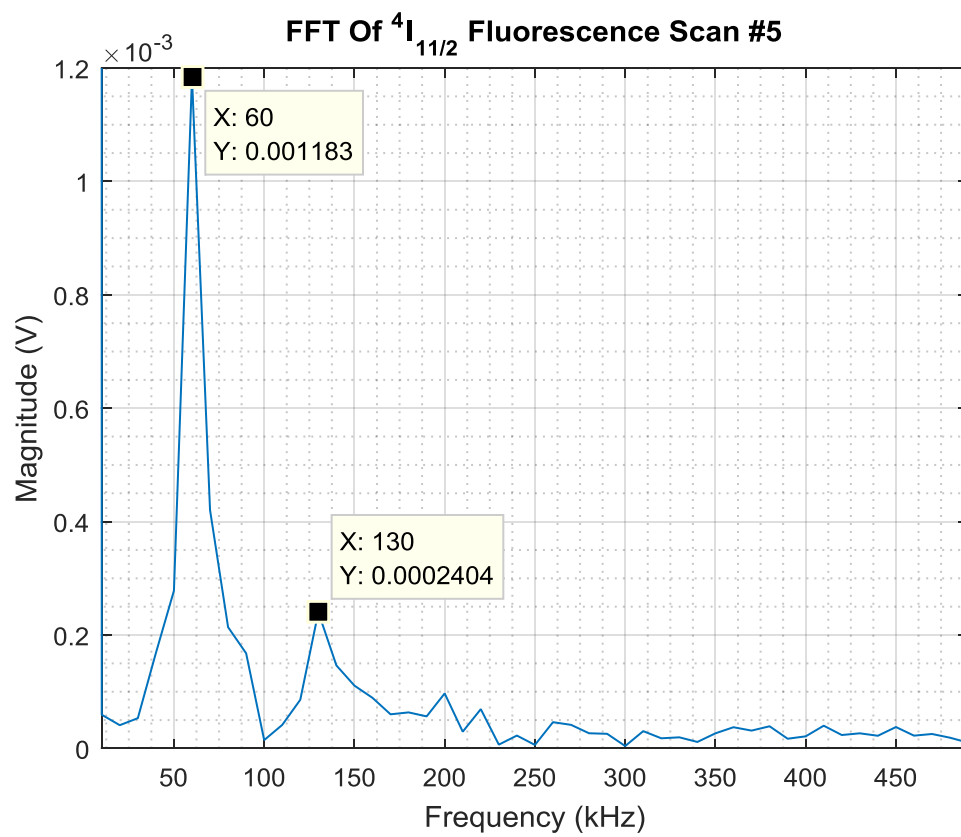


Figure C.2.10: FFT of transient scan of the  ${}^4I_{11/2}$  level.

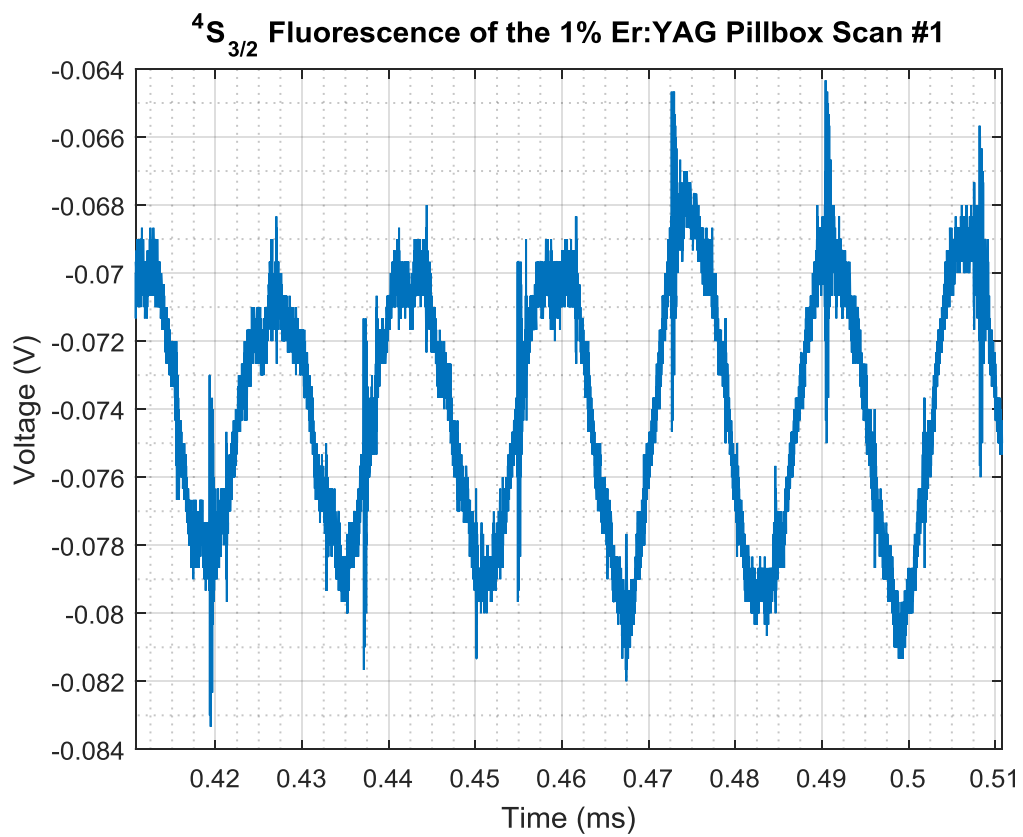


Figure C.2.11: Transient scan of the  $^4S_{3/2}$  level.

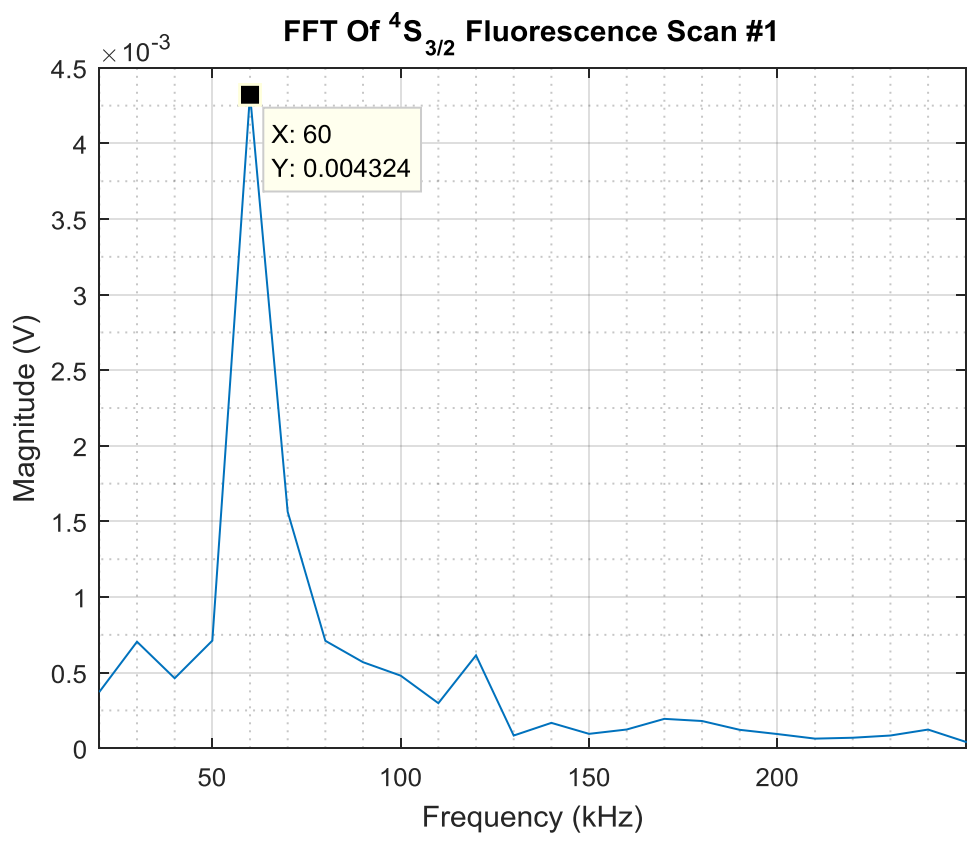


Figure C.2.12: FFT of transient scan of the  $^4S_{3/2}$  level.

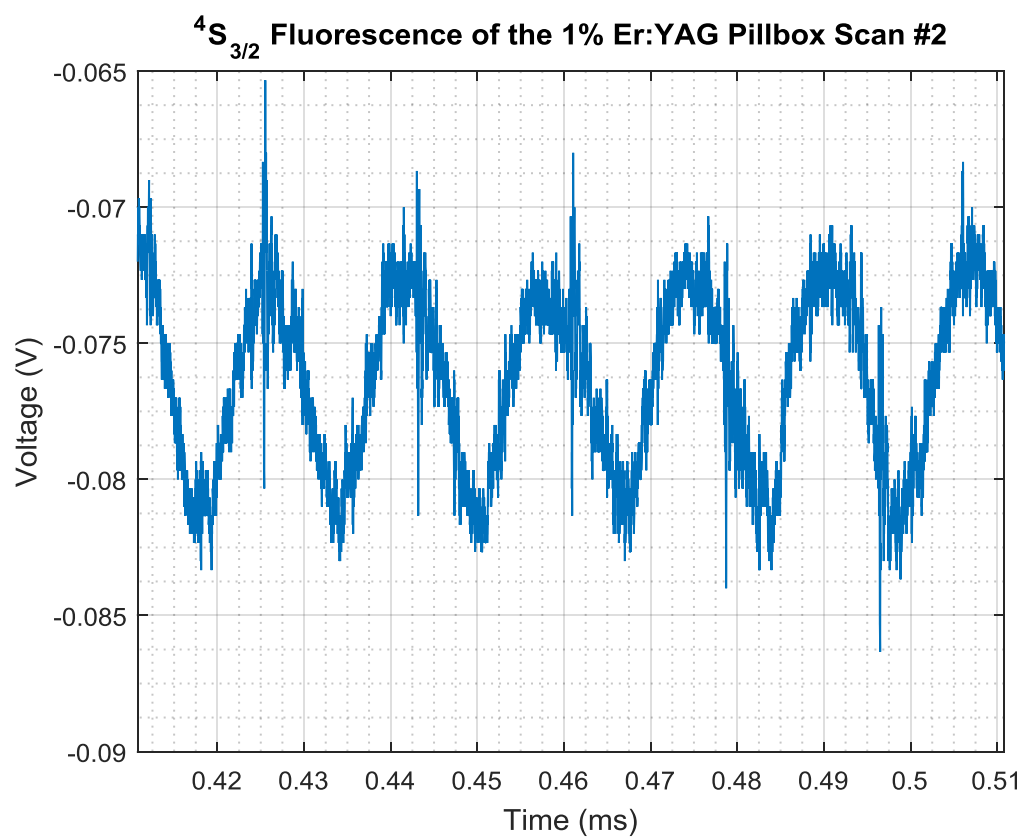


Figure C.2.13: Transient scan of the  $^4S_{3/2}$  level.

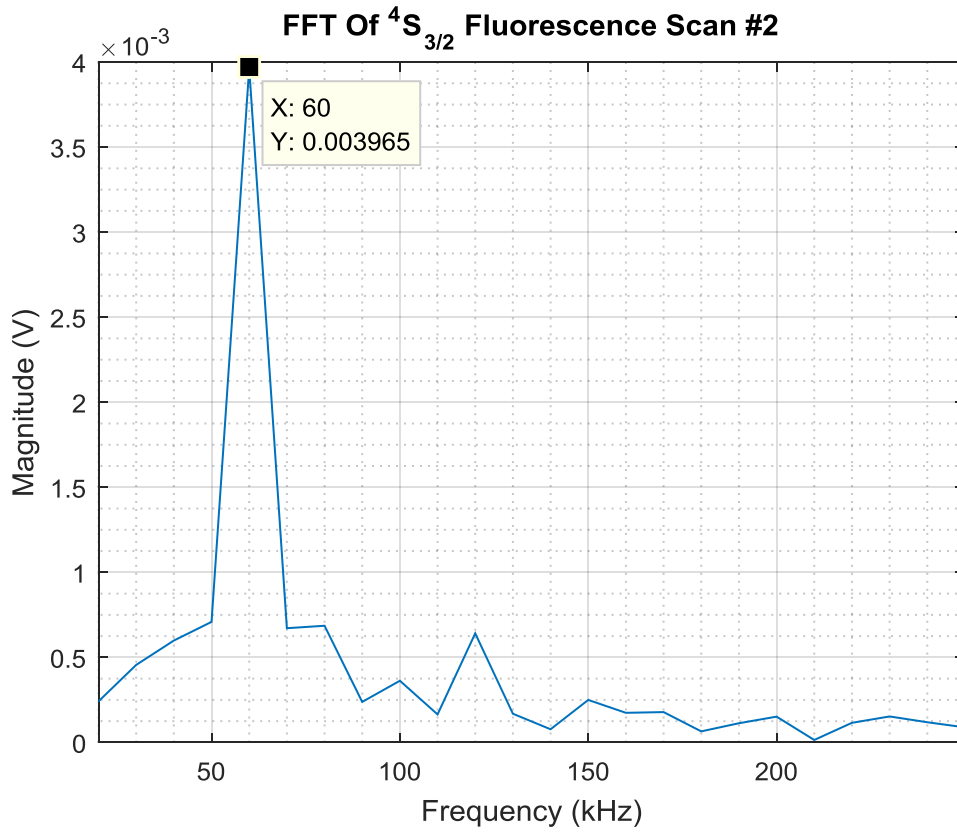


Figure C.2.14: FFT of transient scan of the  $^4S_{3/2}$  level.

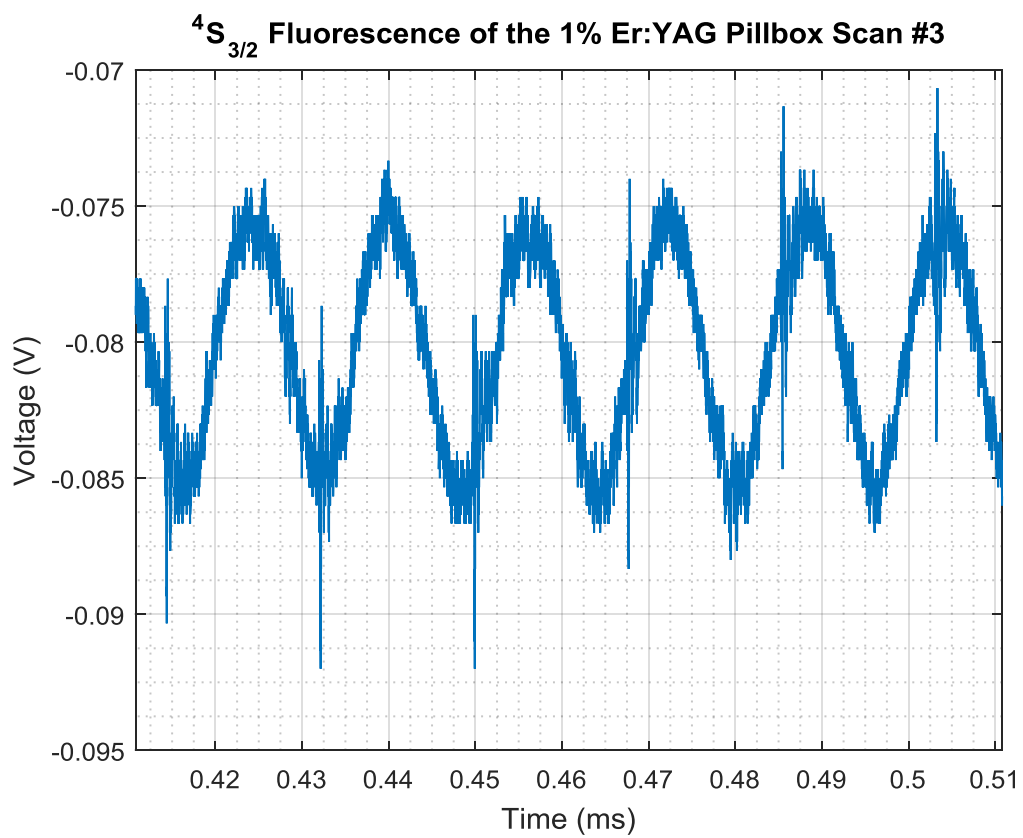


Figure C.2.15: Transient scan of the  $^4S_{3/2}$  level.

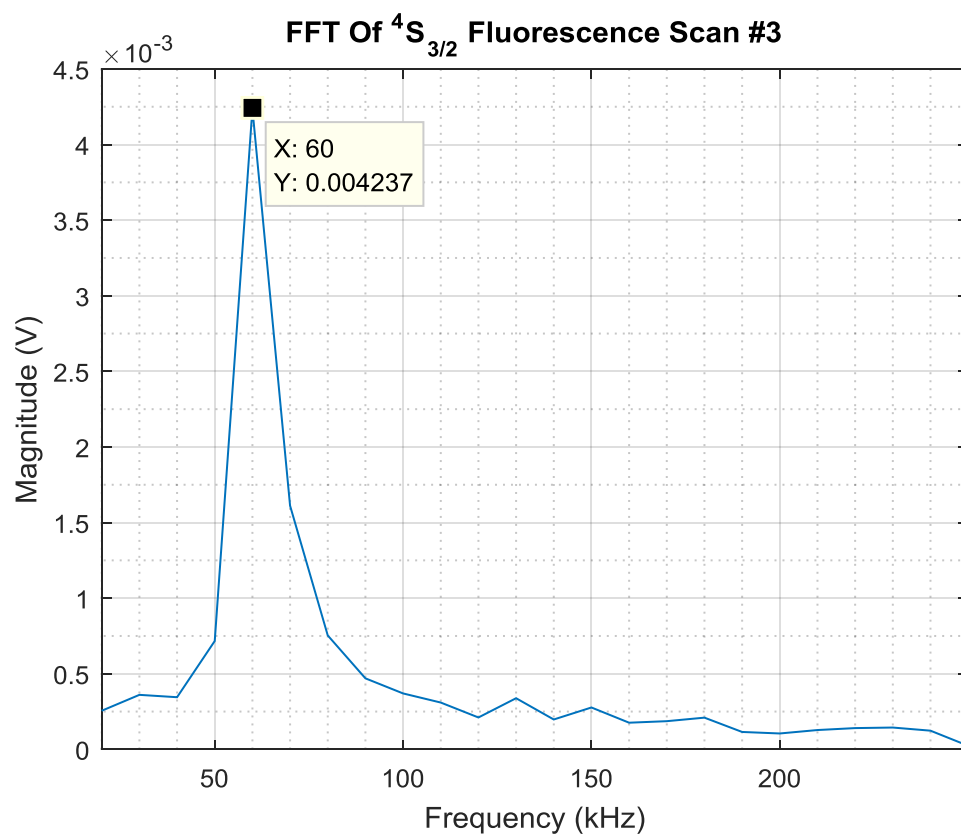


Figure C.2.16: FFT of transient scan of the  $^4S_{3/2}$  level.

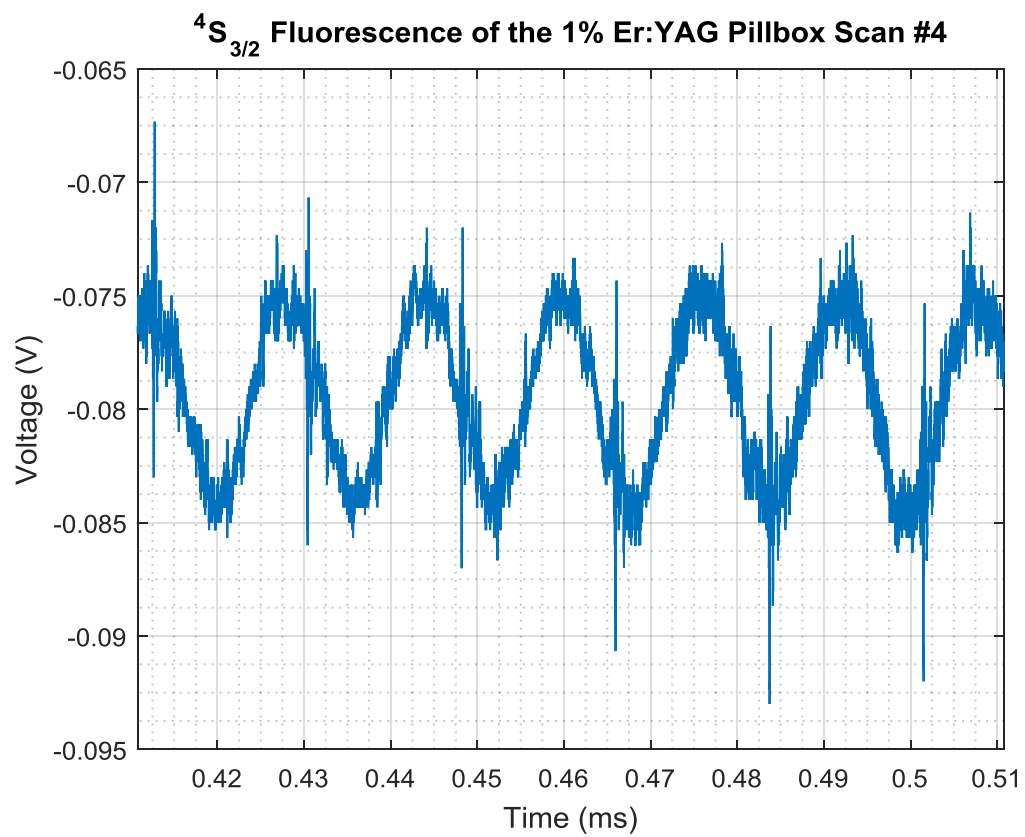


Figure C.2.17: Transient scan of the  $^4S_{3/2}$  level.

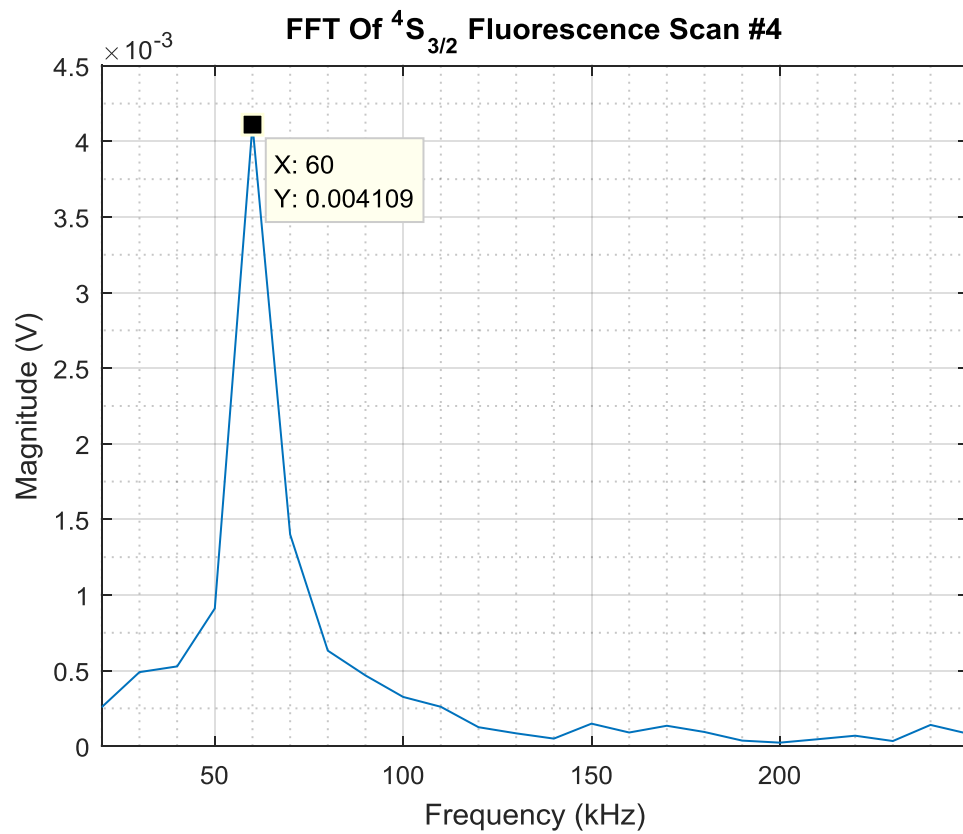


Figure C.2.18: FFT of transient scan of the  $^4S_{3/2}$  level.

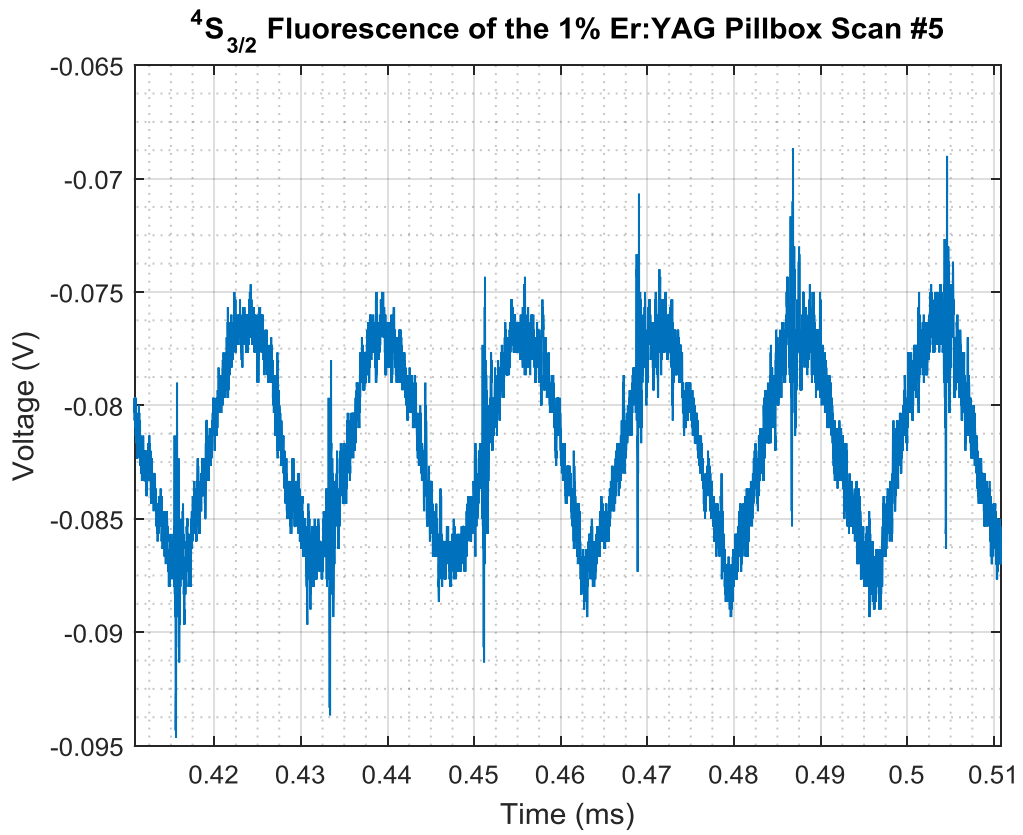


Figure C.2.19: Transient scan of the  $^4S_{3/2}$  level.

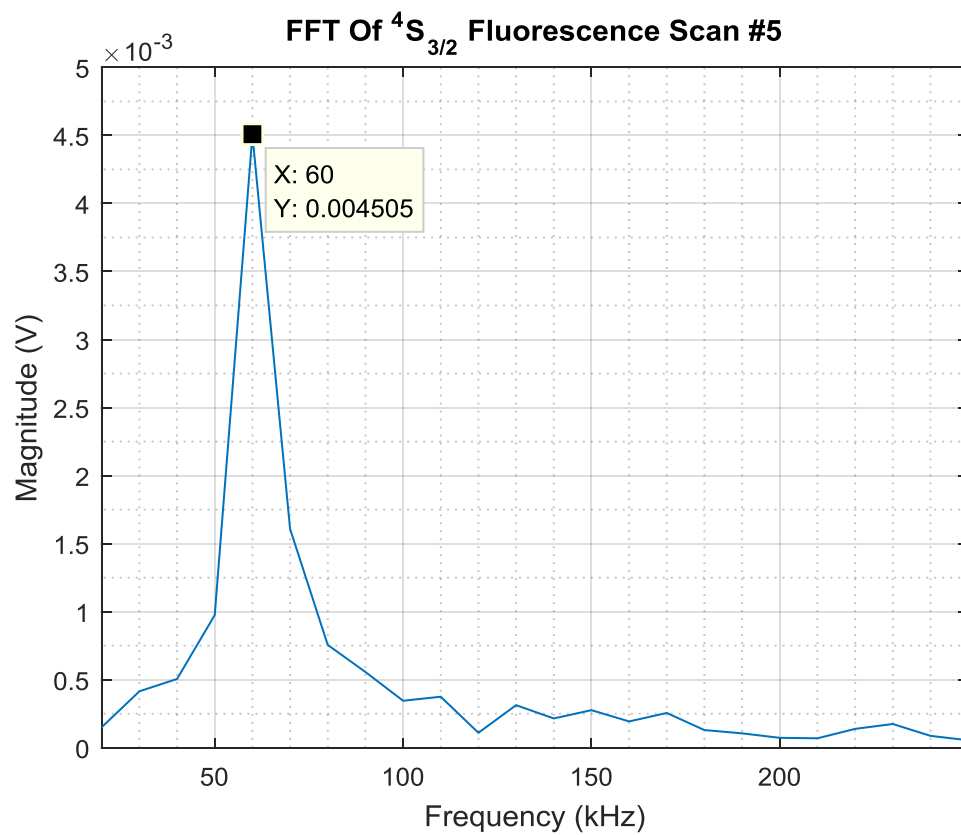


Figure C.2.20: FFT of transient scan of the  $^4S_{3/2}$  level.

Transient Statistics ${}^4I_{11/2}$ Level Fluorescence Oscillation	
Number of Scans	5
Mean Value of Oscillation Frequency (KHz)	59.9988
Standard Deviation of Frequency (KHz)	8.1348 E-15
2 <sup>nd</sup> Harmonic of ${}^4I_{11/2}$ Level Fluorescence Oscillation	
Number of Scans	5
Mean Value of Oscillation Frequency (KHz)	129.9974
Standard Deviation of Frequency (KHz)	1.6270E-14

Table C.2.1: Statistics of the transient scans of the  ${}^4I_{11/2}$  level.

Transient Statistics ${}^4S_{3/2}$ Level Fluorescence Oscillation	
Number of Scans	5
Mean Value of Oscillation Frequency (KHz)	59.9988
Standard Deviation of Frequency (KHz)	8.1348 E-15

Table C.2.2: Statistics of the transient scans of the  ${}^4S_{3/2}$  level.

### C.3 808nm Pulsed Pumped 50% Er:YAG Pillbox with No 3 $\mu$ m Laser

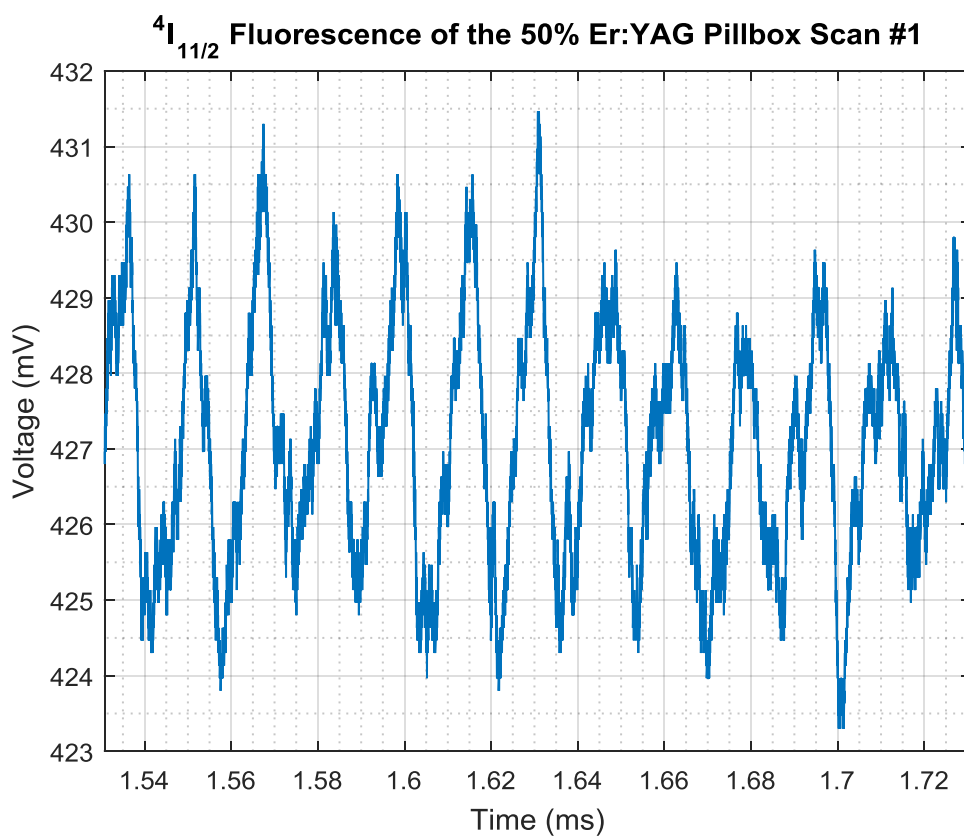


Figure C.3.1: Transient scan of the <sup>4</sup>I<sub>11/2</sub> level.

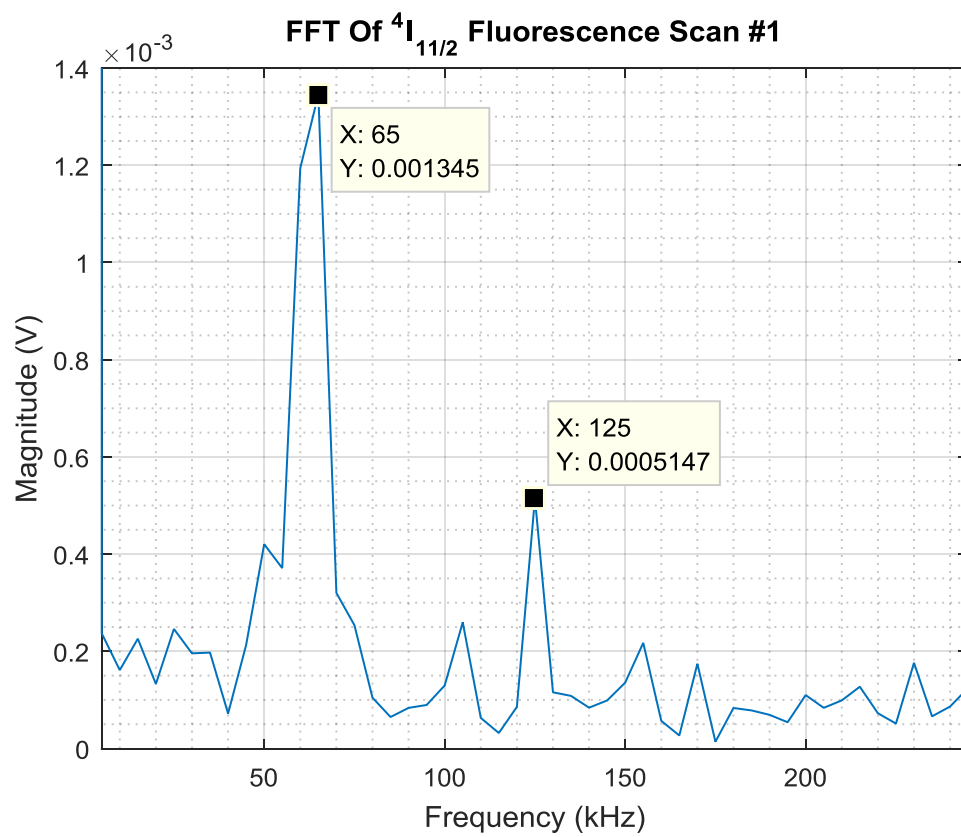


Figure C.3.2: FFT of transient scan of the  ${}^4I_{11/2}$  level.

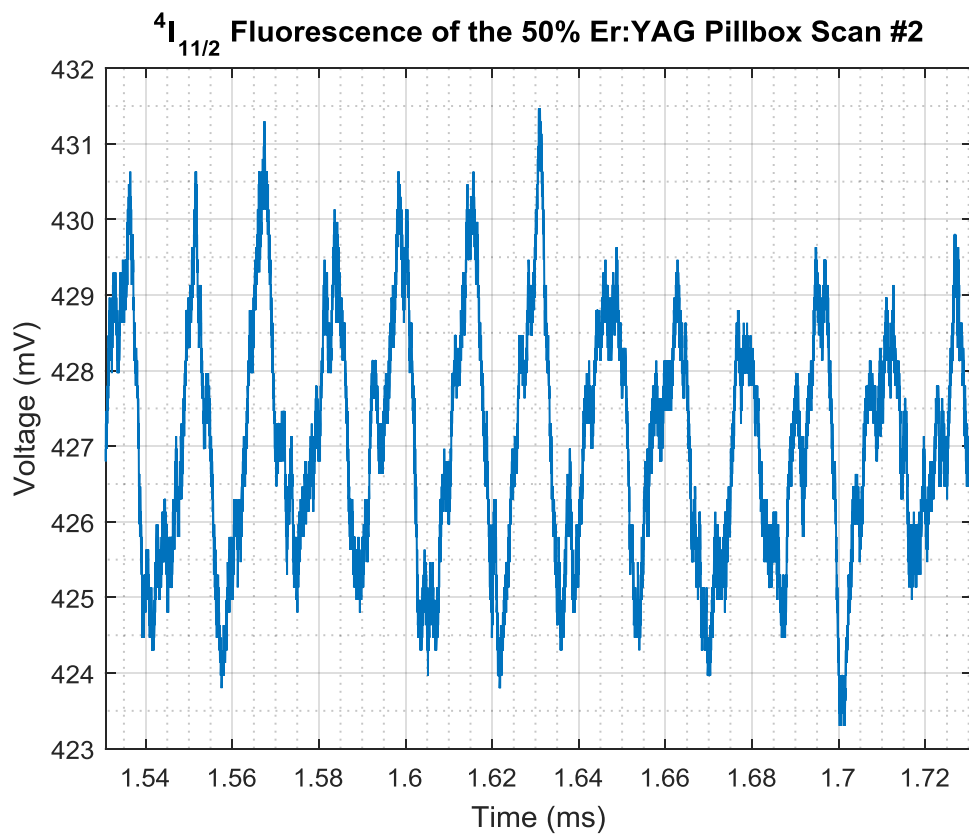


Figure C.3.3: Transient scan of the  $^4I_{11/2}$  level.

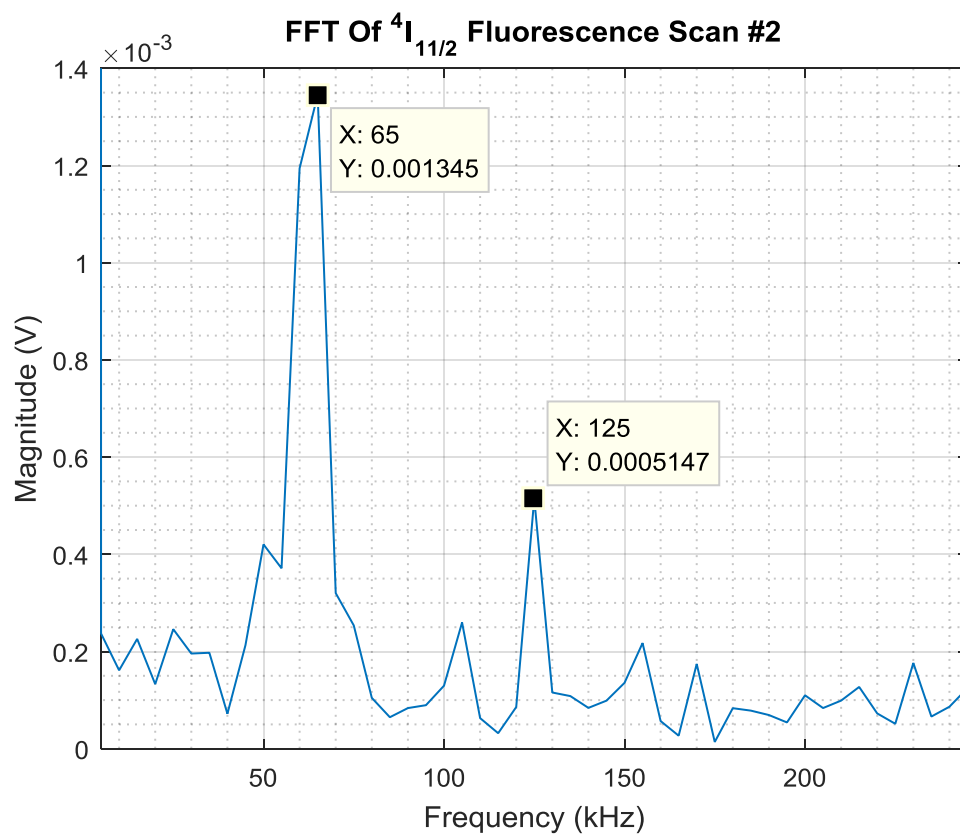


Figure C.3.4: FFT of transient scan of the  ${}^4I_{11/2}$  level.

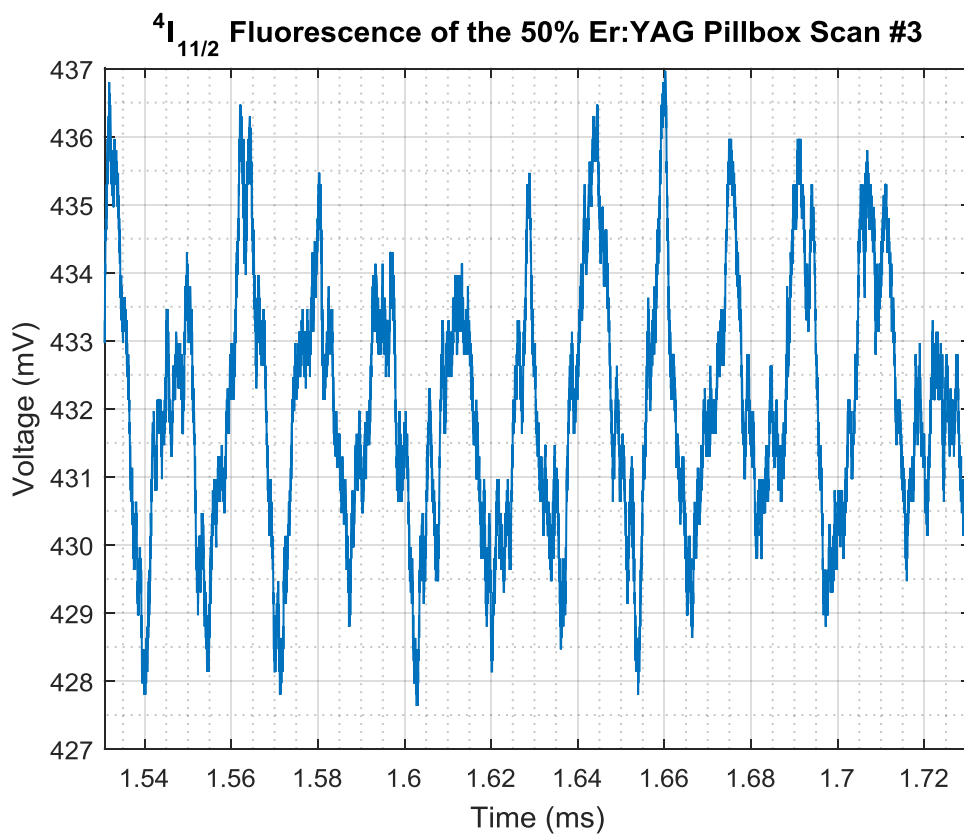


Figure C.3.5: Transient scan of the  $^4I_{11/2}$  level.

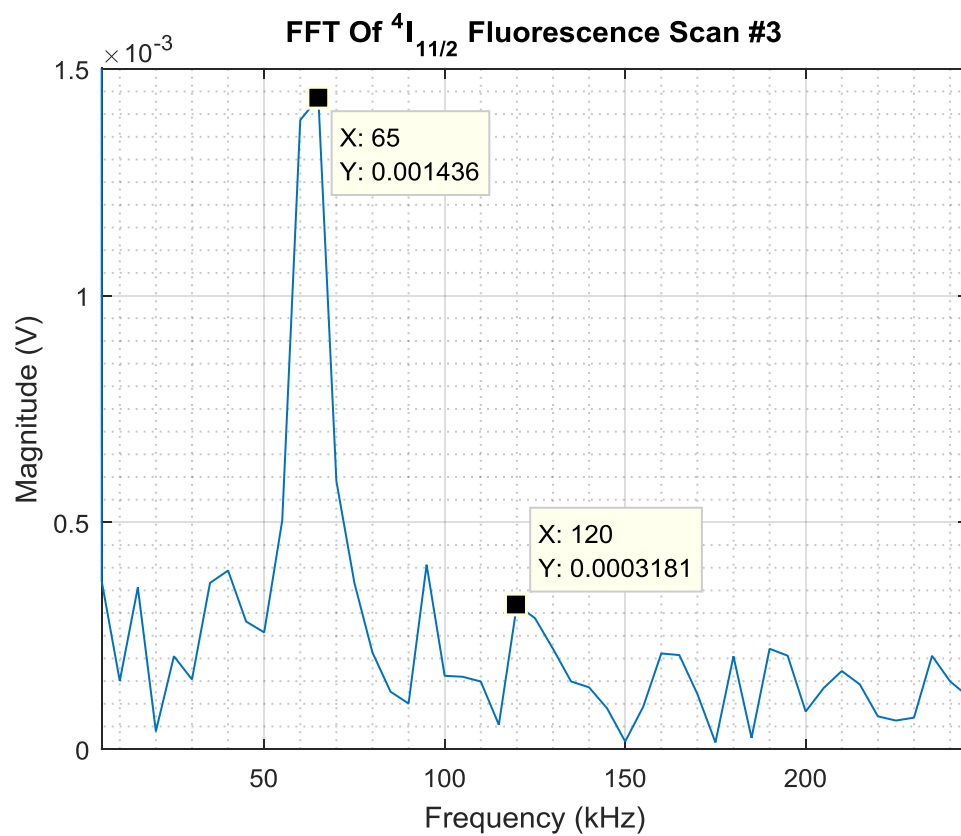


Figure C.3.6: FFT of transient scan of the  $^4I_{11/2}$  level.

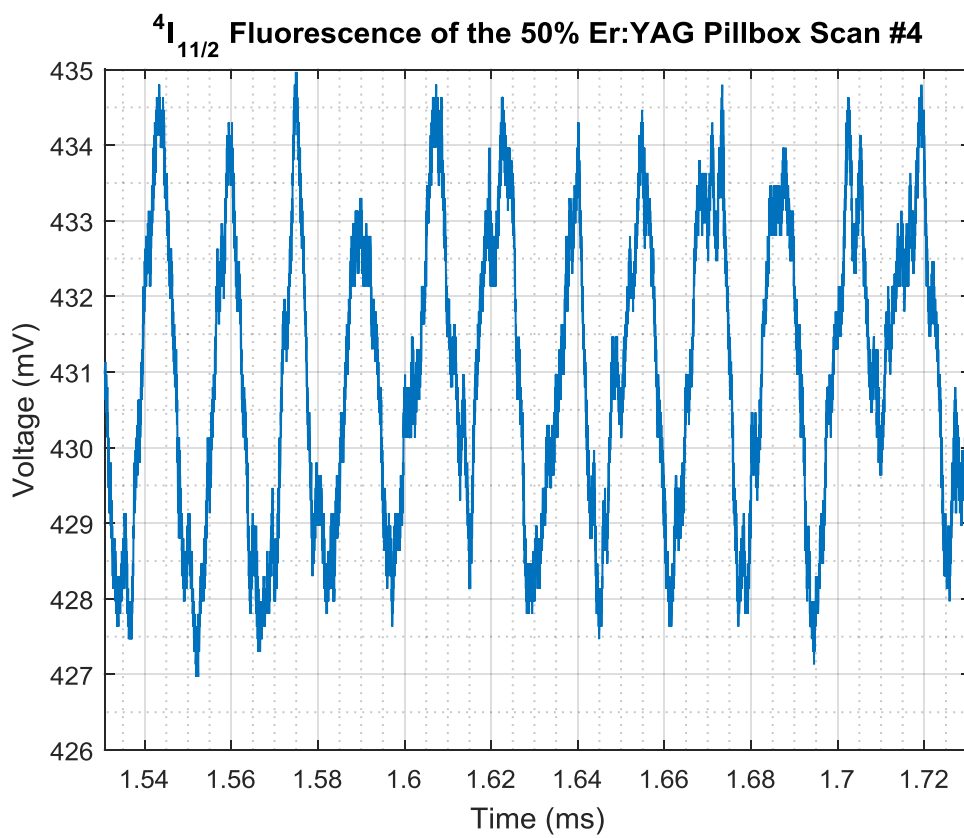


Figure C.3.7: Transient scan of the  $^4I_{11/2}$  level.

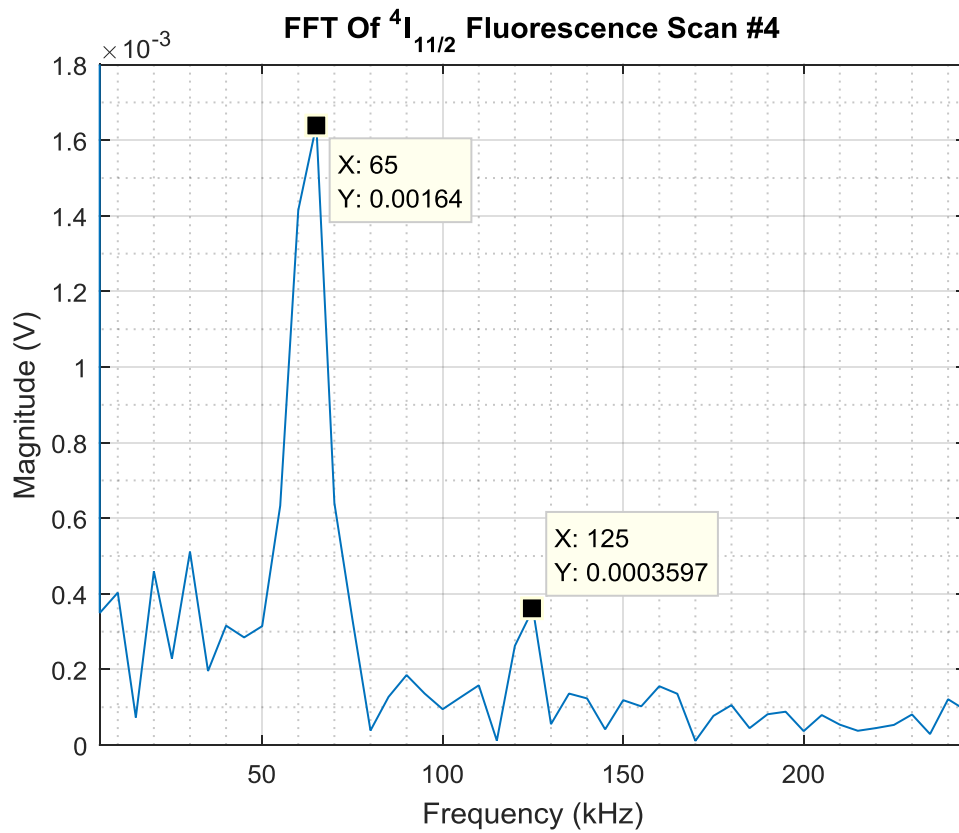


Figure C.3.8: FFT of transient scan of the  ${}^4I_{11/2}$  level.

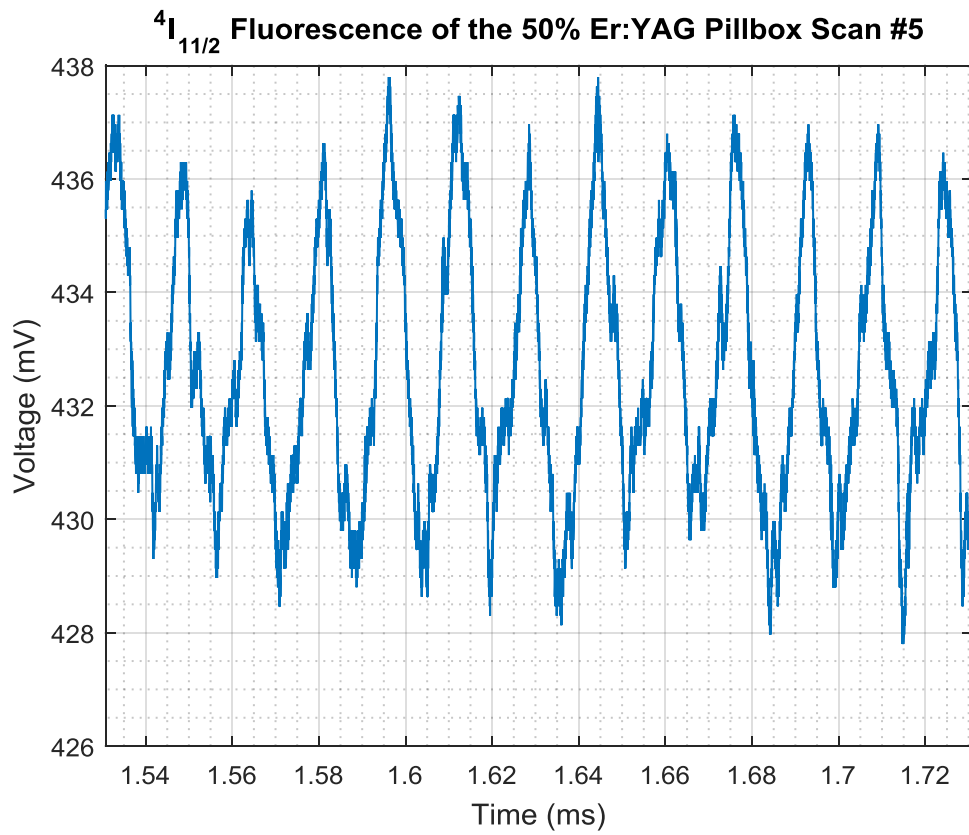


Figure C.3.9: Transient scan of the  $^4I_{11/2}$  level.

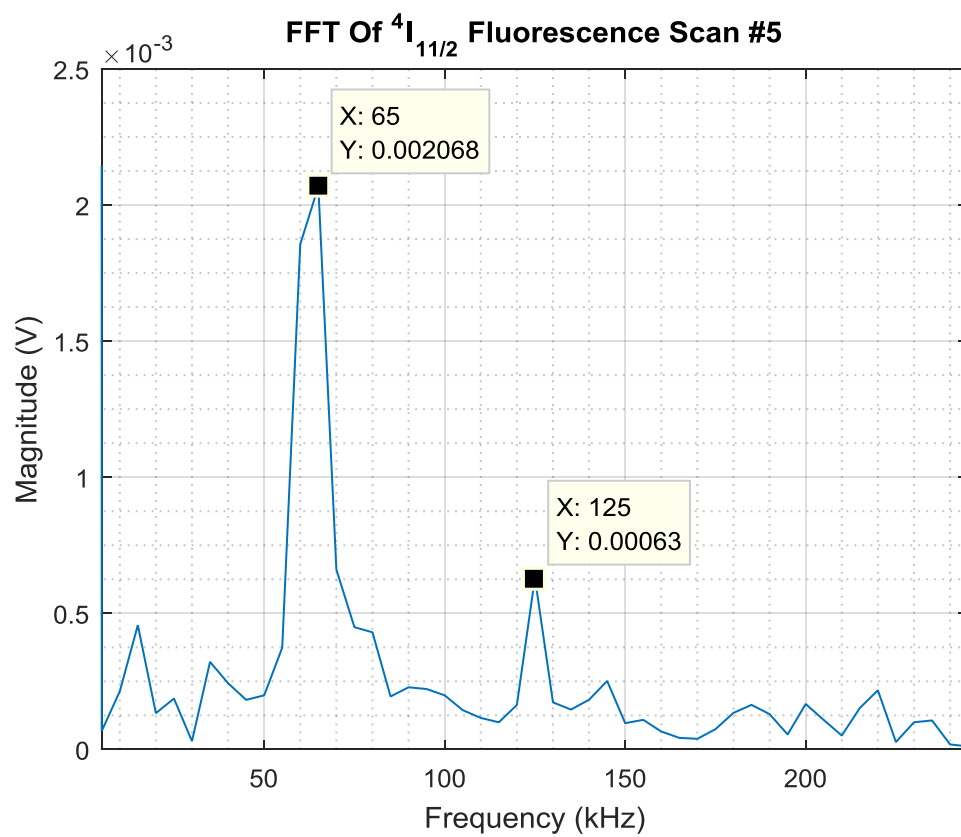


Figure C.3.10: FFT of transient scan of the  ${}^4I_{11/2}$  level.

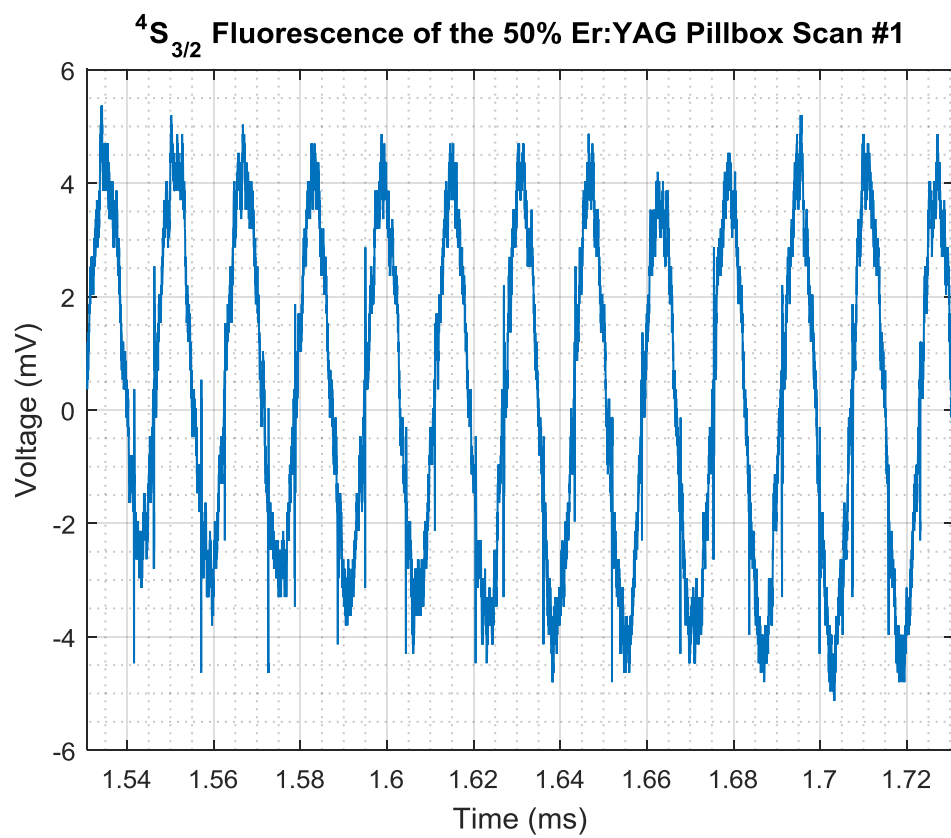


Figure C.3.11: Transient scan of the  $^4S_{3/2}$  level.

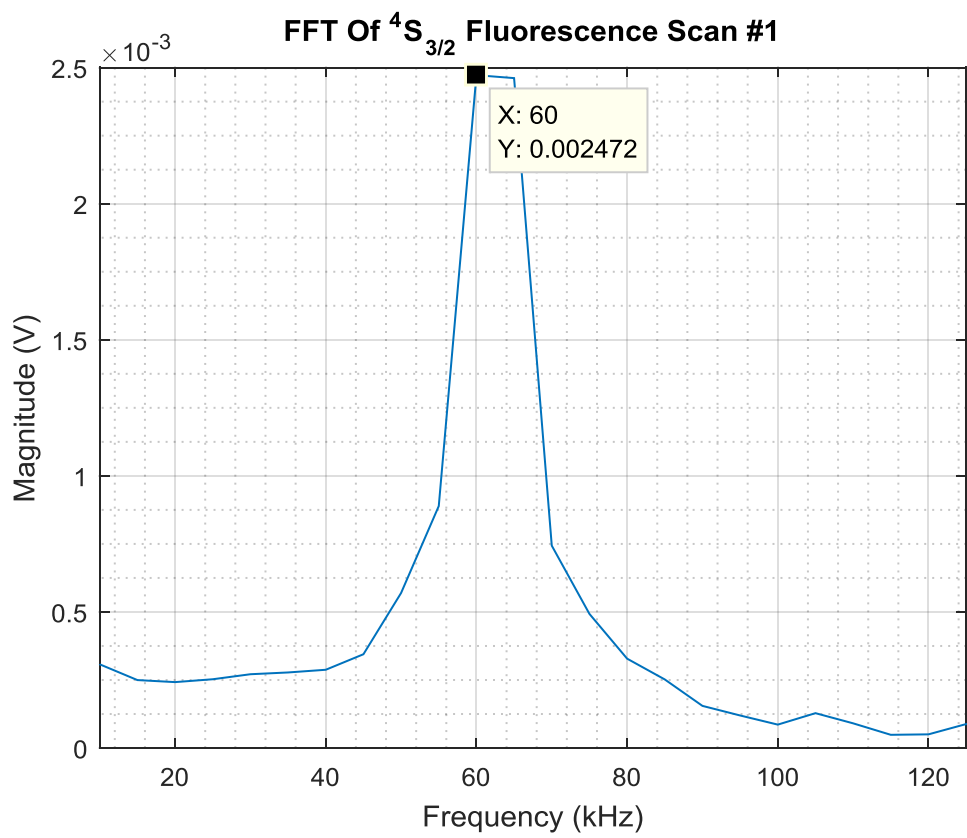


Figure C.3.12: FFT of transient scan of the  $^4S_{3/2}$  level.

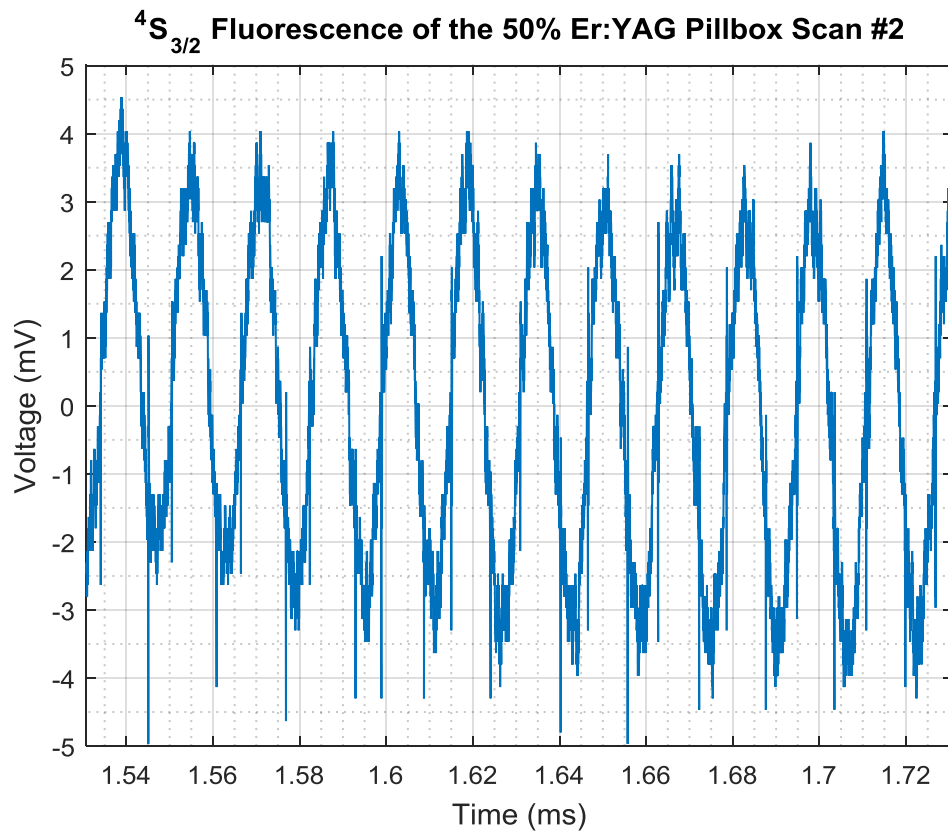


Figure C.3.13: Transient scan of the  $^4S_{3/2}$  level.

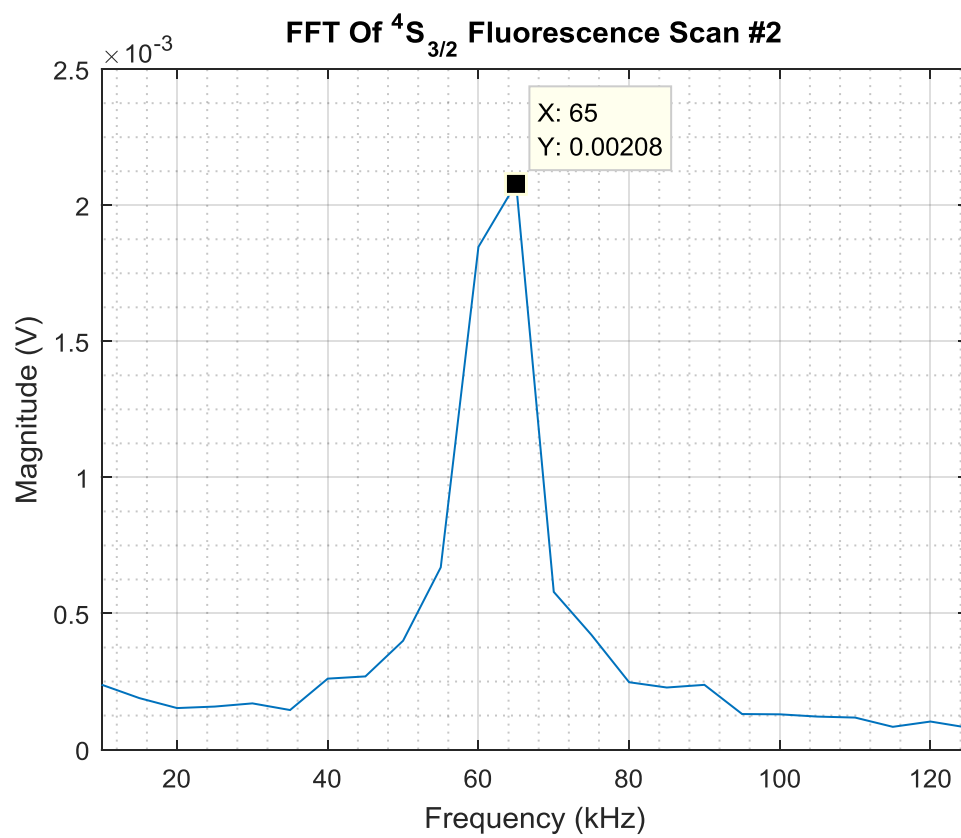


Figure C.3.14: FFT of transient scan of the  $^4S_{3/2}$  level.

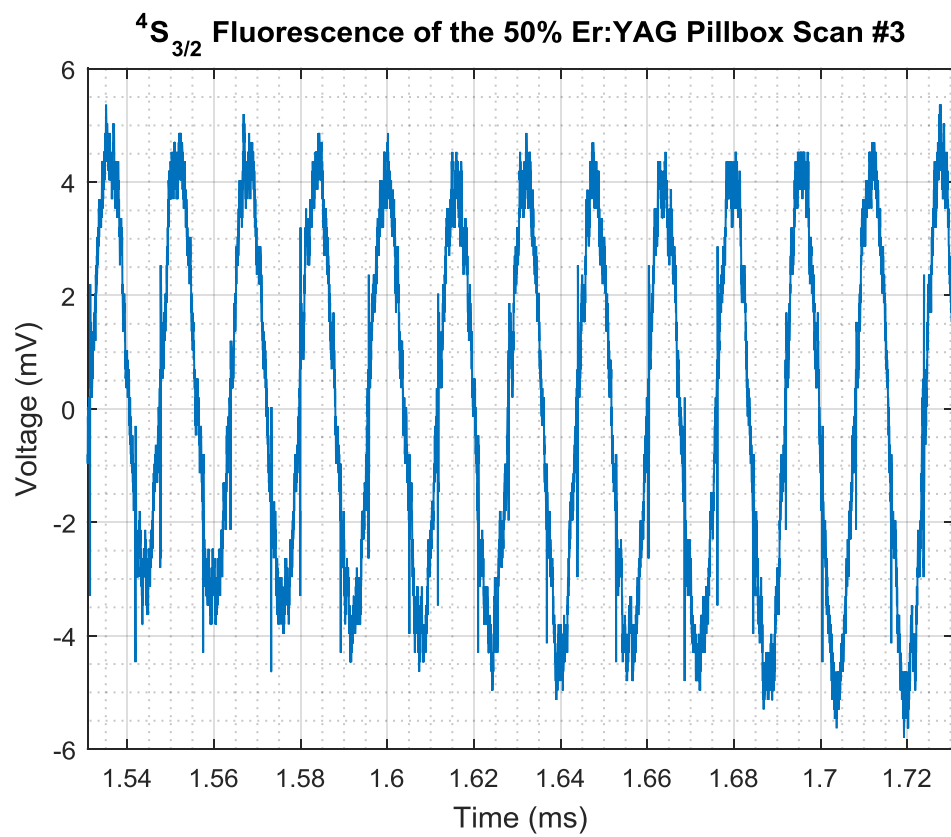


Figure C.3.15: Transient scan of the  $^4S_{3/2}$  level.

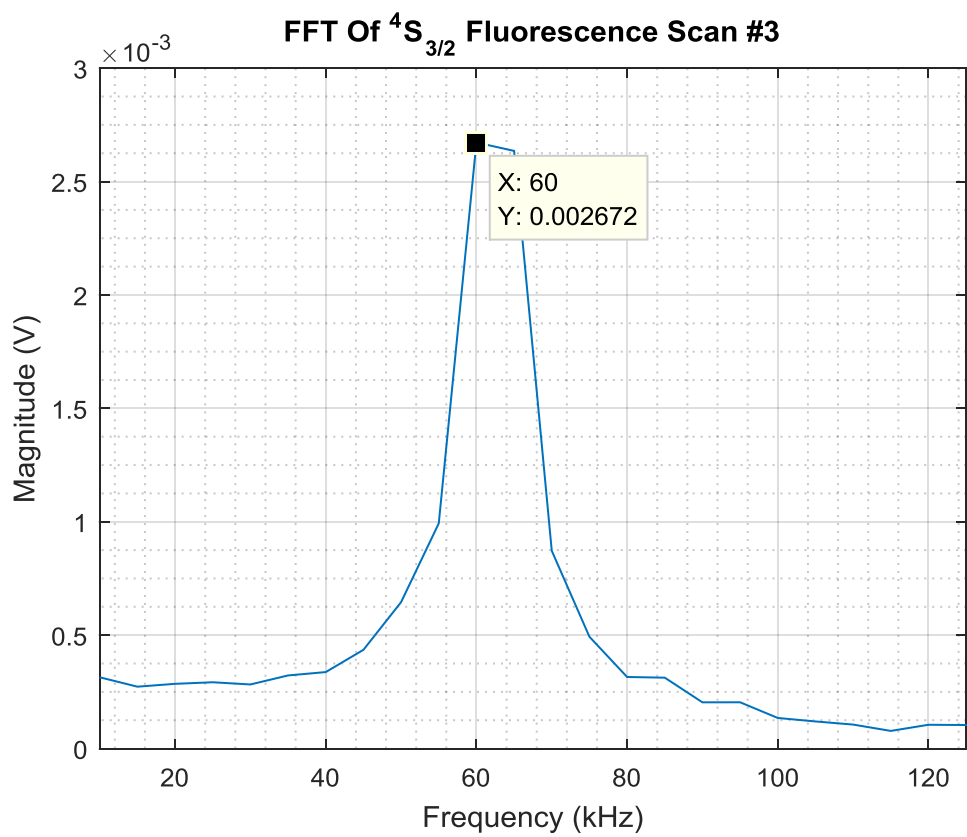


Figure C.3.16: FFT of transient scan of the  $^4S_{3/2}$  level.

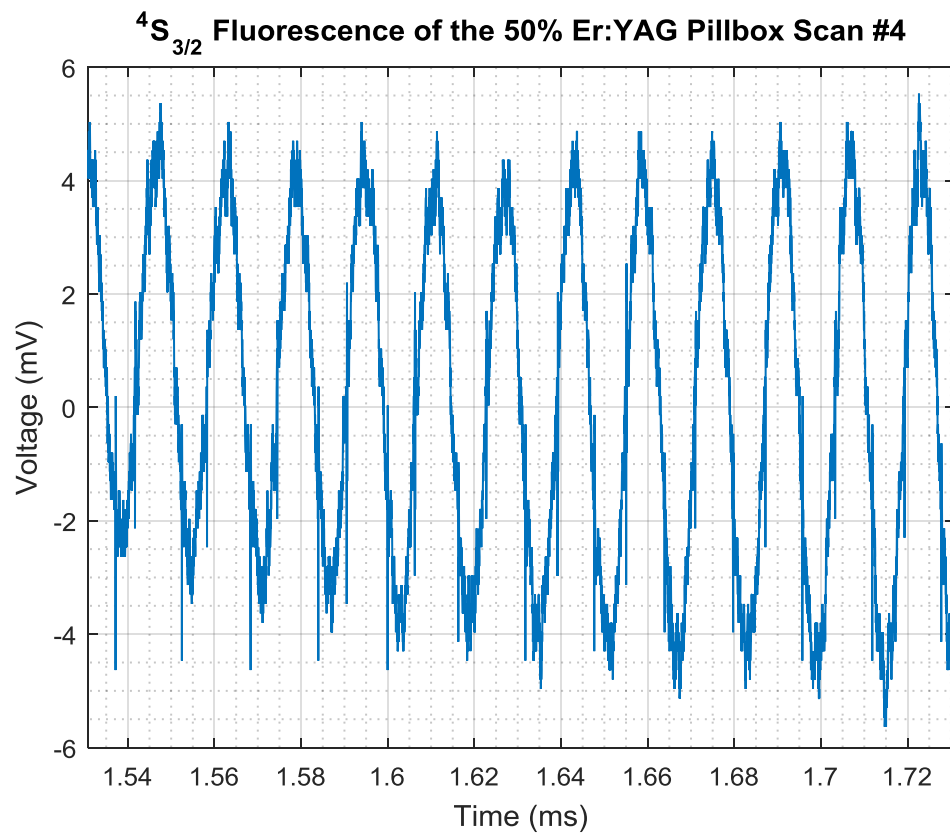


Figure C.3.17: Transient scan of the  $^4S_{3/2}$  level.

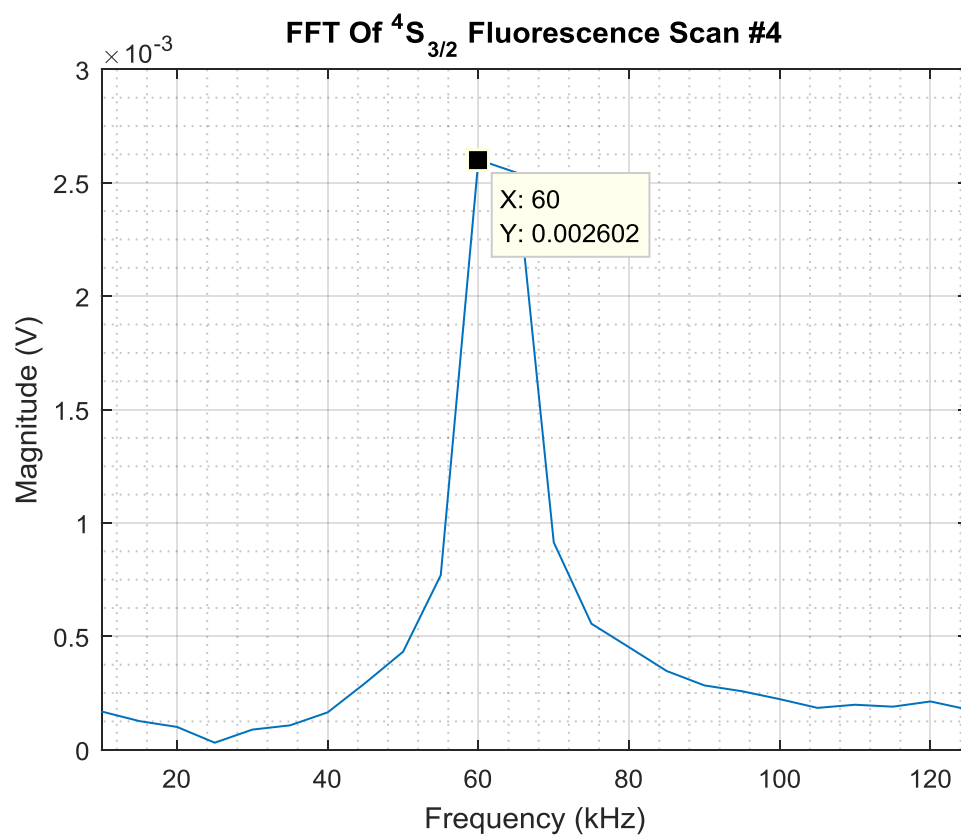


Figure C.3.18: FFT of transient scan of the  $^4S_{3/2}$  level.

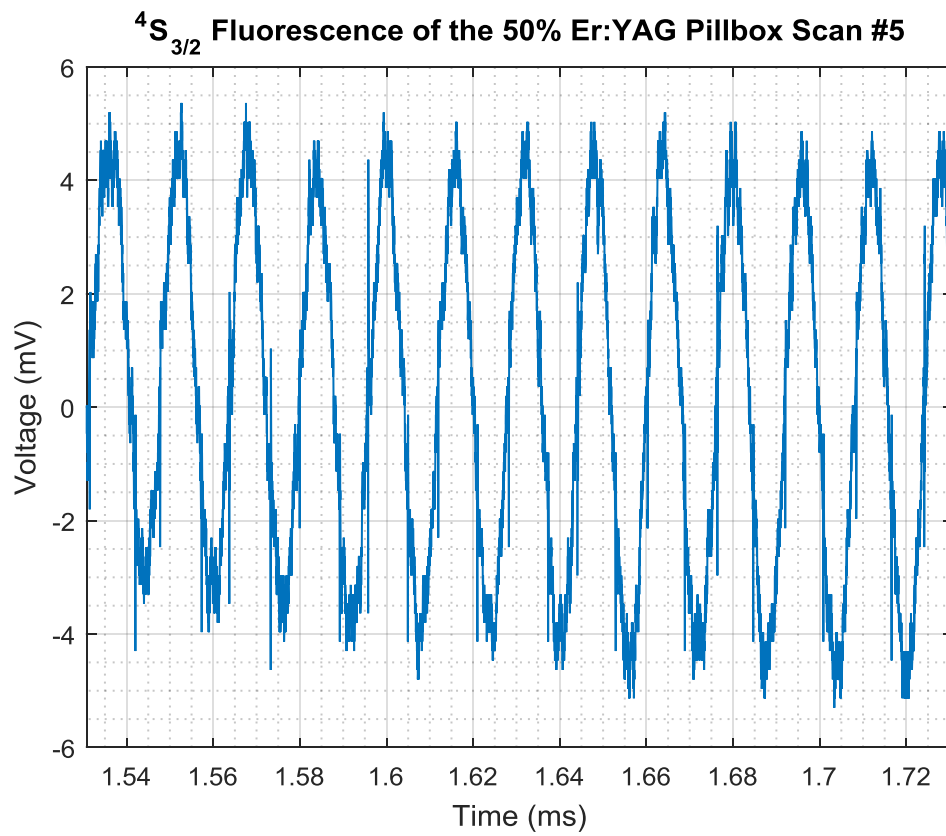


Figure C.3.19: Transient scan of the  $^4S_{3/2}$  level.

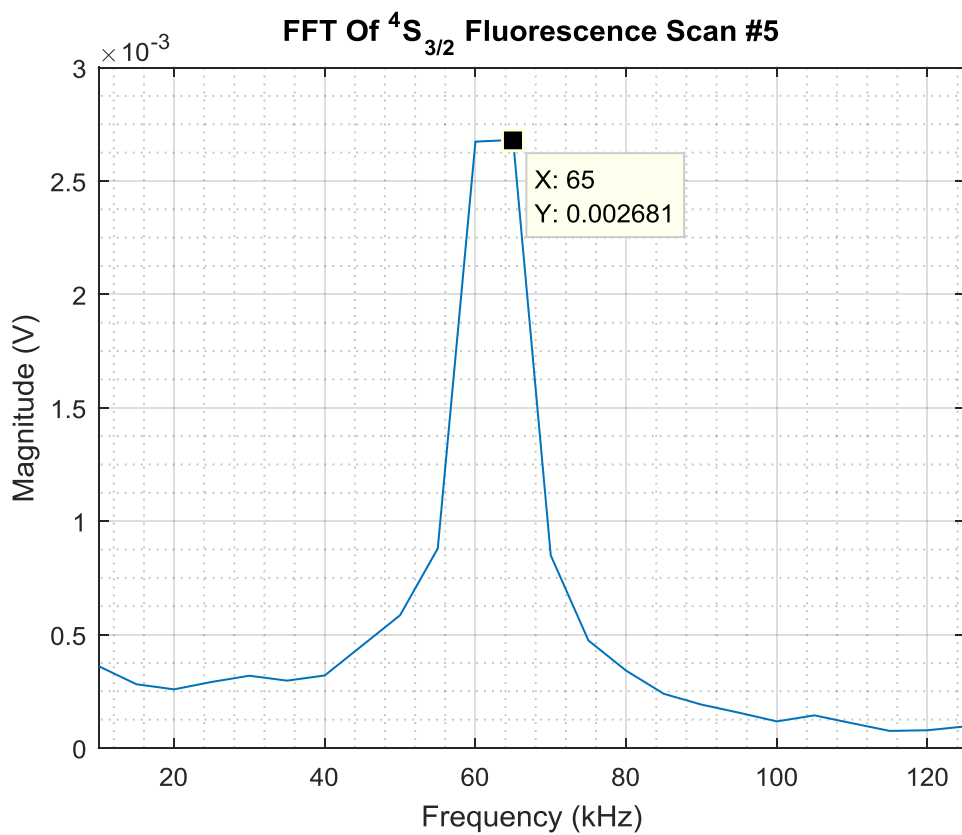


Figure C.3.20: FFT of transient scan of the  $^4S_{3/2}$  level.

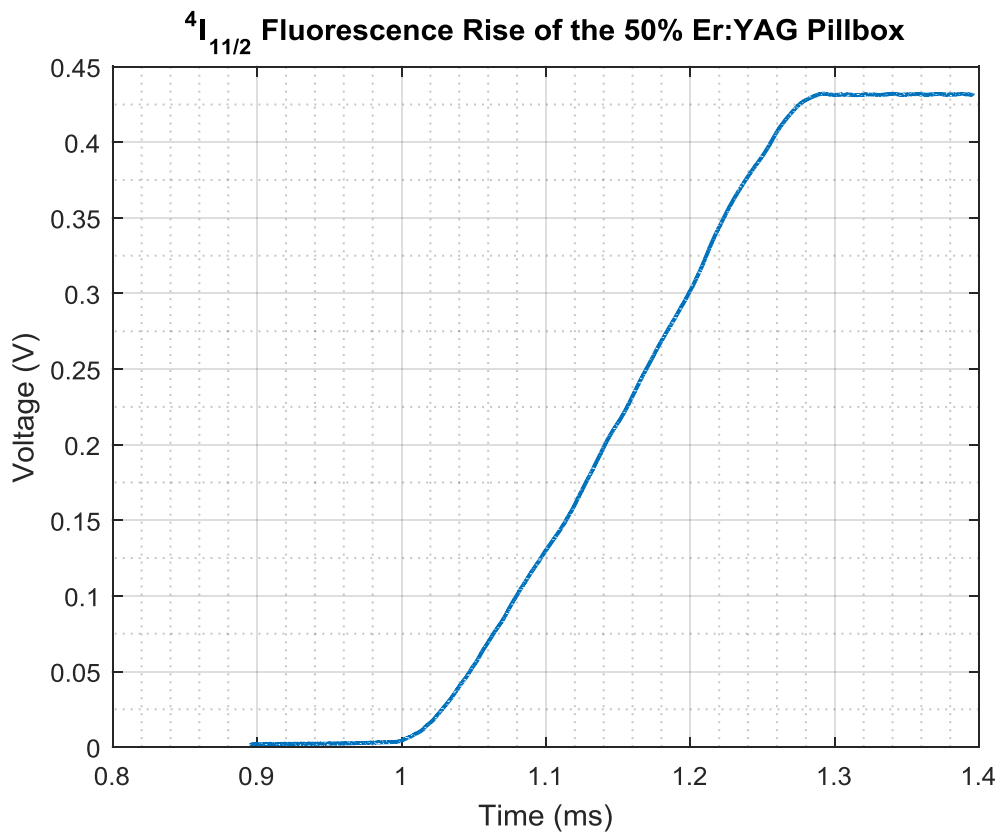


Figure C.3.21: Rise of the  $^4I_{11/2}$  level.

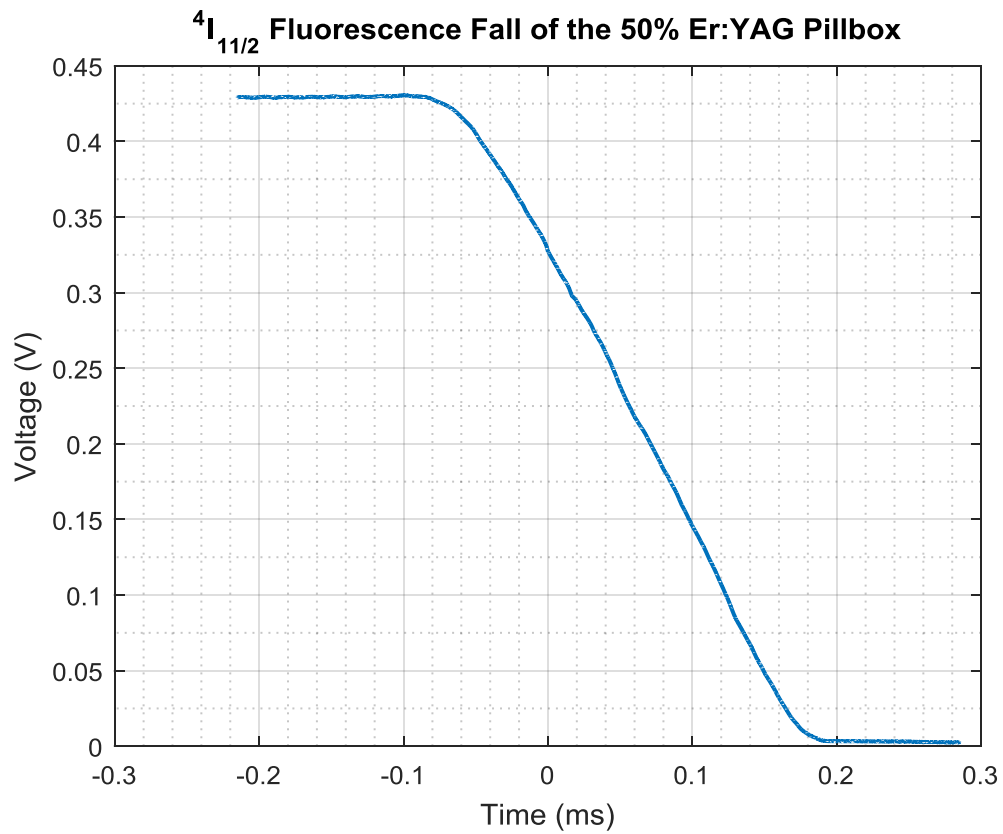


Figure C.3.22: Fall of the  $^4I_{11/2}$  level.

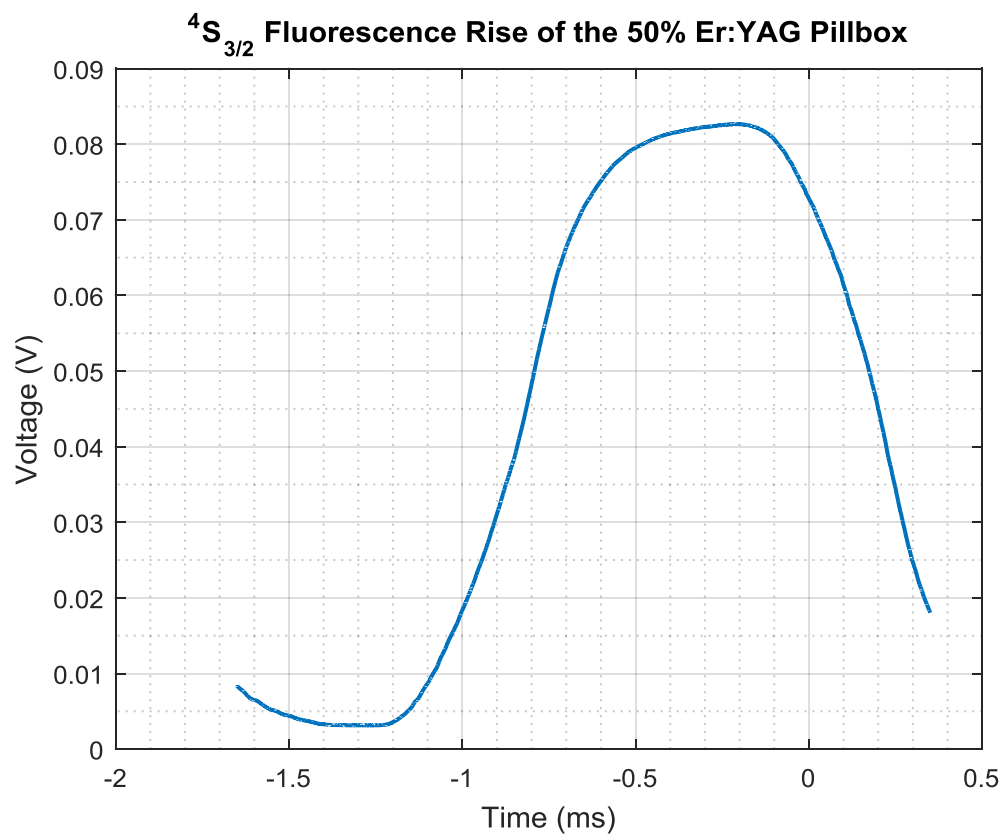


Figure C.3.23: Rise of the  $^4S_{3/2}$  level.

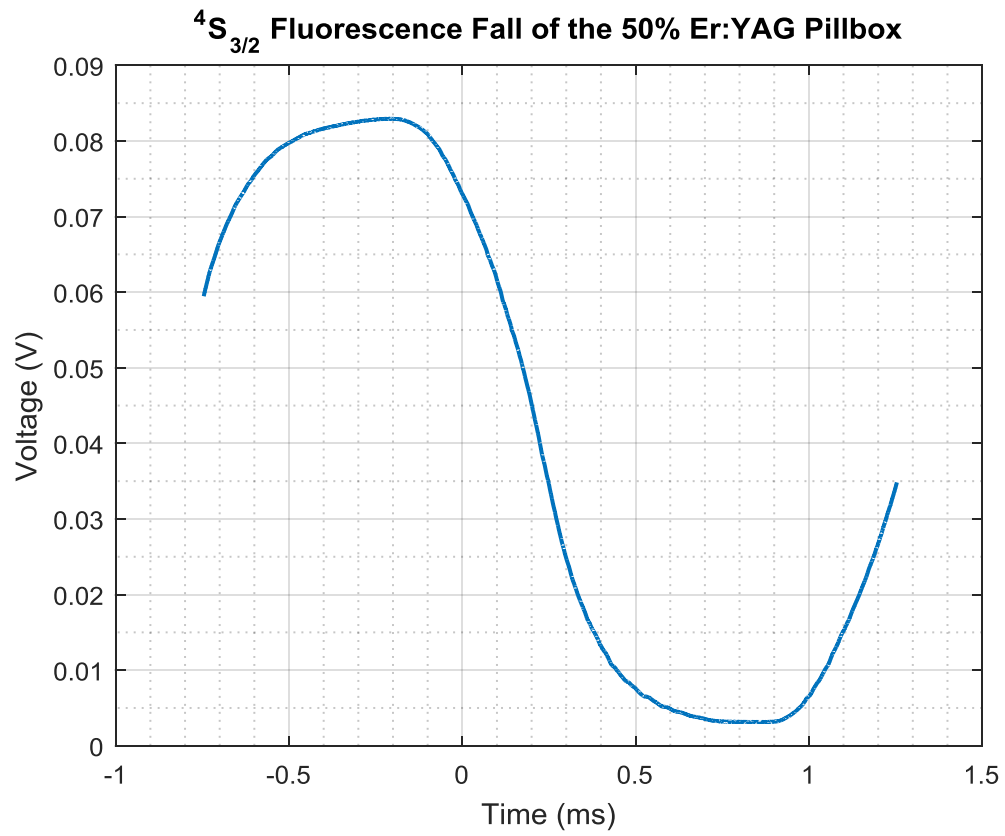


Figure C.3.24: Fall of the  $^4S_{3/2}$  level.

Transient Statistics ${}^4I_{11/2}$ Level Fluorescence Oscillation	
Number of Scans	5
Mean Value of Oscillation Frequency (KHz)	64.9987
Standard Deviation of Frequency (KHz)	8.1348 E-15
2 <sup>nd</sup> Harmonic of ${}^4I_{11/2}$ Level Fluorescence Oscillation	
Number of Scans	5
Mean Value of Oscillation Frequency (KHz)	124.9975
Standard Deviation of Frequency (KHz)	2.2360

Table C.3.1: Statistics of the transient scans of the  ${}^4I_{11/2}$  level.

Transient Statistics ${}^4S_{3/2}$ Level Fluorescence Oscillation	
Number of Scans	5
Mean Value of Oscillation Frequency (KHz)	64.9987
Standard Deviation of Frequency (KHz)	2.7386

Table C.3.2: Statistics of the transient scans of the  ${}^4S_{3/2}$  level.

${}^4I_{11/2}$ Level Fluorescence	
Number of Sweeps	1000
Rise Time ( $\mu\text{s}$ )	202.39
Fall Time ( $\mu\text{s}$ )	187.35

Table C.3.3: Rise and Fall statistics of the transient scans of the  ${}^4I_{11/2}$  level.

${}^4S_{3/2}$ Level Fluorescence	
Number of Sweeps	1000
Rise Time ( $\mu\text{s}$ )	456.46
Fall Time ( $\mu\text{s}$ )	440.72

Table C.3.4: Rise and Fall statistics of the transient scans of the  ${}^4S_{3/2}$  level.

## C.4 808nm CW Pumped 50% Er:YAG Pillbox with No 3μm Laser

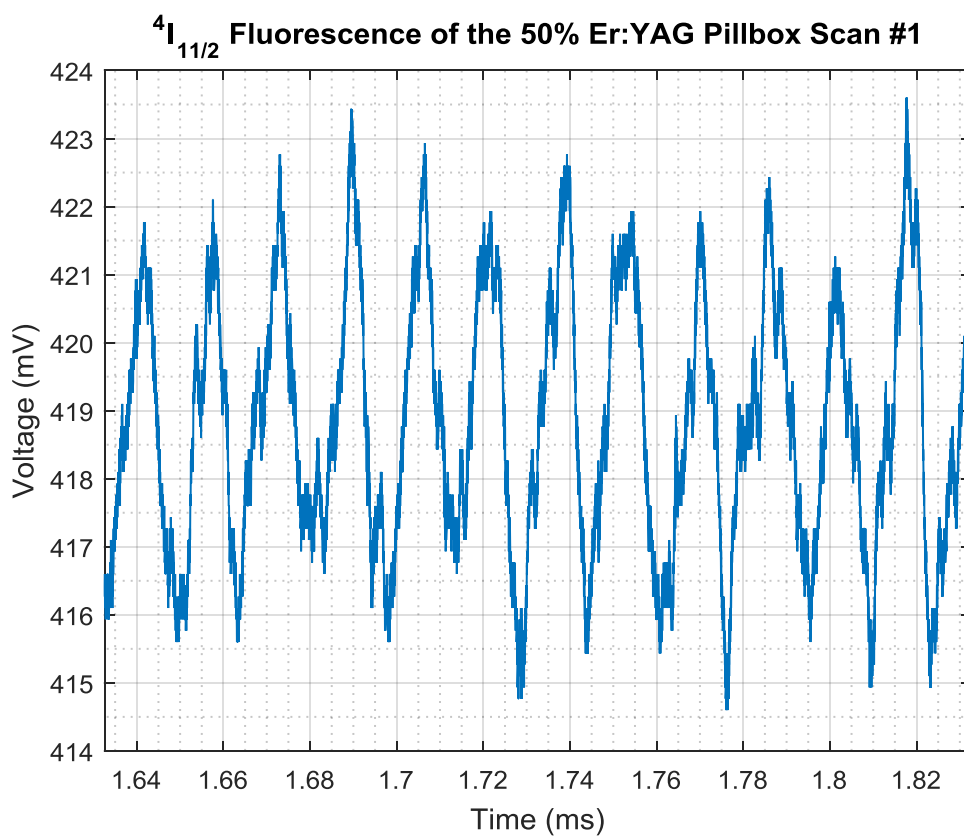


Figure C.4.1: Transient scan of the  $^4I_{11/2}$  level.

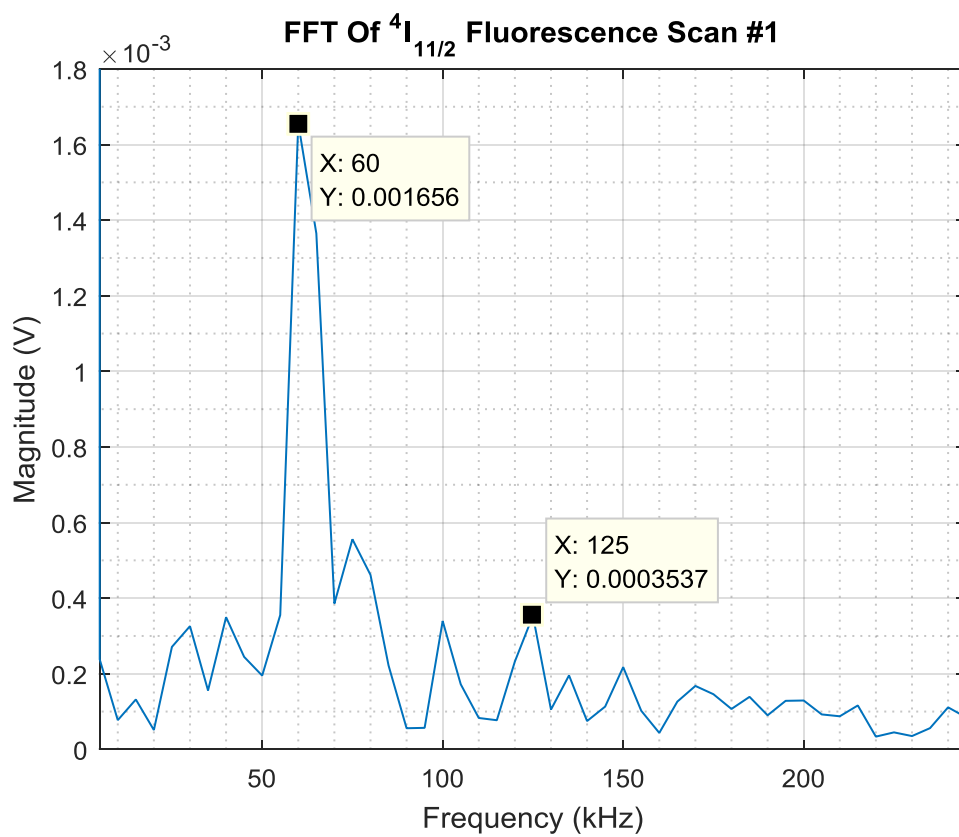


Figure C.4.2: FFT of transient scan of the  $^4I_{11/2}$  level.

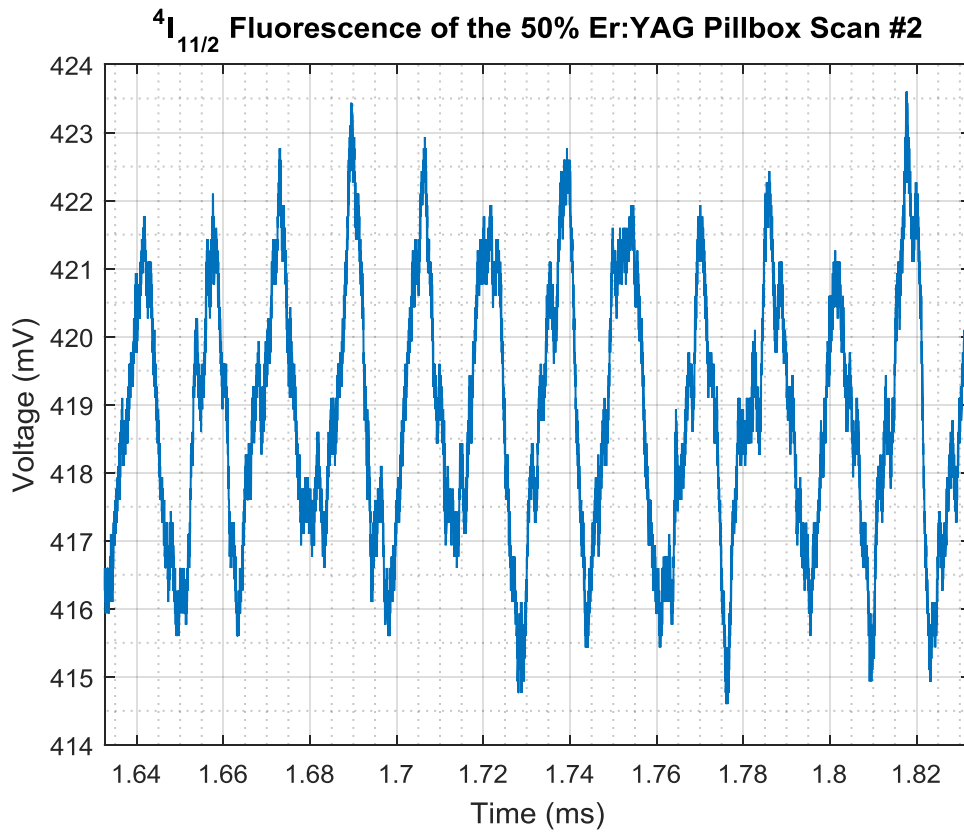


Figure C.4.3: Transient scan of the  $^4I_{11/2}$  level.

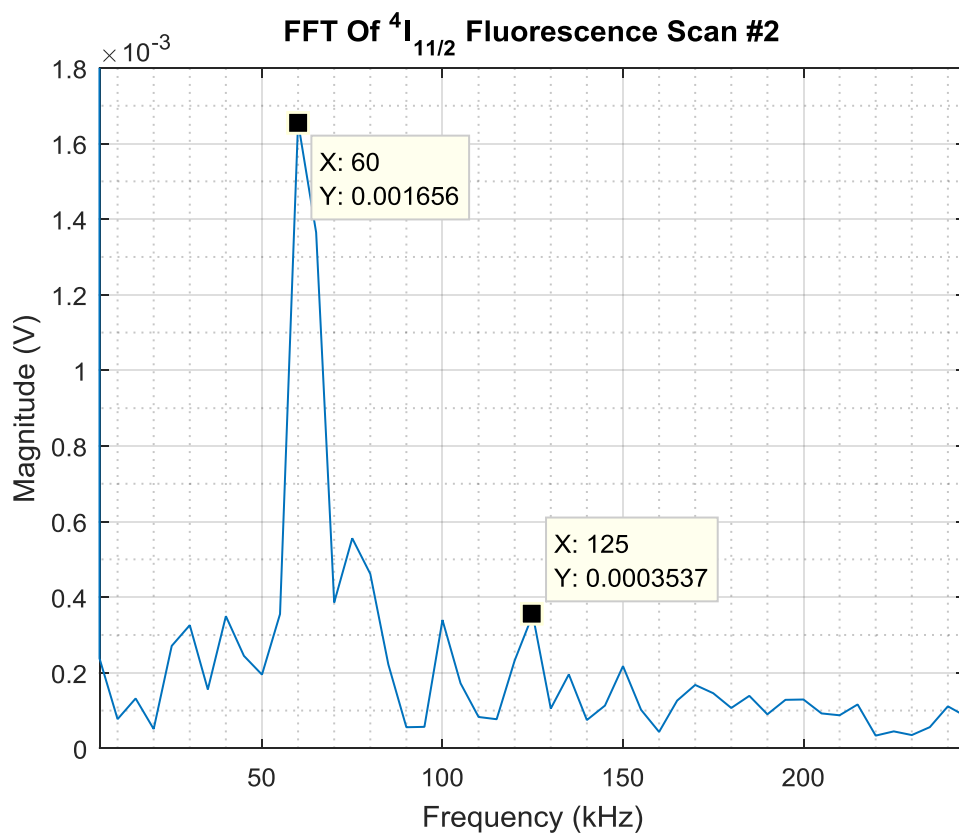


Figure C.4.4: FFT of transient scan of the  ${}^4I_{11/2}$  level.

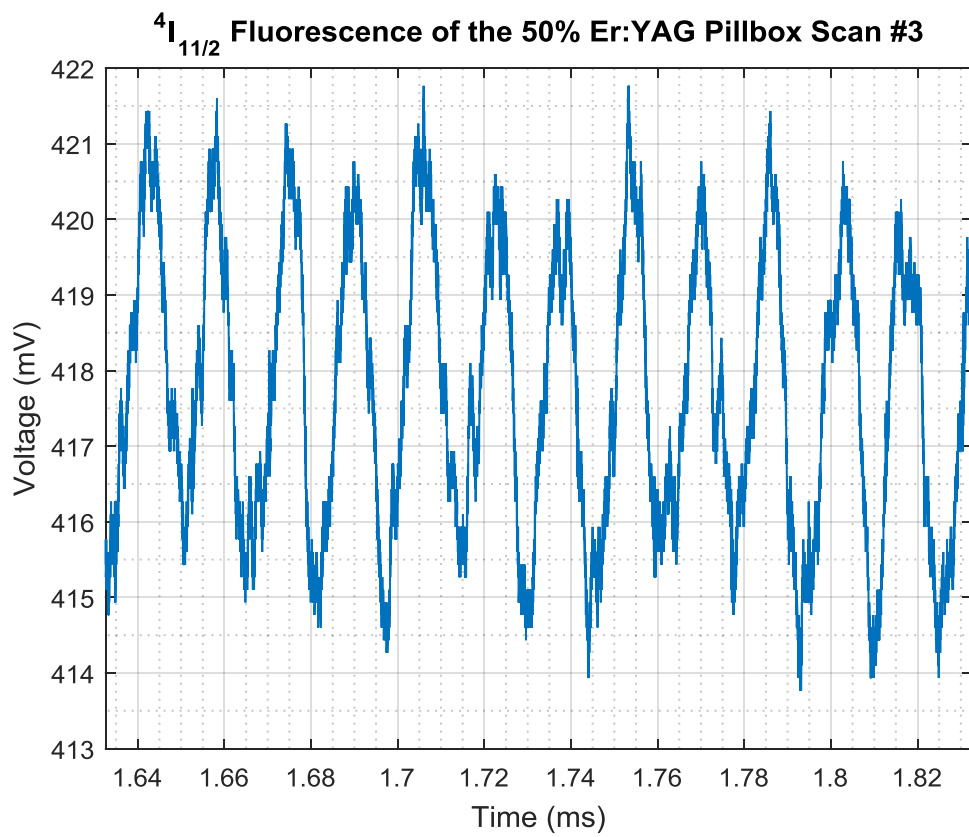


Figure C.4.5: Transient scan of the  $^4I_{11/2}$  level.

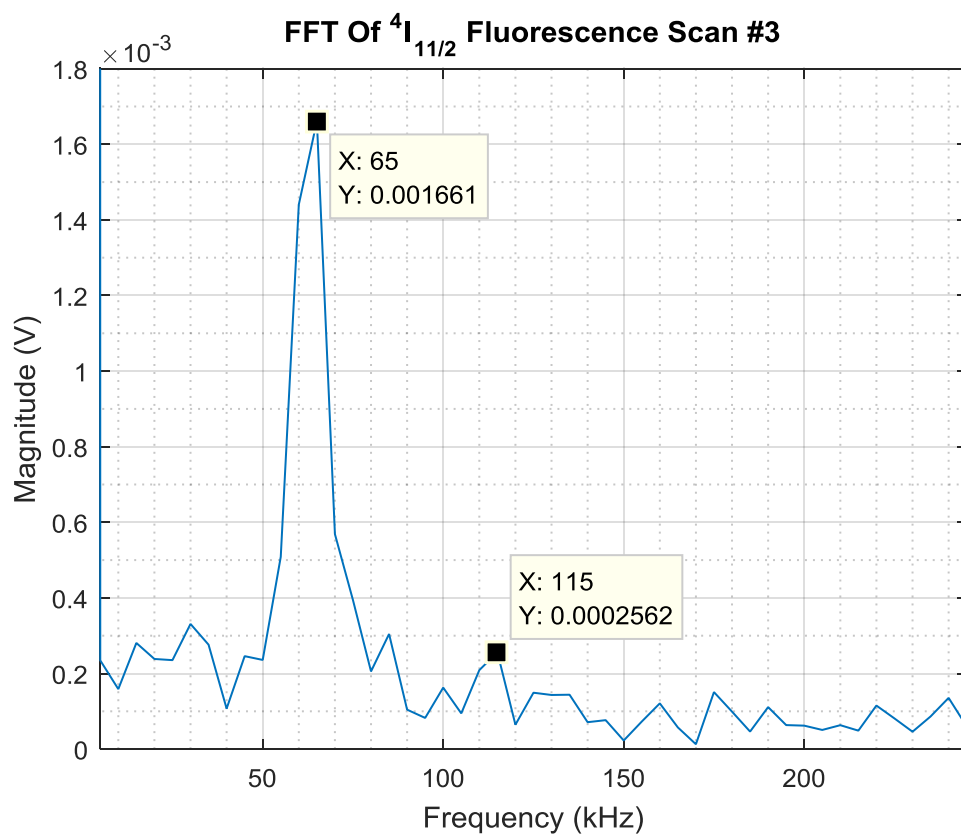


Figure C.4.6: FFT of transient scan of the  ${}^4I_{11/2}$  level.

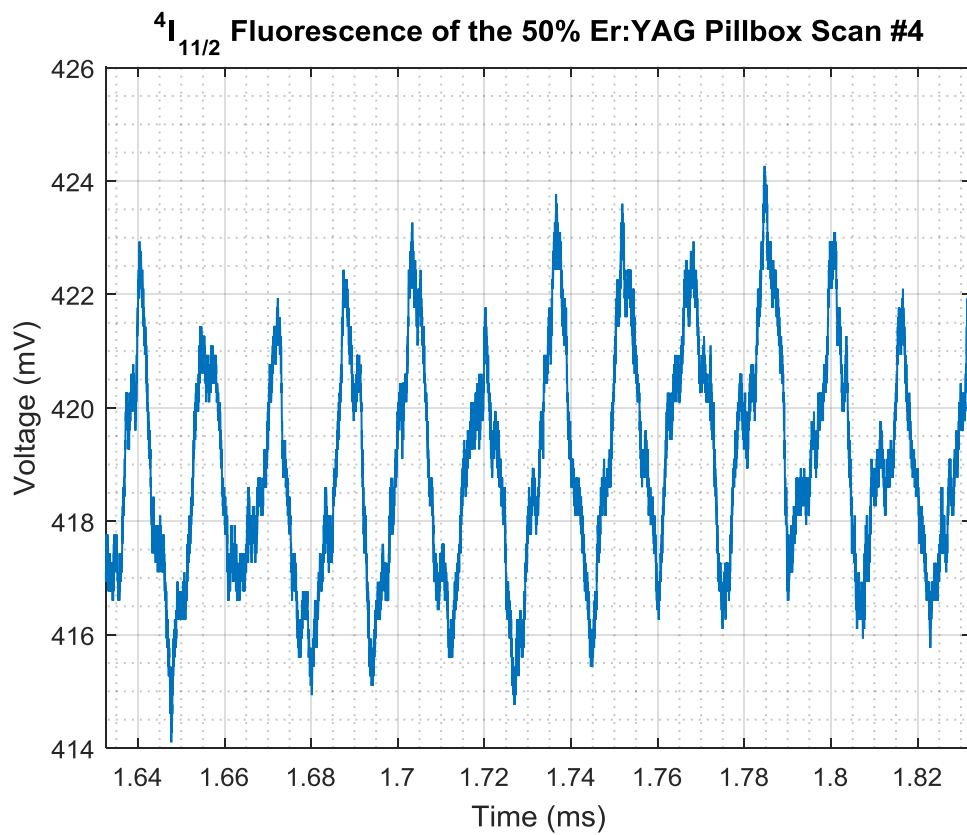


Figure C.4.7: Transient scan of the  $^4I_{11/2}$  level.

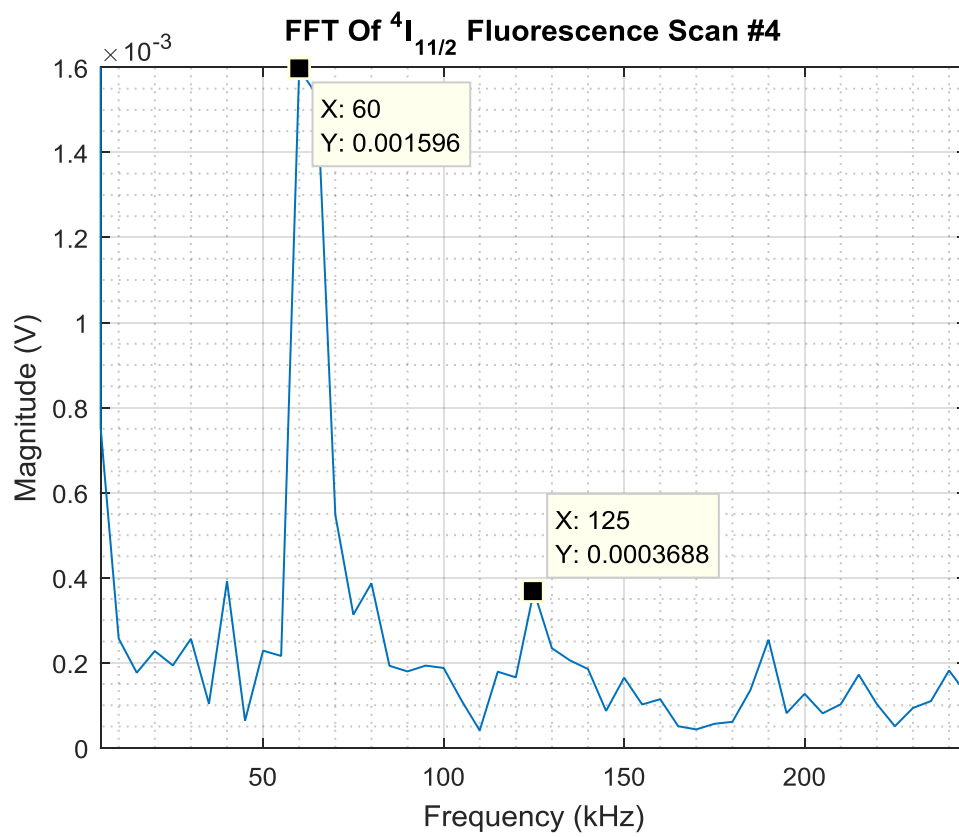


Figure C.4.8: FFT of transient scan of the  ${}^4I_{11/2}$  level.

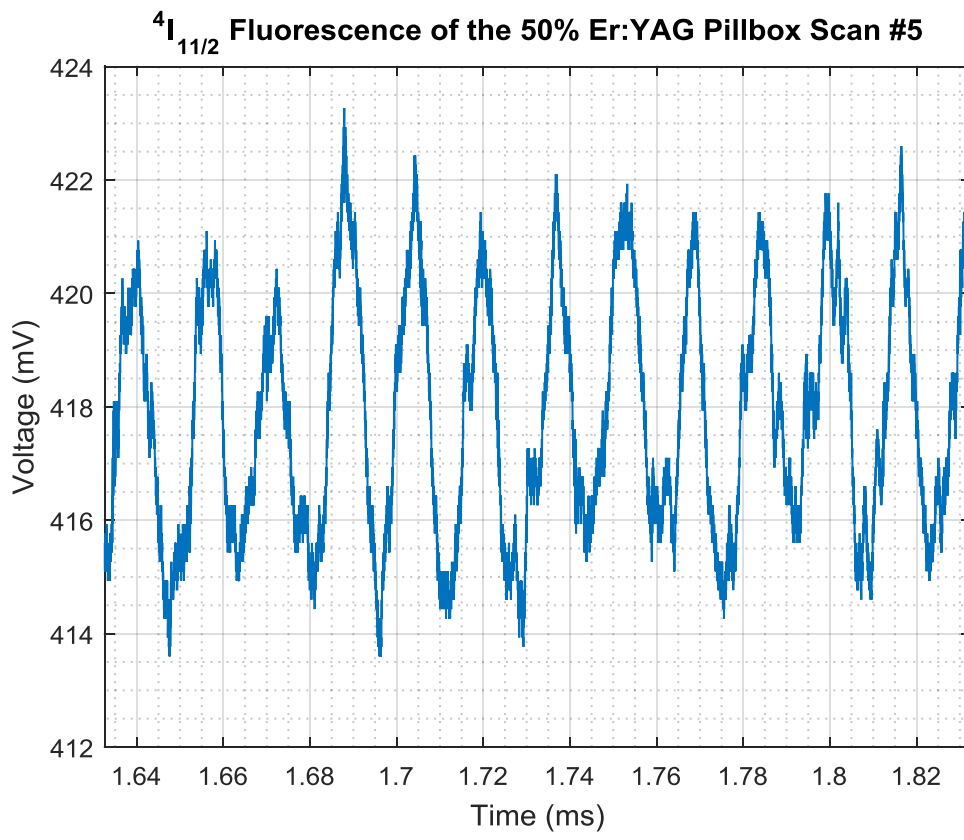


Figure C.4.9: Transient scan of the  $^4I_{11/2}$  level.

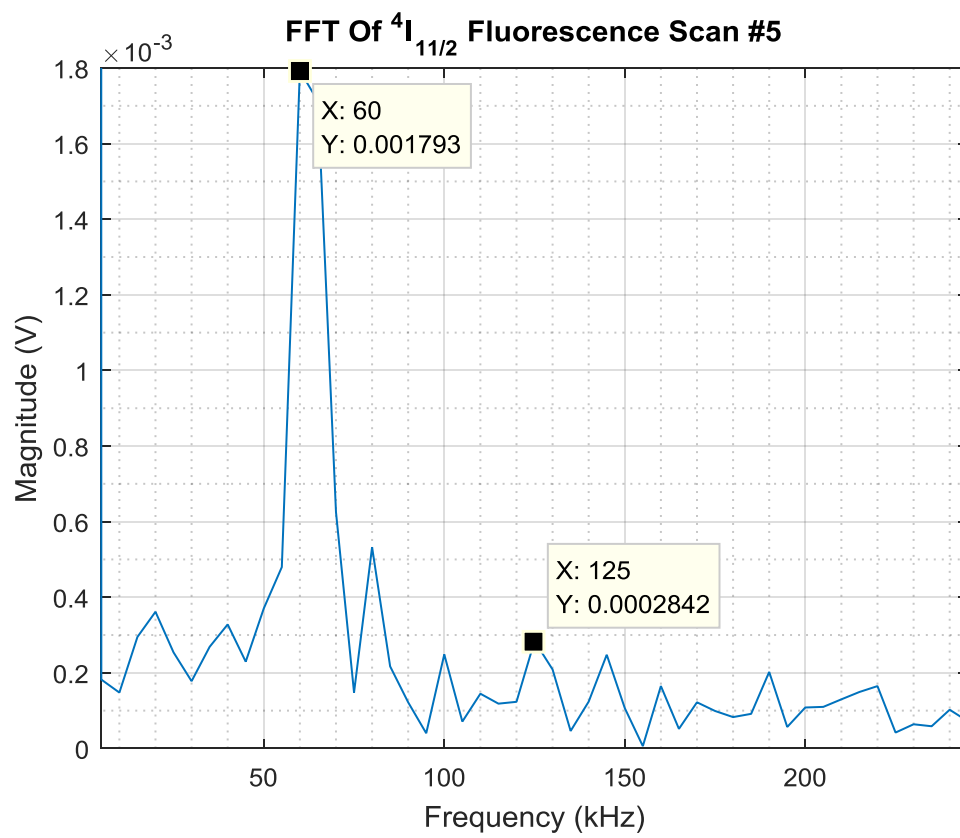


Figure C.4.10: FFT of transient scan of the  $^4I_{11/2}$  level.

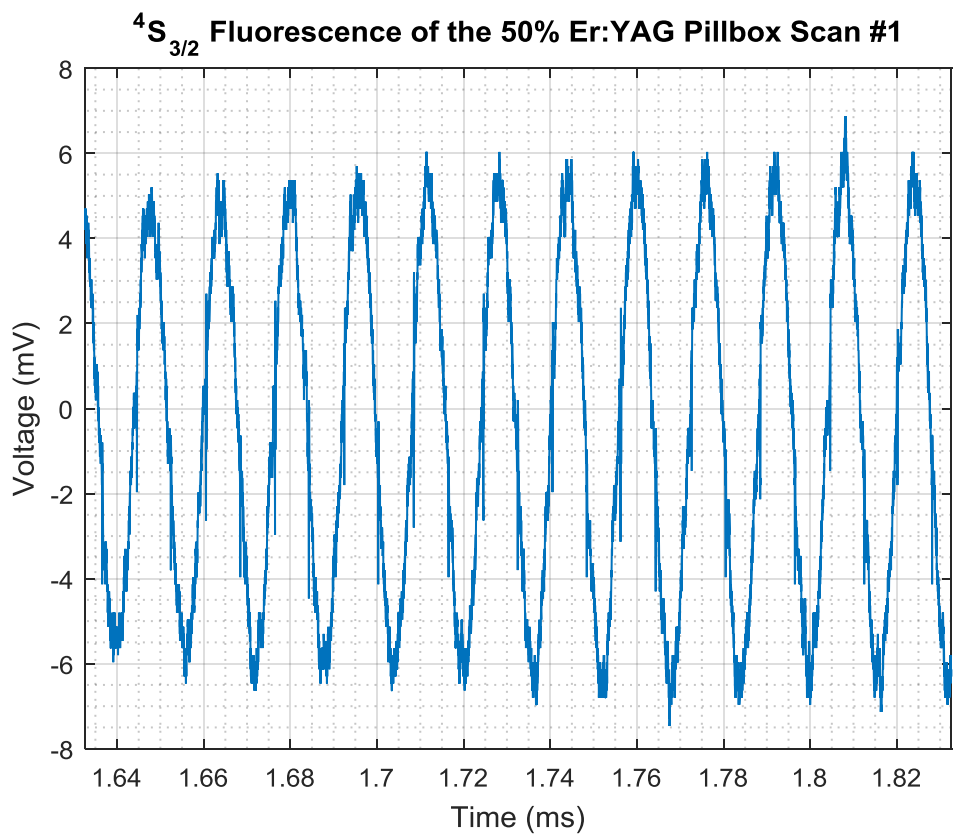


Figure C.4.11: Transient scan of the  $^4S_{3/2}$  level.

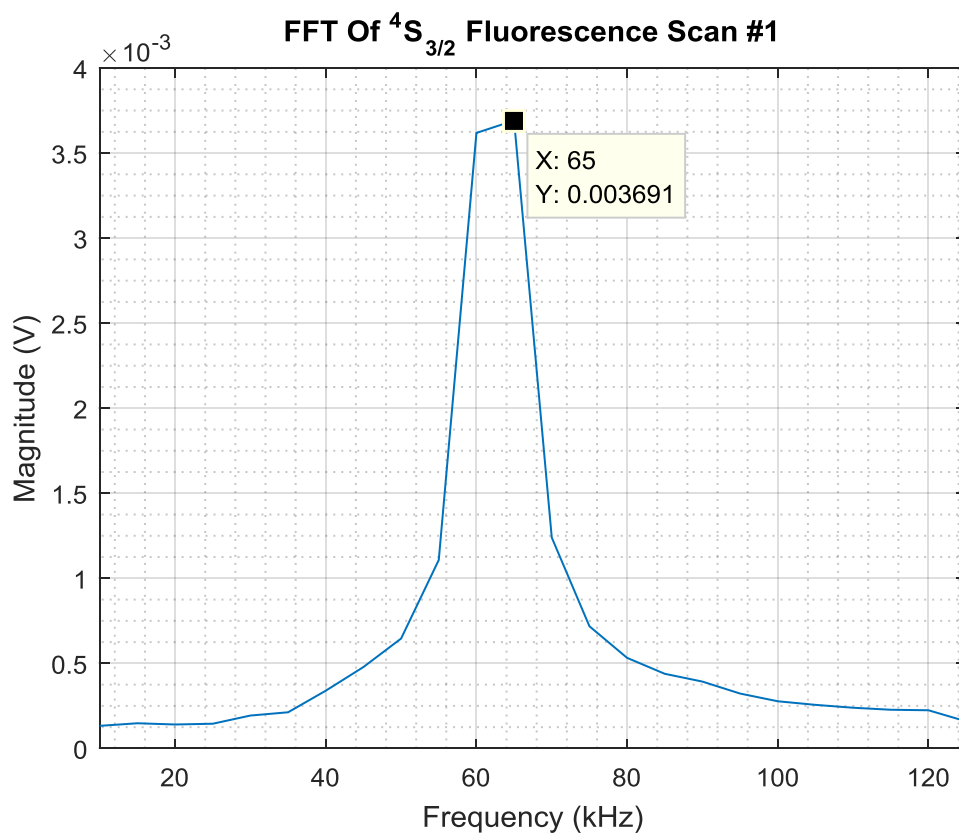


Figure C.4.12: FFT of transient scan of the  $^4S_{3/2}$  level.

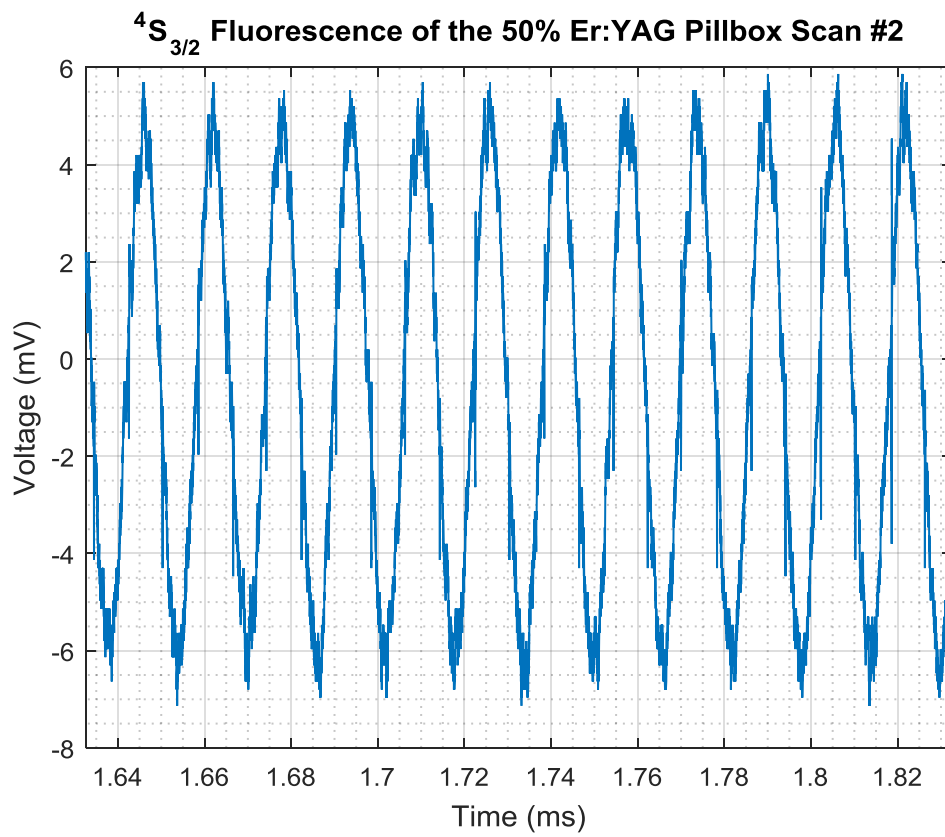


Figure C.4.13: Transient scan of the  $^4S_{3/2}$  level.

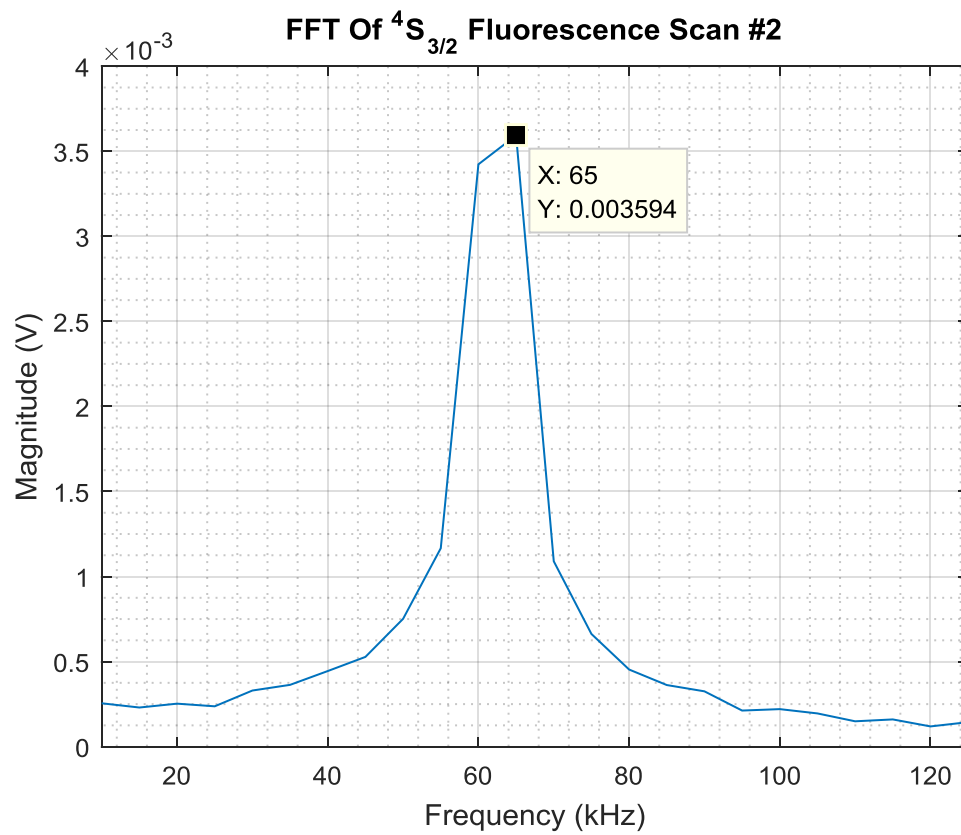


Figure C.4.14: FFT of transient scan of the  $^4S_{3/2}$  level.

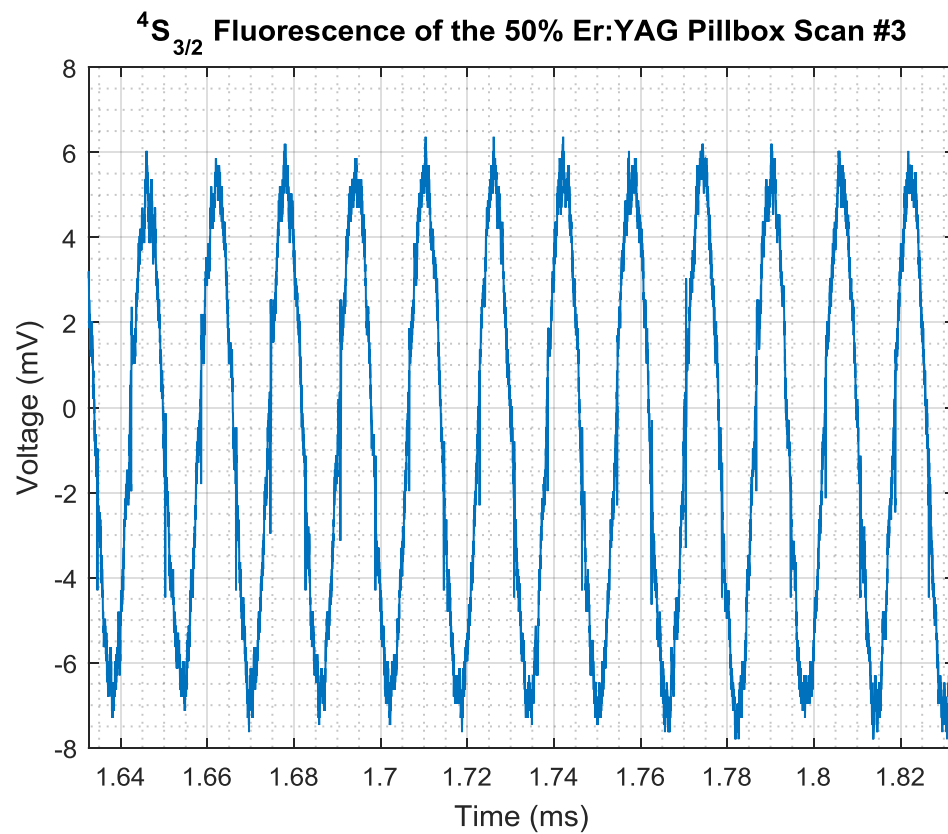


Figure C.4.15: Transient scan of the  $^4S_{3/2}$  level.

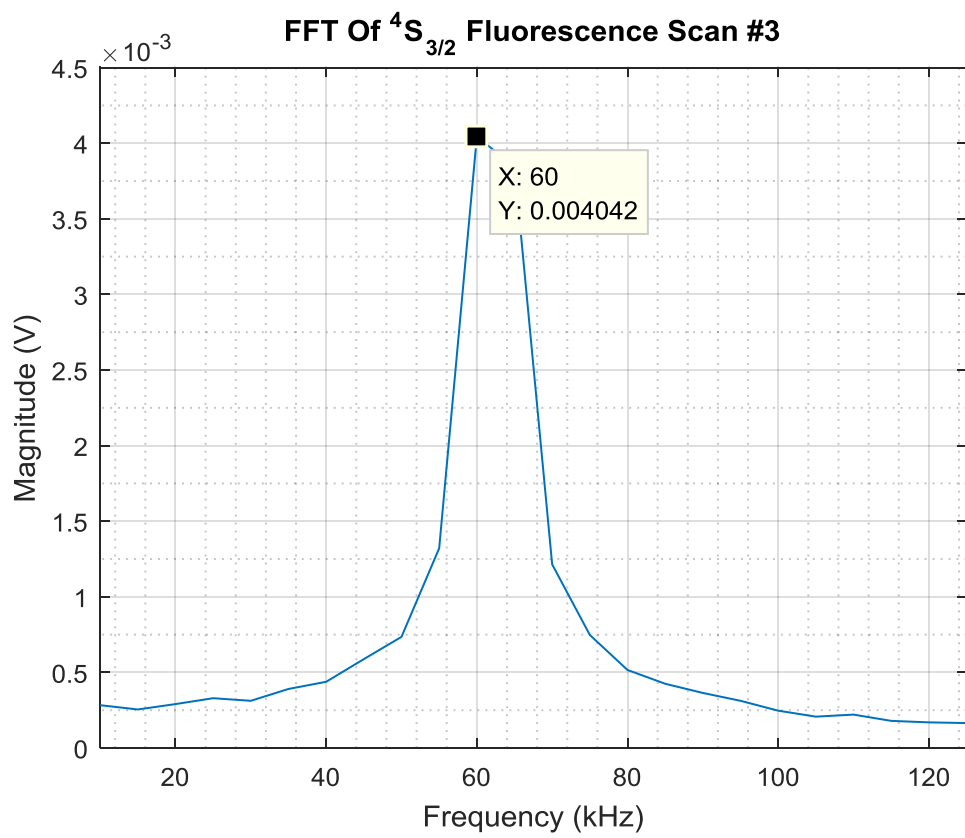


Figure C.4.16: FFT of transient scan of the  $^4S_{3/2}$  level.

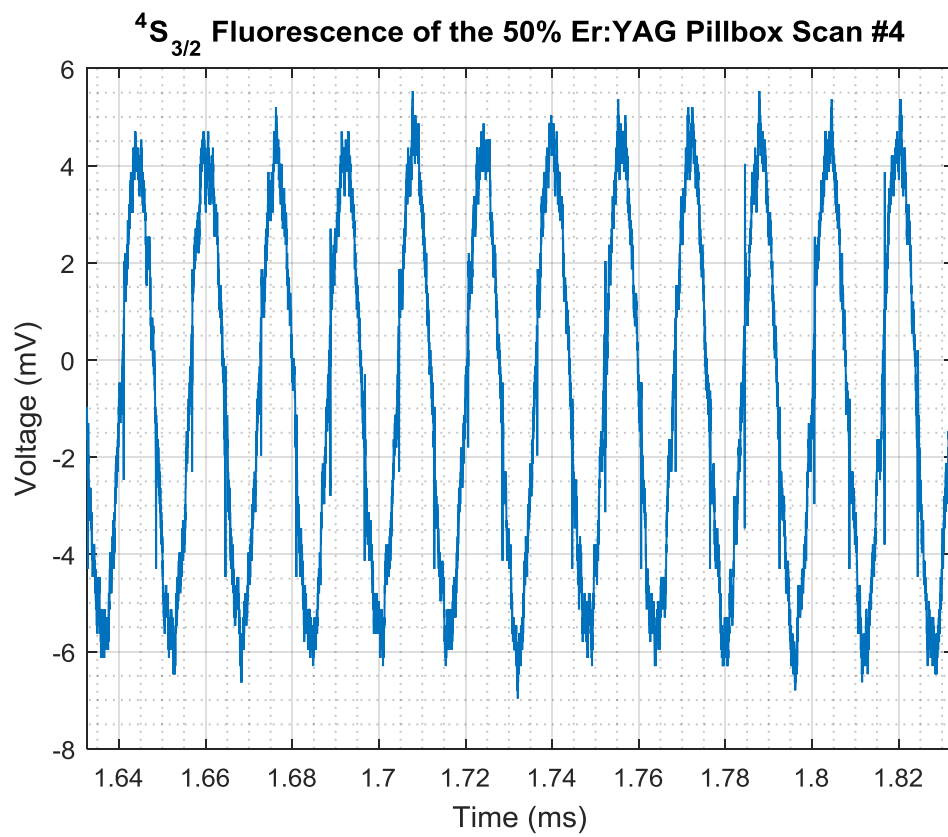


Figure C.4.17: Transient scan of the  $^4S_{3/2}$  level.

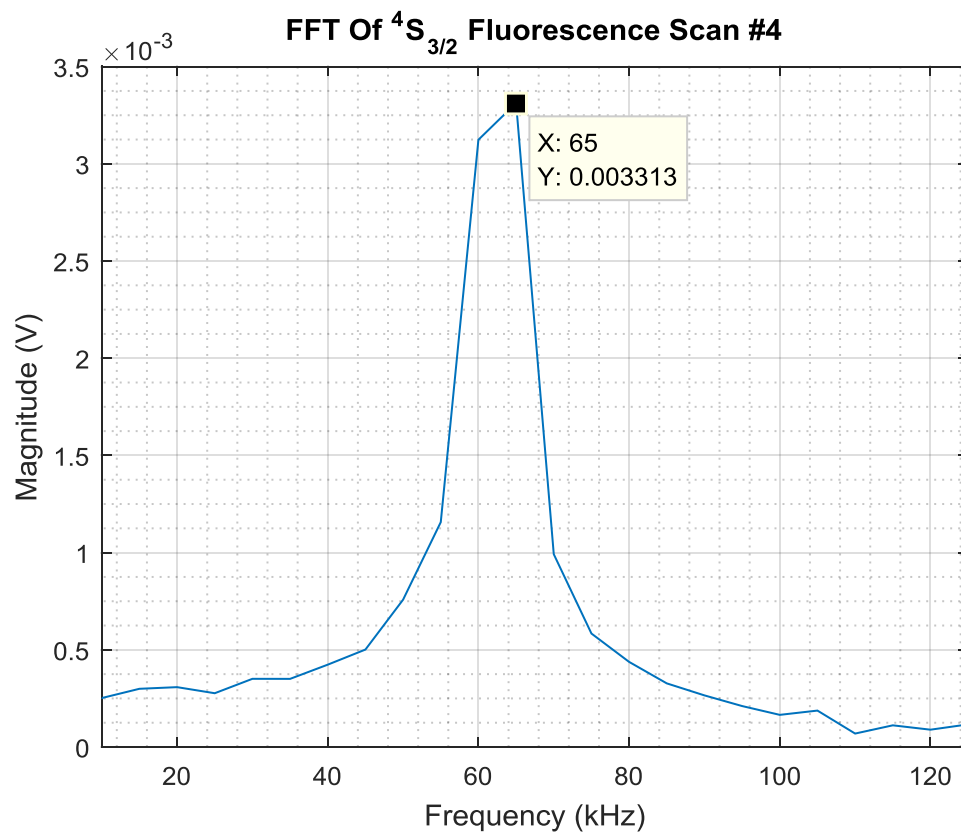


Figure C.4.18: FFT of transient scan of the  $^4S_{3/2}$  level.

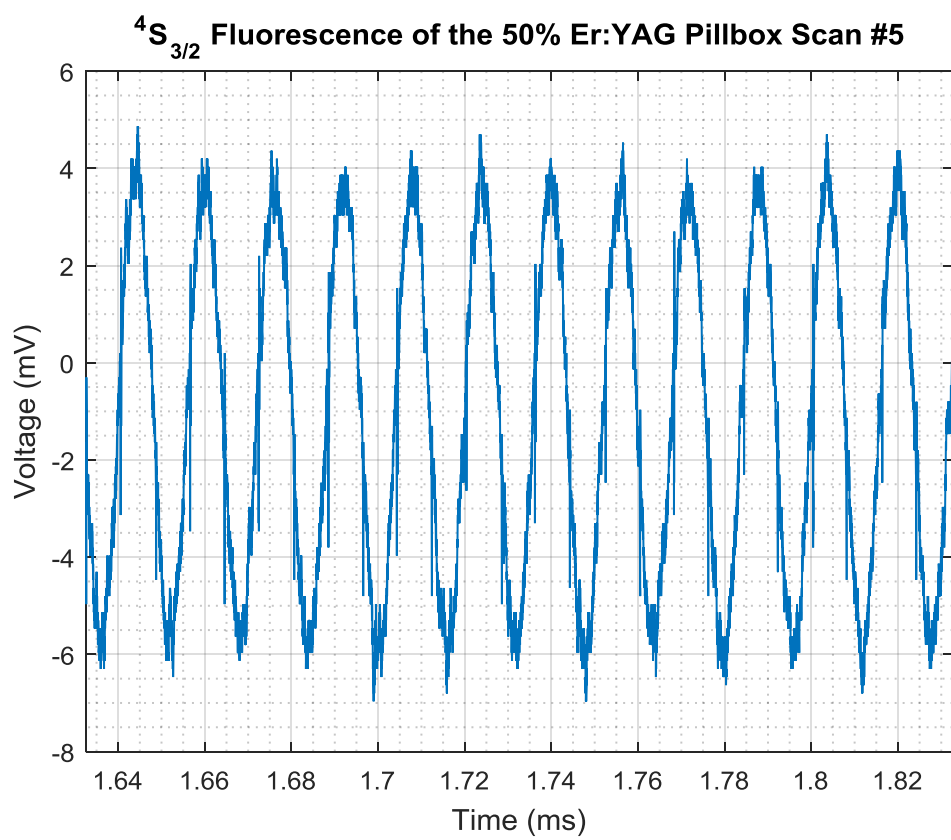


Figure C.4.19: Transient scan of the  $^4S_{3/2}$  level.

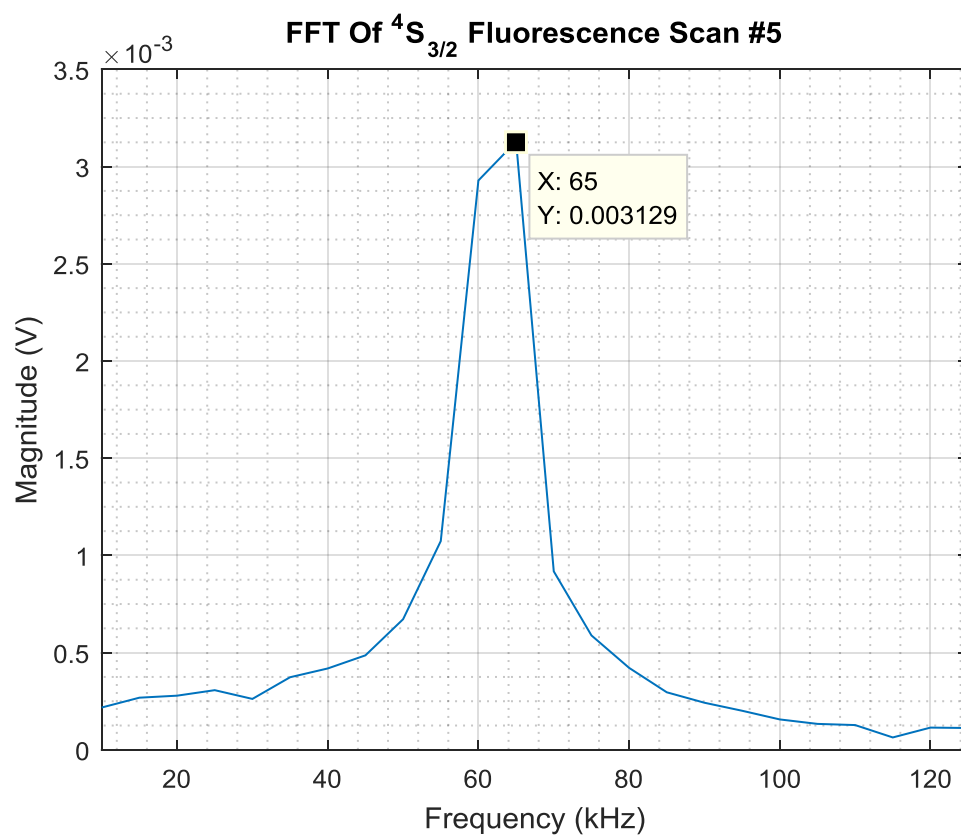


Figure C.4.20: FFT of transient scan of the  $^4S_{3/2}$  level.

Transient Statistics ${}^4I_{11/2}$ Level Fluorescence Oscillation	
Number of Scans	5
Mean Value of Oscillation Frequency (KHz)	60.9988
Standard Deviation of Frequency (KHz)	2.2360
2 <sup>nd</sup> Harmonic of ${}^4I_{11/2}$ Level Fluorescence Oscillation	
Number of Scans	5
Mean Value of Oscillation Frequency (KHz)	124.9975
Standard Deviation of Frequency (KHz)	4.4270

Table C.4.1: Statistics of the transient scans of the  ${}^4I_{11/2}$  level.

Transient Statistics ${}^4S_{3/2}$ Level Fluorescence Oscillation	
Number of Scans	5
Mean Value of Oscillation Frequency (KHz)	64.9987
Standard Deviation of Frequency (KHz)	2.2360

Table C.4.2: Statistics of the transient scans of the  ${}^4S_{3/2}$  level.

## C.5 808nm Pulsed Pumped 50% Er:YAG Wave Guide with No 3 $\mu$ m Laser

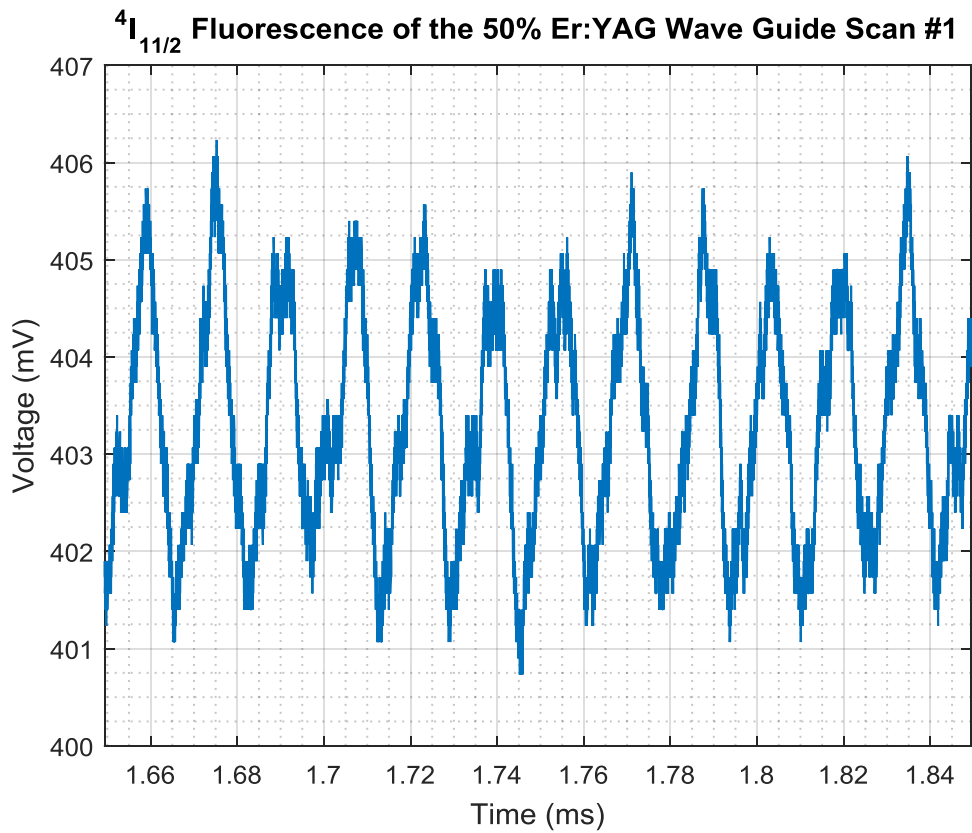


Figure C.5.1: Transient scan of the <sup>4</sup>I<sub>11/2</sub> level.

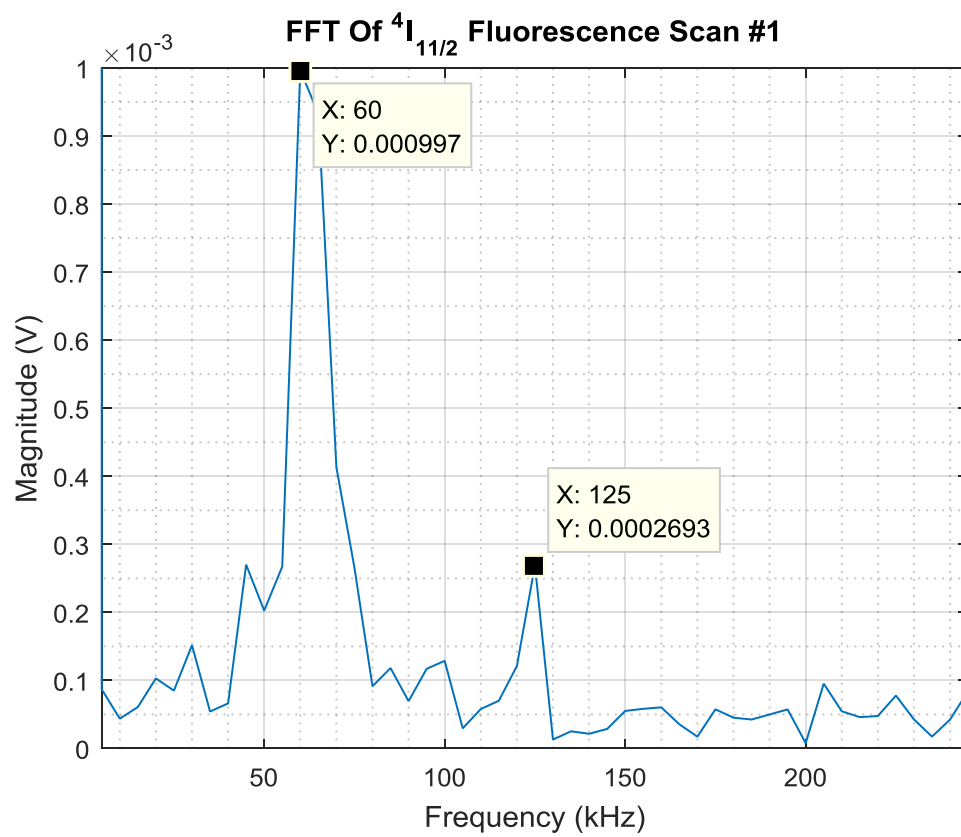


Figure C.5.2: FFT of transient scan of the  ${}^4I_{11/2}$  level.

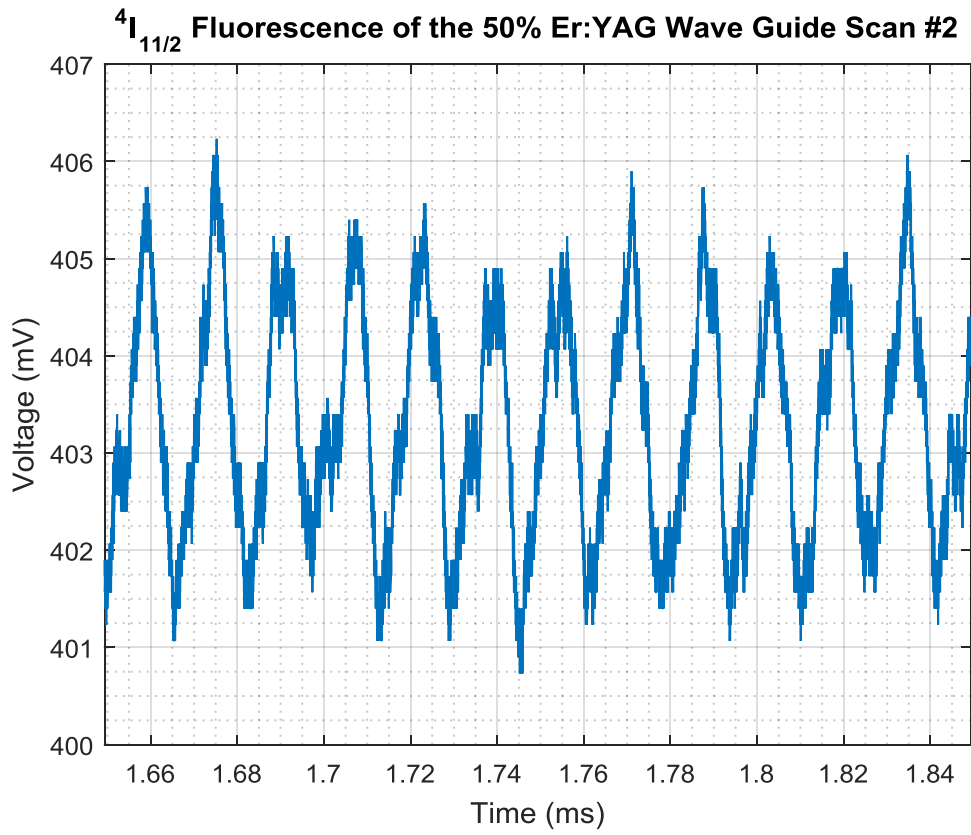


Figure C.5.3: Transient scan of the  $^4I_{11/2}$  level.

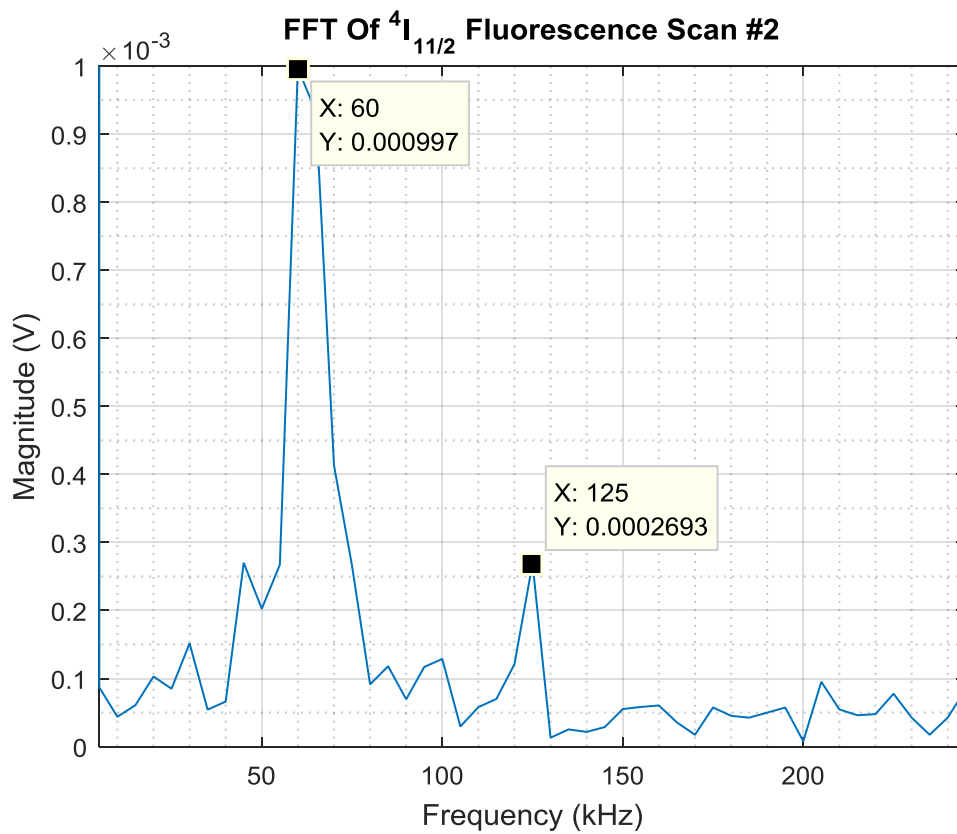


Figure C.5.4: FFT of transient scan of the  ${}^4I_{11/2}$  level.

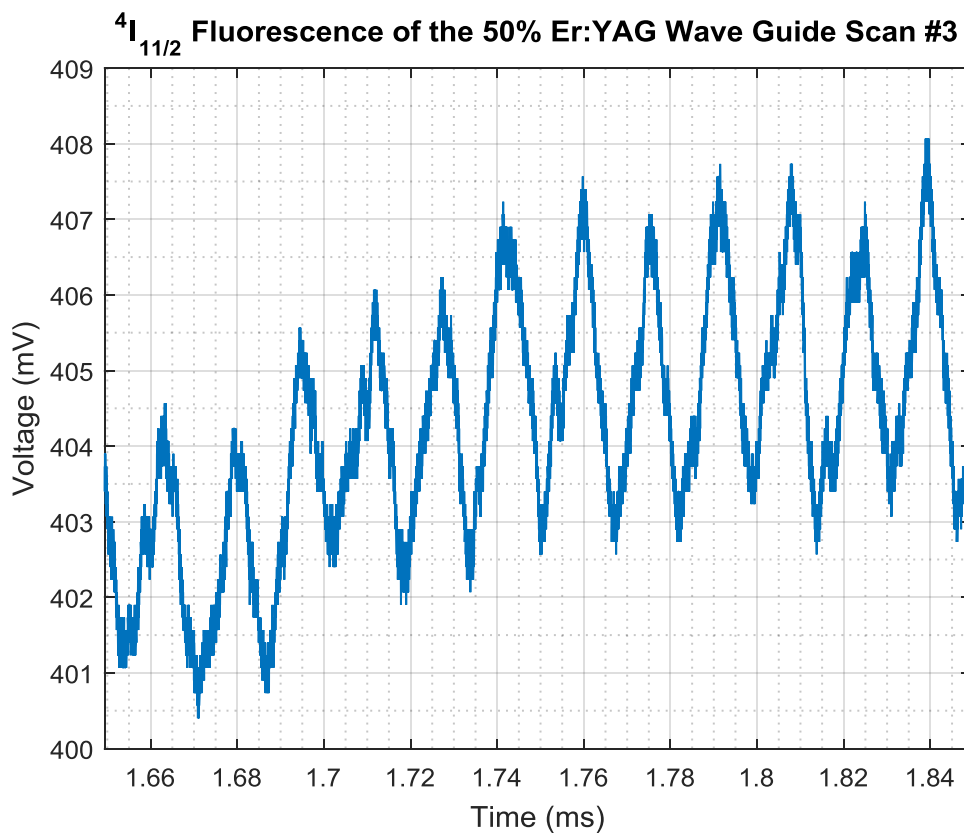


Figure C.5.5: Transient scan of the  $^4I_{11/2}$  level.

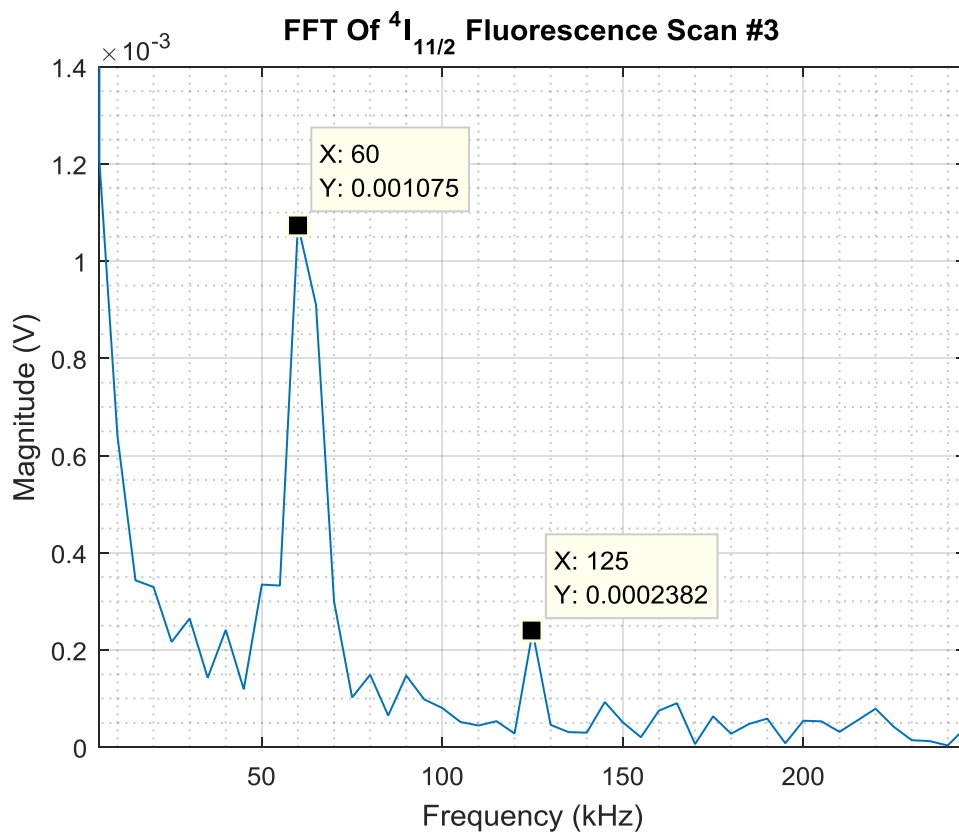


Figure C.5.6: FFT of transient scan of the  ${}^4I_{11/2}$  level.

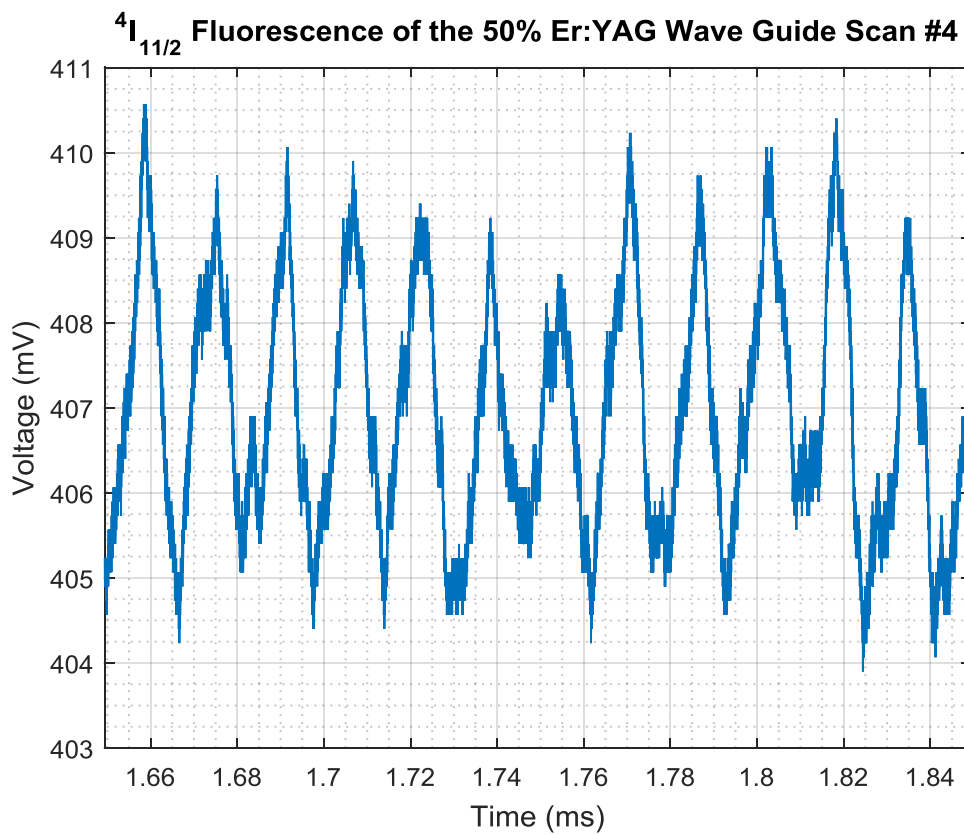


Figure C.5.7: Transient scan of the  $^4I_{11/2}$  level.

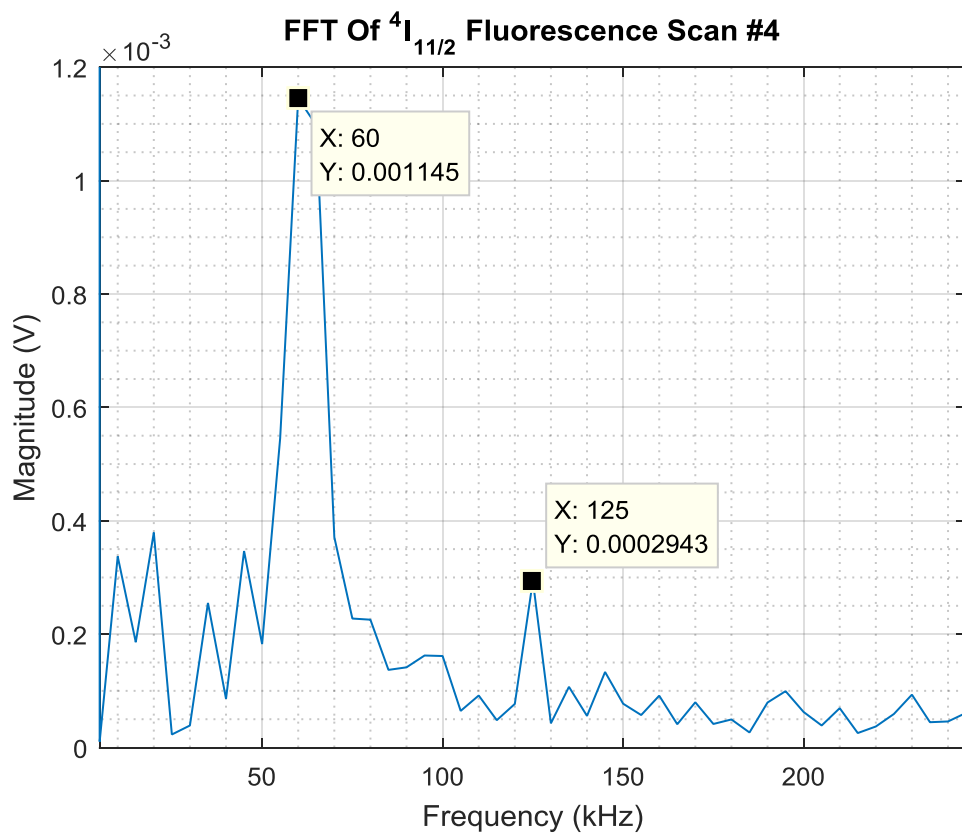


Figure C.5.8: FFT of transient scan of the  ${}^4I_{11/2}$  level.

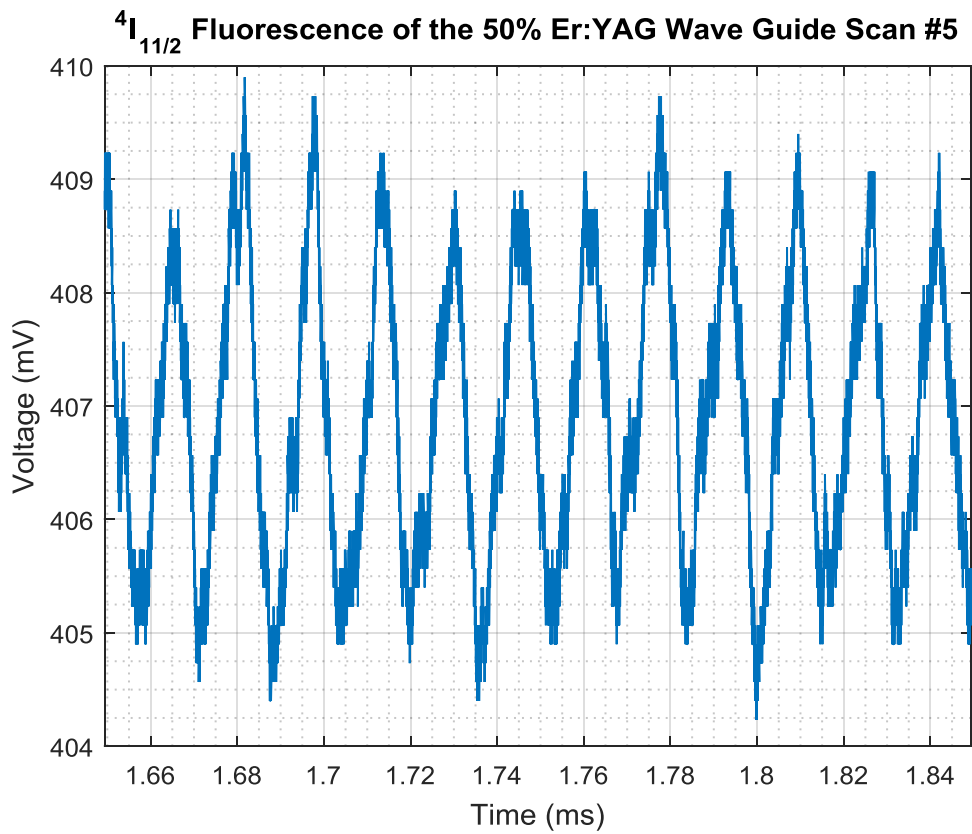


Figure C.5.9: Transient scan of the  $^4I_{11/2}$  level.

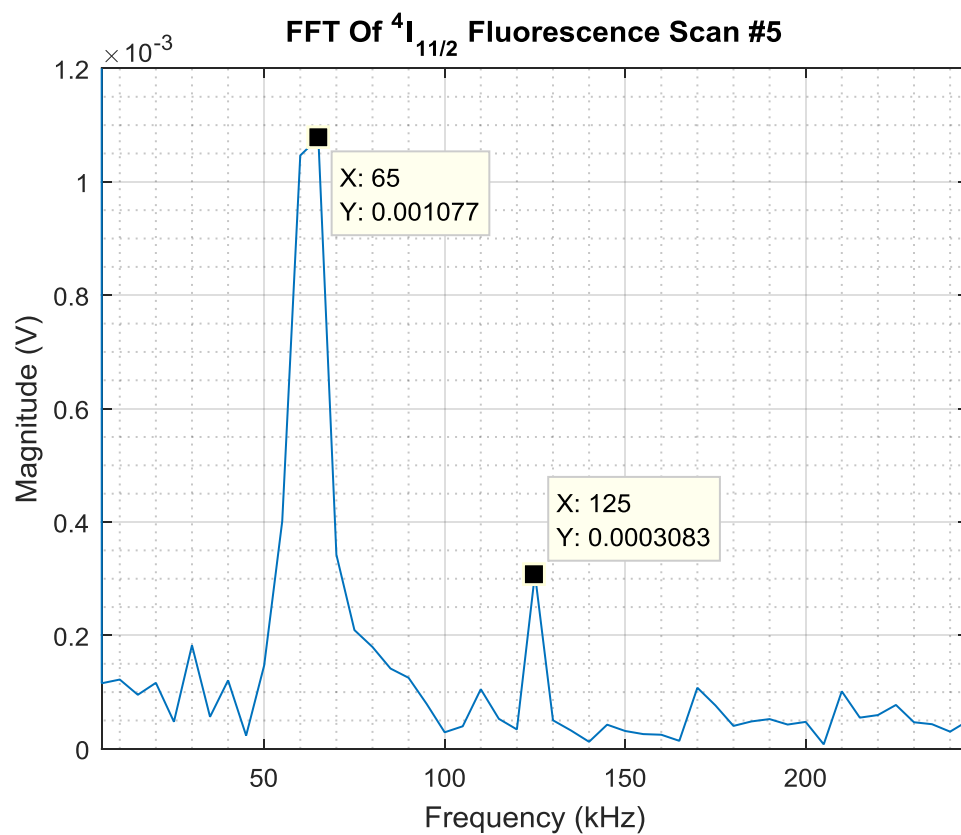


Figure C.5.10: FFT of transient scan of the  ${}^4I_{11/2}$  level.

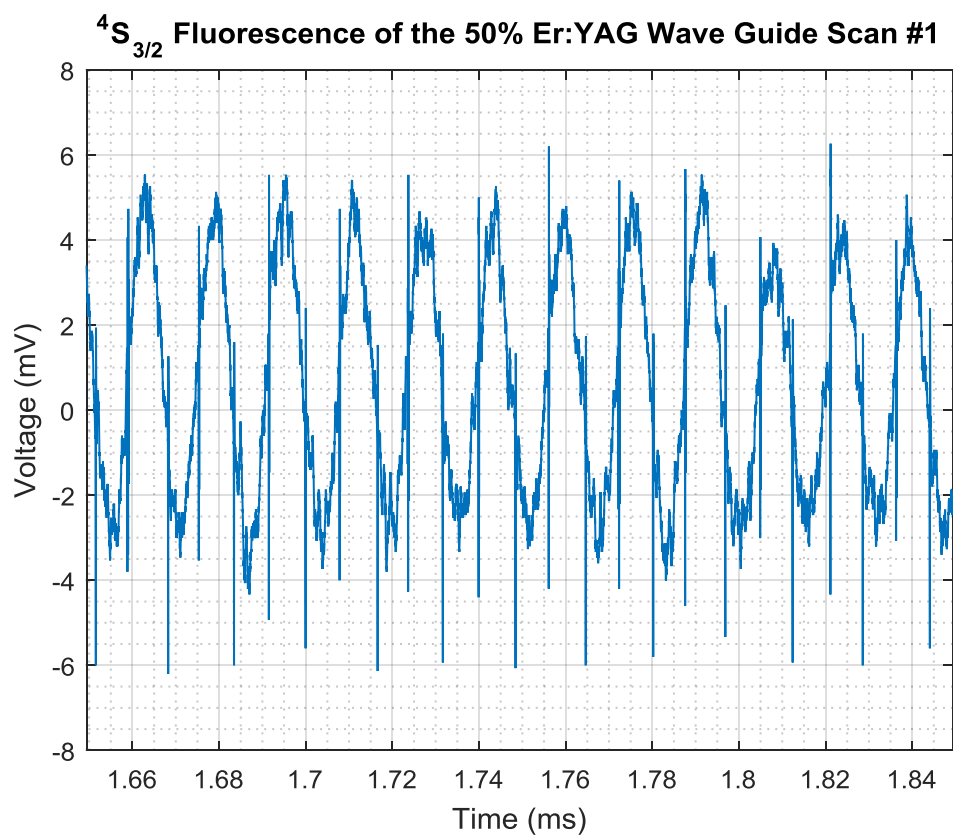


Figure C.5.11: Transient scan of the  $^4S_{3/2}$  level.

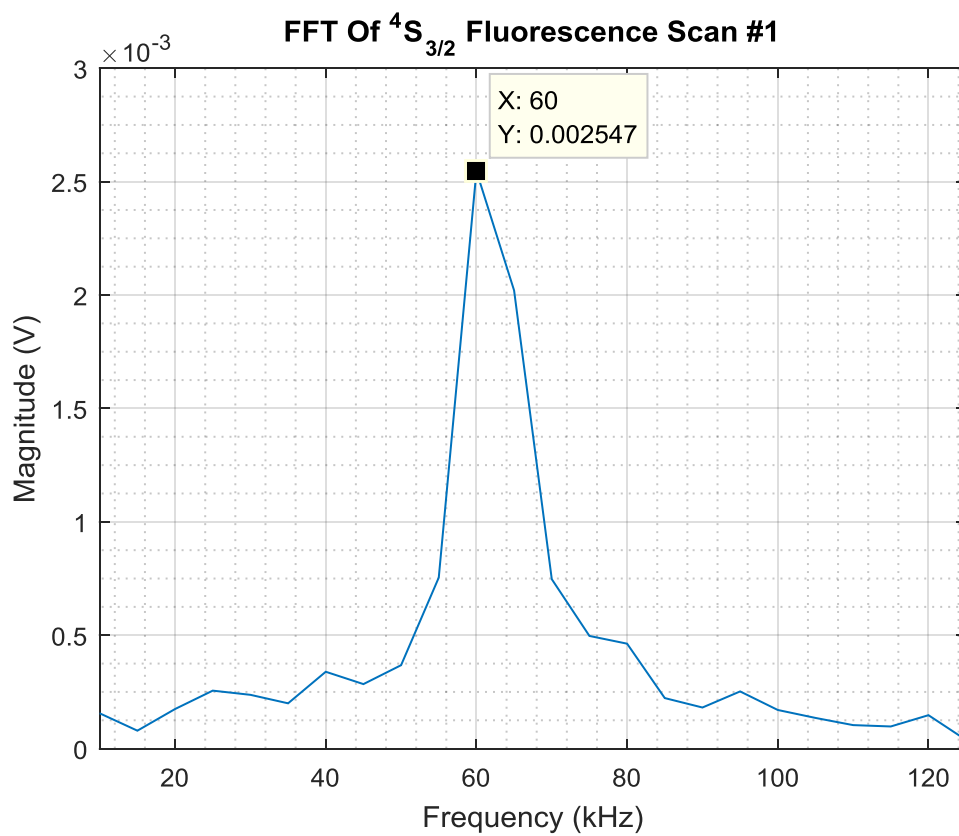


Figure C.5.12: FFT of transient scan of the  $^4S_{3/2}$  level.

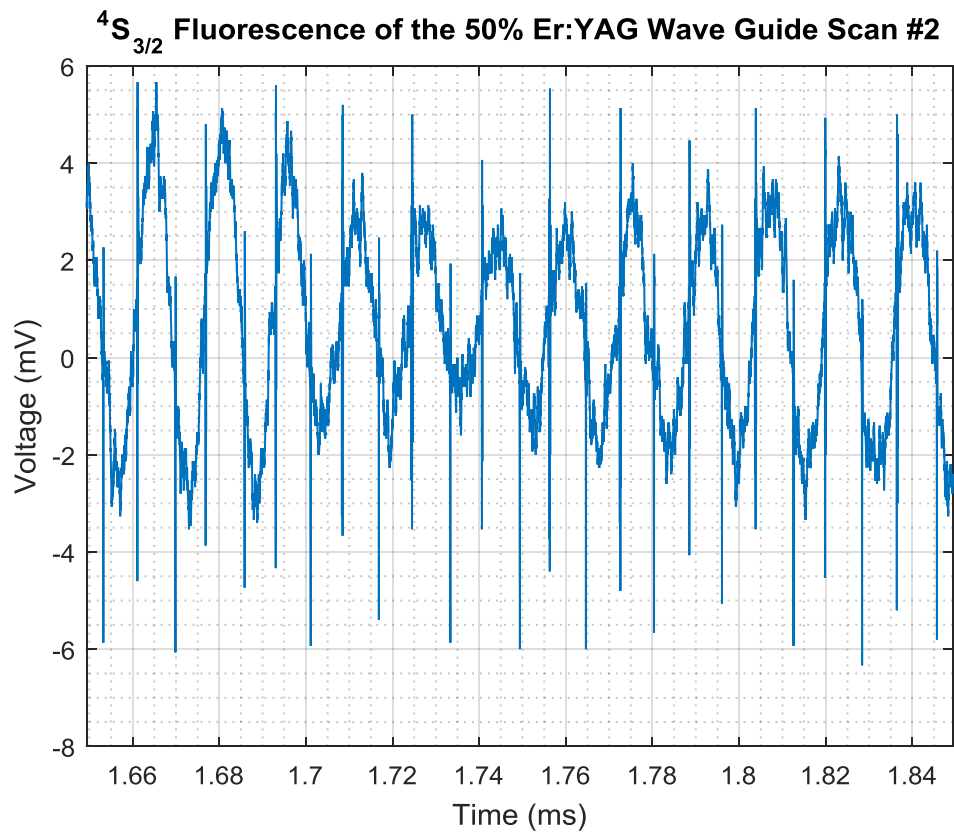


Figure C.5.13: Transient scan of the  $^4S_{3/2}$  level.

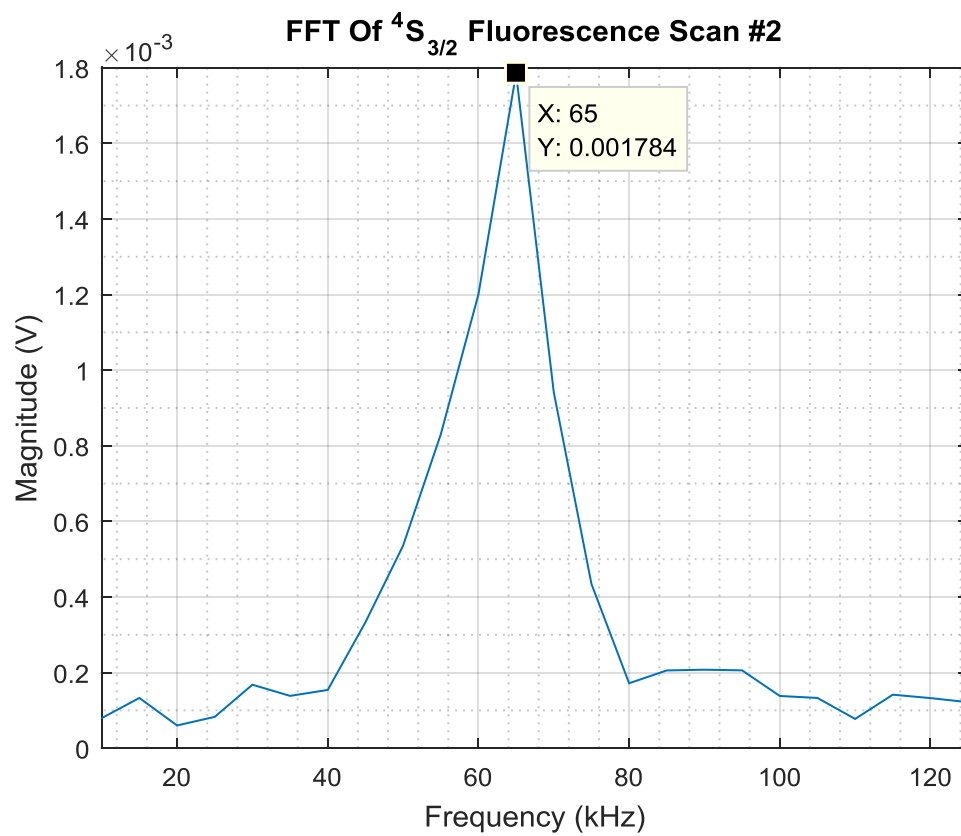


Figure C.5.14: FFT of transient scan of the  $^4S_{3/2}$  level.

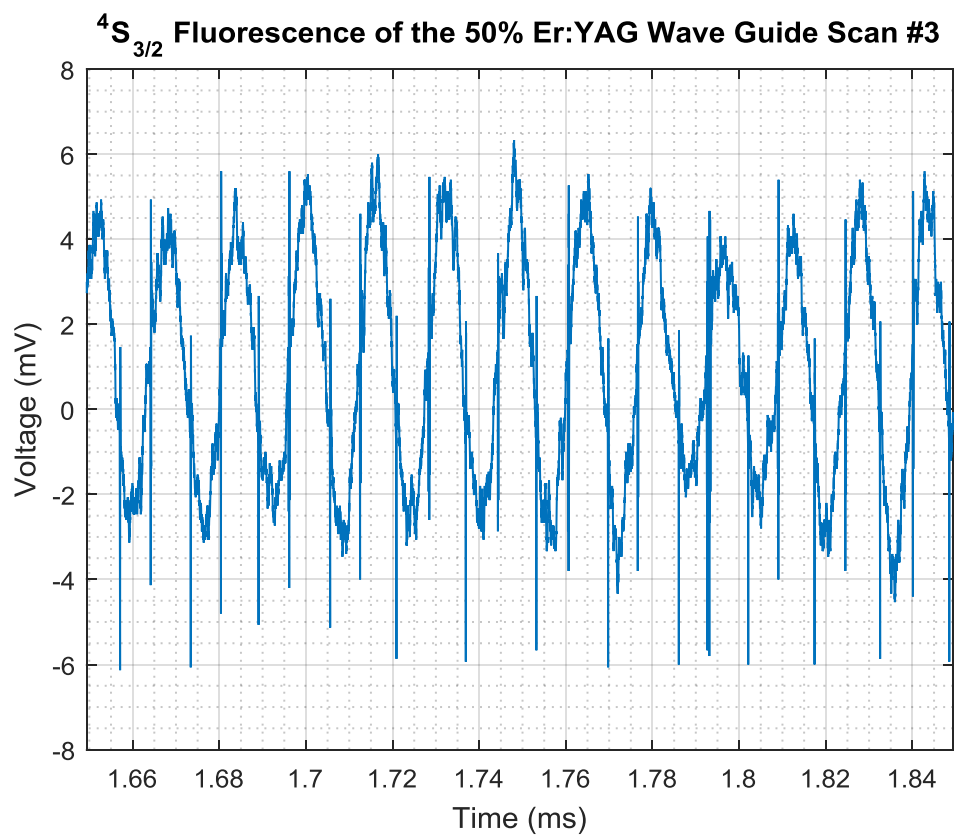


Figure C.5.15: Transient scan of the  $^4S_{3/2}$  level.

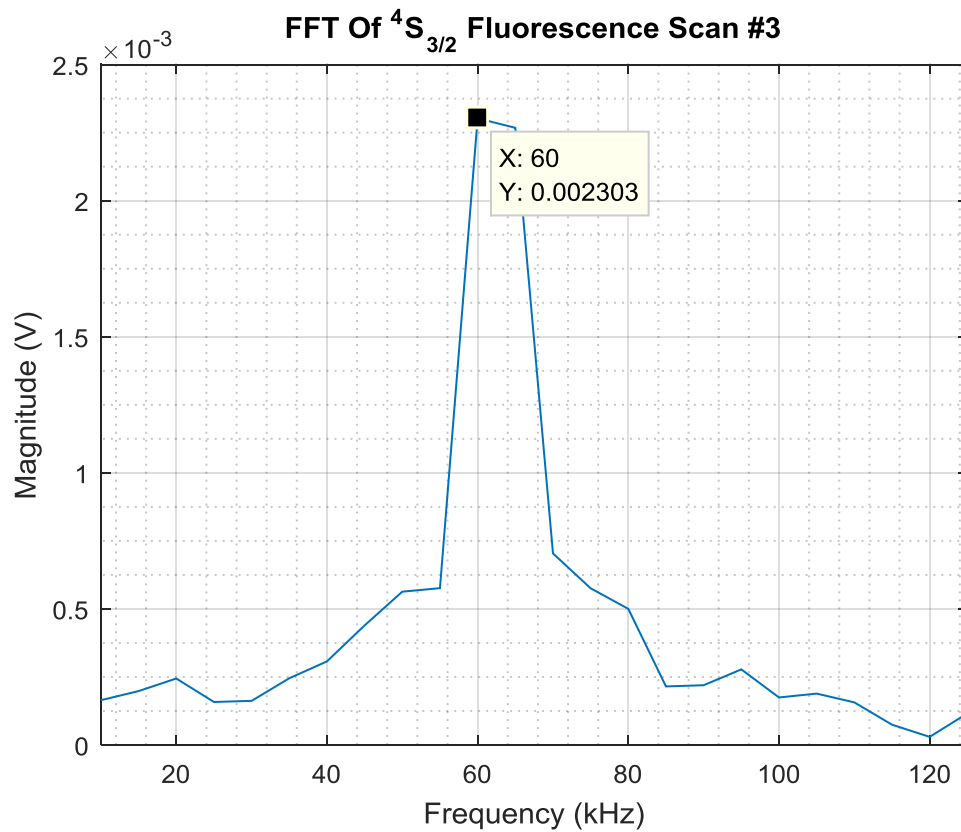


Figure C.5.16: FFT of transient scan of the  $^4S_{3/2}$  level.

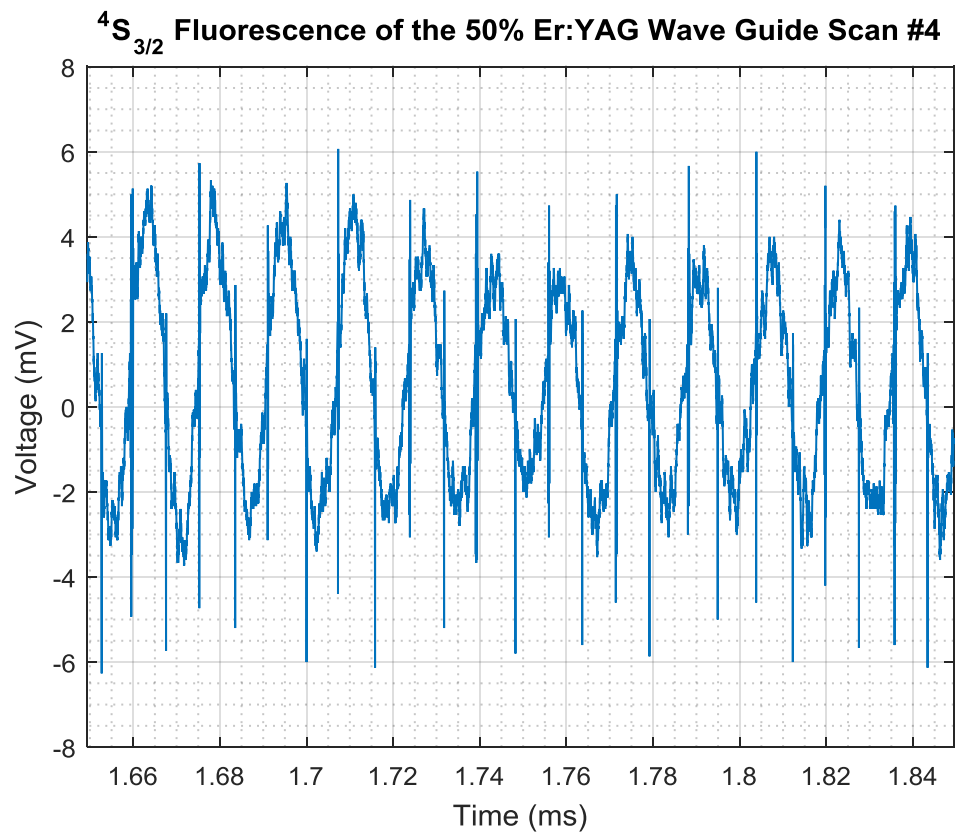


Figure C.5.17: Transient scan of the  $^4S_{3/2}$  level.

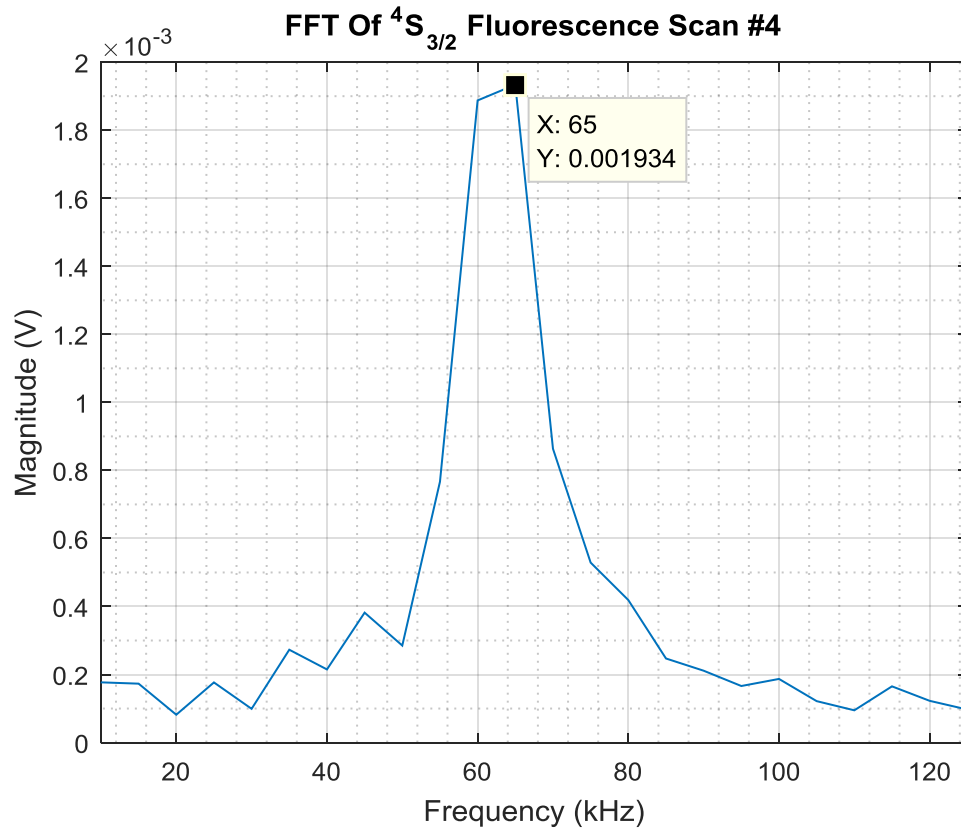


Figure C.5.18: FFT of transient scan of the  $^4S_{3/2}$  level.

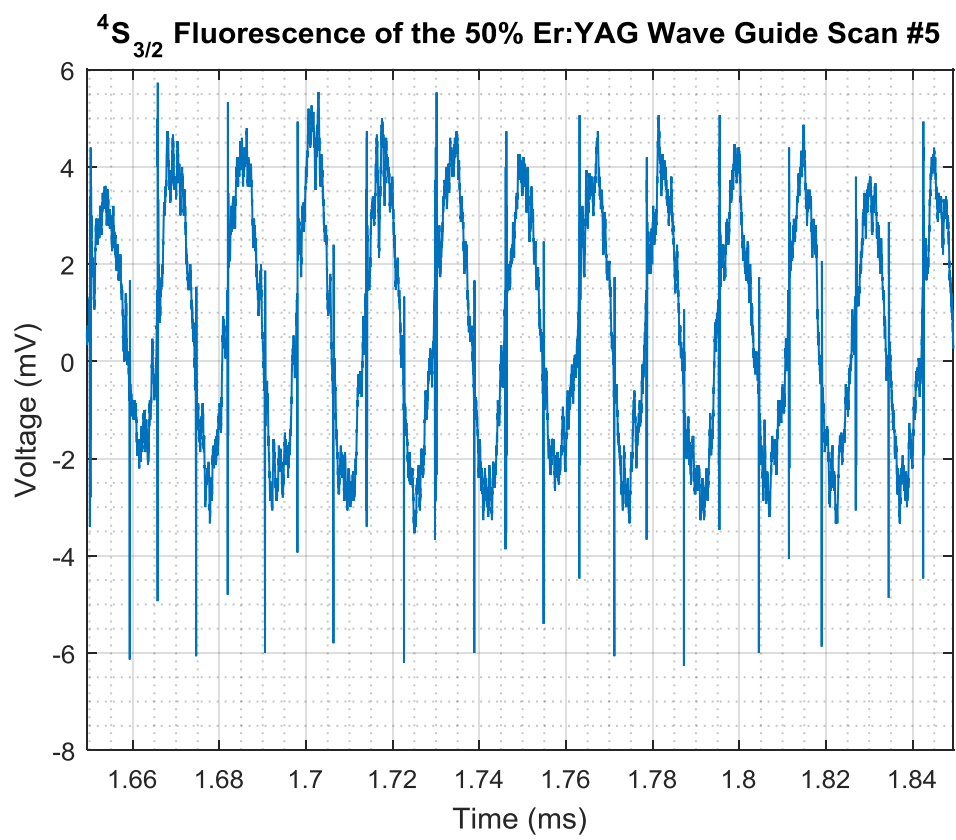


Figure C.5.19: Transient scan of the  $^4S_{3/2}$  level.

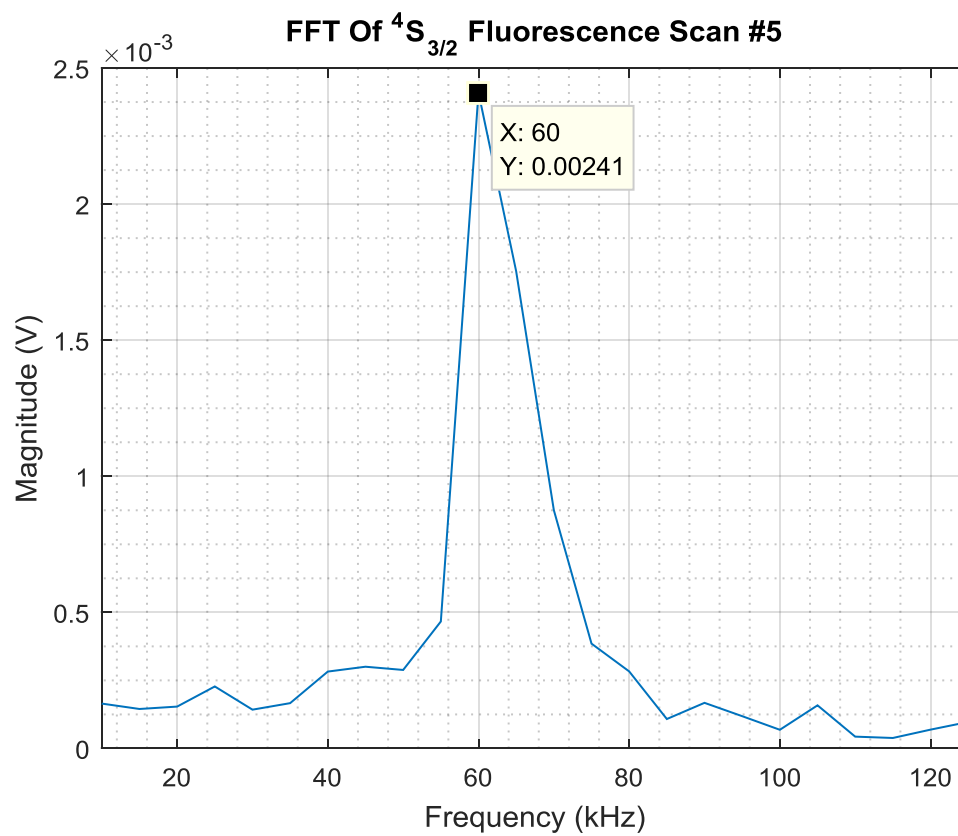


Figure C.5.20: FFT of transient scan of the  $^4S_{3/2}$  level.

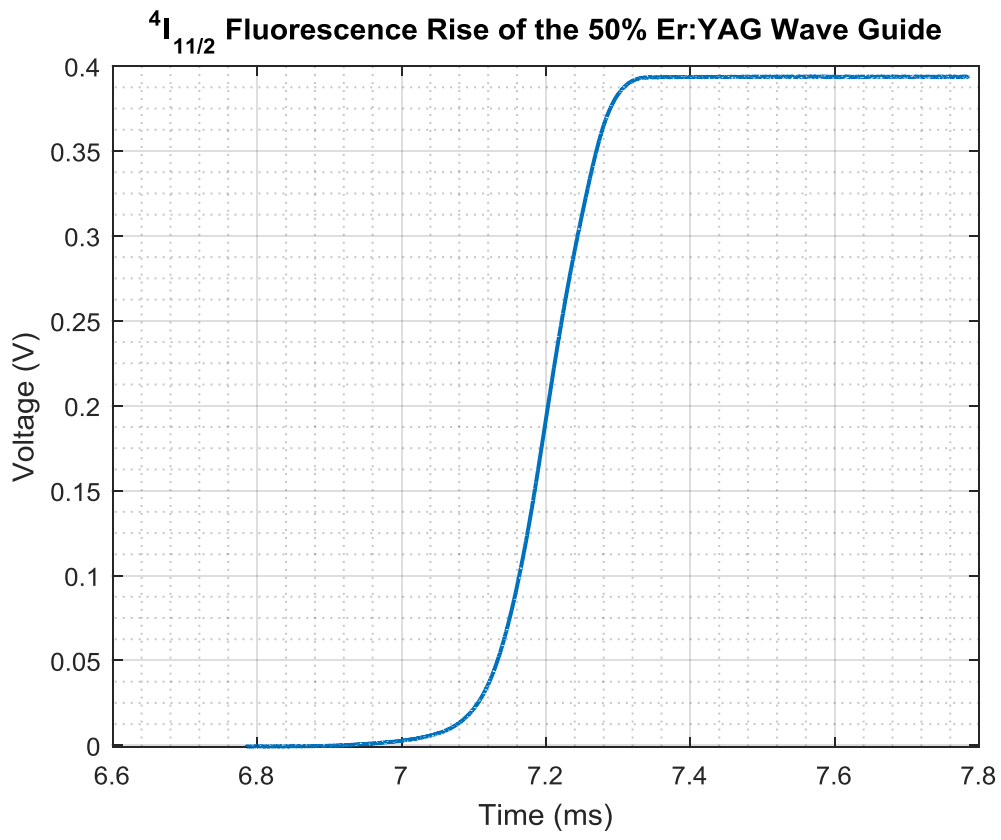


Figure C.5.21: Rise of the  $^4I_{11/2}$  level.

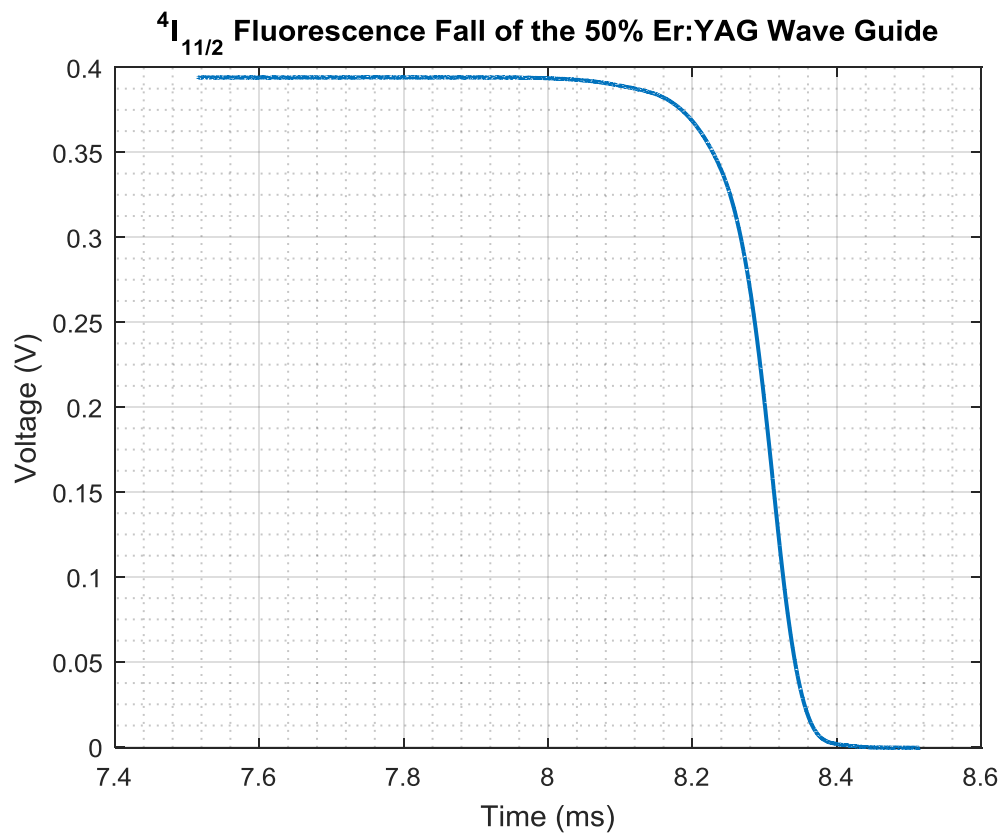


Figure C.5.22: Fall of the  $^4I_{11/2}$  level.

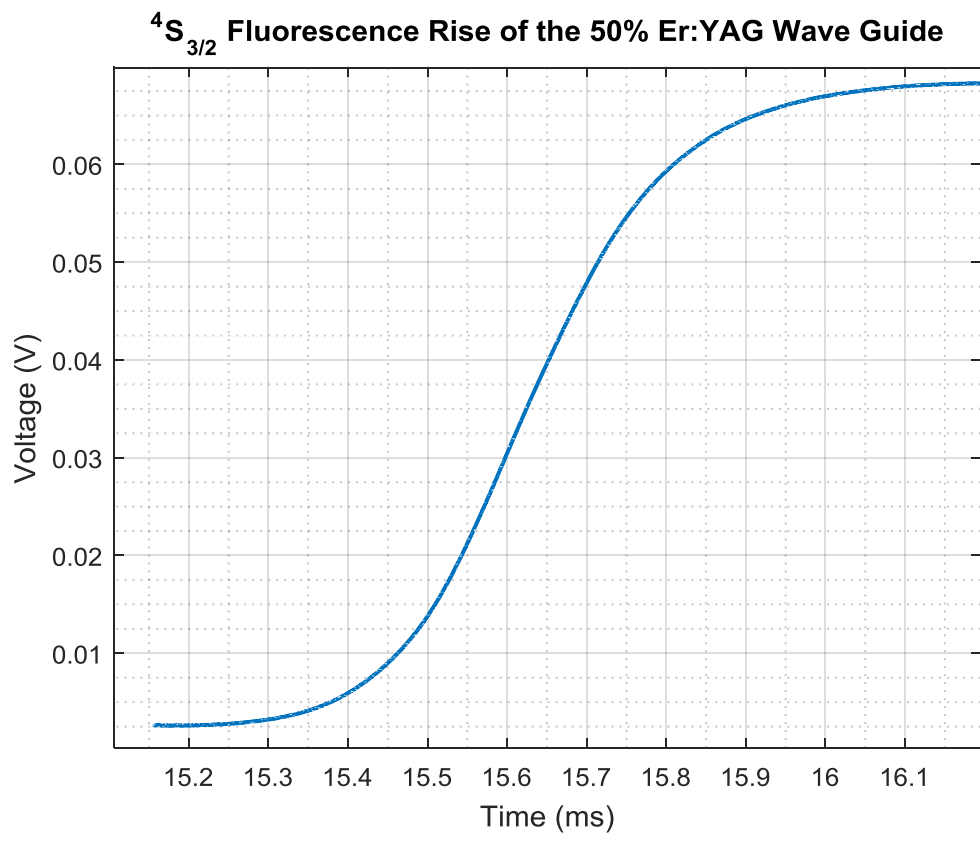


Figure C.5.23: Rise of the  $^4S_{3/2}$  level.

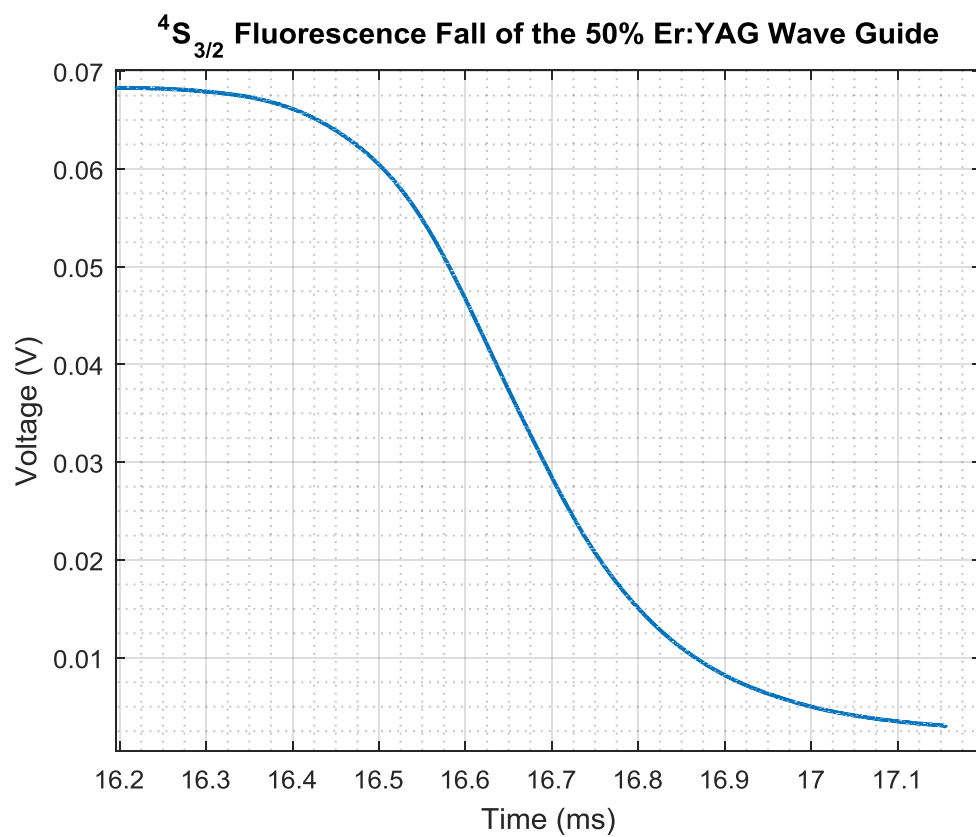


Figure C.3.24: Fall of the  $^4S_{3/2}$  level.

Transient Statistics ${}^4I_{11/2}$ Level Fluorescence Oscillation	
Number of Scans	5
Mean Value of Oscillation Frequency (KHz)	60.9988
Standard Deviation of Frequency (KHz)	2.2360
2 <sup>nd</sup> Harmonic of ${}^4I_{11/2}$ Level Fluorescence Oscillation	
Number of Scans	5
Mean Value of Oscillation Frequency (KHz)	124.9975
Standard Deviation of Frequency (KHz)	1.6270E-14

Table C.5.1: Statistics of the transient scans of the  ${}^4I_{11/2}$  level.

Transient Statistics ${}^4S_{3/2}$ Level Fluorescence Oscillation	
Number of Scans	5
Mean Value of Oscillation Frequency (KHz)	59.9988
Standard Deviation of Frequency (KHz)	2.7386

Table C.5.2: Statistics of the transient scans of the  ${}^4S_{3/2}$  level.

$^4I_{11/2}$ Level Fluorescence	
Number of Sweeps	1000
Rise Time ( $\mu$ s)	147.04
Fall Time ( $\mu$ s)	122.10

Table C.5.3: Rise and Fall statistics of the transient scans of the  $^4I_{11/2}$  level.

$^4S_{3/2}$ Level Fluorescence	
Number of Sweeps	1000
Rise Time ( $\mu$ s)	376.20
Fall Time ( $\mu$ s)	388.51

Table C.5.4: Rise and Fall statistics of the transient scans of the  $^4S_{3/2}$  level.

## C.6 808nm CW Pumped 50% Er:YAG Waveguide with No 3 $\mu$ m Laser

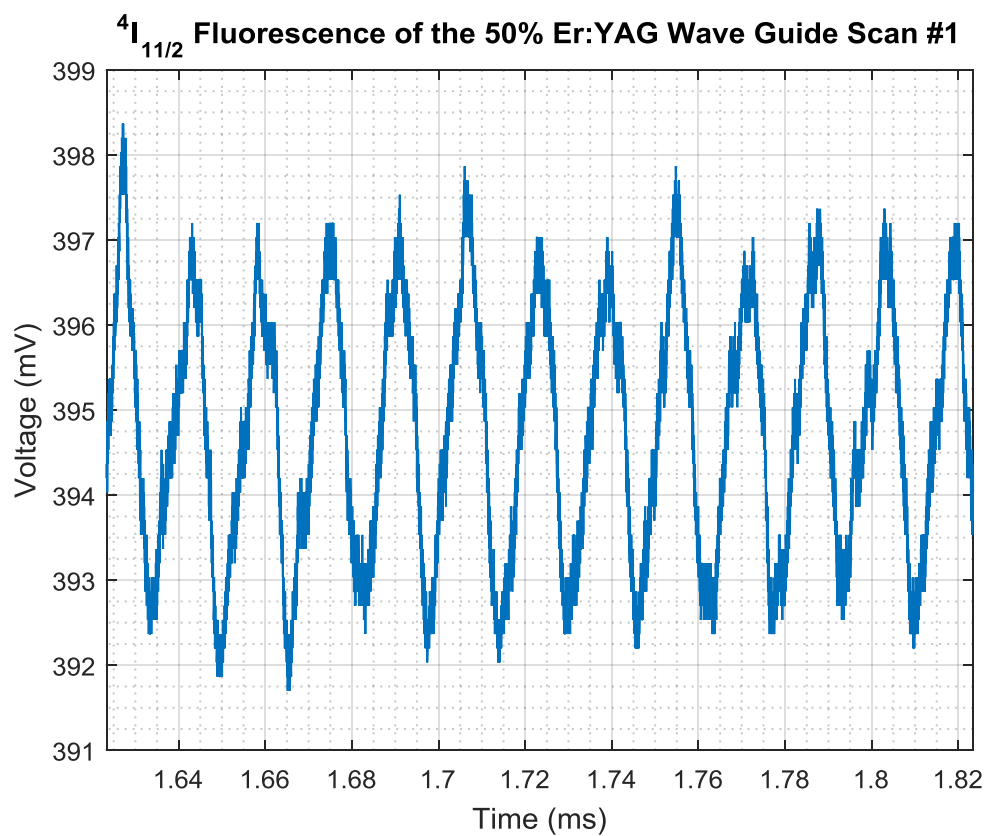


Figure C.6.1: Transient scan of the  $^4I_{11/2}$  level.

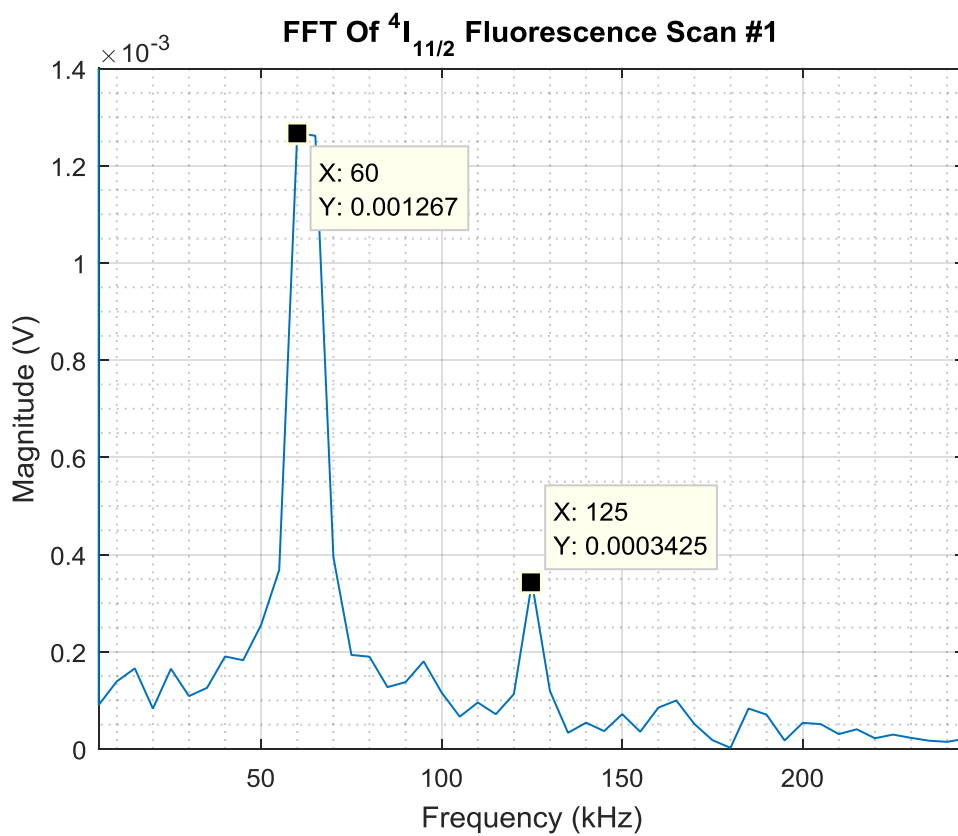


Figure C.6.2: FFT of transient scan of the  ${}^4I_{11/2}$  level.

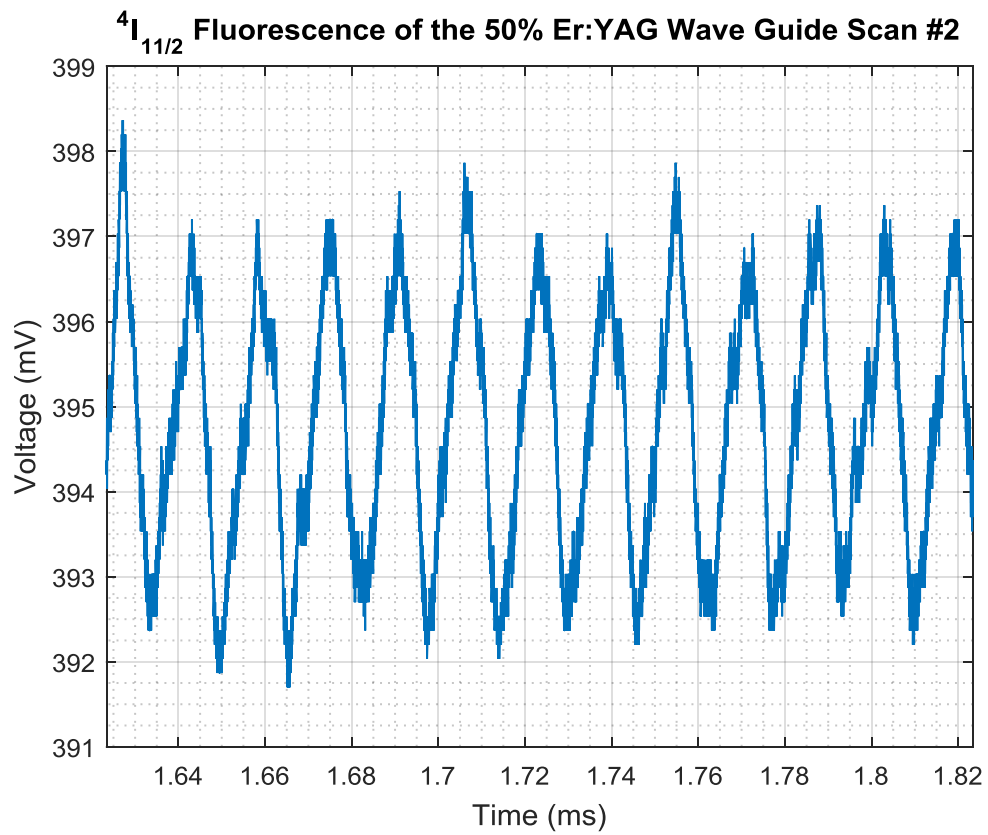


Figure C.6.3: Transient scan of the  $^4I_{11/2}$  level.

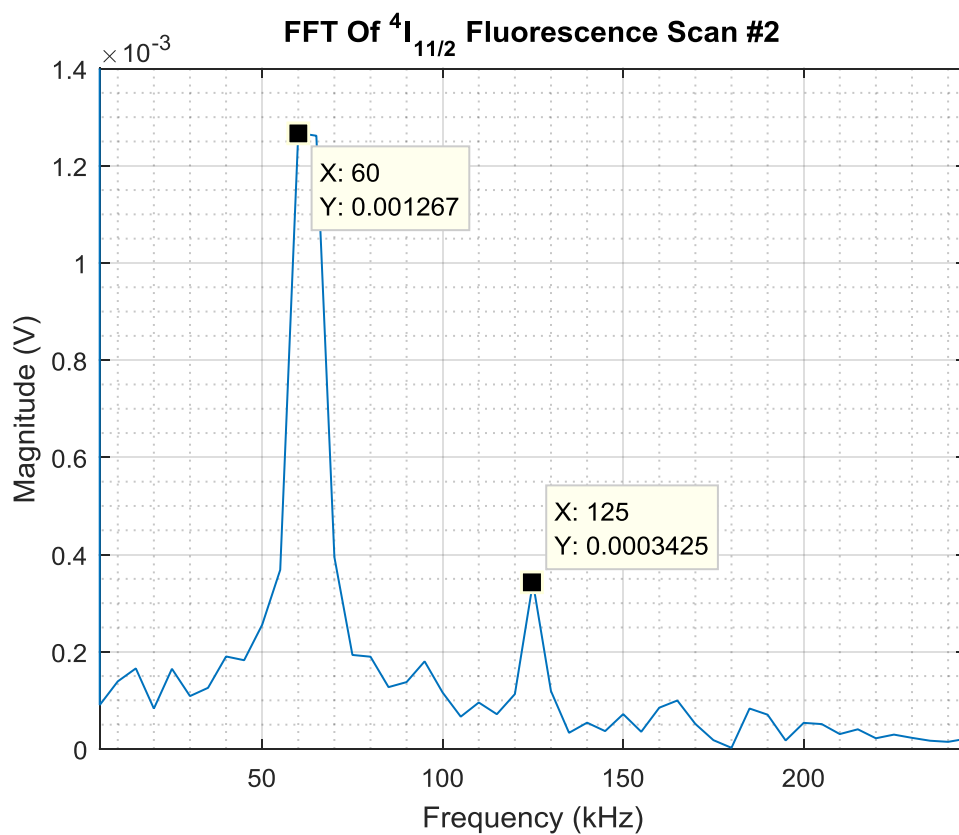


Figure C.6.4: FFT of transient scan of the  ${}^4I_{11/2}$  level.

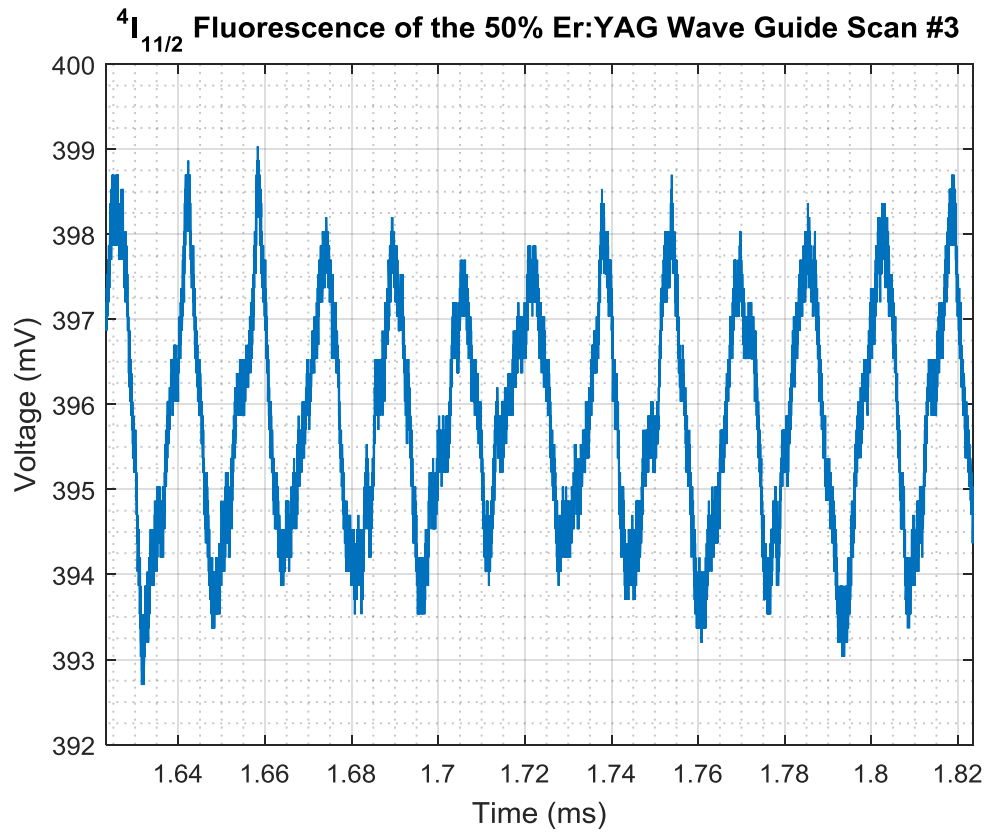


Figure C.6.5: Transient scan of the  $^4I_{11/2}$  level.

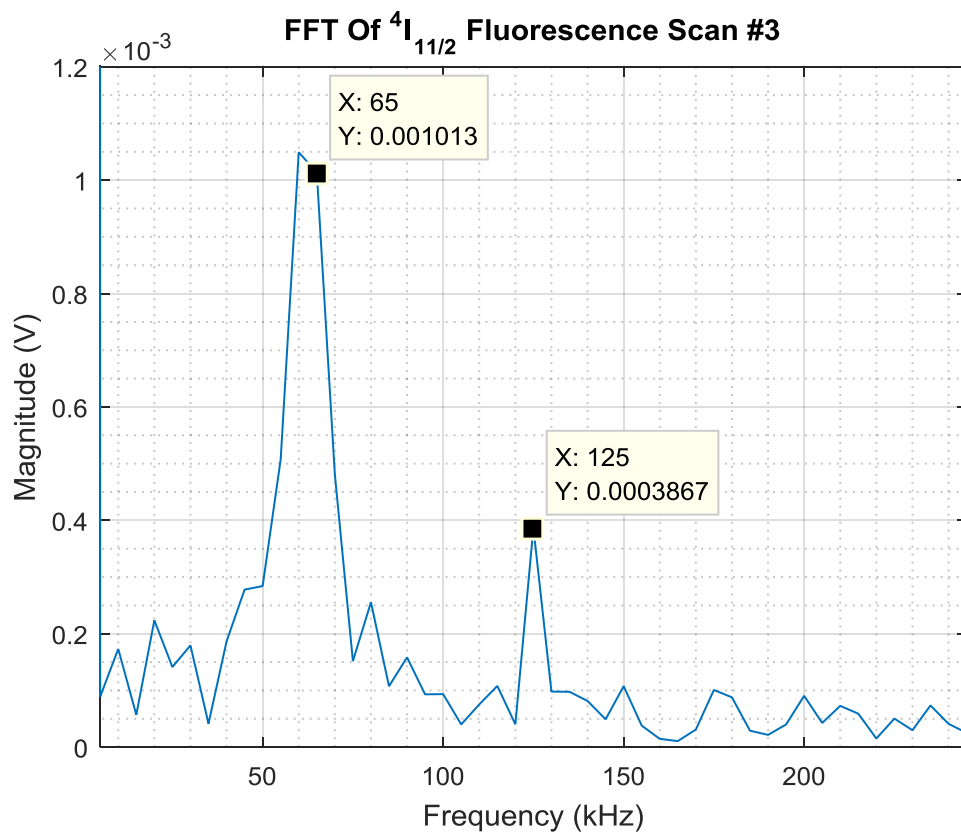


Figure C.6.6: FFT of transient scan of the  ${}^4I_{11/2}$  level.

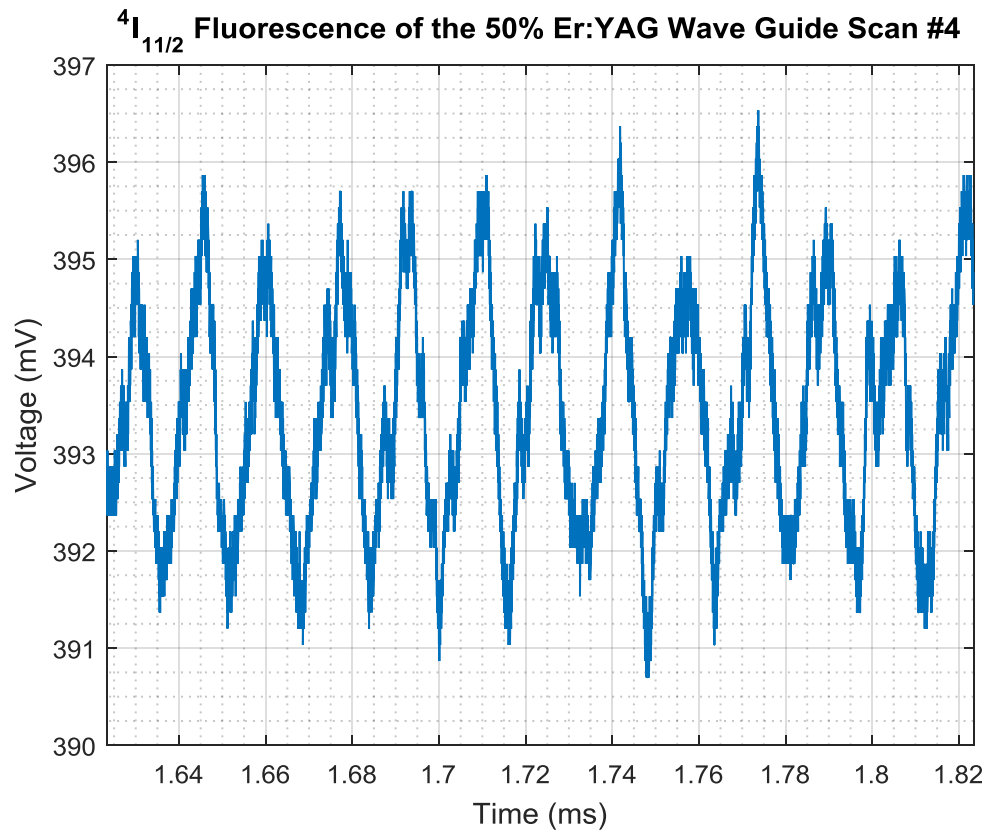


Figure C.6.7: Transient scan of the  $^4I_{11/2}$  level.

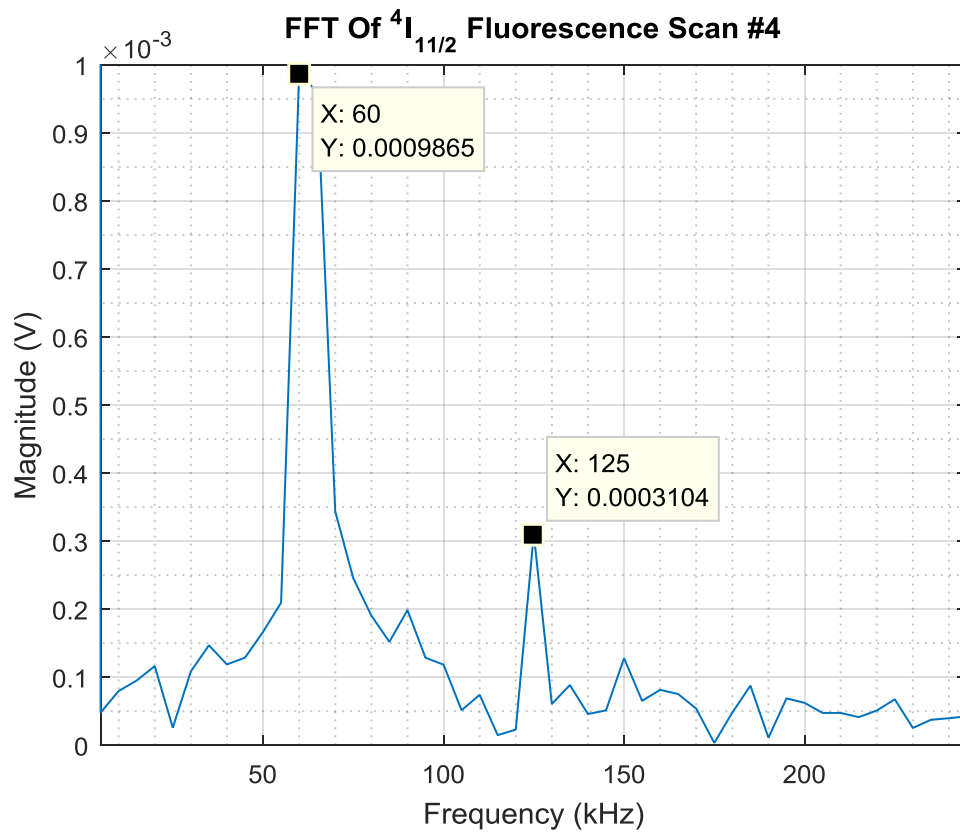


Figure C.6.8: FFT of transient scan of the  ${}^4I_{11/2}$  level.

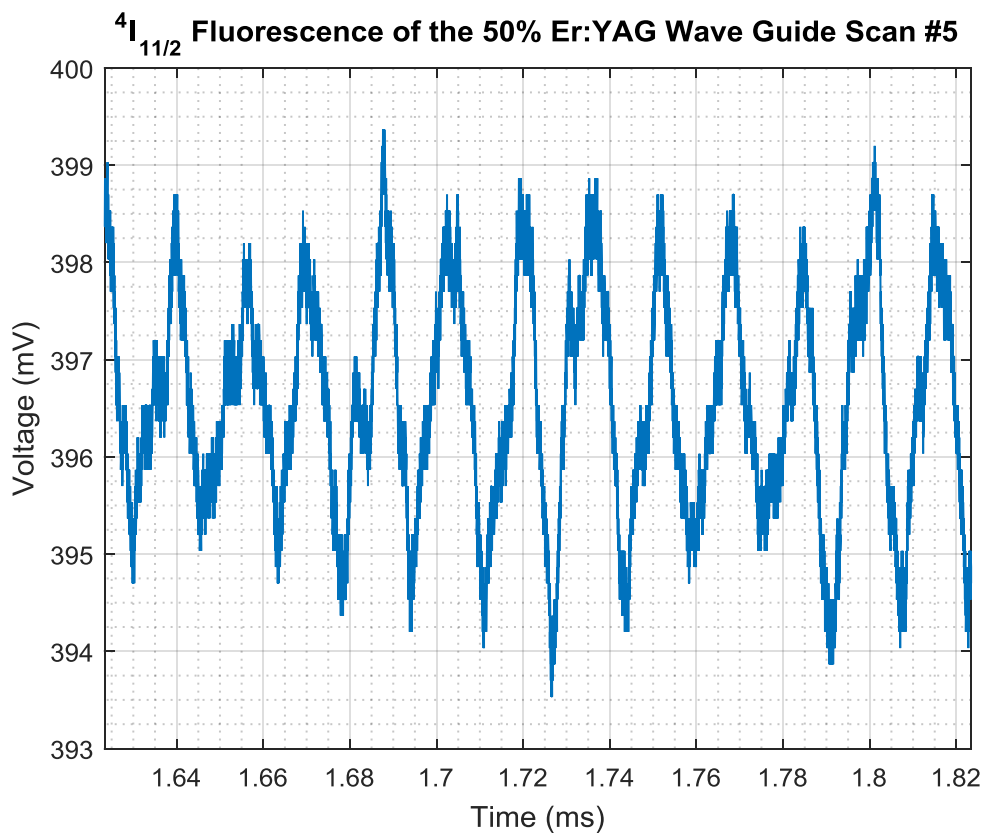


Figure C.6.9: Transient scan of the  $^4I_{11/2}$  level.

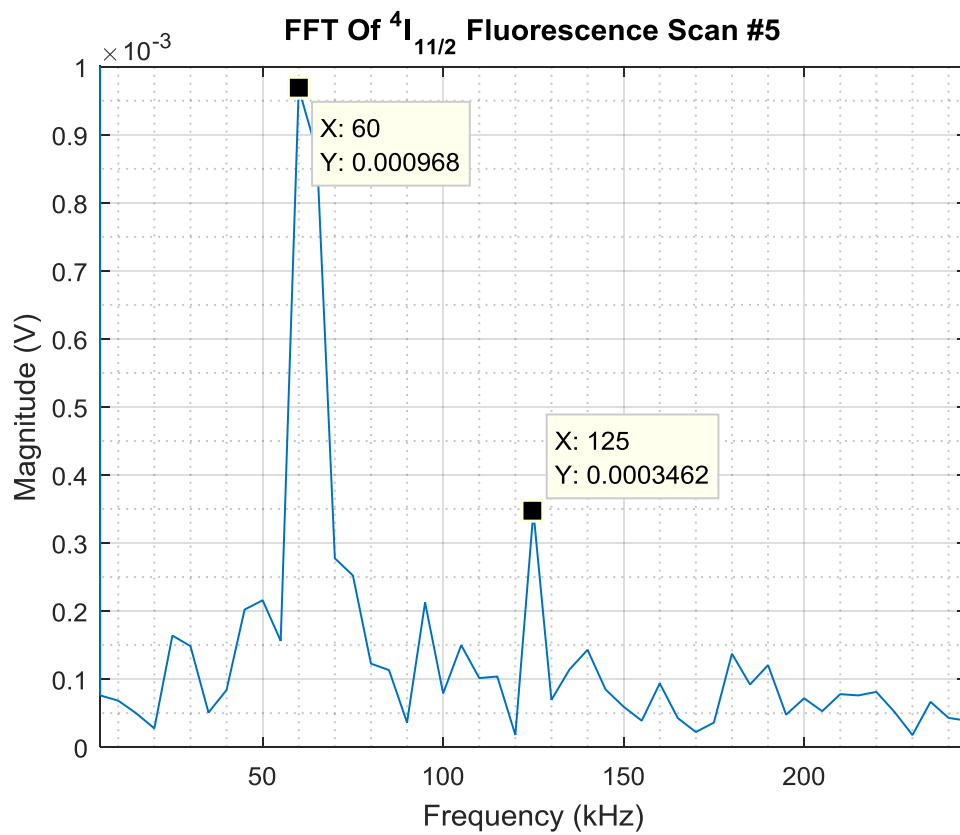


Figure C.6.10: FFT of transient scan of the  ${}^4I_{11/2}$  level.

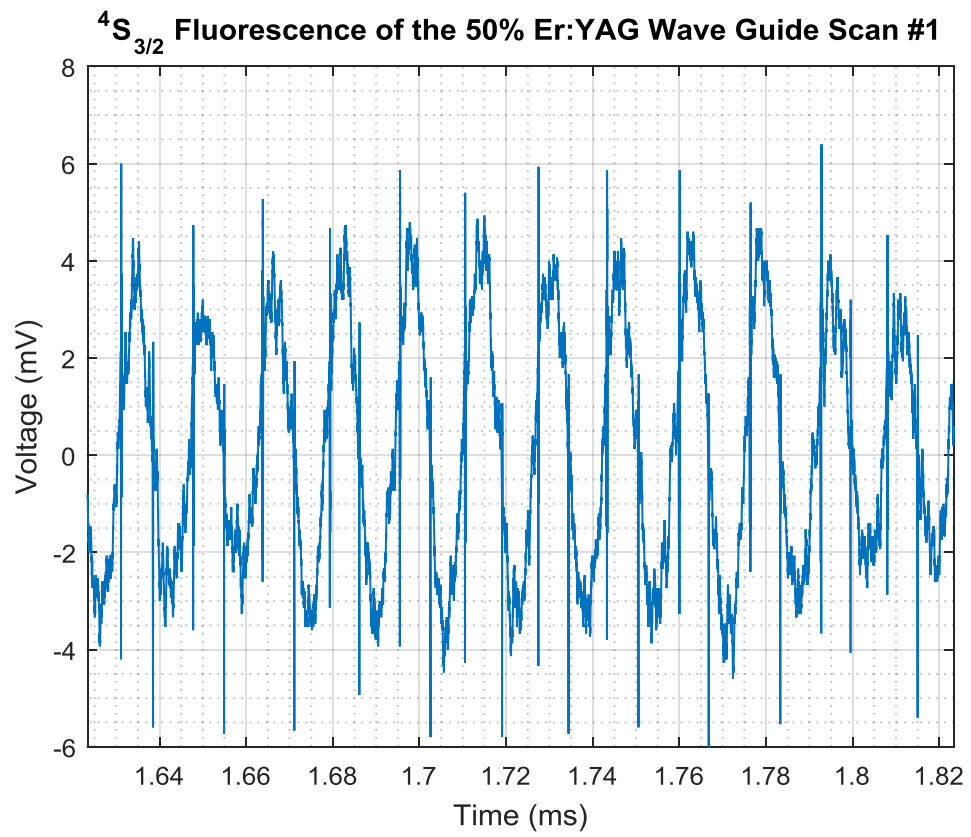


Figure C.6.11: Transient scan of the  $^4S_{3/2}$  level.

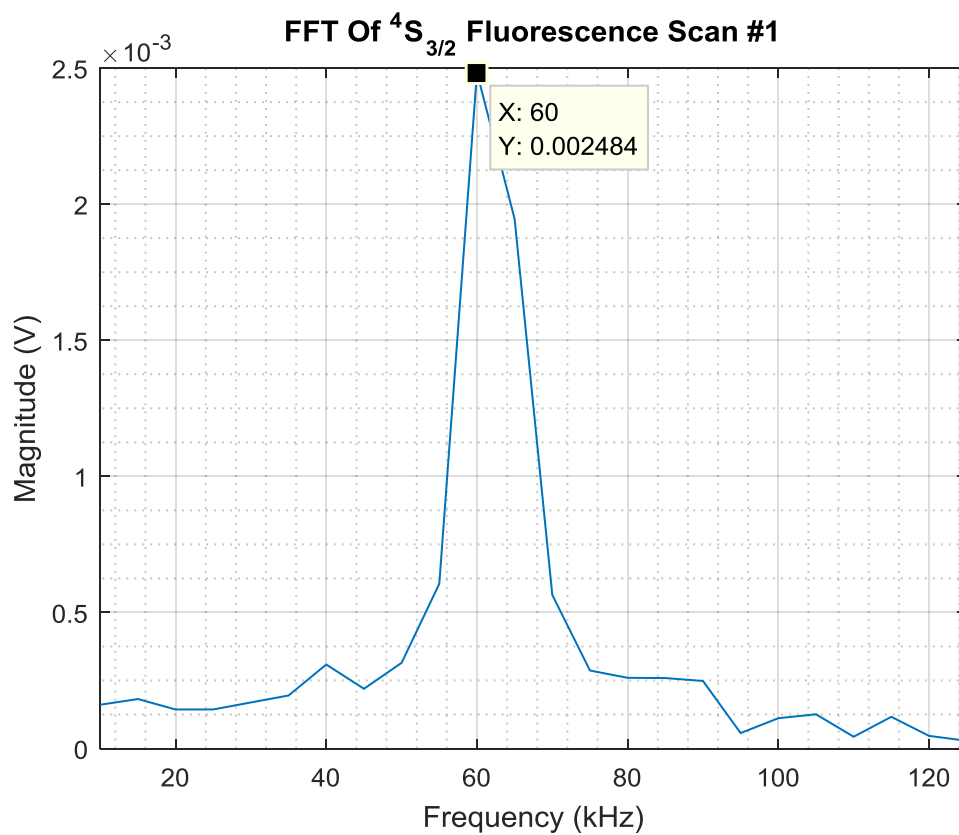


Figure C.6.12: FFT of transient scan of the  $^4S_{3/2}$  level.

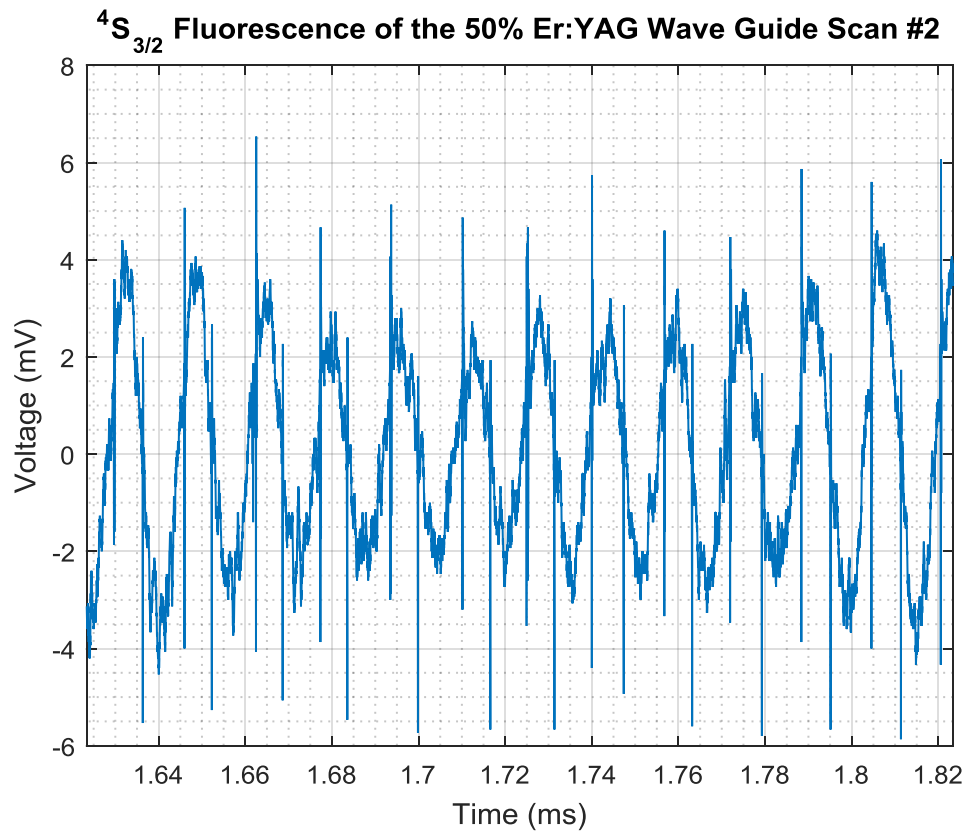


Figure C.6.13: Transient scan of the  $^4S_{3/2}$  level.

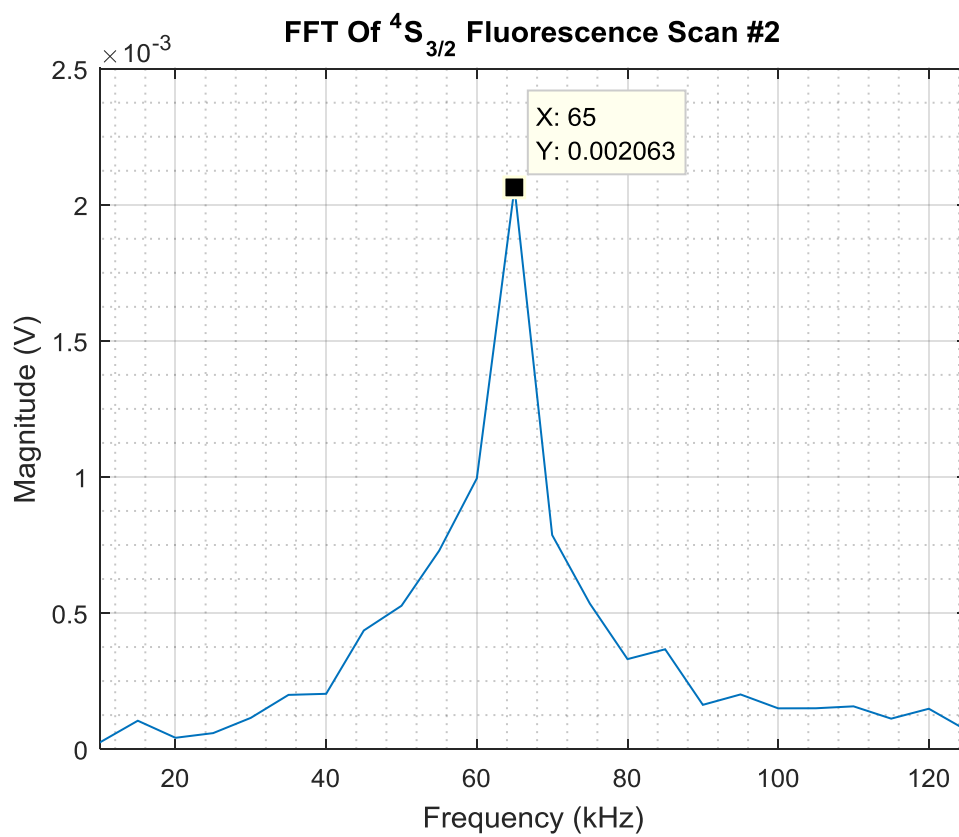


Figure C.6.14: FFT of transient scan of the  $^4S_{3/2}$  level.

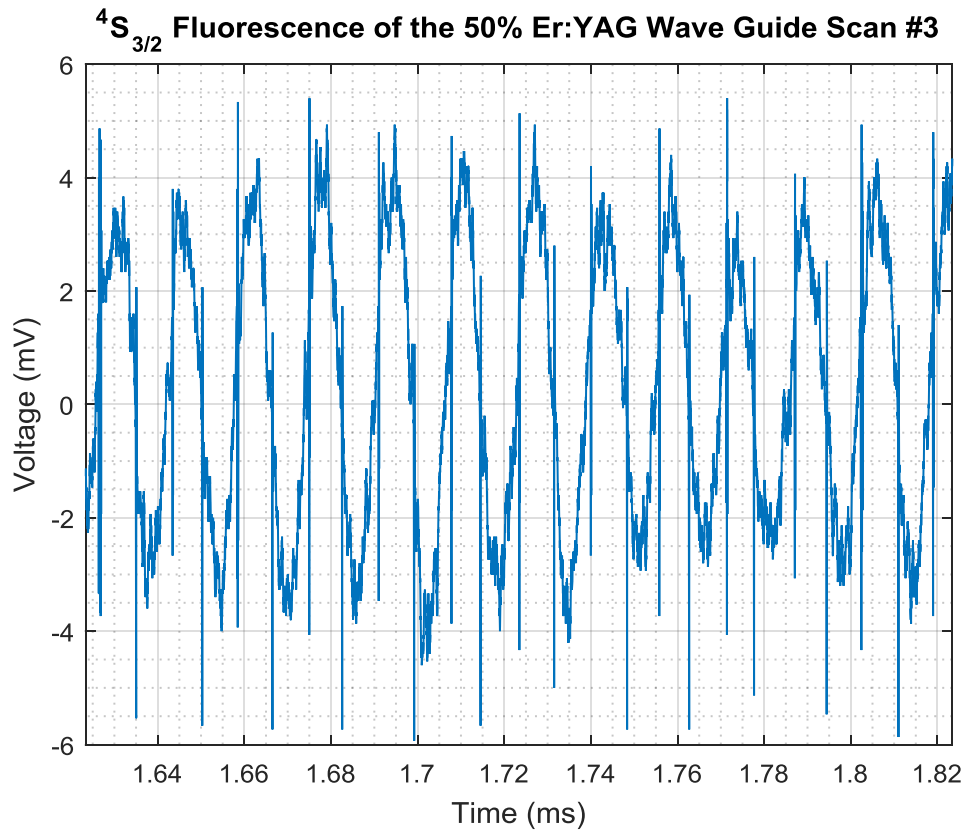


Figure C.6.15: Transient scan of the  $^4S_{3/2}$  level.

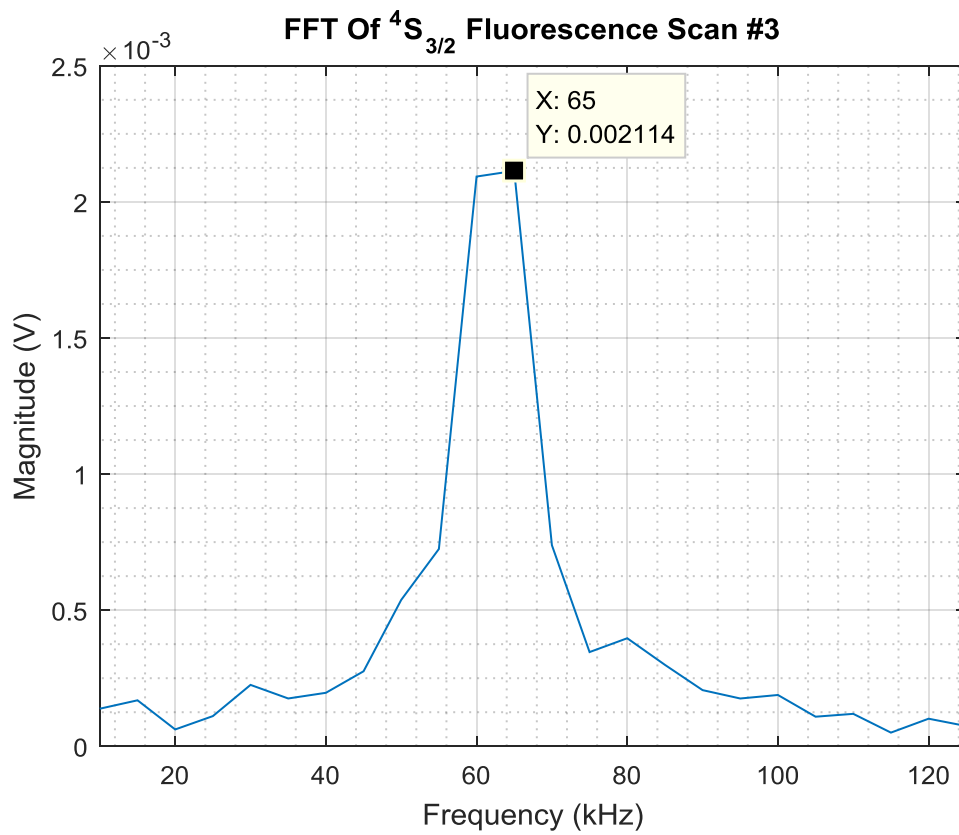


Figure C.6.16: FFT of transient scan of the  $^4S_{3/2}$  level.

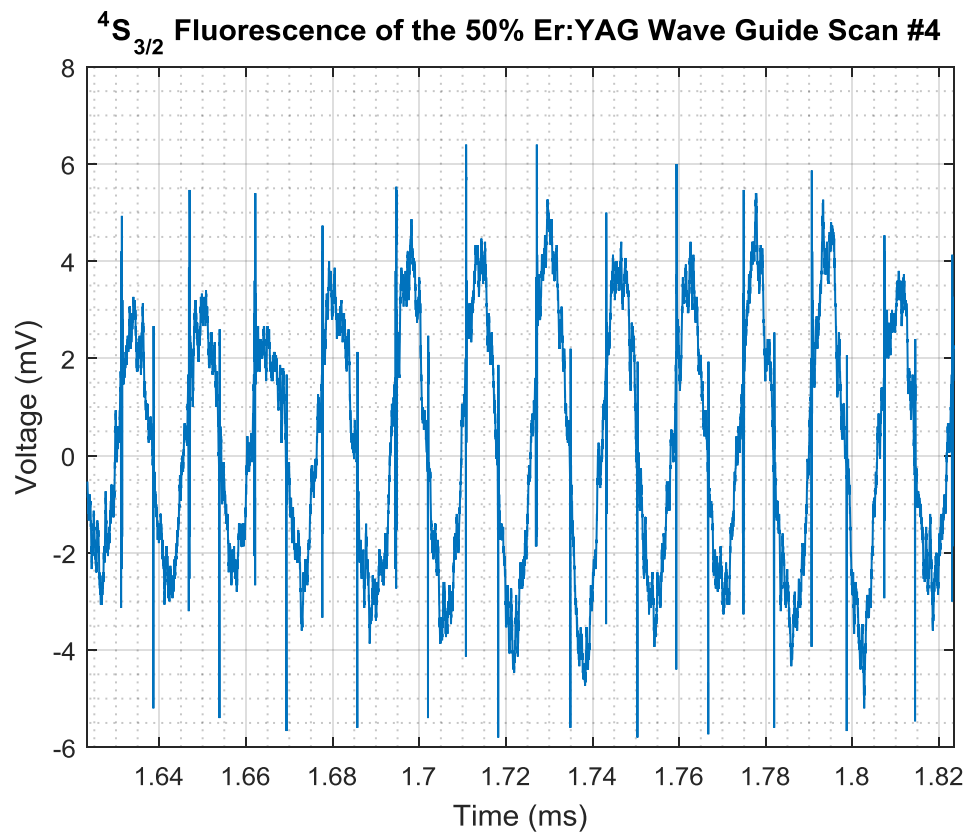


Figure C.6.17: Transient scan of the  $^4S_{3/2}$  level.

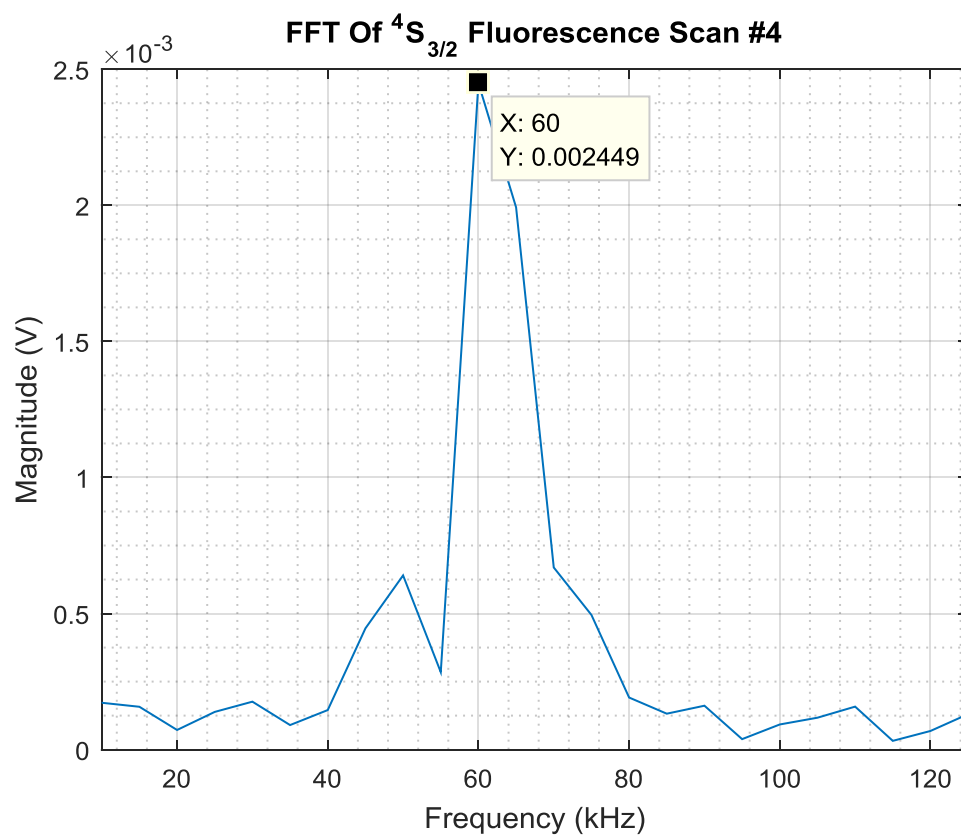


Figure C.6.18: FFT of transient scan of the  $^4S_{3/2}$  level.

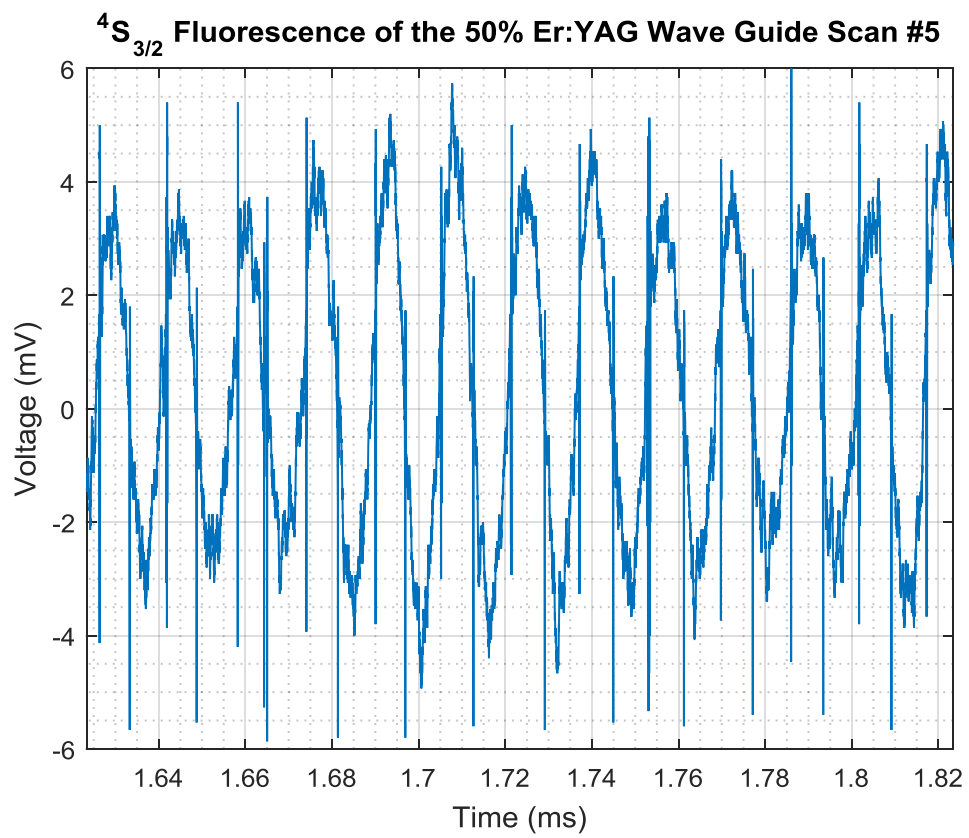


Figure C.6.19: Transient scan of the  $^4S_{3/2}$  level.

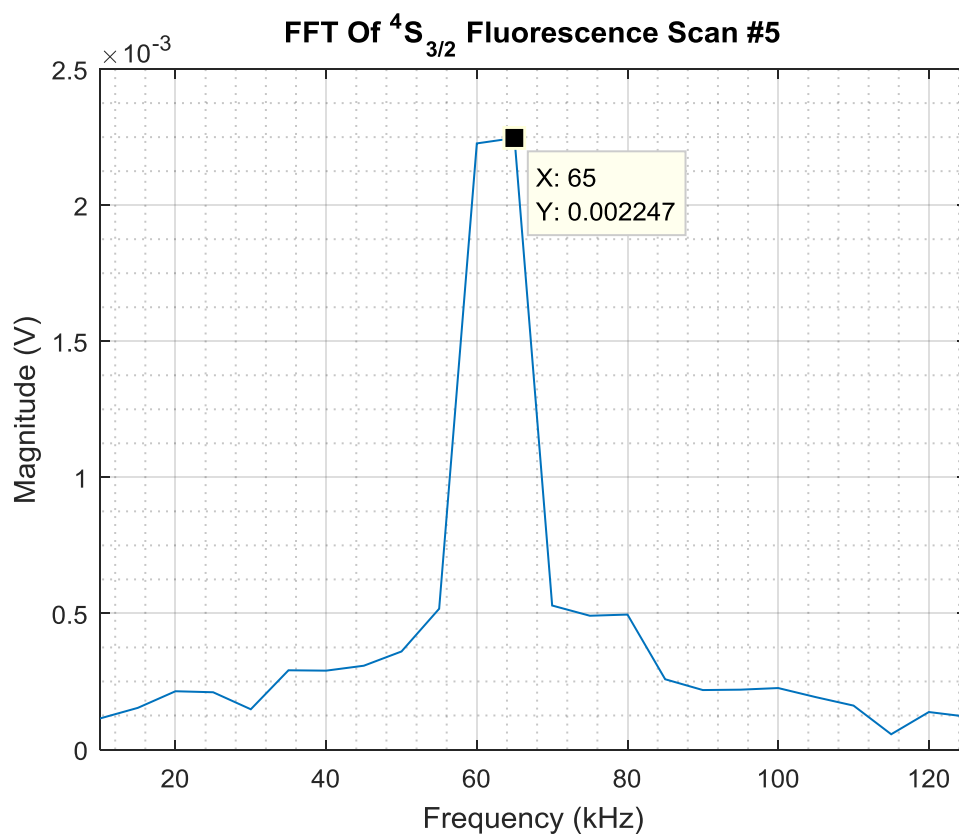


Figure C.6.20: FFT of transient scan of the  $^4S_{3/2}$  level.

Transient Statistics ${}^4I_{11/2}$ Level Fluorescence Oscillation	
Number of Scans	5
Mean Value of Oscillation Frequency (KHz)	60.9988
Standard Deviation of Frequency (KHz)	2.2360
2 <sup>nd</sup> Harmonic of ${}^4I_{11/2}$ Level Fluorescence Oscillation	
Number of Scans	5
Mean Value of Oscillation Frequency (KHz)	124.9975
Standard Deviation of Frequency (KHz)	1.6270E-14

Table C.6.1: Statistics of the transient scans of the  ${}^4I_{11/2}$  level.

Transient Statistics ${}^4S_{3/2}$ Level Fluorescence Oscillation	
Number of Scans	5
Mean Value of Oscillation Frequency (KHz)	64.9987
Standard Deviation of Frequency (KHz)	2.7386

Table C.6.2: Statistics of the transient scans of the  ${}^4S_{3/2}$  level.

## C.7 Pump Beam Profiles

The following plots show the spectra and special beam pattern of the 960nm and 808nm pump beams. The power measurements are also included to derive the intensity profile. The reflected power off the front face of the 50% Er:YAG waveguide sample is provided to demonstrate the reflection loss.

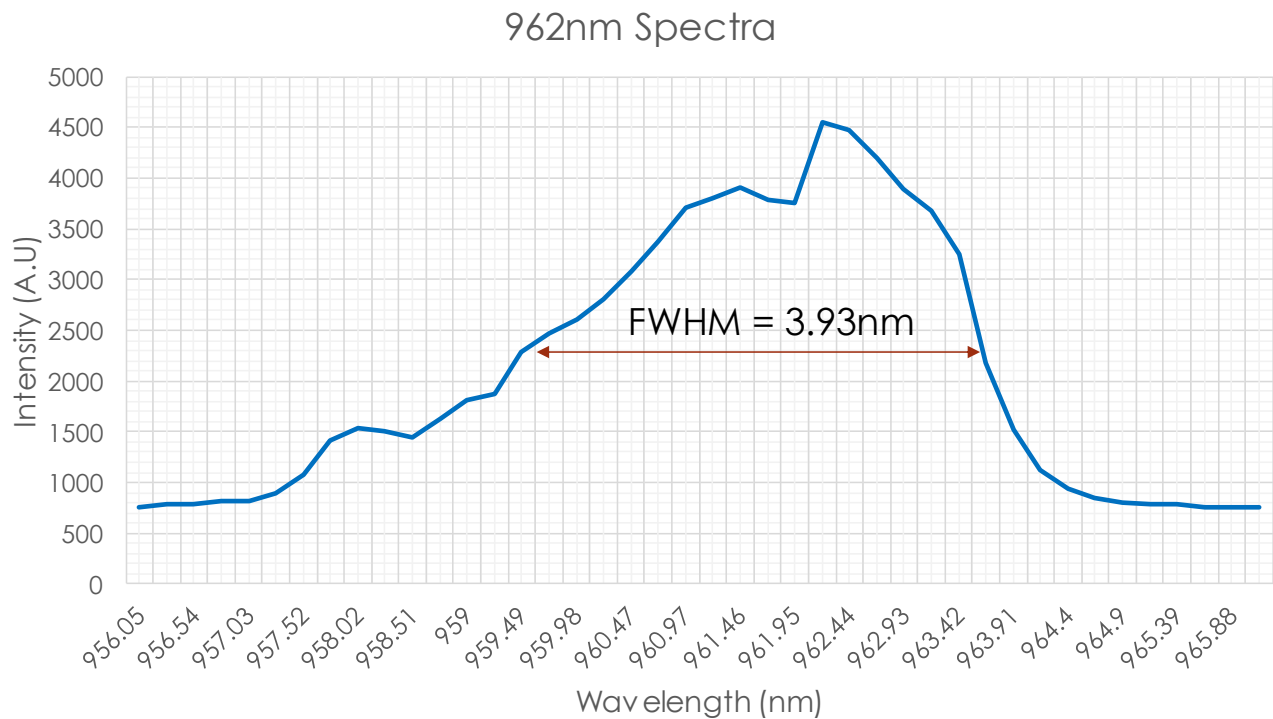


Figure C.7.1: Thermally Stabilized 962nm Pump Laser Spectra

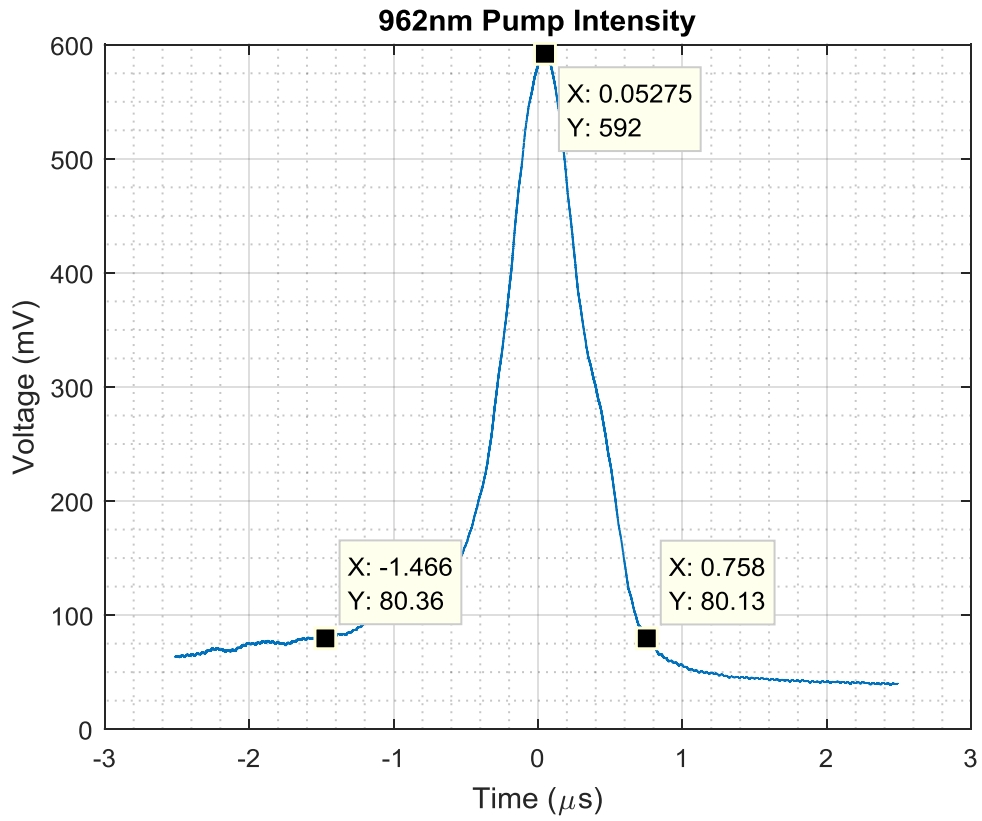


Figure C.7.2: Transient scan of 962nm pump beam. The Gaussian beam radius, using the  $e^{-2}$  definition, is  $142.86\mu\text{m}$ . The Rayleigh length is  $6.665\text{cm}$ . Assuming the beam is in the fundamental TEM mode and therefore symmetric, the intensity is  $1.871\text{ kW/cm}^2$ .

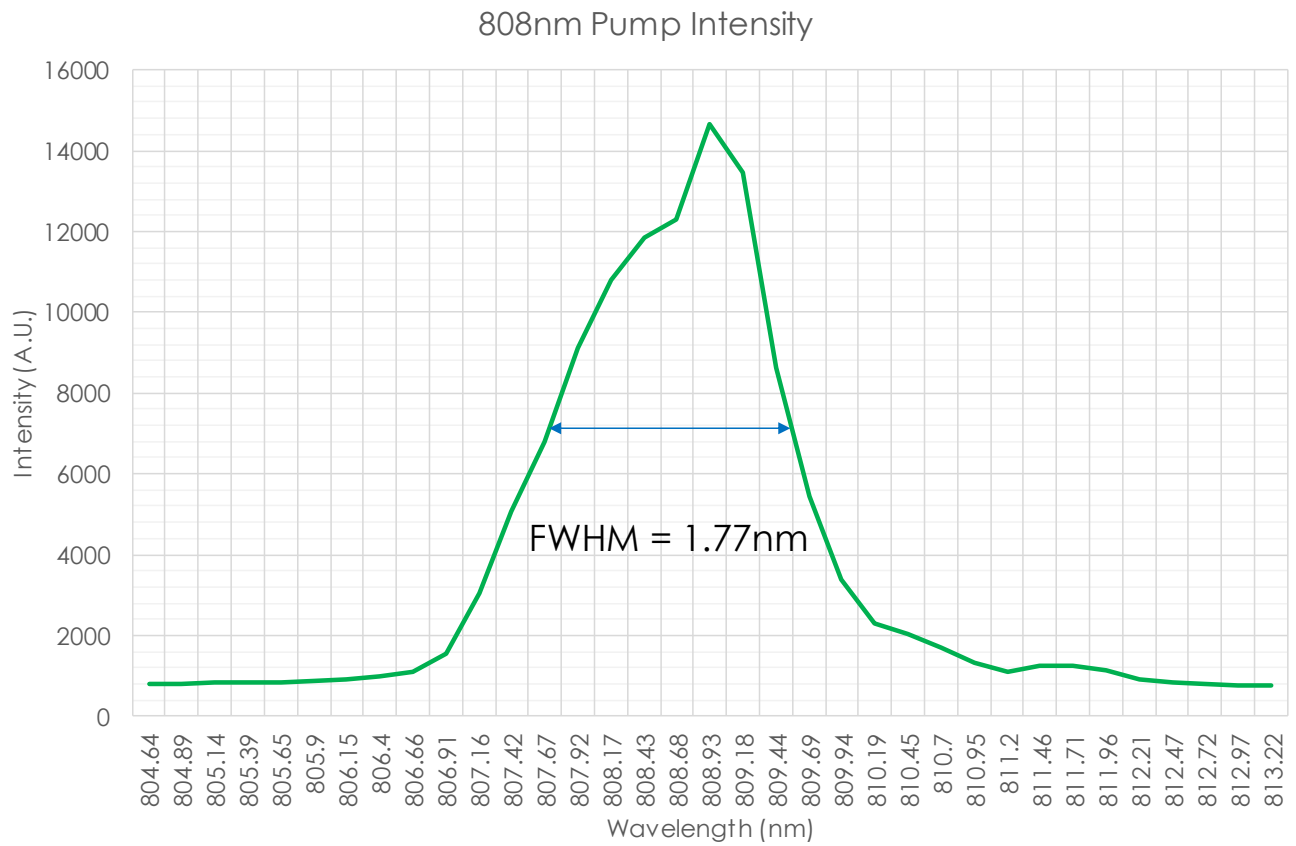


Figure C.7.3: Thermally Stabilized 808nm Pump Laser Spectra

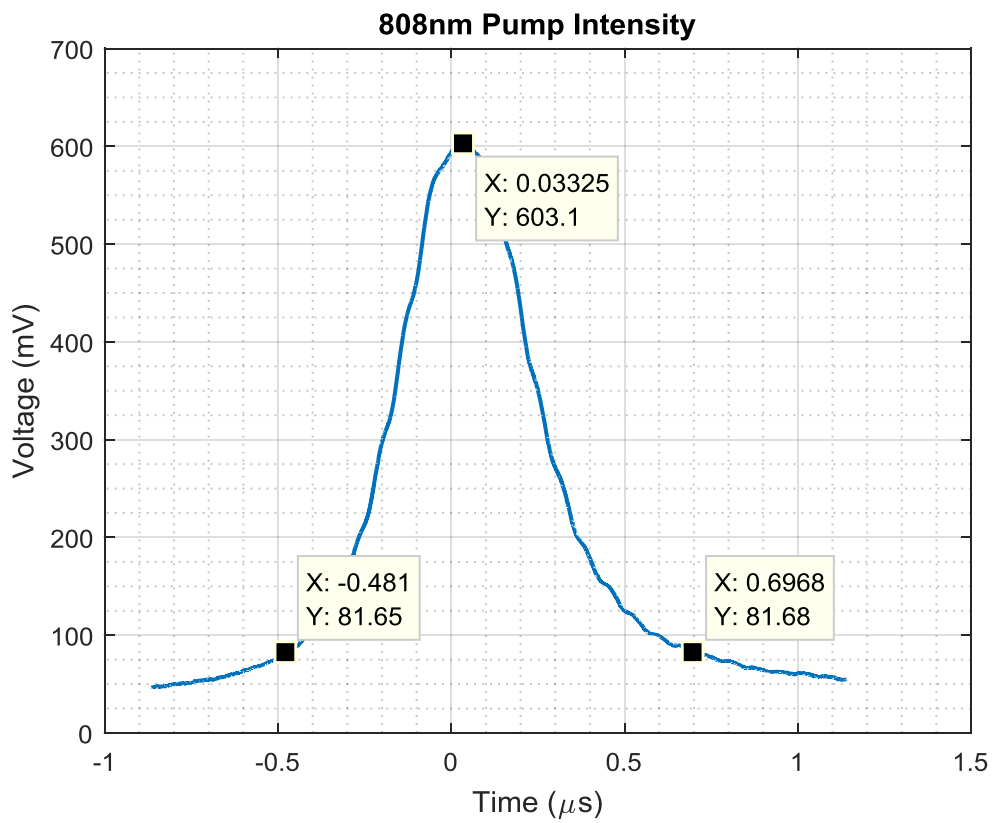


Figure C.7.4: Transient scan of 808nm pump beam. The Gaussian beam radius, using the  $e^{-2}$  definition, is  $75.65\mu\text{m}$ . The Rayleigh length is  $2.225\text{cm}$ . Assuming the beam is in the fundamental TEM mode and therefore symmetric, the intensity is  $50.058\text{ kW/cm}^2$ .

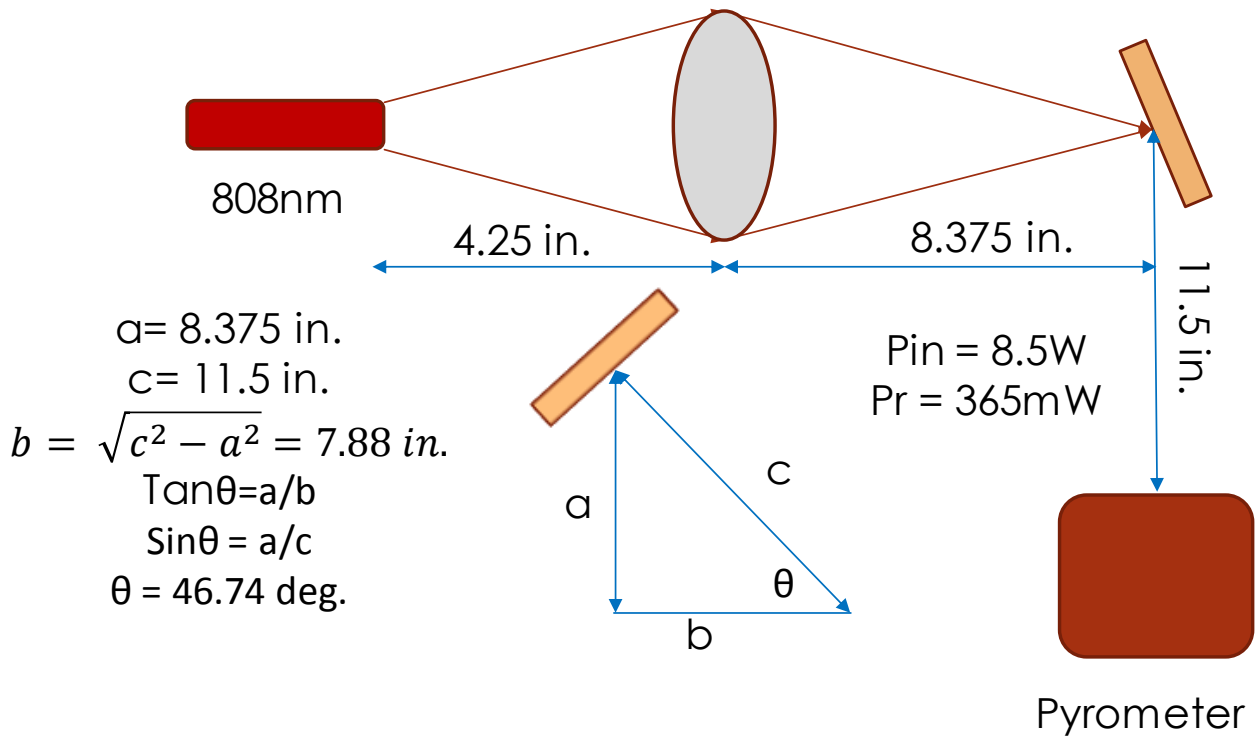


Figure C.7.5: Power reflection measurement off a 50% Er:YAG waveguide sample. The incident power is 8.5W from the 808nm laser diode with a reflected power of 365mW corresponding to a reflection loss of 4.29%. The figure with the triangle is a visual aid in deriving the corresponding incident angle using trigonometry.

## Appendix D: Simulation Code

### D.1 Rate Equation Code

```
clc;
clear all;
close all;
%% Constants
%T1 = 6400E-06; % In seconds
T1 = 1100E-06; % Alternate lifetime on newer samples
T2 = 100E-06; % In seconds
T3 = 0.05E-06;% In seconds
T4 = 1.5E-06;% In seconds
T5 = 16.7E-06;% In seconds
alpha = 0.2;%
beta = 0.04;%
tau = beta*T1/(alpha*T2); % dimensionless lifetime
beta21 = 1;
w11 = 1.3E-15; %cm^-3s^-1
w22 = 3.7E-15; %cm^-3s^-1
w50 = 1.06E-15;%cm^-3s^-1
w54 = 5.56E4; % s^-1
a54 = 0.6; % s^-1
a53 = 60.5; % s^-1
a52 = 31.8; % s^-1
a51 = 446.6; % s^-1
a50 = 1075.5; % s^-1
a20 = 110.8; % s^-1
%Rp = 6.72E+20; %cm^-3*s^-1 (10KW*cm^-2 at 962nm)
I0 = 10E3; % Pump Intensity in Watts/cm^2
I = I0;
h = 6.62606957E-34; % Planck constant (m^2kg/s)
c = 299792458;% Speed of light (m/s)
lambdaP1 = 962E-9;% Wavelength of pump light (m)
lambdaP2 = 808E-9;
lambdaP3 = 2940E-9;
n0 = 1; % Refractive index of air
n1 = 1.8168; % Refractive Index @ 962nm 50% Er:YAG
n2 = 1.8212; % Refractive Index @ 808nm 50% Er:YAG
vP = c/(n1*lambdaP1);% Frequency of pump (Hz)
N0 = 7.1E+21; % cm^-3 (50% doping from synoptics)
sigma21 = 1.8E-20; % cm^2 emission cross section (Georgescu 800nm)
sigma12 = 2.6E-20; % cm^2 GSA cross section (Georgescu 800nm)
ab1 = 40; % cm^-1 absorption constant @ 962nm (Liu) 50% Er:YAG
ab2 = 4.0; % cm^-1 absorption constant @ 808nm (NGAS) 50% Er:YAG
rm = 4.56; % gram*cm^-3 material density {from synoptics}
% Y3Al5O12 Y = 3*88.90585, Al = 5*26.981539, O = 12*15.9994
M = 593.618; % gram*mol^-1 molecular weight (3*Y + 5*Al + 12*O)
Na = 6.022E23; % atoms*mol^-1 Avragadros number
N = (rm*Na)/M; % atoms*cm^-3 atomic number density
sigma02 = 2*ab1/N; % cm^2 absorption cross section (962nm)
sigma03 = 2*ab2/N; % cm^2 absorption cross section (808nm)
sigmax = 2E-21; % cm^2 ESA cross section (Georgescu 0.5%) (800nm pump)
sigmay = 3.7E-21; % cm^2 ESA cross section (Huber 2%) (800nm pump)
```

```

sigmaESA = 2.9284E-17; % cm^2 ESA cross section 50% Er:YAG (962nm Probe)
% @10kW/cm^2
sigmaESA2 = 1.1854E-18; % cm^2 ESA cross section 50% Er:YAG (962nm Probe)
% @50kW/cm^2
RESA = 855; % s^-1 ESA rate (Brad)
alpha15 = 8.55E-2; % cm^2 ESA cross section @ 962nm 10kW/cm^2 (Brad)
% alphax = % cm^2 ESA cross section @ 808nm 1kW/cm^2 (Brad)
% Rp = sigma03*I/(h*vP); % Pump rate 808nm
Rp = sigma02*I/(h*vP); % Pump rate 962nm
% Rp = sigma12*I/(h*vP); % Pump rate 962nm (Georgescu)
ro = 0.01:0.001:0.05; % Round trip cavity loss
p = beta/alpha*sqrt(w22/w11); % Figure of merit

t = (2*w22*beta*T1/alpha^2)*ro/sigma21;
u = 2*w22*T1^2*((w22/alpha^2)*(ro.^2/sigma21^2) +
1/(alpha*T2)*(ro/sigma21));

%% Oscillation Threshold
% s0 = 2*w11*T1^2*Rp*N0; % Intrinsic Oscillation Threshold
s0 = (2*(tau-1)*(1-p^2+tau))/((2-p^2)^2);
s = s0 + u/(1-p^2) + (2*t.^2+(t-u).*(1-p^2-t+tau))/((1-p^2)^2) + ...
((t+tau).*(1-p^2+t+tau).*sqrt(1+2*u.*(1-p^2)/((t+tau).^2)))/((1-p^2)^2);

figure
plot(ro,100*s0./s,'Linewidth',1.5)
title('Ratio of Intrinsic Oscillation Threshold to Oscillation Threshold')
xlabel('Round Trip Cavity Loss (cm^{-1})')
ylabel('S_{o}/S (%)')
grid on
grid minor

%% Population Inversion
R = 0:0.5E+20:7E+20; % cm^{-3}s^{-1}
PoP = alpha*sqrt(2*R*N0/w22)*(1-p*sqrt(1/2)); % Equation 11 Georgescu
Modeling Paper
% Approximate Population inversion using figure of merit and pump rate
figure
plot(R,PoP,R,ro(41)/sigma21,'Linewidth',1.5)
title('Approx. Population Inversion vs. Pump Rate')
xlabel('Pump In Rate (N_{2}) (cm^{-3}s^{-1})')
ylabel('\alpha N_{2}-\beta N_{1} (cm^{-3})')
grid on
grid minor

%% Quantum Efficiency
% Georgescu defined the quantum efficiency

%% Rate Equation Modeling
% Solving the rate equations from Georgescu iteratively using Euler method
% These equations do not consider ESA
% --- Equation Sets 7 (962nm),11(808nm)
% These equations do consider ESA
% --- Equation Sets 13(962nm),12(808nm)
dt = 1E-9; % Time step for Euler method (sec)
y = 0:dt:3E-03; % Time of simulation (sec)

```

```

%I = I0 + 100*randn(size(y)) + 0.05*I0*sqrt(2*pi*1E4*y,50);
%Rp = sigma*I/(h*vP); % Pump rate
Rp2 = zeros(size(y));
%Rp2(1,20000:(0.5*size(y,2)+20000)) = Rp;
Rp2(1,200000:1200000) = Rp;
%Rp2(1,600000:800000) = Rp;
%Rp2(1,1000000:1200000) = Rp;
N2 = zeros(size(y));
N1 = zeros(size(y));
N3 = zeros(size(y));
N4 = zeros(size(y));
N5 = zeros(size(y));
N0 = zeros(size(y));
phi = zeros(size(y));
Ip = zeros(size(y));
%Ip(1,200000:1200000) = I;
T = Rp2(1,200000:1200000);
Ip(1,200000:1200000) = I + 5E2*randn(size(T)); %with normally dist. white
noise
%Ip(1,200000:1200000) = I; %with no noise
%Ip(1,600000:800000) = I;
%Ip(1,1000000:1200000) = I;
lp = 2E-3; % in mm from Chen's paper
l = 2E-3; % in mm from Chen's paper
lz = 3E-3; % in mm from Chen's paper
T1 = 1100E-06; % Alternate lifetime on newer samples
alpha = 0.22;
beta = 0.05;

r0 = 0.0019; % Round trip cavity loss (Chen)
N0(1) = 7.1E+21; % cm^-3 (50% doping)
%R = awgn(Rp,10,'measured');
k = 0.1; % Coefficient of percentage of contribution of spontaneous emission
      % to photon flux
%dN2(1) = Rp*N0(1);
%dN1(1) = 0;
%dN0(1) = -Rp*N0(1);

% Equations diverge
%{
% Custom Rate equation (diverges unfortunately) Set 1
% No ESA included
for z = 1:(size(y,2)-1)
    N2(1+z) = N2(z) + y(z)*(-N2(z)/T2 + w11*N1(z)*N1(z) - w22*N2(z)*N2(z) +
Rp*N0(z));
    N1(1+z) = N1(z) + y(z)*(-N1(z)/T1 + N2(z)/T2 - 2*w11*N1(z)*N1(z));
    N0(1+z) = N0(z) + y(z)*(-Rp*N0(z) + w11*N1(z)*N1(z) + w22*N2(z)*N2(z));
end
%}
% Georgescu's Simplified 2 Level Model (Set 2)
% No ESA included
%{
for z = 1:(size(y,2)-1)

```

```

N2(1+z) = N2(z) + dt*(-N2(z)/T2 + w11*N1(z)*N1(z) - w22*N2(z)*N2(z) + ...
Rp*N0(1) - sigma*phi(z)*(alpha*N2(z) - beta*N1(z)));
N1(1+z) = N1(z) + dt*(-N1(z)/T1 + N2(z)/T2 - 2*w11*N1(z)*N1(z) + ...
w22*N2(z)*N2(z) + sigma*phi(z)*(alpha*N2(z) - beta*N1(z)));
phi(1+z) = phi(z) + dt*(k*N2(z)/T2);
end
%}
% Georgescu's Simplified 5 Level Model (Set 3)
% No ESA included (Main Model)
%{
for z = 1:(size(y,2)-1)
N5(1+z) = N5(z) + dt*(-N5(z)/T5 - w50*N0(1)*N5(z) + w22*N2(z)*N2(z));
N4(1+z) = N4(z) + dt*(-N4(z)/T4 + N5(z)/T5);
N3(1+z) = N3(z) + dt*(-N3(z)/T3 + N4(z)/T4 + w11*N1(z)*N1(z) + ...
w50*N0(1)*N5(z));
N2(1+z) = N2(z) + dt*(-N2(z)/T2 + N3(z)/T3 - 2*w22*N2(z)*N2(z) + ...
Rp2(z)*N0(1));
N1(1+z) = N1(z) + dt*(-N1(z)/T1 + N2(z)/T2 - 2*w11*N1(z)*N1(z) + ...
w50*N0(1)*N5(z));
end
%}
%{
% Georgescu's Simplified 5 Level Model (Set 4)
% ESA included (uses Brad Liu's values) (diverges)
R25 = 809E6; % in s^-1
R15 = 809E6; % in s^-1
for z = 1:(size(y,2)-1)
N5(1+z) = N5(z) + dt*(-N5(z)/T5 - w50*N0(1)*N5(z) + w22*N2(z)*N2(z) + ...
R25*N2(z) + R15*N1(z));
N4(1+z) = N4(z) + dt*(-N4(z)/T4 + N5(z)/T5);
N3(1+z) = N3(z) + dt*(-N3(z)/T3 + N4(z)/T4 + w11*N1(z)*N1(z) + ...
w50*N0(1)*N5(z));
N2(1+z) = N2(z) + dt*(-N2(z)/T2 + N3(z)/T3 - 2*w22*N2(z)*N2(z) + ...
Rp*N0(1) - R25*N2(z));
N1(1+z) = N1(z) + dt*(-N1(z)/T1 + N2(z)/T2 - 2*w11*N1(z)*N1(z) + ...
w50*N0(1)*N5(z) - R25*N2(z));
end
%}
%{
% Georgescu's Simplified 5 Level Model (Set 5)
% No ESA included
% No Cavity (Just Fluorescence)
% Accounts for changing N0
for z = 1:(size(y,2)-1)
N5(1+z) = N5(z) + dt*(-N5(z)/T5 - w50*N0(z)*N5(z) + w22*N2(z)*N2(z));
N4(1+z) = N4(z) + dt*(-N4(z)/T4 + N5(z)/T5);
N3(1+z) = N3(z) + dt*(-N3(z)/T3 + N4(z)/T4 + w11*N1(z)*N1(z) + ...
w50*N0(z)*N5(z));
N2(1+z) = N2(z) + dt*(-N2(z)/T2 + N3(z)/T3 - 2*w22*N2(z)*N2(z) + ...
Rp2(z)*N0(z));
N1(1+z) = N1(z) + dt*(-N1(z)/T1 + N2(z)/T2 - 2*w11*N1(z)*N1(z) + ...
w50*N0(z)*N5(z));
N0(1+z) = N0(z) + dt*(-w50*N0(z)*N5(z) + 1*w22*N2(z)*N2(z) + ...
1*w11*N1(z)*N1(z) - Rp2(z)*N0(z) + N1(z)/T1);
end

```

```

%}

% Georgescu's Simplified 5 Level Model (Set 6)
% No ESA included
% Laser Resonator (Chen)
%{
for z = 1:(size(y,2)-1)
    N5(1+z) = N5(z) + dt*(-N5(z)/T5 - w50*N0(1)*N5(z) + w22*N2(z)*N2(z));
    N4(1+z) = N4(z) + dt*(-N4(z)/T4 + N5(z)/T5);
    N3(1+z) = N3(z) + dt*(-N3(z)/T3 + N4(z)/T4 + w11*N1(z)*N1(z) + ...
        w50*N0(1)*N5(z));
    N2(1+z) = N2(z) + dt*(-N2(z)/T2 + N3(z)/T3 - 2*w22*N2(z)*N2(z) + ...
        Rp2(z)*N0(1));
    N1(1+z) = N1(z) + dt*(-N1(z)/T1 + N2(z)/T2 - 2*w11*N1(z)*N1(z) + ...
        w50*N0(1)*N5(z));
    phi(1+z) = phi(z) + dt*(c*phi(z)*lp/(1z+(n-1)*1)*(sigma*(alpha*N2(z) ...
        - beta*N1(z)) - r0) + k*N2(z)/T2);
end
%}

%{
% Georgescu's Simplified 5 Level Model (Set 7)
% No ESA included 962nm Pump
% Ground State evolution accounted for
% Pump evolution accounted for
for z = 1:(size(y,2)-1)
    N5(1+z) = N5(z) + dt*(-N5(z)/T5 - w50*N0(z)*N5(z) + w22*N2(z)*N2(z));
    N4(1+z) = N4(z) + dt*(-N4(z)/T4 + N5(z)/T5);
    N3(1+z) = N3(z) + dt*(-N3(z)/T3 + N4(z)/T4 + w11*N1(z)*N1(z) + ...
        w50*N0(z)*N5(z));
    N2(1+z) = N2(z) + dt*(-N2(z)/T2 + N3(z)/T3 - 2*w22*N2(z)*N2(z) + ...
        sigma02*Ip(z)*N0(z)/(h*vP));
    N1(1+z) = N1(z) + dt*(-N1(z)/T1 + N2(z)/T2 - 2*w11*N1(z)*N1(z) + ...
        w50*N0(z)*N5(z));
    N0(1+z) = N0(z) + dt*(-w50*N0(z)*N5(z) + 1*w22*N2(z)*N2(z) + ...
        1*w11*N1(z)*N1(z) - sigma02*Ip(z)*N0(z)/(h*vP) + N1(z)/T1);
    %Ip(1+z) = Ip(z) + dt*(-sigma02*Ip(z)*N0(z) + a20*N2(z)*h*vP);
end
%}

%{
% Georgescu's Simplified 5 Level Model (Set 8)
% No ESA included
% Ground State evolution accounted for
% Pump evolution accounted for
% Green Fluorescence looked accounted for
for z = 1:(size(y,2)-1)
    N5(1+z) = N5(z) + dt*(-N5(z)*(a50 + a51 + a52 + a53 + a54 + w54) - ...
        w50*N0(z)*N5(z) + w22*N2(z)*N2(z));
    N4(1+z) = N4(z) + dt*(-N4(z)/T4 + N5(z)*(a54 + w54));
    N3(1+z) = N3(z) + dt*(-N3(z)/T3 + N4(z)/T4 + w11*N1(z)*N1(z) + ...
        w50*N0(z)*N5(z) + a53*N5(z));
    N2(1+z) = N2(z) + dt*(-N2(z)/T2 + N3(z)/T3 - 2*w22*N2(z)*N2(z) + ...
        sigma02*Ip(z)*N0(z)/(h*vP) + a52*N5(z));
    N1(1+z) = N1(z) + dt*(-N1(z)/T1 + N2(z)/T2 - 2*w11*N1(z)*N1(z) + ...

```

```

        w50*N0(z)*N5(z) + a51*N5(z));
    N0(1+z) = N0(z) + dt*(-w50*N0(z)*N5(z) + 1*w22*N2(z)*N2(z) + ...
        1*w11*N1(z)*N1(z) - sigma02*Ip(z)*N0(z)/(h*vP) + N1(z)/T1 +
a50*N5(z));
end
%}
%k1 = find(abs(N1-0.1*max(N1)) < 1E-4);

%{
% Georgescu's Simplified 5 Level Model (Set 9)
% ESA included (Georgescu #)808nm pump
% Ground State evolution accounted for
%
for z = 1:(size(y,2)-1)
    N5(1+z) = N5(z) + dt*(-N5(z)/T5 - w50*N0(z)*N5(z) + w22*N2(z)*N2(z) +
sigma*x*Ip(z)*N1(z)/(h*vP));
    N4(1+z) = N4(z) + dt*(-N4(z)/T4 + N5(z)/T5);
    N3(1+z) = N3(z) + dt*(-N3(z)/T3 + N4(z)/T4 + w11*N1(z)*N1(z) + ...
        w50*N0(z)*N5(z)+ sigma03*Ip(z)*N0(z)/(h*vP));
    N2(1+z) = N2(z) + dt*(-N2(z)/T2 + N3(z)/T3 - 2*w22*N2(z)*N2(z));
    N1(1+z) = N1(z) + dt*(-N1(z)/T1 + N2(z)/T2 - 2*w11*N1(z)*N1(z) + ...
        w50*N0(z)*N5(z)- sigma*x*Ip(z)*N1(z)/(h*vP));
    N0(1+z) = N0(z) + dt*(-w50*N0(z)*N5(z) + 1*w22*N2(z)*N2(z) + ...
        1*w11*N1(z)*N1(z) - sigma03*Ip(z)*N0(z)/(h*vP) + N1(z)/T1);
    %Ip(1+z) = Ip(z) + dt*(-sigma02*Ip(z)*N0(z) + a20*N2(z)*h*vP);
end
%}

%{
% Georgescu's Simplified 5 Level Model (Set 10)
% ESA included (Brads #) 962nm pump
% Ground State evolution accounted for
% Pump evolution accounted for
for z = 1:(size(y,2)-1)
    N5(1+z) = N5(z) + dt*(-N5(z)/T5 - w50*N0(z)*N5(z) + w22*N2(z)*N2(z));
    N4(1+z) = N4(z) + dt*(-N4(z)/T4 + N5(z)/T5 + alpha15*Ip(z)*N1(z));
    N3(1+z) = N3(z) + dt*(-N3(z)/T3 + N4(z)/T4 + w11*N1(z)*N1(z) + ...
        w50*N0(z)*N5(z));
    N2(1+z) = N2(z) + dt*(-N2(z)/T2 + N3(z)/T3 - 2*w22*N2(z)*N2(z) + ...
        sigma02*Ip(z)*N0(z)/(h*vP));
    N1(1+z) = N1(z) + dt*(-N1(z)/T1 + N2(z)/T2 - 2*w11*N1(z)*N1(z) + ...
        w50*N0(z)*N5(z)- alpha15*Ip(z)*N1(z));
    N0(1+z) = N0(z) + dt*(-w50*N0(z)*N5(z) + 1*w22*N2(z)*N2(z) + ...
        1*w11*N1(z)*N1(z) - sigma02*Ip(z)*N0(z)/(h*vP) + N1(z)/T1);
    %Ip(1+z) = Ip(z) + dt*(-sigma02*Ip(z)*N0(z) + a20*N2(z)*h*vP);
end
%}

%{
% Georgescu's Simplified 5 Level Model (Set 11)
% ESA not included (Georgescu)808nm pump
% Ground State evolution accounted for
% Pump evolution accounted for
for z = 1:(size(y,2)-1)
    N5(1+z) = N5(z) + dt*(-N5(z)/T5 - w50*N0(z)*N5(z) + w22*N2(z)*N2(z));

```

```

N4(1+z) = N4(z) + dt*(-N4(z)/T4 + N5(z)/T5);
N3(1+z) = N3(z) + dt*(-N3(z)/T3 + N4(z)/T4 + w11*N1(z)*N1(z) + ...
    w50*N0(z)*N5(z)+ sigma03*Ip(z)*N0(z)/(h*vP));
N2(1+z) = N2(z) + dt*(-N2(z)/T2 + N3(z)/T3 - 2*w22*N2(z)*N2(z));
N1(1+z) = N1(z) + dt*(-N1(z)/T1 + N2(z)/T2 - 2*w11*N1(z)*N1(z) + ...
    w50*N0(z)*N5(z));
N0(1+z) = N0(z) + dt*(-w50*N0(z)*N5(z) + 1*w22*N2(z)*N2(z) + ...
    1*w11*N1(z)*N1(z) - sigma03*Ip(z)*N0(z)/(h*vP) + N1(z)/T1);
%Ip(1+z) = Ip(z) + dt*(-sigma02*Ip(z)*N0(z) + a20*N2(z)*h*vP);
end
%}

% Georgescu's Simplified 5 Level Model (Set 12)
% ESA included (Georgescu)808nm pump sigmax
% ESA from Huber use alphas
% Ground State evolution accounted for
% Pump evolution accounted for
for z = 1:(size(y,2)-1)
    N5(1+z) = N5(z) + dt*(-N5(z)/T5 - w50*N0(z)*N5(z) + w22*N2(z)*N2(z)+
    sigmay*Ip(z)*N1(z));
    N4(1+z) = N4(z) + dt*(-N4(z)/T4 + N5(z)/T5);
    N3(1+z) = N3(z) + dt*(-N3(z)/T3 + N4(z)/T4 + w11*N1(z)*N1(z) + ...
        w50*N0(z)*N5(z)+ sigma03*Ip(z)*N0(z)/(h*vP));
    N2(1+z) = N2(z) + dt*(-N2(z)/T2 + N3(z)/T3 - 2*w22*N2(z)*N2(z));
    N1(1+z) = N1(z) + dt*(-N1(z)/T1 + N2(z)/T2 - 2*w11*N1(z)*N1(z) + ...
        w50*N0(z)*N5(z)- sigmay*Ip(z)*N1(z));
    N0(1+z) = N0(z) + dt*(-w50*N0(z)*N5(z) + 1*w22*N2(z)*N2(z) + ...
        1*w11*N1(z)*N1(z) - sigma03*Ip(z)*N0(z)/(h*vP) + N1(z)/T1);
    %Ip(1+z) = Ip(z) + dt*(-sigma02*Ip(z)*N0(z) + a20*N2(z)*h*vP);
end

%{
% Georgescu's Simplified 5 Level Model (Set 13)
% ESA included (Measured #) 962nm pump
% Ground State evolution accounted for
% Pump evolution accounted for
% sigma02 is calculated GSA for 962nm pump
for z = 1:(size(y,2)-1)
    N5(1+z) = N5(z) + dt*(-N5(z)/T5 - w50*N0(z)*N5(z) + w22*N2(z)*N2(z)+
    sigmaESA*Ip(z)*N1(z));
    N4(1+z) = N4(z) + dt*(-N4(z)/T4 + N5(z)/T5);
    N3(1+z) = N3(z) + dt*(-N3(z)/T3 + N4(z)/T4 + w11*N1(z)*N1(z) + ...
        w50*N0(z)*N5(z));
    N2(1+z) = N2(z) + dt*(-N2(z)/T2 + N3(z)/T3 - 2*w22*N2(z)*N2(z) + ...
        sigma02*Ip(z)*N0(z)/(h*vP) - sigmaESA*Ip(z)*N1(z));
    N1(1+z) = N1(z) + dt*(-N1(z)/T1 + N2(z)/T2 - 2*w11*N1(z)*N1(z) + ...
        w50*N0(z)*N5(z));
    N0(1+z) = N0(z) + dt*(-w50*N0(z)*N5(z) + 1*w22*N2(z)*N2(z) + ...
        1*w11*N1(z)*N1(z) - sigma02*Ip(z)*N0(z)/(h*vP) + N1(z)/T1);
    %Ip(1+z) = Ip(z) + dt*(-sigma02*Ip(z)*N0(z) + a20*N2(z)*h*vP);
end
%}

```

```

%{
% Georgescu's Simplified 5 Level Model (Set 14)
% ESA included (Measured #) 962nm pump
% Ground State evolution accounted for
% Pump evolution accounted for
% sigma02 is calculated GSA for 962nm pump
% Modified version of set 13 includes individual contributions of N5,N2
for z = 1:(size(y,2)-1)
    N5(1+z) = N5(z) + dt*(-N5(z)*(a50 + a51 + a52 + a53 + a54 + w54) - ...
        w50*N0(z)*N5(z) + w22*N2(z)*N2(z) + sigmaESA*Ip(z)*N1(z));
    N4(1+z) = N4(z) + dt*(-N4(z)/T4 + N5(z)*(a54 + w54));
    N3(1+z) = N3(z) + dt*(-N3(z)/T3 + N4(z)/T4 + w11*N1(z)*N1(z) + ...
        w50*N0(z)*N5(z) + a53*N5(z));
    N2(1+z) = N2(z) + dt*(-N2(z)/T2 + N3(z)/T3 - 2*w22*N2(z)*N2(z) + ...
        sigma02*Ip(z)*N0(z)/(h*vP) - sigmaESA*Ip(z)*N1(z) + a52*N5(z));
    N1(1+z) = N1(z) + dt*(-N1(z)/T1 + N2(z)/T2 - 2*w11*N1(z)*N1(z) + ...
        w50*N0(z)*N5(z) + a51*N5(z));
    N0(1+z) = N0(z) + dt*(-w50*N0(z)*N5(z) + 1*w22*N2(z)*N2(z) + ...
        1*w11*N1(z)*N1(z) - sigma02*Ip(z)*N0(z)/(h*vP) + N1(z)/T1 +
a50*N5(z));
    %Ip(1+z) = Ip(z) + dt*(-sigma02*Ip(z)*N0(z) + a20*N2(z)*h*vP);
end
%}

%{
% Georgescu's Simplified 5 Level Model (Set 15)
% ESA included (Georgescu)808nm pump sigmax
% ESA from Huber use alphas
% Ground State evolution accounted for
% Pump evolution accounted for
Modified version of set 12 includes individual contributions of N5,N2,N1
for z = 1:(size(y,2)-1)
    N5(1+z) = N5(z) + dt*(-N5(z)/T5 - w50*N0(z)*N5(z) + w22*N2(z)*N2(z) +
sigmay*Ip(z)*N1(z));
    N4(1+z) = N4(z) + dt*(-N4(z)/T4 + N5(z)/T5);
    N3(1+z) = N3(z) + dt*(-N3(z)/T3 + N4(z)/T4 + w11*N1(z)*N1(z) + ...
        w50*N0(z)*N5(z) + sigma03*Ip(z)*N0(z)/(h*vP));
    N2(1+z) = N2(z) + dt*(-N2(z)/T2 + N3(z)/T3 - 2*w22*N2(z)*N2(z));
    N1(1+z) = N1(z) + dt*(-N1(z)/T1 + N2(z)/T2 - 2*w11*N1(z)*N1(z) + ...
        w50*N0(z)*N5(z) - sigmay*Ip(z)*N1(z));
    N0(1+z) = N0(z) + dt*(-w50*N0(z)*N5(z) + 1*w22*N2(z)*N2(z) + ...
        1*w11*N1(z)*N1(z) - sigma03*Ip(z)*N0(z)/(h*vP) + N1(z)/T1);
    %Ip(1+z) = Ip(z) + dt*(-sigma02*Ip(z)*N0(z) + a20*N2(z)*h*vP);
end
%}

figure
plot(y*1E6,Rp2, 'Linewidth',1.5)
xlim([0 2000])
title('Input Pump Rate (R_{P2})')
xlabel('Time (\mus)')
ylabel('Rate (cm^{-3})')
grid on
grid minor

```

```

figure
plot(y*1E6,Ip, 'Linewidth',1.5)
xlim([0 2000])
title('Input Pump Intensity (I_{P})')
xlabel('Time (\mus)')
ylabel('Intensity (W/cm^{2})')
grid on
grid minor

figure
plot(y*1E6,N1, 'Linewidth',1.5)
xlim([0 2000])
title('Terminal Level Population (N_{1})')
xlabel('Time (\mus)')
ylabel('Population (cm^{-3})')
grid on
grid minor

figure
semilogy(y*1E6,N1, 'Linewidth',1.5)
xlim([0 2000])
title('Terminal Level Population (N_{1})')
xlabel('Time (\mus)')
ylabel('Population (cm^{-3})')
grid on
grid minor

figure
plot(y*1E6,N2, 'Linewidth',1.5)
xlim([0 2000])
title('Initial Level Population (N_{2})')
xlabel('Time (\mus)')
ylabel('Population (cm^{-3})')
grid on
grid minor
% Test the decay to show it is not single exponential
K1 = N2(1200000:2000000);
q = 0:(length(K1)-1);
K2 = N2(1200000)*exp(-q);
figure
semilogy(q*1E-3,K1, 'Linewidth',1.5)
%plot(q*1E-3,K1, 'Linewidth',1.5)
title('Initial Level Population Decay (N_{2})')
xlabel('Time (\mus)')
ylabel('Population (cm^{-3})')
grid on
grid minor

figure
semilogy(y*1E6,N2, 'Linewidth',1.5)
xlim([0 2000])
title('Initial Level Population (N_{2})')
xlabel('Time (\mus)')
ylabel('Population (cm^{-3})')
grid on

```

```

grid minor

P_I = alpha*N2 - beta*N1; % Population inversion using the calculated ...
% from the rate equations
figure
plot(y*1E6,P_I, 'Linewidth',1.5)
xlim([0 2000])
title('Population Inversion')
xlabel('Time (\mus)')
ylabel('\alphaN_{2}-\betaN_{1} (cm^{-3})')
grid on
grid minor

figure
semilogy(y*1E6,P_I, 'Linewidth',1.5)
xlim([0 2000])
title('Population Inversion')
xlabel('Time (\mus)')
ylabel('\alphaN_{2}-\betaN_{1} (cm^{-3})')
grid on
grid minor

figure
plot(y*1E6,N0, 'Linewidth',1.5)
xlim([0 2000])
title('Ground Level Population (N_{0})')
xlabel('Time (\mus)')
ylabel('Population (cm^{-3})')
grid on
grid minor

figure
semilogy(y*1E6,N0, 'Linewidth',1.5)
xlim([0 2000])
title('Ground Level Population (N_{0})')
xlabel('Time (us)')
ylabel('Population (cm^{-3})')
grid on
grid minor

figure
plot(y*1E6,N5, 'Linewidth',1.5)
xlim([0 2000])
title('Green Level Population (N_{5})')
xlabel('Time (\mus)')
ylabel('Population (cm^{-3})')
grid on
grid minor
% Test the decay to show it is not single exponential
K3 = N5(1200000:2000000);
q1 = 0:(length(K3)-1);
K4 = N5(1200000)*exp(-q1);
figure
semilogy(q1*1E-3,K3, 'Linewidth',1.5)
%plot(q1*1E-3,K1, 'Linewidth',1.5)

```

```

title('Green Level Population Decay (N_{5})')
xlabel('Time (\mus)')
ylabel('Population (cm^{-3})')
grid on
grid minor

figure
semilogy(y*1E6,N5, 'Linewidth',1.5)
xlim([0 2000])
title('Green Level Population (N_{5})')
xlabel('Time (us)')
ylabel('Population (cm^{-3})')
grid on
grid minor

[U1 V1] = max(N1);
[U2 V2] = max(N2);
[U3 V3] = max(N3);
[U4 V4] = max(N4);
[U5 V5] = max(N5);
[U V] = max(P_I);

%{
% Solving the rate equations symbolically
syms n1(x) n2(x) n3(x) n4(x) n5(x)
ode1 = diff(n1) == -n1/T1 + n2/T2 - 2*w11*n1*n1 + w50*N0(1)*n5;
ode2 = diff(n2) == -n2/T2 + n3/T3 - 2*w22*n2*n2 + Rp*N0(1);
ode3 = diff(n3) == -n3/T3 + n4/T4 + w11*n1*n1 + w50*N0(1)*n5;
ode4 = diff(n4) == -n4/T4 + n5/T5;
ode5 = diff(n5) == -n5/T5 - w50*N0(1)*n5 + w22*n2*n2;
odes = [ode1; ode2; ode3; ode4; ode5];
S = dsolve(odes);
%}
%% Brad Liu's Rate Equation Model
% Includes ESA Terms

%% Verify Beam Spot Size
% Following calculation of spot size of pump beam in transient scans
% look at page 77 of notebook
wo = 10E-6:1E-6:100E-6; % spot size in meters
zr = (pi/lambdaP1)*wo.*wo; % Rayleigh range
f = 15.24E-2; % Focal length of lens in meters
s1 = 0.5*f; % distance of fiber laser from lens (m)
a = 1;
b = -1*(f*(s1-f)*f*s1)/(s1-f);
c = f^2*s1/(s1-f) + zr.*zr;
sp = (-b + sqrt(b^2-4*a*c))/(2*a); % distance from lens to min spot size
sm = (-b - sqrt(b^2-4*a*c))/(2*a); % distance from lens to min spot size

figure
plot(wo*1E6,zr*1E2, 'Linewidth',1.5)
title('Beam Waist vs. Rayleigh Range')
xlabel('Beam Waist (\mum)')
ylabel('Rayleigh Range (cm)')
grid on

```

```

grid minor

figure
plot(wo*1E6, sp*1E2, 'Linewidth', 1.5)
title('Beam Waist vs. Beam Waist Distance')
xlabel('Beam Waist (\mum)')
ylabel('Beam Waist Distance From Lens (cm)')
grid on
grid minor

%% FFT
X = y(400000:1200000);
Y = N2(400000:1200000);

Fs = 1e9; % Sampling frequency (Hz)
T = 1/Fs; % Sampling period
L = length(Y); % Length of signal subtract last value to
get even length
t = (0:L-1)*T; % Time vector
f = Fs*(0:(L/2))/L;

F = fft(Y);
P2 = abs(F/L); % Two sided spectra
P1 = P2(1:L/2+1); % Single Sided Spectra
P1(2:end-1) = 2*P1(2:end-1);

figure
plot(f*1E-3, P1)
grid on
%xlim([0 6])
%ylim([0 0.001]) % adjust axis to fit window
title('FFT Of N_{2}');
xlabel('Frequency (kHz)');
ylabel('Magnititude (V)');

n = length(X);
fshift = (-n/2:n/2-1)*(Fs/n);
yshift = fftshift(F);

% N5 level
X1 = y(400000:1200000);
Y1 = N5(400000:1200000);

L1 = length(Y1); % Length of signal subtract last value to
get even length
t1 = (0:L1-1)*T; % Time vector
f1 = Fs*(0:(L1/2))/L1;

F1 = fft(Y1);
P4 = abs(F1/L1); % Two sided spectra
P3 = P4(1:L1/2+1); % Single Sided Spectra

```

```

P3(2:end-1) = 2*P3(2:end-1);

figure
plot(f1*1E-3,P3)
grid on
xlim([0 6])
ylim([0 0.001]) % adjust axis to fit window
title('FFT Of N_{5}');
xlabel('Frequency (kHz)');
ylabel('Magnitude (V)');

n1 = length(X1);
fshift1 = (-n1/2:n1/2-1)*(Fs/n1);
yshift1 = fftshift(F1);
%figure
%plot(fshift,abs(yshift))
%% Do FFT on Instability only
% Use cursor to find floor of the oscillation for every plot
%{
%W = find(Y>= 3.0475E18);
V = X(1080257:1200006);
Z = Y(1080257:1200006);
%V = X(W(1:245830));
%Z = Y(W(1:245830));
figure
plot(V,Z)
grid on
grid minor

Fs1 = 2e10; % Sampling frequency (Hz)
T1 = 1/Fs1; % Sampling period
L1 = length(Z); % Length of signal subtract last value to get even
length
t1 = (0:L1-1)*T1; % Time vector
f1 = Fs*(0:(L1/2))/L1;

F1 = fft(Z);
P4 = abs(F1/L1); % Two sided spectra
P3 = P4(1:L1/2+1); % Single Sided Spectra
P3(2:end-1) = 2*P3(2:end-1);

figure
plot(f1,P3)
grid on
grid minor
%axis([0 1E6 0 max(P3)]) % adjust axis to fit window
%}

```

## D.2 ESA Measurement Code

```
clear all;
close all;
clc;
%% Measuring the ESA Cross Section

Wv = xlsread('C:\Users\HomePC\Documents\QE Lab\Thesis\Er_YAG
Data\Er_YAG_50_Per_WG\1ms Pulse\808nm
Pump\No_3um\ESA\8_8_2018\C2Er_YAG_50Per_ESA00004.csv');
Wv1 = xlsread('C:\Users\HomePC\Documents\QE Lab\Thesis\Er_YAG
Data\Er_YAG_50_Per_WG\1ms Pulse\808nm
Pump\No_3um\ESA\8_8_2018\C2Er_YAG_50Per_ESA00005.csv');

X = Wv(1:length(Wv(:,3)),3);
Y = Wv(1:length(Wv(:,4)),4);
figure
plot(X*1E03,Y)
title('962nm Probe Transmission Through 50% Er:YAG Wave Guide')
xlabel('Time (ms)')
ylabel('Voltage (V)')
xlim([X(1)*1E03 X(length(X))*1E03])
grid on
grid minor

X1 = Wv1(1:length(Wv1(:,3)),3);
Y1 = Wv1(1:length(Wv1(:,4)),4);
figure
plot(X1*1E03,Y1)
title('962nm Probe Transmission Through 50% Er:YAG Wave Guide')
xlabel('Time (ms)')
ylabel('Voltage (V)')
xlim([X1(1)*1E03 X1(length(X1))*1E03])
grid on
grid minor

%%
Vp = cursor_info1(2).Position(2) - cursor_info1(2).Position(1);
Vu = cursor_info1(2).Position(1) - cursor_info1(2).Position(2);
DV = Vp-Vu;
ne = 13.68E19;
L = 500E-6;
sigmaGSA = 2.6E-20;
sigmaEM = 1.8E-20;
sigmaESA = sigmaGSA + sigmaEM - DV/(Vu*ne*L);
```

## D.3 Transient Scan Code

```
clear all;
close all;
clc;

%% Load files from File Directory

%{
% 1 Percent Er:YAG Pillbox 808nm CW
% 1 Giga Samples/sec
Hv0 = 'C:\Users\HomePC\Documents\QE Lab\Thesis\Er_YAG
Data\Er_YAG_1_Per_Pillbox\CW Scan\808nm
Pump\No_3um\4_28_2018\C2Er_YAG_1Per_11I2_808nm_CW00000.csv';
Hv1 = 'C:\Users\HomePC\Documents\QE Lab\Thesis\Er_YAG
Data\Er_YAG_1_Per_Pillbox\CW Scan\808nm
Pump\No_3um\4_28_2018\C2Er_YAG_1Per_11I2_808nm_CW00001.csv';
Hv2 = 'C:\Users\HomePC\Documents\QE Lab\Thesis\Er_YAG
Data\Er_YAG_1_Per_Pillbox\CW Scan\808nm
Pump\No_3um\4_28_2018\C2Er_YAG_1Per_11I2_808nm_CW00002.csv';
Hv3 = 'C:\Users\HomePC\Documents\QE Lab\Thesis\Er_YAG
Data\Er_YAG_1_Per_Pillbox\CW Scan\808nm
Pump\No_3um\4_28_2018\C2Er_YAG_1Per_11I2_808nm_CW00003.csv';
Hv4 = 'C:\Users\HomePC\Documents\QE Lab\Thesis\Er_YAG
Data\Er_YAG_1_Per_Pillbox\CW Scan\808nm
Pump\No_3um\4_28_2018\C2Er_YAG_1Per_11I2_808nm_CW00004.csv';

Hu0 = 'C:\Users\HomePC\Documents\QE Lab\Thesis\Er_YAG
Data\Er_YAG_1_Per_Pillbox\CW Scan\808nm
Pump\No_3um\4_28_2018\C4Er_YAG_1Per_11I2_808nm_CW00000.csv';
Hu1 = 'C:\Users\HomePC\Documents\QE Lab\Thesis\Er_YAG
Data\Er_YAG_1_Per_Pillbox\CW Scan\808nm
Pump\No_3um\4_28_2018\C4Er_YAG_1Per_11I2_808nm_CW00001.csv';
Hu2 = 'C:\Users\HomePC\Documents\QE Lab\Thesis\Er_YAG
Data\Er_YAG_1_Per_Pillbox\CW Scan\808nm
Pump\No_3um\4_28_2018\C4Er_YAG_1Per_11I2_808nm_CW00002.csv';
Hu3 = 'C:\Users\HomePC\Documents\QE Lab\Thesis\Er_YAG
Data\Er_YAG_1_Per_Pillbox\CW Scan\808nm
Pump\No_3um\4_28_2018\C4Er_YAG_1Per_11I2_808nm_CW00003.csv';
Hu4 = 'C:\Users\HomePC\Documents\QE Lab\Thesis\Er_YAG
Data\Er_YAG_1_Per_Pillbox\CW Scan\808nm
Pump\No_3um\4_28_2018\C4Er_YAG_1Per_11I2_808nm_CW00004.csv';
%}

% 50 Percent Er:YAG Pillbox 808nm Pulsed
% 500 Mega samples/sec
Hv0 = 'C:\Users\HomePC\Documents\QE Lab\Thesis\Er_YAG
Data\Er_YAG_50_Per_Pillbox\lms Pulse\808nm
Pump\No_3um\4_29_2018\C2Er_YAG_50Per_11I2_808nm_lms00006.csv';
Hv1 = 'C:\Users\HomePC\Documents\QE Lab\Thesis\Er_YAG
Data\Er_YAG_50_Per_Pillbox\lms Pulse\808nm
Pump\No_3um\4_29_2018\C2Er_YAG_50Per_11I2_808nm_lms00007.csv';
```

```
Hv2 = 'C:\Users\HomePC\Documents\QE Lab\Thesis\Er_YAG
Data\Er_YAG_50_Per_Pillbox\lms Pulse\808nm
Pump\No_3um\4_29_2018\C2Er_YAG_50Per_11I2_808nm_lms00008.csv';
Hv3 = 'C:\Users\HomePC\Documents\QE Lab\Thesis\Er_YAG
Data\Er_YAG_50_Per_Pillbox\lms Pulse\808nm
Pump\No_3um\4_29_2018\C2Er_YAG_50Per_11I2_808nm_lms00009.csv';
Hv4 = 'C:\Users\HomePC\Documents\QE Lab\Thesis\Er_YAG
Data\Er_YAG_50_Per_Pillbox\lms Pulse\808nm
Pump\No_3um\4_29_2018\C2Er_YAG_50Per_11I2_808nm_lms00010.csv';
```

```
Hu0 = 'C:\Users\HomePC\Documents\QE Lab\Thesis\Er_YAG
Data\Er_YAG_50_Per_Pillbox\lms Pulse\808nm
Pump\No_3um\4_29_2018\C4Er_YAG_50Per_11I2_808nm_lms00006.csv';
Hu1 = 'C:\Users\HomePC\Documents\QE Lab\Thesis\Er_YAG
Data\Er_YAG_50_Per_Pillbox\lms Pulse\808nm
Pump\No_3um\4_29_2018\C4Er_YAG_50Per_11I2_808nm_lms00007.csv';
Hu2 = 'C:\Users\HomePC\Documents\QE Lab\Thesis\Er_YAG
Data\Er_YAG_50_Per_Pillbox\lms Pulse\808nm
Pump\No_3um\4_29_2018\C4Er_YAG_50Per_11I2_808nm_lms00008.csv';
Hu3 = 'C:\Users\HomePC\Documents\QE Lab\Thesis\Er_YAG
Data\Er_YAG_50_Per_Pillbox\lms Pulse\808nm
Pump\No_3um\4_29_2018\C4Er_YAG_50Per_11I2_808nm_lms00009.csv';
Hu4 = 'C:\Users\HomePC\Documents\QE Lab\Thesis\Er_YAG
Data\Er_YAG_50_Per_Pillbox\lms Pulse\808nm
Pump\No_3um\4_29_2018\C4Er_YAG_50Per_11I2_808nm_lms00010.csv';
```

```
%{
% 50 Percent Pillbox 808nm CW
% 500 Mega Samples/sec
Hv0 = 'C:\Users\HomePC\Documents\QE Lab\Thesis\Er_YAG
Data\Er_YAG_50_Per_Pillbox\CW Scan\808nm
Pump\No_3um\4_29_2018\C2Er_YAG_50Per_11I2_808nm_CW00003.csv';
Hv1 = 'C:\Users\HomePC\Documents\QE Lab\Thesis\Er_YAG
Data\Er_YAG_50_Per_Pillbox\CW Scan\808nm
Pump\No_3um\4_29_2018\C2Er_YAG_50Per_11I2_808nm_CW00004.csv';
Hv2 = 'C:\Users\HomePC\Documents\QE Lab\Thesis\Er_YAG
Data\Er_YAG_50_Per_Pillbox\CW Scan\808nm
Pump\No_3um\4_29_2018\C2Er_YAG_50Per_11I2_808nm_CW00006.csv';
Hv3 = 'C:\Users\HomePC\Documents\QE Lab\Thesis\Er_YAG
Data\Er_YAG_50_Per_Pillbox\CW Scan\808nm
Pump\No_3um\4_29_2018\C2Er_YAG_50Per_11I2_808nm_CW00008.csv';
Hv4 = 'C:\Users\HomePC\Documents\QE Lab\Thesis\Er_YAG
Data\Er_YAG_50_Per_Pillbox\CW Scan\808nm
Pump\No_3um\4_29_2018\C2Er_YAG_50Per_11I2_808nm_CW00010.csv';
```

```
Hu0 = 'C:\Users\HomePC\Documents\QE Lab\Thesis\Er_YAG
Data\Er_YAG_50_Per_Pillbox\CW Scan\808nm
Pump\No_3um\4_29_2018\C4Er_YAG_50Per_11I2_808nm_CW00003.csv';
Hu1 = 'C:\Users\HomePC\Documents\QE Lab\Thesis\Er_YAG
Data\Er_YAG_50_Per_Pillbox\CW Scan\808nm
Pump\No_3um\4_29_2018\C4Er_YAG_50Per_11I2_808nm_CW00004.csv';
Hu2 = 'C:\Users\HomePC\Documents\QE Lab\Thesis\Er_YAG
Data\Er_YAG_50_Per_Pillbox\CW Scan\808nm
Pump\No_3um\4_29_2018\C4Er_YAG_50Per_11I2_808nm_CW00006.csv';
```

```

Hu3 = 'C:\Users\HomePC\Documents\QE Lab\Thesis\Er_YAG
Data\Er_YAG_50_Per_Pillbox\CW Scan\808nm
Pump\No_3um\4_29_2018\C4Er_YAG_50Per_11I2_808nm_CW00008.csv';
Hu4 = 'C:\Users\HomePC\Documents\QE Lab\Thesis\Er_YAG
Data\Er_YAG_50_Per_Pillbox\CW Scan\808nm
Pump\No_3um\4_29_2018\C4Er_YAG_50Per_11I2_808nm_CW00010.csv';
%}

```

```

%{
% 50 Percent Waveguide 808nm Pulsed
% 500 Mega Samples/sec
Hv0 = 'C:\Users\HomePC\Documents\QE Lab\Thesis\Er_YAG
Data\Er_YAG_50_Per_WG\lms Pulse\808nm
Pump\No_3um\C2Er_YAG_50Per_11I2_808nm_lms00001.csv';
Hv1 = 'C:\Users\HomePC\Documents\QE Lab\Thesis\Er_YAG
Data\Er_YAG_50_Per_WG\lms Pulse\808nm
Pump\No_3um\C2Er_YAG_50Per_11I2_808nm_lms00002.csv';
Hv2 = 'C:\Users\HomePC\Documents\QE Lab\Thesis\Er_YAG
Data\Er_YAG_50_Per_WG\lms Pulse\808nm
Pump\No_3um\C2Er_YAG_50Per_11I2_808nm_lms00004.csv';
Hv3 = 'C:\Users\HomePC\Documents\QE Lab\Thesis\Er_YAG
Data\Er_YAG_50_Per_WG\lms Pulse\808nm
Pump\No_3um\C2Er_YAG_50Per_11I2_808nm_lms00005.csv';
Hv4 = 'C:\Users\HomePC\Documents\QE Lab\Thesis\Er_YAG
Data\Er_YAG_50_Per_WG\lms Pulse\808nm
Pump\No_3um\C2Er_YAG_50Per_11I2_808nm_lms00006.csv';

```

```

Hu0 = 'C:\Users\HomePC\Documents\QE Lab\Thesis\Er_YAG
Data\Er_YAG_50_Per_WG\lms Pulse\808nm
Pump\No_3um\C4Er_YAG_50Per_11I2_808nm_lms00001.csv';
Hu1 = 'C:\Users\HomePC\Documents\QE Lab\Thesis\Er_YAG
Data\Er_YAG_50_Per_WG\lms Pulse\808nm
Pump\No_3um\C4Er_YAG_50Per_11I2_808nm_lms00002.csv';
Hu2 = 'C:\Users\HomePC\Documents\QE Lab\Thesis\Er_YAG
Data\Er_YAG_50_Per_WG\lms Pulse\808nm
Pump\No_3um\C4Er_YAG_50Per_11I2_808nm_lms00004.csv';
Hu3 = 'C:\Users\HomePC\Documents\QE Lab\Thesis\Er_YAG
Data\Er_YAG_50_Per_WG\lms Pulse\808nm
Pump\No_3um\C4Er_YAG_50Per_11I2_808nm_lms00005.csv';
Hu4 = 'C:\Users\HomePC\Documents\QE Lab\Thesis\Er_YAG
Data\Er_YAG_50_Per_WG\lms Pulse\808nm
Pump\No_3um\C4Er_YAG_50Per_11I2_808nm_lms00006.csv';
%}

```

```

%{
% 50 Percent Waveguide 808nm CW
% 500 Mega Samples/sec
Hv0 = 'C:\Users\HomePC\Documents\QE Lab\Thesis\Er_YAG Data\Er_YAG_50_Per_WG\CW
Scan\808nm Pump\No_3um\C2Er_YAG_50Per_11I2_808nm_CW00000.csv';
Hv1 = 'C:\Users\HomePC\Documents\QE Lab\Thesis\Er_YAG Data\Er_YAG_50_Per_WG\CW
Scan\808nm Pump\No_3um\C2Er_YAG_50Per_11I2_808nm_CW00001.csv';
Hv2 = 'C:\Users\HomePC\Documents\QE Lab\Thesis\Er_YAG Data\Er_YAG_50_Per_WG\CW
Scan\808nm Pump\No_3um\C2Er_YAG_50Per_11I2_808nm_CW00002.csv';
Hv3 = 'C:\Users\HomePC\Documents\QE Lab\Thesis\Er_YAG Data\Er_YAG_50_Per_WG\CW
Scan\808nm Pump\No_3um\C2Er_YAG_50Per_11I2_808nm_CW00003.csv';

```

```

Hv4 = 'C:\Users\HomePC\Documents\QE Lab\Thesis\Er_YAG Data\Er_YAG_50_Per_WG\CW
Scan\808nm Pump\No_3um\C2Er_YAG_50Per_11I2_808nm_CW00004.csv';

Hu0 = 'C:\Users\HomePC\Documents\QE Lab\Thesis\Er_YAG Data\Er_YAG_50_Per_WG\CW
Scan\808nm Pump\No_3um\C4Er_YAG_50Per_11I2_808nm_CW00000.csv';
Hu1 = 'C:\Users\HomePC\Documents\QE Lab\Thesis\Er_YAG Data\Er_YAG_50_Per_WG\CW
Scan\808nm Pump\No_3um\C4Er_YAG_50Per_11I2_808nm_CW00001.csv';
Hu2 = 'C:\Users\HomePC\Documents\QE Lab\Thesis\Er_YAG Data\Er_YAG_50_Per_WG\CW
Scan\808nm Pump\No_3um\C4Er_YAG_50Per_11I2_808nm_CW00002.csv';
Hu3 = 'C:\Users\HomePC\Documents\QE Lab\Thesis\Er_YAG Data\Er_YAG_50_Per_WG\CW
Scan\808nm Pump\No_3um\C4Er_YAG_50Per_11I2_808nm_CW00003.csv';
Hu4 = 'C:\Users\HomePC\Documents\QE Lab\Thesis\Er_YAG Data\Er_YAG_50_Per_WG\CW
Scan\808nm Pump\No_3um\C4Er_YAG_50Per_11I2_808nm_CW00004.csv';
%}

% I 11/2 Level fluorescence
Wv0 = xlsread(Hv1);
Wv1 = xlsread(Hv1);
Wv2 = xlsread(Hv2);
Wv3 = xlsread(Hv3);
Wv4 = xlsread(Hv4);
A = [Wv0(:,3:4) Wv1(:,3:4) Wv2(:,3:4) Wv3(:,3:4) Wv4(:,3:4)];

% S 3/2 Level Fluorescence
Wu0 = xlsread(Hu0);
Wu1 = xlsread(Hu1);
Wu2 = xlsread(Hu2);
Wu3 = xlsread(Hu3);
Wu4 = xlsread(Hu4);
B = [Wu0(:,3:4) Wu1(:,3:4) Wu2(:,3:4) Wu3(:,3:4) Wu4(:,3:4)];

%{
% 1 Percent Er:YAG Pillbox 808nm Pulsed
% 200 Mega Samples/sec
Hv0 = 'C:\Users\HomePC\Documents\QE Lab\Thesis\Er_YAG Data\Data
Archive\Er_YAG_1_Per_Pillbox\1ms Pulse\808nm
Pump\No_3um\4_29_2018\C2Er_YAG_1Per_11I2_808nm_1ms00000.csv';
Hv1 = 'C:\Users\HomePC\Documents\QE Lab\Thesis\Er_YAG Data\Data
Archive\Er_YAG_1_Per_Pillbox\1ms Pulse\808nm
Pump\No_3um\4_29_2018\C4Er_YAG_1Per_11I2_808nm_1ms00000.csv';
% C:\Users\HomePC\Documents\QE Lab\Thesis\Er_YAG Data\Data
Archive\Er_YAG_1_Per_Pillbox\1ms Pulse\808nm
Pump\No_3um\4_29_2018\C2Er_YAG_1Per_11I2_808nm_1ms00001.csv
% C:\Users\HomePC\Documents\QE Lab\Thesis\Er_YAG Data\Data
Archive\Er_YAG_1_Per_Pillbox\1ms Pulse\808nm
Pump\No_3um\4_29_2018\C4Er_YAG_1Per_11I2_808nm_1ms00001.csv
% C:\Users\HomePC\Documents\QE Lab\Thesis\Er_YAG Data\Data
Archive\Er_YAG_1_Per_Pillbox\1ms Pulse\808nm
Pump\No_3um\4_29_2018\C2Er_YAG_1Per_11I2_808nm_1ms00002.csv
% C:\Users\HomePC\Documents\QE Lab\Thesis\Er_YAG Data\Data
Archive\Er_YAG_1_Per_Pillbox\1ms Pulse\808nm
Pump\No_3um\4_29_2018\C4Er_YAG_1Per_11I2_808nm_1ms00002.csv
% C:\Users\HomePC\Documents\QE Lab\Thesis\Er_YAG Data\Data
Archive\Er_YAG_1_Per_Pillbox\1ms Pulse\808nm
Pump\No_3um\4_29_2018\C2Er_YAG_1Per_11I2_808nm_1ms00003.csv

```

```

% C:\Users\HomePC\Documents\QE Lab\Thesis\Er_YAG Data\Data
Archive\Er_YAG_1_Per_Pillbox\1ms Pulse\808nm
Pump\No_3um\4_29_2018\C4Er_YAG_1Per_11I2_808nm_1ms00003.csv
% C:\Users\HomePC\Documents\QE Lab\Thesis\Er_YAG Data\Data
Archive\Er_YAG_1_Per_Pillbox\1ms Pulse\808nm
Pump\No_3um\4_29_2018\C2Er_YAG_1Per_11I2_808nm_1ms00004.csv
% C:\Users\HomePC\Documents\QE Lab\Thesis\Er_YAG Data\Data
Archive\Er_YAG_1_Per_Pillbox\1ms Pulse\808nm
Pump\No_3um\4_29_2018\C4Er_YAG_1Per_11I2_808nm_1ms00004.csv
%}

% H = 'C:\Users\HomePC\Documents\QE Lab\Thesis\Er_YAG
Data\Er_YAG_50_Per_Pillbox\1ms Pulse\808nm
Pump\No_3um\4_29_2018\C2Er_YAG_50Per_11I2_808nm_1ms00004.csv'
% C:\Users\HomePC\Documents\QE Lab\Thesis\Er_YAG
Data\Er_YAG_50_Per_Pillbox\1ms Pulse\808nm
Pump\No_3um\4_29_2018\C4Er_YAG_50Per_11I2_808nm_1ms00004.csv

% C:\Users\HomePC\Documents\QE Lab\Thesis\Er_YAG Data\Er_YAG_50_Per_WG\1ms
Pulse\808nm Pump\No_3um\C2Er_YAG_50Per_11I2_808nm_1ms00001.csv
% C:\Users\HomePC\Documents\QE Lab\Thesis\Er_YAG Data\Er_YAG_50_Per_WG\1ms
Pulse\808nm Pump\No_3um\C4Er_YAG_50Per_11I2_808nm_1ms00001.csv

X = zeros(length(A(:,1)),5);
X1 = zeros(length(A(:,1)),5);
Y = zeros(length(B(:,1)),5);
Y1 = zeros(length(B(:,1)),5);
k = 1:1:5;
X(:,k) = A(:,(2*k-1));
Y(:,k) = A(:,2*k);
X1(:,k) = B(:,(2*k-1));
Y1(:,k) = B(:,2*k);

% Plotting the transient fluorescence scans of the upper laser level and
% green level
for K = 1:1:5

    figure
    plot(X(:,K)*1E03,Y(:,K)*1E3)
    title(['^4I_{11/2} Fluorescence of the 50% Er:YAG Wave Guide Scan
#',num2str(K)])
    %title('^4S_{3/2} Fluorescence of the 1% Er:YAG Pillbox')
    %title('Pump Intensity')
    xlabel('Time (ms)')
    ylabel('Voltage (mV)')
    xlim([X(1,K)*1E03 X(length(X(:,K)),K)*1E03])
    grid on
    grid minor

    figure
    plot(X1(:,K)*1E03,Y1(:,K)*1E3)
    %title(['^4I_{11/2} Fluorescence of the 1% Er:YAG Pillbox Scan
#',num2str(k)])

```

```

    title(['^4S_{3/2} Fluorescence of the 50% Er:YAG Wave Guide Scan
#',num2str(K)])
    %title('Pump Intensity')
    xlabel('Time (ms)')
    ylabel('Voltage (mV)')
    xlim([X1(1,K)*1E03 X1(length(X1(:,K)),K)*1E03])
    grid on
    grid minor

end

%% FFT
% Some scans were sampled at different rates please see header on csv file
Fs = 5E8; % Sampling frequency (Hz)
%Fs = 2E8; % Sampling Frequency (Hz)
%Fs = 1E9; % Sampling Frequency (Hz)
T = 1/Fs; % Sampling period
L = length(Y(:,1)); % Length of signal subtract last value to
get even length
t = (0:L-1)*T; % Time vector
f = Fs*(0:(L/2))/L;

F = fft(Y(:,k));
P2 = abs(F(:,k)/L); % Two sided spectra
P1 = P2(1:L/2+1,k); % Single Sided Spectra
P1(2:end-1,k) = 2*P1(2:end-1,k);

[aa, indices] = sort(P1, 'descend');
%Mar = 18; % Marker Index to find second harmonic (50% Pillbox 808nm Pulsed)
%Mar = 20; % Marker Index to find second harmonic (50% Pillbox 808nm CW)
Mar = 24; %50 Percent Er:YAG Pillbox 808nm Pulsed
[sh, Ind] = max(P1(Mar:length(P1),:));
Index = Ind + Mar - 1;

F1 = fft(Y1(:,k));
P4 = abs(F1(:,k)/L); % Two sided spectra
P3 = P4(1:L/2+1,k); % Single Sided Spectra
P3(2:end-1,k) = 2*P3(2:end-1,k);

[bb, Indices] = sort(P3, 'descend');

Mx = indices(2,:); % Indices for I 11/2
Mx1 = Indices(1,:); % Indices For S 3/2

%Mx(1,3) = indices(3,3); % Only for 50% WG with 808nm Pulses (Glitch)

U1 = f(:,Mx);
U2 = P1(Mx,:);
UA = [transpose(U1), transpose(U2(1,:))];

```

```

U3 = f(:,Mx1);
U4 = P3(Mx1,:);
UB = [transpose(U3),transpose(U4(1,:))];

Qa = zeros(k);
Qp = zeros(k);
Qb = zeros(k);
Qf = zeros(k);

xL = 2;
xU = 50;

xL1 = 3;
xU1 = 26;
% Plot FFT of fluorescence of upper laser level (with 2nd harmonic) and green
level
for K = 1:1:5

    h = figure;
    hplot = plot(f*1E-3,P1(:,K));
    cursorMode = datacursormode(h);
    hDatatip = cursorMode.createDatatip(hplot);
    pos = [f(Mx(K))*1E-3 P1(Mx(K)) 0];
    set(hDatatip, 'Position', pos)
    HDatatip = cursorMode.createDatatip(hplot);
    posA = [f(Index(K))*1E-3 P1(Index(K)) 0];
    set(HDatatip, 'Position', posA)
    updateDataCursors(cursorMode)
    grid on
    grid minor
    xlim([f(xL)*1E-3 f(xU)*1E-3])
    %ylim([0 15*1E-4]) % adjust axis to fit window
    title(['FFT Of 4I11/2 Fluorescence Scan #',num2str(K)]);
    %title('FFT Of 4S3/2 Fluorescence');
    %title('FFT Of Pump Intensity')
    xlabel('Frequency (kHz)');
    ylabel('Magnititude (V)');

    h1 = figure;
    hplot1 = plot(f*1E-3,P3(:,K));
    cursorModel = datacursormode(h1);
    hDatatip1 = cursorModel.createDatatip(hplot1);
    pos1 = [f(Mx1(K))*1E-3 P3(Mx(K)) 0];
    set(hDatatip1, 'Position', pos1)
    updateDataCursors(cursorModel)
    grid on
    grid minor
    xlim([f(xL1)*1E-3 f(xU1)*1E-3])
    %ylim([0 15*1E-4]) % adjust axis to fit window
    %title(['FFT Of 4I11/2 Fluorescence Scan #',K]);
    title(['FFT Of 4S3/2 Fluorescence Scan #',num2str(K)]);
    %title('FFT Of Pump Intensity')
    xlabel('Frequency (kHz)');
    ylabel('Magnititude (V)');

```

end

```
Av = mean(f(Mx(k)))*1E-3; % Average of Upper laser level oscillation
frequency
Av1 = mean(f(Index(K)))*1E-3; % Average of 2nd harmonic of upper laser level
Av2 = mean(f(Mx1(K)))*1E-3; % Average of green level oscillation frequency
```

```
SD = std(f(Mx(k)))*1E-3; % Std Dev of upper laser level oscillation freq
SD1 = std(f(Index(k)))*1E-3; % Std Dev of 2nd harmonic of upper laser level
SD2 = std(f(Mx1(k)))*1E-3; % Std Dev of green level oscillation freq
```

```
%{
% Plotting Error Bars
figure
err = SD*ones(size(k));
errorbar(k,f(Mx(k))*1E-3,err)
%}
%n = length(X);
%fshift = (-n/2:n/2-1)*(Fs/n);
%yshift = fftshift(F);
%figure
%plot(fshift,abs(yshift))
```

```
%% Rise and Fall Graphs
```

```
% 1 Percent Er:YAG Pillbox 808nm Pulsed
Hv5 = 'C:\Users\HomePC\Documents\QE Lab\Thesis\Er_YAG
Data\Er_YAG_1_Per_Pillbox\1ms Pulse\808nm
Pump\No_3um\4_29_2018\F2Er_YAG_1Per_11I2_808nm_1ms_Rise00000.csv';
Hu5 = 'C:\Users\HomePC\Documents\QE Lab\Thesis\Er_YAG
Data\Er_YAG_1_Per_Pillbox\1ms Pulse\808nm
Pump\No_3um\4_29_2018\F2Er_YAG_1Per_11I2_808nm_1ms_Rise00001.csv';
Hv6 = 'C:\Users\HomePC\Documents\QE Lab\Thesis\Er_YAG
Data\Er_YAG_1_Per_Pillbox\1ms Pulse\808nm
Pump\No_3um\4_29_2018\F2Er_YAG_1Per_11I2_808nm_1ms_Fall00000.csv';
Hu6 = 'C:\Users\HomePC\Documents\QE Lab\Thesis\Er_YAG
Data\Er_YAG_1_Per_Pillbox\1ms Pulse\808nm
Pump\No_3um\4_29_2018\F2Er_YAG_1Per_11I2_808nm_1ms_Fall00001.csv';
```

```
%{
% 50 Percent Er:YAG Pillbox 808nm Pulsed
Hv5 = 'C:\Users\HomePC\Documents\QE Lab\Thesis\Er_YAG
Data\Er_YAG_50_Per_Pillbox\1ms Pulse\808nm
Pump\No_3um\4_29_2018\F2Er_YAG_50Per_11I2_808nm_1ms_Rise00000.csv';
Hu5 = 'C:\Users\HomePC\Documents\QE Lab\Thesis\Er_YAG
Data\Er_YAG_50_Per_Pillbox\1ms Pulse\808nm
Pump\No_3um\4_29_2018\F2Er_YAG_50Per_11I2_808nm_1ms_Rise00001.csv';
Hv6 = 'C:\Users\HomePC\Documents\QE Lab\Thesis\Er_YAG
Data\Er_YAG_50_Per_Pillbox\1ms Pulse\808nm
Pump\No_3um\4_29_2018\F2Er_YAG_50Per_11I2_808nm_1ms_Fall00000.csv';
Hu6 = 'C:\Users\HomePC\Documents\QE Lab\Thesis\Er_YAG
Data\Er_YAG_50_Per_Pillbox\1ms Pulse\808nm
Pump\No_3um\4_29_2018\F2Er_YAG_50Per_11I2_808nm_1ms_Fall00001.csv';
%}
```

```

%{
% 50 Perent Er:YAG Waveguide 808nm Pulsed
Hv5 = 'C:\Users\HomePC\Documents\QE Lab\Thesis\Er_YAG
Data\Er_YAG_50_Per_WG\1ms Pulse\808nm
Pump\No_3um\F2Er_YAG_50Per_11I2_808nm_1ms_RF00000.csv';
Hu5 = 'C:\Users\HomePC\Documents\QE Lab\Thesis\Er_YAG
Data\Er_YAG_50_Per_WG\1ms Pulse\808nm
Pump\No_3um\F1Er_YAG_50Per_11I2_808nm_1ms_RF00002.csv';
Hv6 = 'C:\Users\HomePC\Documents\QE Lab\Thesis\Er_YAG
Data\Er_YAG_50_Per_WG\1ms Pulse\808nm
Pump\No_3um\F2Er_YAG_50Per_11I2_808nm_1ms_RF00001.csv';
Hu6 = 'C:\Users\HomePC\Documents\QE Lab\Thesis\Er_YAG
Data\Er_YAG_50_Per_WG\1ms Pulse\808nm
Pump\No_3um\F1Er_YAG_50Per_11I2_808nm_1ms_RF00002.csv';
%}
Wv5 = xlsread(Hv5); %I11/2
Wu5 = xlsread(Hu5);
Wv6 = xlsread(Hv6); %S3/2
Wu6 = xlsread(Hu6);

figure
plot(Wv5(:,3)*1E03,Wv5(:,4),'Linewidth',1.5)
title('^4I_{11/2} Fluorescence Rise of the 1% Er:YAG Pillbox')
%title('^4S_{3/2} Fluorescence of the 1% Er:YAG Pillbox')
%title('Pump Intensity')
xlabel('Time (ms)')
ylabel('Voltage (V)')
%xlim([X(1,K)*1E03 X(length(X(:,K)),K)*1E03])
grid on
grid minor
[TvR,lt,ut,1l,ul] = risetime(Wv5(:,4),Wv5(:,3)); % I 11/2 Rise
%{
hold on
plot([lt ut],[1l ul],'o')
hold off
%}

%{
Tv9 = find(Wv5(:,4) == round(0.9*max(Wv5(:,4)),4)*1E3,1);
Tv1 = find(Wv5(:,4) == round(0.1*max(Wv5(:,4)),4)*1E3,1);
TvR = Wv5(Tv9,3)-Wv5(Tv1,3);
%}

figure
plot(Wu5(:,3)*1E03,Wu5(:,4),'Linewidth',1.5)
%title(['^4I_{11/2} Fluorescence of the 1% Er:YAG Pillbox Scan
#',num2str(k)])
title('^4S_{3/2} Fluorescence Rise of the 1% Er:YAG Pillbox')
%title('Pump Intensity')
xlabel('Time (ms)')
ylabel('Voltage (V)')
%xlim([X1(1,K)*1E03 X1(length(X1(:,K)),K)*1E03])
grid on

```

```

grid minor
TuR = risetime(Wu5(:,4),Wu5(:,3)); % S 3/2 Rise
%{
Tu9 = round(0.9*max(Wu5(:,4)),4);
Tu1 = round(0.1*max(Wu5(:,4)),4);
TuR = Tu9-Tu1;
%}
figure
plot(Wv6(:,3)*1E03,Wv6(:,4),'Linewidth',1.5)
title('^4I_{11/2} Fluorescence Fall of the 1% Er:YAG Pillbox')
%title('^4S_{3/2} Fluorescence of the 1% Er:YAG Pillbox')
%title('Pump Intensity')
xlabel('Time (ms)')
ylabel('Voltage (V)')
%xlim([X(1,K)*1E03 X(length(X(:,K)),K)*1E03])
grid on
grid minor
TvF = falltime(Wv6(:,4),Wv6(:,3)); % I 11/2 Fall
%{
Tv9a = round(0.9*max(Wv6(:,4)),4);
Tv1a = round(0.1*max(Wv6(:,4)),4);
TvF = Tv9a-Tv1a;
%}
figure
plot(Wu6(:,3)*1E03,Wu6(:,4),'Linewidth',1.5)
%title(['^4I_{11/2} Fluorescence of the 1% Er:YAG Pillbox Scan
#',num2str(k)])
title('^4S_{3/2} Fluorescence Fall of the 1% Er:YAG Pillbox')
%title('Pump Intensity')
xlabel('Time (ms)')
ylabel('Voltage (V)')
%xlim([X1(1,K)*1E03 X1(length(X1(:,K)),K)*1E03])
grid on
grid minor
TuF = falltime(Wu6(:,4),Wu6(:,3)); % S 3/2 Fall
%{
Tu9a = round(0.9*max(Wu6(:,4)),4);
Tula = round(0.1*max(Wu6(:,4)),4);
TuF = Tu9a-Tula;
%}

%% Plot Beam Profile Of The Pumps
Hv7 = 'C:\Users\HomePC\Documents\QE Lab\Thesis\Er_YAG Data\Beam
Measurements\962nm\8_26_2018\F2Beam_960nm00967.csv';
Hu7 = 'C:\Users\HomePC\Documents\QE Lab\Thesis\Er_YAG Data\Beam
Measurements\808nm\8_29_2018\F2Beam_808nm00009.csv';

Wv7 = xlsread(Hv7); %962nm beam
Wu7 = xlsread(Hu7); %808nm beam

[U U1] = max(Wv7(:,4));
[U2 U3] = max(Wu7(:,4));

h2 = figure;
hplot2 = plot(Wv7(:,3)*1E6,Wv7(:,4)*1E3);

```

```

cursorMode2 = datacursormode(h2);
hDatatip2 = cursorMode2.createDatatip(hplot2);
pos2 = [Wv7(U1,3)*1E6 Wv7(U1,4) 0];
set(hDatatip2, 'Position', pos2)
updateDataCursors(cursorMode2)
%title(['^4I_{11/2} Fluorescence of the 50% Er:YAG Wave Guide Scan
#',num2str(K)])
%title('^4S_{3/2} Fluorescence of the 1% Er:YAG Pillbox')
title('962nm Pump Intensity','Linewidth',1.5)
xlabel('Time (\mus)')
ylabel('Voltage (mV)')
%xlim([X(1,K)*1E03 X(length(X(:,K)),K)*1E03])
grid on
grid minor

h3 = figure;
hplot3 = plot(Wu7(:,3)*1E6,Wu7(:,4)*1E3,'Linewidth',1.5);
cursorMode3 = datacursormode(h3);
hDatatip3 = cursorMode3.createDatatip(hplot3);
pos3 = [Wu7(U3,3)*1E6 Wu7(U3,4) 0];
set(hDatatip3, 'Position', pos3)
updateDataCursors(cursorMode3)
%title(['^4I_{11/2} Fluorescence of the 50% Er:YAG Wave Guide Scan
#',num2str(K)])
%title('^4S_{3/2} Fluorescence of the 1% Er:YAG Pillbox')
title('808nm Pump Intensity')
xlabel('Time (\mus)')
ylabel('Voltage (mV)')
%xlim([X(1,K)*1E03 X(length(X(:,K)),K)*1E03])
grid on
grid minor

%% Do FFT on Instability only
%{
% Use cursor to find floor of the oscillation for every plot

W = find(Y>= 4.659);
V = X(W);
Z = Y(W);
figure
plot(V,Z)
grid on
grid minor

L1 = length(Z);           % Length of signal subtract last value to get even
length
t1 = (0:L1-1)*T;         % Time vector
f1 = Fs*(0:(L1/2))/L1;

F1 = fft(Z);
P4 = abs(F1/L1);         % Two sided spectra

```

```
P3 = P4(1:L1/2+1);      % Single Sided Spectra
P3(2:end-1) = 2*P3(2:end-1);

figure
plot(f1,P3)
grid on
grid minor
%axis([0 1E6 0 max(P3)]) % adjust axis to fit window
%}
% Seem to notice a 4.3 MHz and 6.3 MHz spikes
```

# Bibliography

- 1) Liu, Brad Chun-Ting. "Investigation of Dynamic Behavior in Erbium-Doped Yttrium Aluminum Garnet and Yttria." *University of California, Los Angeles*, ProQuest LLC, 2015.
- 2) Joshi, Abhijeet, et al. "Small-signal gain measurements for highly doped and co-doped  $\text{Er}^{3+}$  : YAG at 2.936  $\mu\text{m}$ ." *Optics & Laser Technology* 56 (2014): 58-64.
- 3) Furtado, Mario K., et al. "Multiphonon relaxation studies of  $^4I_{11/2}$  and  $^4I_{13/2}$  energy levels in Er:YAG and Er,Pr:YAG laser crystals." *Advanced Solid-State Photonics*. Optical Society of America, 2005.
- 4) Liu, Brad Chun-Ting, Ramesh K. Shori, and Oscar M. Stafsudd. "Direct measurement of up-conversion processes in diode pumped erbium-doped YAG." *Solid State Lasers XXIV: Technology and Devices*. Vol. 9342. International Society for Optics and Photonics, 2015.
- 5) Shori, Ramesh K., et al. "Lasing characteristics of free-running and Q-switched high-energy 2.69- $\mu\text{m}$  Cr, Tm, Er: YAG laser." *Solid State Lasers IX*. Vol. 3929. International Society for Optics and Photonics, 2000.
- 6) Shori, Ramesh K., et al. "Quantification and modeling of the dynamic changes in the absorption coefficient of water at  $\lambda = 2.94\mu\text{m}$ ." *IEEE Journal of selected topics in quantum electronics* 7.6 (2001): 959-970.
- 7) Diaci, Janez, and Boris Gaspirc. "Comparison of Er:YAG and Er, Cr:YSGG lasers used in dentistry." *J laser health Acad* 1.1 (2012): 1-13.

- 8) Moritz, A., et al. "The bactericidal effect of Nd: YAG, Ho:YAG, and Er:YAG laser irradiation in the root canal: an in vitro comparison." *Journal of clinical laser medicine & surgery* 17.4 (1999): 161-164.
- 9) Trauner, Kenneth, Norman Nishioka, and Dinesh Patel. "Pulsed holmium: yttrium-aluminum-garnet (Ho:YAG) laser ablation of fibrocartilage and articular cartilage." *The American journal of sports medicine* 18.3 (1990): 316-320.
- 10) Budni, P. A., et al. "Efficient mid-infrared laser using 1.9- $\mu$ m-pumped Ho: YAG and ZnGeP<sub>2</sub> optical parametric oscillators." *JOSA B* 17.5 (2000): 723-728.
- 11) Stoneman, R. C., and L. Esterowitz. "Efficient, broadly tunable, laser-pumped Tm:YAG and Tm:YSGG cw lasers." *Optics letters* 15.9 (1990): 486-488.
- 12) Suni, Paul JM, and Sammy W. Henderson. "1-mJ/pulse Tm:YAG laser pumped by a 3-W diode laser." *Optics letters* 16.11 (1991): 817-819.
- 13) Lai, K. S., et al. "120-W continuous-wave diode-pumped Tm:YAG laser." *Optics letters* 25.21 (2000): 1591-1593.
- 14) Pinto, Joseph F., Leon Esterowitz, and Gregg H. Rosenblatt. "Continuous-wave mode-locked 2- $\mu$ m Tm: YAG laser." *Optics letters* 17.10 (1992): 731-732.
- 15) Dinerman, Bradley J., and Peter F. Moulton. "3- $\mu$ m cw laser operations in erbium-doped YSGG, GGG, and YAG." *Optics letters* 19.15 (1994): 1143-1145.
- 16) Chen, Da-Wun, et al. "Diode-pumped 1-W continuous-wave Er:YAG 3- $\mu$ m laser." *Optics letters* 24.6 (1999): 385-387.
- 17) Sousa, John Gary, David Welford, and Josh Foster. "Efficient, 1.5 W CW and 7mJ quasi-CW TEM 00 mode operation of a compact diode-laser-pumped 2.94  $\mu$ m Er:YAG

- laser." *Solid State Lasers XIX: Technology and Devices*. Vol. 7578. International Society for Optics and Photonics, 2010.
- 18) Barnes, Norman P., et al. "Measurement of Up Conversion in Er:YAG and Influence on Laser Performance." *IEEE Journal of Quantum Electronics* 49.2 (2013): 238-246.
  - 19) Walsh, Brian M., Keith E. Murray, and Norman P. Barnes. "Cr:Er:Tm:Ho:yttrium aluminum garnet laser exhibiting dual wavelength lasing at 2.1 and 2.9  $\mu\text{m}$ : Spectroscopy and laser performance." *Journal of applied physics* 91.1 (2002): 11-17.
  - 20) Barnes, Norman P., et al. "Up conversion measurements in Er:YAG; comparison with 1.6  $\mu\text{m}$  laser performance." *Optical Materials Express* 1.4 (2011): 678-685.
  - 21) Spangler, Lee H., et al. "A computational study of host effects on Er<sup>3+</sup> upconversion and self-quenching efficiency in ten garnets." *Journal of applied physics* 79.2 (1996): 573-577.
  - 22) Toma, Octavian, and Serban Georgescu. "Dynamics of an upconversion Er:YAG laser with reabsorption losses." *JOSA B* 21.9 (2004): 1630-1637.
  - 23) Georgescu, Serban, and Octavian Toma. "Er:YAG three-micron laser: performances and limits." *IEEE Journal of selected topics in quantum electronics* 11.3 (2005): 682-689.
  - 24) Georgescu, Serban. "Mathematical modeling of 3- $\mu\text{m}$  Erbium lasers." *Proceedings of The First French-Romanian Colloquium of Numerical Physics*. 2000.
  - 25) Georgescu, Serban, Octavian Toma, and H. Totia. "Intrinsic limits of the efficiency of erbium 3- $\mu\text{m}$  lasers." *IEEE journal of quantum electronics* 39.6 (2003): 722-732.
  - 26) Georgescu, Serban, and Octavian Toma. "Energy transfer processes in Er-doped crystals." *physica status solidi (c)* 2.1 (2005): 280-283.

- 27) Georgescu, S., O. Toma, and I. Ivanov. "Upconversion from the  $^4I_{13/2}$  and  $^4I_{11/2}$  levels in Er:YAG." *Journal of luminescence* 114.1 (2005): 43-52.
- 28) Georgescu, S., et al. "Excited-state-absorption in low concentrated Er:YAG crystals for pulsed and cw pumping." *Journal of luminescence* 93.4 (2001): 281-292.
- 29) Georgescu, S., et al. "Concentration effects on the up-conversion from the  $^4I_{13/2}$  level of Er<sup>3+</sup> in YAG." *Optics communications* 81.3-4 (1991): 186-192.
- 30) Toma, Octavian, and Serban Georgescu. "Dynamics of an Upconversion Er:YAG Laser with Reabsorption Losses." *Journal of the Optical Society of America B*, vol. 21, no. 9, Sept. 2004, p. 1630. *Crossref*, doi:10.1364/JOSAB.21.001630.
- 31) Georgescu, S., et al. "ESA Processes Responsible for Infrared Pumped, Green and Violet Luminescence in Low-Concentrated Er:YAG." *Journal of Luminescence*, vol. 101, no. 1–2, Jan. 2003, pp. 87–99. *Crossref*, doi:10.1016/S0022-2313(02)00392-7.
- 32) Lupei, Voicu, Serban Georgescu, and V. Florea. "On the dynamics of population inversion for 3  $\mu\text{m}$  Er<sup>3+</sup> lasers." *IEEE journal of quantum electronics* 29.2 (1993): 426-434.
- 33) Georgescu, Serban, and Voicu Lupei. "Q-switch regime of 3 $\mu\text{m}$  Er:YAG lasers." *IEEE journal of quantum electronics* 34.6 (1998): 1031-1040.
- 34) Georgescu, S., et al. "Population dynamics of the three-micron emitting level of Er<sup>3+</sup> in YAlO<sub>3</sub>." *Journal of applied physics* 80.12 (1996): 6610-6613.
- 35) Zharikov, Evgeny V., et al. "Stimulated emission from Er<sup>3+</sup> ions in yttrium aluminum garnet crystals at  $\lambda = 2.94 \mu\text{m}$ ." *Soviet Journal of Quantum Electronics* 4.8 (1975): 1039.
- 36) Bagdasarov, Khachik S., et al. "Steady-state emission from a Y<sub>3</sub>Al<sub>5</sub>O<sub>12</sub>: Er<sup>3+</sup> laser ( $\lambda = 2.94 \mu\text{m}$ , T = 300° K)." *Soviet Journal of Quantum Electronics* 13.2 (1983): 262.

- 37) Zhekov, V. I., et al. "Cooperative process in  $\text{Y}_3\text{Al}_5\text{O}_{12}:\text{Er}^{3+}$  crystals." *Soviet Journal of Quantum Electronics* 16.2 (1986): 274.
- 38) Zhekov, V. I., et al. "Mechanism of a population inversion between the  ${}^4I_{11/2}$  and  ${}^4I_{13/2}$  levels of the  $\text{Er}^{3+}$  ion in  $\text{Y}_3\text{Al}_5\text{O}_{12}$  crystals." *Quantum Electronics* 10.4 (1980): 428-430.
- 39) Zharikov, Evgeny V., et al. "Cross section of the  ${}^4I_{11/2}-{}^4I_{13/2}$  laser transition in  $\text{Er}^{3+}$  ions in yttrium-erbium-aluminum garnet crystals." *Soviet Journal of Quantum Electronics* 7.1 (1977): 117.
- 40) Zhekov, V. I., et al. "Efficient cross-relaxation laser emitting at  $\lambda = 2.94 \mu\text{m}$ ." *Soviet Journal of Quantum Electronics* 13.9 (1983): 1235.
- 41) Zhekov, V. I., et al. "Cooperative phenomena in yttrium erbium aluminum garnet crystals." *Quantum Electronics* 14.1 (1984): 128-130.
- 42) Koetke, J., and G. Huber. "Infrared excited-state absorption and stimulated-emission cross sections of  $\text{Er}^{3+}$ -doped crystals." *Applied Physics B* 61.2 (1995): 151-158.
- 43) Le Boulanger, P., et al. "Excited-state absorption spectroscopy of  $\text{Er}^{3+}$ -doped  $\text{Y}_3\text{Al}_5\text{O}_{12}$ ,  $\text{YVO}_4$ , and phosphate glass." *Physical Review B* 60.16 (1999): 11380.
- 44) Liu, M., et al. "Dominant red emission ( ${}^4F_{9/2} \rightarrow {}^4I_{15/2}$ ) via upconversion in YAG ( $\text{Y}_3\text{Al}_5\text{O}_{12}$ ):  $\text{Yb}^{3+}$ ,  $\text{Er}^{3+}$  nanopowders." *Optical Materials* 29.11 (2007): 1352-1357.
- 45) Sardar, Dhiraj K., et al. "Absorption intensities and emission cross sections of principal intermanifold and inter-Stark transitions of  $\text{Er}^{3+}$  ( $4f^{11}$ ) in polycrystalline ceramic garnet  $\text{Y}_3\text{Al}_5\text{O}_{12}$ ." *Journal of applied physics* 97.12 (2005): 123501.
- 46) Gruber, John B., et al. "Spectral analysis and energy-level structure of  $\text{Er}^{3+}$  ( $4f^{11}$ ) in polycrystalline ceramic garnet  $\text{Y}_3\text{Al}_5\text{O}_{12}$ ." *Journal of applied physics* 97.6 (2005): 063519.

- 47) Gruber, John B., et al. "Analyses of the ultraviolet spectra of Er<sup>3+</sup> in Er<sub>2</sub>O<sub>3</sub> and Er<sup>3+</sup> in Y<sub>2</sub>O<sub>3</sub>." *Journal of Applied Physics* 108.2 (2010): 023109.
- 48) Miniscalco, William J., and Richard S. Quimby. "General procedure for the analysis of Er<sup>3+</sup> cross sections." *Optics letters* 16.4 (1991): 258-260.
- 49) Shi, W. Q., Michael Bass, and Milton Birnbaum. "Effects of energy transfer among Er<sup>3+</sup> ions on the fluorescence decay and lasing properties of heavily doped Er:Y<sub>3</sub>Al<sub>5</sub>O<sub>12</sub>." *JOSA B* 7.8 (1990): 1456-1462.
- 50) Bass, M., et al. "Operation of the High Dopant Density Er:YAG at 2.94 μm." *Tunable Solid-State Lasers II*. Springer, Berlin, Heidelberg, 1986. 300-305.
- 51) Dexter, David L. "A theory of sensitized luminescence in solids." *The Journal of Chemical Physics* 21.5 (1953): 836-850.
- 52) Dexter, D. L. "Cooperative optical absorption in solids." *Physical Review* 126.6 (1962).
- 53) Förster, Th. "Zwischenmolekulare energiewanderung und fluoreszenz." *Annalen der physik* 437.1-2 (1948): 55-75.
- 54) Inokuti, Mitio, and Fumio Hirayama. "Influence of energy transfer by the exchange mechanism on donor luminescence." *The Journal of Chemical Physics* , 43.6(1965): 1978-1989
- 55) Wang, Hong, et al. "Up-conversion luminescence of Y<sub>2</sub>O<sub>3</sub>: Yb, Er under 1.55 μm excitation." *Ceramics International* 41.1 (2015): 259-263.
- 56) Zhou, Jun, et al. "Upconversion luminescence of high content Er-doped YAG transparent ceramics." *Ceramics International* 36.1 (2010): 193-197.
- 57) Zhou, Jun, et al. "Optical properties of Er, Yb co-doped YAG transparent ceramics." *Ceramics International* 37.2 (2011): 513-519.

- 58) Qin, Guanshi, et al. "Upconversion luminescence of Er<sup>3+</sup> in highly transparent YAG ceramics." *Solid State Communications* 132.2 (2004): 103-106.
- 59) Tang, Pinghua, et al. "Stable high-energy Q-switched resonantly diode-pumped Er:YAG laser at 1645 nm." *Applied optics* 53.32 (2014): 7773-7777.
- 60) Schweizer, T., et al. "Spectroscopic properties and diode pumped 1.6 μm laser performance in Yb-codoped Er:Y<sub>3</sub>Al<sub>5</sub>O<sub>12</sub> and Er:Y<sub>2</sub>SiO<sub>5</sub>." *Optics Communications* 118.5-6 (1995): 557-561.
- 61) Eichhorn, Marc, et al. "Spectroscopic properties of Er<sup>3+</sup>: YAG at 300–550 K and their effects on the 1.6 μm laser transitions." *Applied Physics B* 91.2 (2008): 249-256.
- 62) Merkle, Larry D., et al. Temperature Dependence of a Diode-pumped Cryogenic Erbium (Er): Yttrium Aluminum Garnet (YAG) Laser. No. ARL-TR-4885. ARMY RESEARCH LAB ADELPHI MD, 2009.
- 63) Barbosa-García, Oracio, et al. "Neodymium-to-erbium nonradiative energy transfer and fast initial fluorescence decay of the <sup>4</sup>F<sub>3/2</sub> state of neodymium in garnet crystals." *JOSA B* 14.10 (1997): 2731-2734.
- 64) Silversmith, Ann. "Upconversion excitation of green fluorescence in Er:YAG." *Journal of luminescence* 60 (1994): 636-639.
- 65) Xu, H. L., and Stefan Kröll. "Upconversion dynamics in Er<sup>3+</sup> -doped YAG." *Journal of luminescence* 111.3 (2005): 191-198.
- 66) Jander, Peter, Jayanta K. Sahu, and W. Andrew Clarkson. "High-power Er:YAG laser at 1646 nm pumped by an Er, Yb fiber laser." *Solid State Laser Technologies and Femtosecond Phenomena*. Vol. 5620. International Society for Optics and Photonics, 2004.

- 67) Sumida, D. S., and T. Y. Fan. "Effect of radiation trapping on fluorescence lifetime and emission cross section measurements in solid-state laser media." *Optics letters* 19.17 (1994): 1343-1345.
- 68) Sugawara, Toshiki, et al. "Observation of synchronization in laser chaos." *Physical review letters* 72.22 (1994): 3502.
- 69) Arecchi, F. T. "The physics of laser chaos." *Nuclear Physics B-Proceedings Supplements* 2 (1987): 13-24.
- 70) Goedgebuer, Jean-Pierre, Laurent Larger, and Henri Porte. "Optical cryptosystem based on synchronization of hyperchaos generated by a delayed feedback tunable laser diode." *Physical Review Letters* 80.10 (1998): 2249.
- 71) Fischer, Ingo, Yun Liu, and Peter Davis. "Synchronization of chaotic semiconductor laser dynamics on subnanosecond time scales and its potential for chaos communication." *Physical Review A* 62.1 (2000): 011801.
- 72) Dykstra, Robert, Ding Y. Tang, and Norman R. Heckenberg. "Experimental control of single-mode laser chaos by using continuous, time-delayed feedback." *Physical Review E* 57.6 (1998): 6596.
- 73) Lin, Fan-Yi, and Jia-Ming Liu. "Chaotic radar using nonlinear laser dynamics." *IEEE Journal of Quantum Electronics* 40.6 (2004): 815-820.
- 74) Powell, Richard C. *Physics of solid-state laser materials*. Vol. 1. Springer Science & Business Media, 1998.
- 75) Lakowicz, Joseph R. *Principles of Fluorescence Spectroscopy*. 2nd ed., Springer, 1999.
- 76) Siegman, Anthony E. *Lasers*. University Science Books, 1986

- 77) Ursu, I., et al. "Energy transfer characteristics of the  $^4S_{3/2}$  level of  $Er^{3+}$  in YAG." *Optics communications* 72.3-4 (1989): 209-213.
- 78) Song, Feng, et al. "Three-photon phenomena in the upconversion luminescence of erbium–ytterbium-codoped phosphate glass." *Applied Physics Letters* 79.12 (2001): 1748-1750.
- 79) Knowles, David S. *Energy Transfer Under Strong Pumping in High Concentration Rare Earth Doped Laser Crystals*. No. TR-1. MASSACHUSETTS INST OF TECH CAMBRIDGE CENTER FOR MATERIALS SCIENCE AND ENGINEERING, 1991.
- 80) Brede, R., et al. "Green Up-conversion Laser Emission in Er-doped Crystals at Room Temperature." *Applied Physics Letters*, vol. 63, no. 15, Oct. 1993, pp. 2030–31. *Crossref*, doi:10.1063/1.110581.
- 81) Zou, Xuelu, and Teturo Izumitani. "Spectroscopic Properties and Mechanisms of Excited State Absorption and Energy Transfer Upconversion for  $Er^{3+}$  -Doped Glasses." *Journal of Non-Crystalline Solids*, vol. 162, no. 1–2, Sept. 1993, pp. 68–80. *Crossref*, doi:10.1016/0022-3093(93)90742-G.
- 82) Danger, T., et al. "Spectroscopy and Green Upconversion Laser Emission of  $Er^{3+}$  -doped Crystals at Room Temperature." *Journal of Applied Physics*, vol. 76, no. 3, Aug. 1994, pp. 1413–22. *Crossref*, doi:10.1063/1.357745.
- 83) Pollnau, M., et al. "Time-Resolved Spectra of Excited-State Absorption in  $Er^{3+}$  Doped  $YAlO_3$ ." *Applied Physics A Solids and Surfaces*, vol. 54, no. 5, May 1992, pp. 404–10. *Crossref*, doi:10.1007/BF00324164.

- 84) Schweizer, T., et al. "Spectroscopic properties and diode pumped 1.6  $\mu\text{m}$  laser performance in Yb-codoped Er:Y<sub>3</sub>Al<sub>5</sub>O<sub>12</sub> and Er:Y<sub>2</sub>SiO<sub>5</sub>." *Optics Communications* 118.5-6 (1995): 557-561.
- 85) Xu, Huailiang, and Zhankui Jiang. "Ultraviolet and violet upconversion luminescence in Er 3+-doped yttrium aluminum garnet crystals." *Physical Review B* 66.3 (2002): 035103.
- 86) Minelly, J. D., et al. "Diode-array pumping of E<sup>3+</sup>/Yb<sup>3+</sup> Co-doped fiber lasers and amplifiers." *IEEE Photonics Technology Letters* 5.3 (1993): 301-303.
- 87) Wojtowicz, A. J. "Physics of Solid-State Laser Materials." *Acta Physica Polonica A* 80.2 (1991): 193-205.
- 88) Self, Sidney A. "Focusing of spherical Gaussian beams." *Applied optics* 22.5 (1983): 658-661.
- 89) Yoshida, A., and T. Asakura. "A simple technique for quickly measuring the spot size of Gaussian laser beams." *Optics & Laser Technology* 8.6 (1976): 273-274.
- 90) Sedra, Adel S., and Kenneth C. Smith. *Microelectronic Circuits*. 6th ed., Oxford University Press, 2009